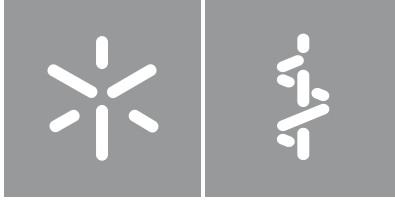**Universidade do Minho**
Escola de Medicina

João Luís Gomes da Fonseca

Surgical Navigation System for Percutaneous Renal Access: electromagnetic guidance and imaging working together

dezembro de 2020

Universidade do Minho
Escola de Medicina

João Luís Gomes da Fonseca

Surgical Navigation System for Percutaneous Renal Access: electromagnetic guidance and imaging working together

Tese de Doutoramento
Ciências da Saúde

Trabalho efetuado sob a orientação do
Professor Doutor Estêvão Augusto Rodrigues Lima
e do
Professor Doutor João Luís Araújo Martins Vilaça

dezembro de 2020

DIREITOS DE AUTOR E CONDIÇÕES DE UTILIZAÇÃO DO TRABALHO POR TERCEIROS

Este é um trabalho académico que pode ser utilizado por terceiros desde que respeitadas as regras e boas práticas internacionalmente aceites, no que concerne aos direitos de autor e direitos conexos.

Assim, o presente trabalho pode ser utilizado nos termos previstos na licença abaixo indicada.

Caso o utilizador necessite de permissão para poder fazer um uso do trabalho em condições não previstas no licenciamento indicado, deverá contactar o autor, através do RepositóriUM da Universidade do Minho.

Acknowledgements

At the end of this thesis, I would like to manifest my esteem and gratitude to everyone who traveled with me along this journey. First and foremost, I would like to thank my supervisors, Professors Estêvão Lima and João Vilaça, for their guidance, encouragement, and advice over the last years. To Professor Estêvão Lima, I would like to thank you for the passion that you put into all your projects, and also your effort in giving me the best conditions as possible to successfully conclude this thesis. To Professor João Vilaça, I truly appreciate your friendship, for challenging me with this project, and continuous motivation. Thank you for giving me opportunities to grow scientifically, academically, and professionally. I would also like to acknowledge the board of directors of the School of Medicine, ICVS, and Surgical Sciences Research Domain for all their institutional support. To all members of iSurgical3D (Professor António Marques Pinto, Professor Jaime Fonseca, Professor João Vilaça, Professor Jorge Correia-Pinto, and Manuel Gomes), I am thankful for your support during this thesis. This journey would not be possible without the important contribution of several colleagues.

Agradeço-vos, Sandro e Pedro, pela vossa disponibilidade diária, pelas discussões e novas ideias, pela preparação de documentos e experiências, por ter aprendido convosco a ser mais investigador e, principalmente, pelo companheirismo e amizade. Agradeço também aos restantes colegas, amigos e coautores, Alice, António, Bruno, Fernando, Helena, e Pedro pelo vosso trabalho, ideias e críticas que tanto ajudaram a aprimorar esta tese, acompanhadas diariamente de um enorme companheirismo. Não posso, também, deixar de agradecer a todos médicos e técnicos de saúde dos departamentos de Imagiologia e Urologia do Hospital de Braga pela disponibilidade. Igualmente, quero deixar um apreço a todos os membros do ICVS e investigadores do domínio de Ciências Cirúrgicas, especialmente à Manuela e à Rute, assim como agradecer aos colegas dos programas doutorais que se cruzaram comigo nesta jornada. Quero também celebrar esta conquista com todos os outros amigos cujo apoio foi incansável. À minha família, em especial aos meus pais e irmã. Mãe, obrigado por me incentivares a querer ser mais e melhor. Obrigado por seres um exemplo de superação e resiliência. Pai, obrigado pelo exemplo que foste e és, e me mostrares que sermos bons e corretos, em todas as vertentes da vida, é a forma mais nobre de trilharmos este caminho e perdurarmos. Espero que, onde quer que estejas, sintas orgulho deste meu percurso. Rita, obrigado por me tranquilizares nos momentos menos bons e pela força que me transmitiste sempre que precisei. Agradeço-vos o vosso amor incondicional. Por fim, à Margarida, por me mostrares o mais importante na vida, pelo teu apoio e preocupação constantes, e pelo carinho, amizade e amor.
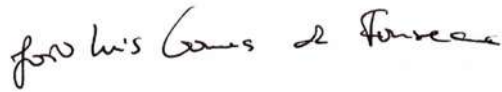
STATEMENT OF INTEGRITY

I hereby declare having conducted this academic work with integrity. I confirm that I have not used plagiarism or any form of undue use of information or falsification of results along the process leading to its elaboration.

I further declare that I have fully acknowledged the Code of Ethical Conduct of the University of Minho.

João Luís Gomes da Fonseca

Sistema de navegação cirúrgica para acesso renal percutâneo: sinergia entre guiamento eletromagnético e imagem

Resumo

O acesso renal percutâneo (ARP) é importante no tratamento de várias doenças renais, sobretudo na nefrolitíase (cálculos renais) através da nefrolitotomia percutânea (NLPC). O sucesso da NLPC depende do acesso inicial ao rim, sendo que uma correta punção diminui as complicações e facilita as etapas cirúrgicas seguintes. Embora o ARP seja convencionalmente guiado por fluoroscopia e/ou ecografia, continua a ser desafiante aprendê-lo e executá-lo. Recentemente, soluções baseadas em *tracking* eletromagnético (TEM) têm sido propostas para auxiliar o ARP, permitindo punções rápidas e precisas ao cálice renal. Porém, limitações ainda subsistem, como a falta da perceção tridimensional (3D) da anatomia ou a incapacidade de aceder ao cálice se obstruído por um cálculo. Para mitigar estas limitações, esta tese focou-se em melhorar as soluções baseadas em TEM através da integração de dados de tomografia axial computadorizada (TAC) pré-operatória e de ecografia intra-operatória, e desenvolver um novo sistema de navegação cirúrgica. Para alcançar este objetivo, as seguintes etapas foram realizadas: (1) estudo do impacto dos instrumentos de ureteroscopia e ecografia na precisão dos sistemas de TEM; (2) desenvolvimento de um protocolo para criar fantomas de rim para avaliar estratégias de fusão de imagens; (3) avaliação num ambiente *in-silico* de uma técnica de registo (baseado em pontos) e de um protocolo de aquisição de imagens intra-operatórias para fundir dados de ecografia e de TAC; (4) proposta de uma nova abordagem intra-operatória para fundir dados de ecografia e TAC, usando uma estratégia de segmentação semi-automática e um algoritmo de registo (baseado em pontos); e (5) integração de todas as contribuições mencionadas num novo sistema de navegação cirúrgica, incluindo características adicionais para melhorar a navegação cirúrgica em tempo real, como: a projeção da trajetória da agulha e da posição do cateter sobre as imagens de ecografia; integração de instrumentos e dados das imagens num ambiente virtual 3D; *tracking* contínuo dos órgãos (compensando movimentos internos destes); e *feedback* visual focado na agulha. Este sistema foi avaliado por médicos e comparado com outras soluções baseadas em TEM num fantoma abdominal. O desempenho dos médicos foi superior com o sistema proposto, evitando lesões em órgãos próximos ao rim e destacando-se em cenários mais complexos. O sistema proposto foi classificado como a solução mais segura, obtendo níveis de confiança superiores durante os testes. Globalmente, este sistema provou auxiliar o ARP durante o NLPC. Considerando os excelentes resultados obtidos pela integração de dados pré-operatórios num cenário intra-operatório, o sistema proposto poderá ter aplicabilidade noutras intervenções cirúrgicas.

Palavras chave: acesso renal percutâneo; fusão de imagem; navegação cirúrgica; *tracking* eletromagnético.

Surgical navigation system for percutaneous renal access: electromagnetic guidance and imaging working together

Summary

Percutaneous renal access (PRA) has a key role on the treatment of several kidney diseases, particularly in nephrolithiasis (or kidney stone disease) through percutaneous nephrolithotomy (PCNL). The success of PCNL is highly dependent on the initial renal access where an accurate needle puncture decreases the overall complications and facilitates the following surgical steps. Although PRA is conventionally performed under fluoroscopy and/or ultrasonography, it remains challenging to learn and to perform. Recently, electromagnetic tracking (EMT)-based solutions have been proposed to aid PRA, allowing fast and accurate punctures to the renal calyx. However, some limitations still exist, namely the lack of three-dimensional (3D) perception of the anatomy, and the incapacity to achieve the calyx if it is fully occupied by a stone. To mitigate these constraints, this thesis focused on enhancing EMT-based solutions using preoperative computed tomography (CT) and intraoperative tracked ultrasound (US) image data, and, ultimately, deliver a novel surgical navigation system that can be translated to the clinic. To accomplish this goal, the following steps/contributions were fulfilled: (1) study the impact of ureteroscopy and US instruments in the EMT systems' reliability and accuracy; (2) development of a protocol to create kidney phantom models to assess image fusion strategies; (3) assessment in an *in-silico* environment of a point set registration technique and an US acquisition protocol to fuse two-dimensional US and 3D CT data; (4) proposal of a new approach to intraoperatively fuse CT and US data based on a semi-automatic US segmentation strategy and a point set registration algorithm; and (5) gathering of all above-mentioned contributions into a novel surgical navigation system, including additional features to improve real-time guidance, like: needle trajectory and catheter position' projection over US images; integration of instruments and imaging data into a 3D virtual environment; continuous organ-tracking (compensating internal organ movements); and needle-based visual feedback. This system was assessed by physicians and compared against other EMT-based solutions in a close-to-real scenario using an abdominal phantom model. The physicians' performance was superior with the proposed system, preventing injuries to nearby organs and excelling in complex scenarios. The proposed system was classified as the safest solution, obtaining the highest confidence levels during tests. Overall, it proved its added value to assist PRA during PCNL. Considering the applicability of enhancing intraoperative scenarios with preoperative data and guidance feedback, the proposed system may be broadened to other surgical interventions.

Keywords: electromagnetic tracking; image fusion; percutaneous renal access; surgical navigation.

Contents

#

2D	Two-dimensional
3D	Three-dimensional
4D	Four-dimensional

A

AAOF	Anatomical Affine Optical Flow
ARP	*Acesso renal percutâneo*
AUR	Analogic Flexible Ureterorenoscope
AVD	Average Distance

B

BP	Bi-plane

C

CAD	Computer Aided-Design
CPD	Coherent Point Drift
CPU	Central Processing Unit
CT	Computed Tomography

D

DARRT	Direct Alignment Radiation Reduction Technique
DO	Discriminative Optimization
DOF	Degrees-of-Freedom
DSC	Dice Similarity Coefficient
DUR	Digital Flexible Ureterorenoscope

E

EMT	Electromagnetic Tracking

F

FG	Field Generator
FM	Fiducial Marker
FOV	Field-of-View
FPS	Frames per second
FRE	Fiducial Registration Error

G

GMM	Gaussian Mixture Model
GMMREG	Gaussian Mixture Models Registration
GPU	Graphics Processing Unit
GUI	Graphical User Interface

H

HD   Hausdorff Distance

I

ICP   Iterative Closest Point
ICP-PL   Iterative Closest Point - Point-to-plane
ICP-PT   Iterative Closest Point - Point-to-point
IP   Internet Protocol
IQR   Interquartile Range
ITK   Insight Toolkit

L

LRT   Low Radiation Targeting

M

MAS   Multi-atlas Segmentation
MIKI   Minimally Invasive Kidney Interventions
MIS   Minimal Invasive Surgery
MITT   Medical Image Tracking Toolbox
MRI   Magnetic Resonance Imaging

N

NLPC   *Nefrolitotomia Percutânea*

P

PAKY   Percutaneous Access of the Kidney
PCNL   Percutaneous Nephrolithotomy
PFG   Planar Field Generator
PLA   Polylactic Acid
PLUS   Public Software Library for Ultrasound
PRA   Percutaneous Renal Access
PUJ   Pelvic Ureteric Junction
PVA-C   Polyvinyl Alcohol Cryogel

R

RCM   Remote Center Motion
RMS   Root-mean-square

S

SAVN   Surgical Approach Visualization and Navigation
SD   Standard Deviation
SP   Single-plane
SP_L Single-plane longitudinal
SP_T Single-plane transverse
SSM   Statistical Shape Model
SVD   Singular Value Decomposition

T

TAC	*Tomografía Axial Computadorizada*
TCP	Transmission Control Protocol
TEM	*Tracking electromagnético*
TMM	Tissue Mimicking Material
TRE	Target Registration Error
TTFG	Tabletop Field Generator

U

US	Ultrasound

V

VTK	Visualization Toolkit

Chapter 1

Introduction

1.1. Percutaneous renal access

Percutaneous renal access (PRA) plays a key role in a multitude of minimally invasive surgeries of upper urinary tract and this surgical step involves creating a tract from the skin until the kidney using a needle. The development and acceptance of this surgical step helped to replace the open renal surgery in several pathologies, mainly in renal lithiasis, along the past decades. The first case reporting the use of PRA was in 1865 by Thomas Hillier to treat a 4-year-old boy with congenital obstruction of the ureteropelvic junction. It is consider the first case of percutaneous nephrostomy [1]. Decades later, in 1944, the first image-guided renal biopsy was performed by Nils Alwall using a radiograph and retrograde pyelogram to localize the kidney. The first attempt was performed with the patient in the sitting position, while subsequent punctures were made in the prone position [2], [3]. In 1955, Godwin *et al.* reported the treatment of hydronephrosis with percutaneous nephrostomy to decompress obstructed kidneys in 16 patients [4], being later extended with the use of percutaneous antegrade pyelography to improve diagnose [5]. Extraction of a renal calculus via a percutaneous nephrolithotomy (PCNL) was first described by Fernström and Johansson in 1976 based on percutaneous nephrostomy, where the established tract was dilated and used to remove kidney stones [6]. In the following years, more works described successful outcomes of this new technique [7]–[9]. In 1985, with growing experience, the stone-free rate for patients with renal and ureteral stones was 99% and 94.5%, respectively [10]. Although PRA followed by chemolysis was also used to dissolve kidneys stones [11], due to the excellent outcomes of percutaneous nephrolithotomy, percutaneous chemolysis did not completely succeed. Being continuously extended to other surgical approaches, PRA was reported to the treatment of upper tract urothelial carcinomas in 1987, where the resection of the kidney was performed through a percutaneous nephrostomy [12]. Other examples include antegrade insertion of ureteral stents, ureteral dilation, and ureteral catheters [13], as well as, the treatment of obstructed ureter, in which PRA makes the access to ureteropelvic junction easier and in turn endoscopic incision feasible.

Currently, PRA is used to treat several pathologies such as [14]:

- Drainage of hydronephrotic kidney;

- Nephrolithiasis (kidney stones);

- Pelvic ureteric junction (PUJ) obstruction;

- Renal transitional cell carcinoma;

- Calyceal diverticulum;

- Intrarenal infusion therapy (chemolysis, chemotherapy);

- Renal cysts;

- Removal of foreign bodies (encrusted stents, fungal bezoar);

- Access to the upper ureter;

- Renal biopsy.

Despite the vast use of PRA in different pathologies, it has gained a particular importance in the treatment of **nephrolithiasis (or kidney stone disease)** due to the rising prevalence and incidence of this disease [15] and being a significant worldwide source of morbidity and cost to society [16]. Indeed, **percutaneous nephrolithotomy** became the first-line technique to treat large and complex kidney stones over the last 20 years [17].

1.1.1. Percutaneous nephrolithotomy

Percutaneous nephrolithotomy (PCNL) is a minimally invasive surgery (MIS) used to treat nephrolithiasis. Nephrolithiasis is a common clinical condition, acutely painful, and often recurrent, and affects all ages, races, and genders [16]. In this condition, it is observed the formation of stones inside the kidney's collecting system. The causes of stones development can be infectious, non-infectious, genetic, or adverse drug effects [18]. Globally, prevalence rates of nephrolithiasis range from 7–13% in North America, 5–9% in Europe, and 1–5% in Asia [19], and this prevalence has been growing over the past decades. According to the National Health and Nutrition Examination Survey study, the overall prevalence of nephrolithiasis in the United States population was 5.2% between 1988 to 1994, which increased for 8.8% between 2007 to 2010, being more prevalent in men (10.6%) than women (7.1%) [20]. This growing has occurred across all ages, races, and genders. It is estimated that its growth and impact on health and economy will continue to rise in the next years [21].

Given the high prevalence of the disease and different clinical conditions according to type, size, and location of the kidney stone, beyond open surgery and PCNL, different treatments have been applied over time, such as extracorporeal shock-wave lithotripsy, and, more recently, flexible ureterorenoscopy. However, as abovementioned, PCNL remains the standard surgical procedure for large and complex kidney stones. In fact, the guidelines of the European Urology Association recommend PCNL for [18], [22], [23]:

- Staghorn calculi;

- Large calculi > 2 cm;

- Impacted or large proximal ureteral calculi;

- Calyceal diverticular calculi;

- Ectopic renal calculi (horseshoe kidney, pelvic kidney, or transplant kidney);

- Coexisting ureteropelvic junction obstruction and renal calculi;

- Lower pole renal calculi > 1 cm;

- Ureteroscopy or shock wave lithotripsy failures.

Anatomy for percutaneous renal access in nephrolithotomy

Generically, the urinary system is formed by two kidneys, two ureters, one bladder, and one urethra. The kidney is responsible to control the body's fluid and electrolyte balance and to remove waste products producing the urine. Then, the urine flows from the kidneys to the bladder through ureters, and the bladder stores the urine until releasing it by the urethra. All abovementioned organs can lodge stones, which are usually formed in kidneys and eventually migrate to different locations in the urinary tract. When large and complex stones remain in the kidney, PCNL is used to remove them.

As initial step of PCNL, PRA is performed to create a tract until the kidney. However, both kidneys have their own anatomical particularities being surrounded by different anatomical structures. Basically, the kidney is composed of an external capsule that encases the renal parenchyma. Involved by renal parenchyma, the collecting system begins with minor calyces which coalesce frequently into major calyces, and then, unite to form the infundibulum, and sequentially, renal pelvis, PUJ, and ureter (Figure 1.1 - A). The only portion of the collecting system that is physically attached to the renal parenchyma is the furthest tip of the calyx at the fornix, while the infundibula and pelvis are unsupported and mobile [24].

The kidney is usually divided into three drainage zones: the upper pole, the middle region, and the lower pole (Figure 1.1 - B). Frequently, the upper and the lower poles have one major calyceal system each. In the middle region, the calyceal system usually drains into one or both upper and lower systems, but in some cases it combines into a middle major calyx, or even middle minor calyces that drain directly
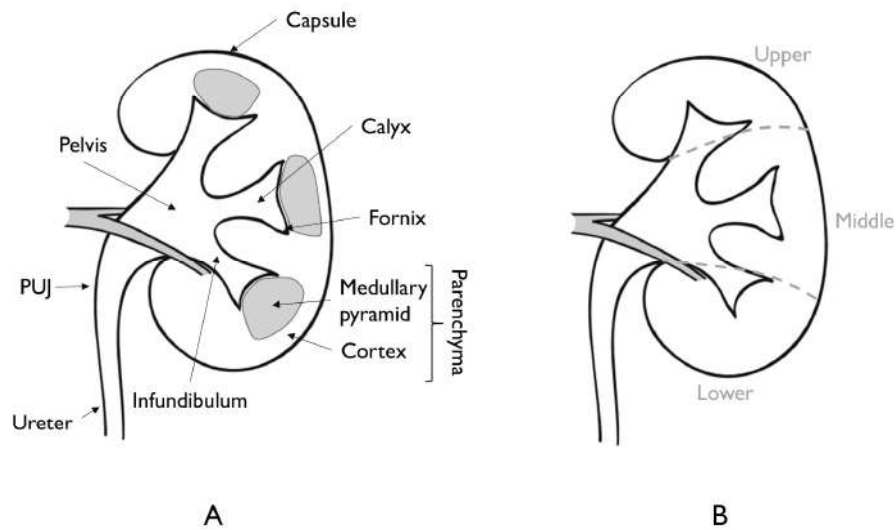
Figure 1.1 – Illustrations of the kidney's anatomy and drainage zones.
(A) Illustration of the main constituents of kidney anatomy. (B) Illustration of the three drainage zones: the upper pole, the middle region, and the lower pole.

into the renal pelvis. There are 5 to 14 minor calyces in each kidney (70% of kidneys having 7 to 9 minor calyces), being oriented anteriorly and posteriorly (Figure 1.2) [25]. Since PRA is made using a posterior or posterolateral approach (puncture is performed from behind), it is vital to understand the anterior-posterior orientation of the calyces. Puncturing the posterior calyces allows relatively straight access to the collecting system, while the access is more difficult for the anterior calyces (an acute angulation to entry is necessary) [24]. However, different configurations of paired anterior and posterior calyces can be found in kidneys. In a Brödel-type kidney (Figure 1.2 – Left), the posterior calyces are about 20 degrees behind the frontal plane and the anterior calyces are 70 degrees in front of the frontal plane. The Hodson-
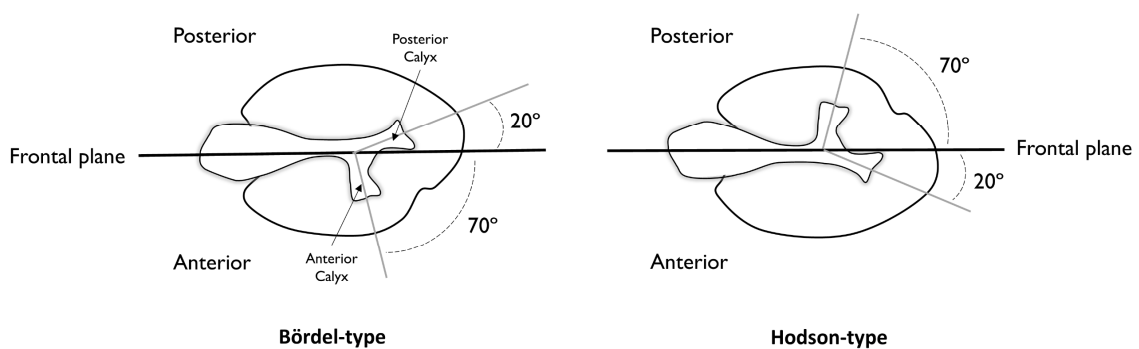
Figure 1.2 – Bördel-type and Hodson-type calyces' orientation.

5

type kidney is the opposite (Figure 1.2 - Right); the posterior calyces are 70 degrees behind the frontal plane and the anterior calyces are 20 degrees in front of the frontal plane. Sixty-nine percent of the right kidneys have a Brödel-type orientation (posterior calyces are lateral) and 79% of the left kidneys have a Hodson-type orientation (posterior calyces are medial) [26].

Knowledge of renal vasculature is also crucial during PRA. The vasculature of the kidney is composed of the main renal artery which separates into an anterior and a posterior branch (Figure 1.3). The anterior branch divides into four anterior segmental arteries: the apical segmental artery (which supplies the tip of the upper pole); the upper segmental artery (which supplies the remainder of the upper pole); the middle segmental arteries (which supplies the middle pole), and the lower segmental artery (which supplies the entire lower pole). The posterior branch of the renal artery supplies the posterior half of the kidney [25]. Then, the anterior segmental arteries and the posterior branch divide into infundibular arteries which are adjacent to the infundibula, and each infundibular artery divides into two arcuate arteries near the base of the renal pyramids. Additionally, arcuate arteries divide into the interlobular arteries, which split into renal arterioles in the peripheral renal cortex [26]. Therefore, renal arterial vascular damage must be prevented to avoid loss of renal function. The risk for arterial injury is least in Brödel's line (Figure 1.3), which is an avascular plane approximately at the lateral margin of the kidney between the posterior and anterior segmental arteries (usually limited by the circulation of the apical/upper anterior segmental artery and the middle/lower anterior segmental artery) [27]. The relationship of the vascular anatomy to calyces indicates that upper pole and infundibulum punctures are associated with a high risk of arterial injury, as well as the posterior segmental artery. Puncturing the lower pole is considered the safest, but infundibular arteries are found in a large percentage of patients
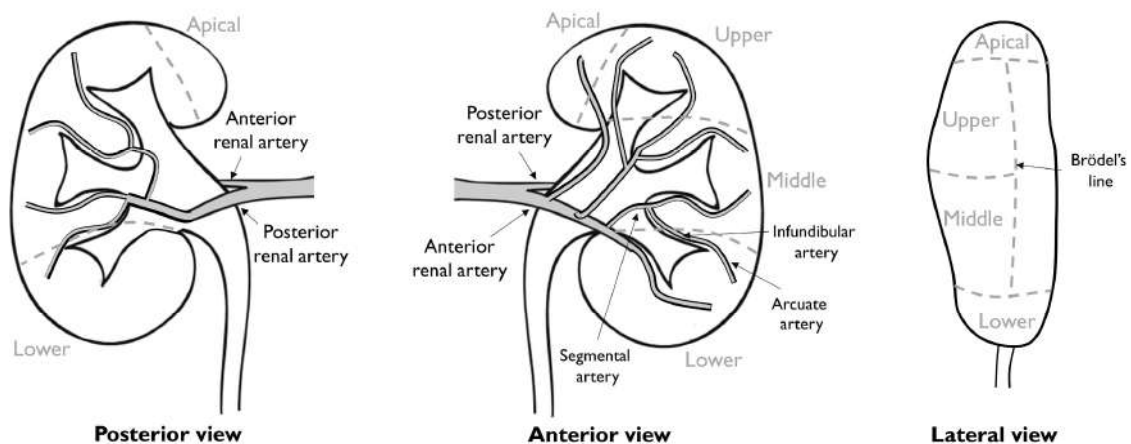
Figure 1.3 – Different views of the renal vasculature.
Brodel's line is considered relatively avascular and the safest zone to access the kidney.

[28]. Thus, no region is completely safe to puncture, except the calyx itself. The tip of the calyx (fornix) is the safest entry site for renal puncturing since it is the only portion of the collecting system that is attached to the parenchyma (where only microvasculature is present) and will avoid the infundibular and arcuate arteries [24].

Considering the contiguous anatomy, kidneys are located anteriorly to the quadratus lumborum and psoas muscles, between the 11th and 12th thoracic and 2nd and 3rd lumbar vertebrae. Indeed, the left kidney is positioned slightly higher than the right kidney (Figure 1.4 – A), meaning that supra-costal puncture is more likely. The upper pole is crossed by the 11th and 12th ribs in the left kidney, while the right one is crossed only by the 12th rib being the diaphragm posteriorly positioned in both poles [25]. The left kidney is slightly larger than the right kidney, and the upper pole of the left kidney is wider than the lower pole [26]. Moreover, the kidneys are tilted 30 degrees relative to the coronal and sagittal planes (Figure 1.4 – A and B).

During intercostal punctures to the upper pole of the kidney, the diaphragm is traversed, and sometimes even in punctures below the 12th rib (Figure 1.4 – C). Pleura can be traversed as well, especially when it extends below the 12th rib too, although generally without adverse effects [26]. Usually, the lung is not violated if an intercostal puncture is performed below the 11th rib. The risk of lung injury increases if the 10th intercostal space is used. Additionally, the liver, spleen, and colon positions are also relevant since they lie close to the kidneys increasing their risk of injury. Indeed, the liver is anterior to
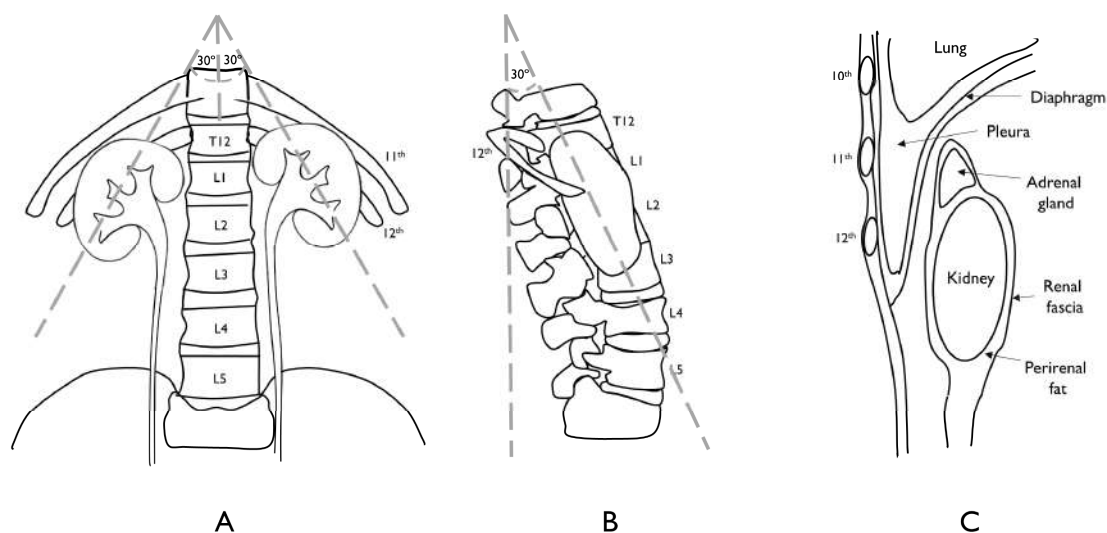
Figure 1.4 – Relative position and orientation of the kidneys into the abdominal cavity.
Kidneys are tilted 30 degrees relative to the (A) sagittal and (B) coronal planes. (C) Kidneys are also surrounded by different structures that have a high risk to be punctured considering the initial needle position.

the upper pole of the kidney and, in some cases, can cover the entire anterior surface of the kidney. The spleen covers less of the kidney anteriorly. The risk of injury to the liver and spleen increases if both extend lateral to the kidneys. However, this is very uncommon [24]. The right and left colon can be injured if they are positioned laterally or even posteriorly to the right and left kidneys, which can occur in some cases. Their position varies significantly more on the left side and proximal to the lower pole of the kidney [29]. Moreover, there is also a risk of injury to the adrenal glands, duodenum, gallbladder, pancreas, hilum, and large vessels if a misoriented or excessively deep puncture is done.

Surgical planning, and procedure

Typically, the surgical planning relies on standard computed tomography (CT) images. Here, the surgeon sets out the favored path to target the surgical site considering the surrounding organs, and can obtain preoperative information about the location, size, complexity, and density of the kidney stone. To reduce the radiation exposure of the patient, low-dose CT protocols have been used (radiation exposure reduction: 10.0 to 3.0 mSv), achieving similar sensitivity and specificity of standard CT [30]. Nevertheless, the accuracy may be lower in obese patients. Moreover, the use of ultrasound (US) imaging and magnetic resonance imaging (MRI) as preoperative data has been proposed. Although both modalities do not use ionizing radiation, US presents lower image quality and less sensitivity and specificity than CT, while MRI is costly and kidney stones are difficult to visualize [30].

The standard surgical procedure begins with general anesthesia. Then, the patient is positioned in the dorsal lithotomy position for the placement of a ureteral catheter using a cystoscope or flexible cystoscope. This step is initially used to perform a retrograde opacification of the collecting system by injecting contrast through the catheter. Using fluoroscopy, the visualization of the urinary collecting system is achieved, and stone details are confirmed, such as location, shape, and size. The patient is repositioned usually to the classical prone position in PCNL (Figure 1.5 - A). Since the first description of the technique by Fernström and Johansson in 1976, different alternatives to classical prone position have been proposed [31]. No position imposed itself as the best, being dependent on multiple factors, including patient-related factors, stone burden, and surgeon's preference.

Whether positioned in prone, supine or in any of the modified positions, gaining adequate access to the collecting system is key to successfully perform PCNL. Based on guidance systems (commonly fluoroscopy), the surgeon determines the calyx orientation and selects the best optimal point of entry [14]. The optimal point of entry into the collecting system is along the axis of the calyx (Figure 1.5 – B). Aligning the access with the infundibulum allows the most efficient use of a rigid nephroscope and reduces
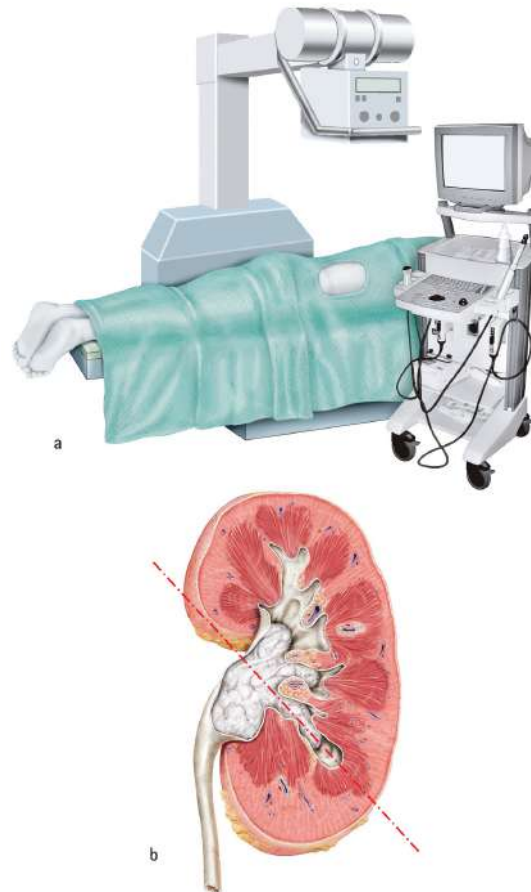
Figure 1.5 – Standard surgical procedure for PRA.
(A) Patient positioned in the classical prone position to perform PCNL. Fluoroscopy is commonly used to aid PRA. Ultrasonography is gaining supporters in the past few years. (B) The optimal point of entry into the collecting system is along the axis of the calyx with straight access to renal pelvis. Used with permission of Stephan Spitzer, copyright Stephan Spitzer, www.medizillu.de

the need for excessive torque on the rigid instruments, which may cause renal trauma and bleeding [22]. Once the proper orientation of the line of puncture has been obtained (Figure 1.6 – A), respirations are suspended in full expiration. Then, the surgeon uses a surgical needle (18-gauge of diameter) to create a tract from the skin to the selected renal calyx (Figure 1.6 – B). The needle progresses towards the desired calyx in the oblique position to gauge the depth of puncture. Before puncturing the renal capsule, final corrections must be made. Needle manipulation must be prevented after entering renal parenchyma because it may displace the kidney and in turn affect the position of the selected calyx. When the needle reaches the selected calyx, aspiration of urine will verify proper puncture.

After puncturing, a guidewire is passed through the needle into the collecting system until the ureter (if possible). An incision of 1 cm is made over the needle and the needle is removed leaving the guidewire in place. Then, several wires and dilators are exchanged and maneuvered to create an
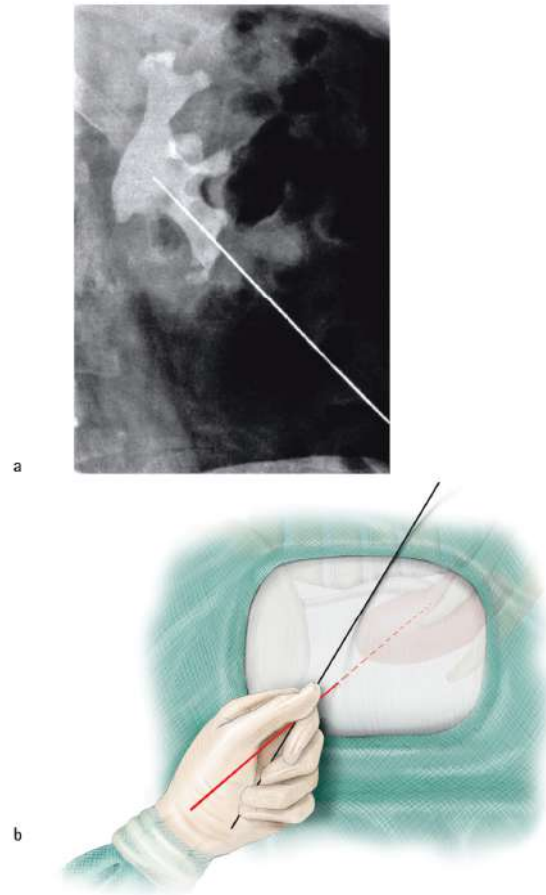
Figure 1.6 – Needle puncture in PRA.
During PRA, a surgical needle creates a tract from the skin until the selected renal calyx. (A) fluoroscopy image helps to determine the target calyx and the needle orientation. (B) Illustration of the ideal puncture (orange line). Used with permission of Stephan Spitzer, copyright Stephan Spitzer, www.medizillu.de

expanded tract (approximately 1 cm) directly into the kidney. Through the access sheath, a nephroscope, rigid graspers, stone baskets, and instruments to perform intracorporeal lithotripsy (ultrasonic, pneumatic, electrohydraulic, and laser) can be introduced to remove stones (Figure 1.7). Once the stone removal is complete, a nephrostomy tube may be left for a few days for drainage through the tract. There are contraindications for performing PCNL such as: uncontrolled coagulopathy, urinary tract infection (with fever); tumor in the presumptive access tract; potential malignant kidney tumor; pregnancy; and uncontrolled hypertension [14], [18], [32].

1.1.2. Percutaneous renal access: a demanding surgical step

PRA remains a challenging task for surgeons with a steep learning curve [33] with higher complication rates in first cases [34]. In fact, the technical complexity and risk associated with PRA discourage many urologists from obtaining their own access, being frequently performed by radiologists.
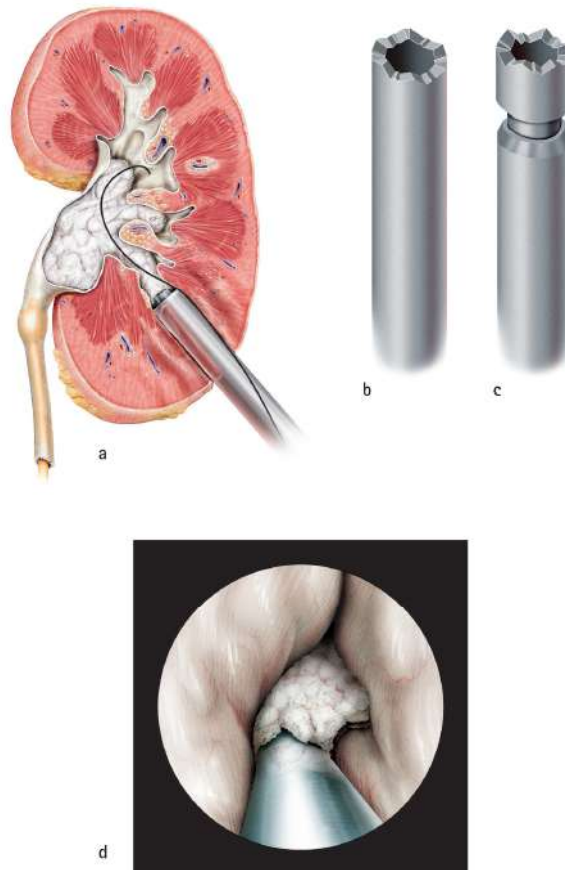
Figure 1.7 – Kidney stone removal.
(A) Use of nephroscopy to visualize within the collecting system during stone removal. (B) and (C) Examples of intracorporeal lithotripsy (stone fragmentation) instruments. (D) Illustration of nephroscopy view during stone fragmentation. Used with permission of Stephan Spitzer, copyright Stephan Spitzer, www.medizillu.de

Initial studies revealed that in the United States less than 20% of urologists obtain their own access after residency [35], [36]. Nonetheless, in the past decades, this number has been increasing significantly [37]–[39]. Moreover, PRA obtained by urologists was associated with a statistical improvement in overall stone-free rate, less unusable access, and less access-related complications than radiologists [36], [40], [41]. These studies reinforce the crucial role of urologists in obtaining appropriate PRA, where they can use their knowledge and expertise in renal anatomy and surgical technique to select the correct puncture site. The appropriateness of the access influences the success and complication rates. Inaccurate and multiple punctures can cause injuries in the kidney and adjacent organs, compromising the percutaneous procedure and the surgical outcome. Complications associated to PRA include fever, sepsis, bleeding, thoracic complications, organ injury, kidney failure, urinoma, conversion to open surgery due to difficulties encountered during the procedure and rarely death [14], [32], [42]–[44].

1.1.3. State-of-the-art: conventional and new guidance techniques for percutaneous renal access

Different techniques have been applied and developed to guide PRA. In this section, the conventional techniques used to perform PRA are described, and innovations that have been developed during the past few years to improve them are also presented. For more details, the reader is kindly referred to the following reviews on this topic [31], [45]–[50] and the references below.

Conventional techniques

Fluoroscopy-guided

As mentioned previously, fluoroscopy is commonly used to aid PRA, representing 64-86% of the global usage [38], [39], [51]. Fluoroscopy requires the insertion of a ureteral catheter in the renal pelvis to inject contrast to opacify and dilate the collecting system. This allows the correct visualization of the collecting system anatomy and pathology during puncture. The puncture is usually based on the bull's eye technique or triangulation technique and is obtained by an antegrade access (although retrograde access is also possible) [52]. Despite its benefits, fluoroscopy is only a two-dimensional (2D) imaging modality (three-dimensional perception is challenging), presents a low soft-tissue contrast, is highly dependent on the surgeon's technical expertise, and exposes patients, surgeons and medical staff to a significant amount of radiation. However, low-dose and pulsed fluoroscopy have been introduced to reduce the amount of radiation [50], [53].

Ultrasonography-guided

Although it is estimated that ultrasonography is used in 4-14% of the PRA worldwide only [38], [39], [51], it is currently gaining several supporters as it avoids radiation exposure. Ultrasonography provides a real-time depiction of the renal collecting system and adjacent structures, reducing potential injuries. The needle can be visualized in the US images as well, supporting the antegrade access of the intended calyx. Ultrasonography is more portable, easier to maneuver, and usually no retrograde injection of contrast is needed when compared to fluoroscopy. Ultrasonography is the first choice when retrograde access is difficult or impossible to obtain. However, it displays only 2D images with a limited field-of-view (FOV), images may be difficult to analyze (experience is required), and puncturing is highly operator-dependent since images hamper the tracking and visualization of the needle tip. Additional difficulties may be found in obese patients, with abnormal anatomies, or in poorly dilated pyelocaliceal systems.

Combined fluoroscopy and ultrasonography-guided

Fluoroscopy and ultrasonography have been used together to take advantages of both techniques. Studies revealed that 15-21% of urologists performed PRA using both techniques [38], [39]. The combination significantly reduces the amount of radiation used during PRA with equivalent outcomes [54].

Combined fluoroscopy and ureteroscopy-guided

Although not so common as previous approaches, PRA can also be obtained using ureteroscopy combined with fluoroscopy. Using direct vision to select the correct calyx and a small needle in the working channel of the flexible ureteroscope, a retrograde access is performed by puncturing from the calyx to the skin. Fluoroscopy guidance is used to confirm needle advance. It can be advantageous in morbid obesity, hypermobile kidney, and abnormal kidney position. This technique decreases the radiation exposure as well, but it increases the risk of creating an errant tract [55].

In addition, combination of antegrade and retrograde approaches has also been described. Using a conventional antegrade access with a needle, retrograde approach was used to have a direct visualization of the selected calyx. Puncturing is monitored under fluoroscopy control with initial anterior–posterior views to position the needle over the selected calix and the tip of the ureteroscope [56].

Combined ultrasonography and ureteroscopy-guided

As in the previous technique, the surgeon chooses the optimal calyx to puncture through real-time visualization using flexible ureteroscopy, replacing the traditional fluoroscopy by ultrasonography to guide the antegrade insertion of the needle. Alsyouf *et al.* used US images to help identify the correct calyx through the movement caused by the ureteroscope deflection [57]. The aforementioned advantages and disadvantages of ultrasonography are also associated to this technique.

New techniques

In the past few years, several innovations have been introduced to improve and aid PRA [45]–[50], which are here grouped as fluoroscopy-based, ultrasonography-based, computed tomography-based, endoscopic-based, electromagnetic tracking-based, robotic-based, and combination of multiple systems. The works, which were published after the beginning of this project, are marked with "†".

Fluoroscopy-based

Mechanical, laser and needle-based innovations have been introduced in fluoroscopy to support the needle puncture.

A low-cost, light-weight, portable mechanical gantry with a needle guiding device was designed by Zarrabi *et al.* [58]. The mechanical gantry together with a specific software was able to help surgeons to perform PRA. After acquiring two fluoroscopic images, the optimal calyx can be selected in the software. The software retrieves specific coordinates and puncture depth to be set in the gantry and supports the antegrade needle puncture. Tests were only performed in plastic and phantom models. The procedure duration was 15 minutes, and radiation exposure was reduced to two images.

The laser direct alignment radiation reduction technique (DARRT) was designed by Khater *et al.* to simplify PRA based on the bull's eye approach [59][†]. A C-arm attached with a laser beam was used to select the needle entry site. Then, the needle tip was positioned at the skin place indicated by the laser aiming beam and oriented to be aligned with the laser. The antegrade access was performed manually maintaining the needle aligned with laser beam and using tactile feedback. Fluoroscopy was used to confirm the needle position and depth. The authors concluded that laser DARRT reduced fluoroscopy time by 63% compared with the conventional bull's eye approach.

Moreover, Wu *et al.* presented a similar system, *i.e.* the Surgical Approach Visualization and Navigation (SAVN) [60][†]. Similarly, the main purpose was to assist puncture and reduce intraoperative radiation. The laser beam was attached to the C-arm and its position and direction was automatically adjusted by a laser driver device after data processing based on fluoroscopy images. Tested in 20 cadaveric kidneys, the results revealed less puncture time, puncture attempts and fluoroscopy time.

Wilkinson *et al.* presented a novel low-radiation targeting (LRT) needle technique. The LRT needle used a specialized radiodense ring targeting system to facilitate the use of low radiation systems [61][†]. The authors compared the antegrade access using LRT needle against conventional bull's eye technique and laser DARRT technique. Total mean fluoroscopy time was reduced compared to the conventional technique, although no significant differences were observed in the number of course corrections or number of punctures needed to reach the calyx.

Ultrasonography-based

Due to the increased interest in ultrasonography, innovations have also been introduced to improve needle puncture, including solutions based on enhanced needle visibility, three-dimensional (3D) US, injection of contrast, and projection of needle trajectory on the screen.

Hopkins *et al.* tested standard and echogenic needles to improve needle visibility in the US images, and they observed that echogenically enhanced needles may provide advantages of needle visibility for thinner gauge needles and when needle to transducer angle is suboptimal [62]. An enhanced perception of the needle reduces the risk of misunderstanding the needle position in the US images. Moreover, Cheung *et al.* proposed an automatic algorithm to enhance needle visibility in the US images for percutaneous procedures [63]. The results demonstrate significantly improved needle visibility. This type of technology is currently commercialized by ultrasound companies, *e.g.* Bk Ultrasound – X-Shine [64].

Contrast-enhanced US has also been used to improve renal imaging. Indeed, Cui *et al.* tested the use of antegrade US contrast agent injection to improve PRA. The authors used the contrast agent to confirm the position of the needle or catheter and evaluate complications a day after renal access. Successful results were obtained in accessing the kidney, while being associated with the advantages of lack of radiation exposure [65][†]. Additionally, retrograde injection of US contrast agent was also studied. Usawachintachit *et al.* suggested that renal puncture can be performed effectively in all cases, without intraoperative complications or adverse events related to ultrasound contrast injection. Retrograde contrast injection improved visualization of all renal calyces and consequently the target calyx for puncture when compared to B-mode [66][†].

Three-dimensional ultrasonography has been tested as well to improve renal access. Li *et al.* tested the 3D US as the main source of information for a US-based navigation framework and compared it to 2D US. The results indicated that 3D US potentially increases the accuracy and robustness of renal puncturing [67]. Similarly, Hongzhang *et al.* performed a study comparing 2D and 3D US-guided PRA. Real-time 3D US-guided had superior performance in terms of visualization of the needle tract, length of puncture time and number of puncture times for experience surgeons [68][†].

Projection of the needle trajectory on the screen was also developed. One example is the Clear Guide One® stereoscopic camera system (by Clear Guide Medical, Baltimore, MD, USA), designed to be attached to an US probe and track the needle pose in real-time [69]. This system enables the projection of an estimated trajectory of the needle over the US image, being able to successfully improve US targeting. However, camera occlusion can affect needle tracking [70][†]. The same principle was proposed in the SonixGPS® system (Ultrasonix Medical Corp, Richmond, BC, Canada). In this case, an electromagnetic tracking (EMT) system was used, where two EMT sensors track the probe and needle simultaneously. Thus, by integrating US and EMT systems, SonixGPS® can project the needle trajectory on the screen even if it is not in the image plane during puncture. Results revealed fewer attempts, lower

time, and less blood loss to obtain a successful puncture [71], [72][†]. Similar EMT technologies have been tested in other US machines [73]. Recently, a novel wireless portable US was presented and tested for renal access, *i.e.* the U-Probe-2® (Sonostar Technologies CO, Guangzhou, Guangdong, China). It consisted of a probe with integrated ultrasound circuit boards, an intelligent terminal that installed specific ultrasound software, and a puncture trestle [74][†]. The US image is streamed to an iPad or other terminals via Wi-Fi and the projection of the needle trajectory (rigidly attached to the trestle) is displayed over the image. Initial results were positive and indicated that U-Probe-2 is safe and effective for puncture guidance, but further tests need to be performed.

Endoscopic-based

In addition to the flexible ureteroscopy, another endoscopic innovation was proposed to improve renal access. A needle with 1.6 mm diameter and a micro optical system with an integrated light was presented, known as "all-seeing needle". The image of the optical system was captured with a standard endoscopic camera system and then displayed on a screen. The real-time vision from the needle tip allowed direct visualization of the adjacent organs and the renal collecting system. During experiments, PRA was performed under the supervision of ultrasonography. Despite interesting results, this system did not allow the redirection of the needle path. In fact, in a total of 15 cases, four patients needed re-puncturing due to a poor tract [75].

Computed tomography-based

A new technique based on 3D imaging was proposed to help accomplish complex punctures. The Uro Dyna-CT (Siemens Healthcare solutions, Erlangen, Germany) provides interventional 3D imaging and cross-sectional image reconstructions, in addition to a 3D planning and laser-guiding puncture tool (syngo iGuide). The image acquisition is performed by rotating the C-arm around the patient (for 8 seconds) and then, the CT volume is reconstructed (less than 2 min). The puncture is planned in a custom software, and later the C-arm is positioned in the bull's eye position to indicate the puncture site and direction with a laser cross. Next, the needle is inserted into the target site, keeping it aligned with the laser light during the entire procedure. The correct placement of the needle can be checked and corrected by fluoroscopy using the same system [76]. Ritter *et al.* showed that, in 27 attempts for different procedures, 24 punctures were successfully achieved. However, the failed punctures occurred mostly in PRA [76]. Jiao *et al.* reported a higher success rate, with 32 out of 33 attempts [77][†].

Electromagnetic tracking-based

Already mentioned in US needle trajectory projection, the application of EMT systems was also tested to perform renal access using a different strategy. After selecting the target calyx using ureteroscopy, the idea was to insert in the working channel of the ureteroscope a catheter with an EMT sensor on its tip [78], [79]. Then, with the catheter tip visible on the ureteroscopy image and after path assessment using ultrasonography, antegrade PRA was executed using a needle with an EMT sensor on its tip as well. The puncturing was supported in real-time using a custom software where both needle and catheter are virtually referenced [79], [80][†]. This technique was easy to learn and use, with the needle being precisely inserted into the calyx. In the first human report, Lima *et al.* reported that all cases were successful accessed at the first attempt with a mean puncture time of 20-22 s [80][†], [81][†]. Later, Borofsky *et al.* compared the EMT and fluoroscopy-guidance performance in beginner, intermediate and expert surgeons. EMT presented shorter access time, fewer attempts, and shorter fluoroscopy time. Trainees showed comparable success rates and outcomes relative to experts despite higher access times [82][†].

Robotic-based

Robotic innovations have also been proposed. One of the innovations is PAKY-RCM. This robotic system consists in 2 parts: a percutaneous access of the kidney (PAKY) device, and a remote center motion (RCM) device. While PAKY device is a radiolucent and serializable needle driver positioned at the end of the robot arm, RCM is an active robotic arm that allows the tip of the needle to pivot about a fixed point on the skin [83]. RCM was fixed to a passive robot arm with 7 degrees-of-freedom that allows mounting the system to a surgical table and stabilize the PAKY-RCM itself. PAKY-RCM was tested against standard manual techniques and no significant differences were obtained. Actually, 20 of 23 cases were punctured successfully [83].

Recently, Oo *et al.* presented a new robotic innovation, the Automated Needle Targeting with X-ray (ANT-X) system (NDR Medical Pte. Ltd.). The ANT-X system was developed to be used with fluoroscopy and bull's eye technique. It relies on a robotic needle holder and software which computes the correct needle trajectory from fluoroscopy data. This system was also attached to an articulated arm mounted in a surgical table. Puncture was still controlled by the surgeon. The authors stated that this system reduced radiation exposure, but no respiratory movement compensation and limitation to prone technique were still important shortcomings [84][†].

Combination of multiple systems

Here, new solutions that merge, in the same virtual or augmented reality environment, different imaging modalities, tracking systems, or other devices to perform PRA are presented. Thus, solutions that combine more than two different systems were included here.

Mozer *et al.* presented a computer-assisted solution to renal access [85]. The system rigidly fuses preoperative CT data with intraoperative US data (spatially tracked with optical tracking system) based on the kidney surface. Using a navigation user interface, the surgeon can pre-plan the puncture site and transfer this information to the surgical environment. A virtual needle was visible in the user interface. Fusion strategy was tested in one patient and by puncturing a kidney phantom. Most of the puncturing errors were associated with the needle tip deflection since the needle was coupled to a passive rigid body localizer on its top.

Soon after, Mozer *et al.* presented another computer-assisted solution to aid PRA by projecting the US puncture tract onto fluoroscopic images [86]. Using an optical tracking system to reference different equipment and instruments, the US probe, needle guide and C-arm fluoroscope were attached to a localizer. After calibration, all systems were in the same world coordinates. To avoid kidney movement, several fluoroscopic images were acquired at the end of expiration, and then saved in the software. Puncturing was computer-assisted by displaying the trajectory of the needle in fluoroscopic and US images in real-time. The same respiratory phase was needed to ensure image fusion. The authors performed experiments on a phantom and one patient with success.

Oliveira-Santos *et al.* reported a computer-assisted solution where no intraoperative image is used. Indeed, fusion was obtained through radio-opaque markers positioned before preoperative CT imaging. CT data was acquired with the patient lying in the selected surgical position, and radio-opaque markers were removed after surgical pen marking. These marks were used to perform intraoperative registration based on optical tracking. Needle guidance was supported by a graphical user interface with 3D CT data overlaid. The needle position was confirmed during puncture by fluoroscopy. Phantom experiments were undertaken [87].

Optical tracking systems have also been used to track the US probe and needle. Li *et al.* proposed to fuse 3D kidney models from CT or MRI and US imaging [88], [89]. The fusion technique was based on a complete 3D model and orthogonal US slices. To improve fusion, each slice is acquired at the maximum exhalation using an optical tracking-based respiratory gating method. Registered models together with a virtual needle were displayed in a graphical user interface (GUI) which was used to support PRA. Four volunteers and kidney phantoms were used to test registration accuracy and puncture

accuracy, respectively. Registration accuracy revealed a mean target registration error of 3.53 mm, and a puncture accuracy of 1.97 mm [89]. Later, Li *et al.* tested the kidney reconstruction using a statistical shape model only based on sparse US slices. Experiments were performed in pig models and suggested that PRA complications can be reduced [90], [91].

Presenting a similar setup using optical tracking and ultrasonography systems, Liang *et al.* described a computer-assisted solution for PRA [92]. The authors fused MRI and US data based on anatomical landmarks selected in both images. Using the tracked US probe, anatomical landmarks close to the kidney edges were obtained intraoperatively. Then, a point set registration algorithm (*i.e.* iterative closest point) was used to minimize the distances between landmarks from MRI and US. The authors pointed out that the results of fusion may not be accurate enough due to deformation and difficulty in localizing the landmarks. Although, they considered the results acceptable in a phantom model.

Comprehensive planning and assistance for PRA was also assessed by Li *et al.* [93]. Prone position was used during preoperative CT acquisition and 3D models were detailly segmented by an experienced urologist and a radiology technician using a commercial software. Besides, surgical planning was performed by defining the puncture trajectory in the same software. Intraoperatively, with the patient in prone position, the surgeon manually drew in the US image the needle trajectory based on pre-planned trajectory. No tracking system was used. This strategy was tested in 15 patients with complex anatomical and pathological conditions. Detailed 3D models were suggested to be beneficial for planning and assisting PRA.

Rassweiller *et al.* presented an innovative solution that includes the usage of an iPad to support renal access [94], [95]. Preoperative CT images were obtained in the prone position, the exact same position was used intraoperatively. Moreover, five colored radiopaque markers were placed around the puncture zone during CT acquisition. Using these markers which were visible in the CT and iPad camera (at least four), and after image segmentation, 3D models of kidney and surrounding tissues were fused in the iPad virtual environment and displayed over the surgical scenario. An augmented reality and a virtual view from inside the patient were created by overlaying video images with 3D CT models. PRA was obtained successfully in a phantom [95] and in two patients [94]. Prone position and respiratory cycle must be preserved during CT acquisition and puncturing. Recent studies revealed a favorable puncturing method and puncture time for the standard technique (combined fluoroscopy and ultrasonography guidance) comparing to the iPad approach [96][†].

A tablet-based solution was also tested by Marien *et al.* [97]. Here, the authors associated a preoperative CT image, an EMT system, a workstation, and a movable tablet to assist PRA. Preoperative

CT was acquired with 6 superficial skin markers and a Foley catheter (with an EMT sensor) inserted in the urethra. CT images were three-dimensionally reconstructed in the workstation, and CT-patient registration was obtained by picking the position of the 6 markers with a registration tool and the catheter. Integrated into the movable tablet, which was attached to an EMT sensor, the surgical navigation software was able to display predictive puncture lines over the 3D models with a feedback color-code in real-time. This system was positively tested in one cadaveric model. However, critical registration errors were observed, and the authors suggested that an additional organ-tracking system is needed.

An interesting idea was also presented by Ungi *et al.* [98]. Using ultrasonography combined with an EMT system to track US probe and the needle tip, the authors proposed a computer-assisted solution to improve renal access based on tracked US snapshots. Hence, after US inspection and location of the optimal puncture site, a tracked US snapshot was recorded in the selected site remaining static in a 3D virtual environment. The user can select the target site and the needle entry in the snapshot. Then, using a virtual needle representation, the puncture can be performed and supported in real-time by ultrasonography. Ten operators tested this new approach in a phantom model. The results revealed that snapshot strategy improved needle path length, number of attempts, and procedure and puncture time.

Zhang *et al.* combined an optical tracking system, a needle steering robot, and pre- and intraoperative imaging into a surgical navigation interface. After calibrating all systems, where the optical tracking system worked as an intermediate coupling tool, phantom tests were performed. Needle-target distance was 2.15 mm [99].

Hamamoto and colleagues reported a new navigation system for PRA [100][†]. For that, they used an US machine together with a EMT system to track the movements of the US probe coupled with a needle. Then, the navigation system provides a cross-sectional multiplanar reconstructed image of the kidney by combining real-time US with CT volume data. CT and US images appeared side-by-side on the monitor. Image synchronization was performed with the patient in prone position (as for CT) and the same respiratory phase (end point of expiration by holding their breath for about 30 seconds). It took approximately 10 minutes to synchronize images. Few technical details about image synchronization were disclosed. Ureteroscopic vision helped monitoring the location of the needle puncture. Lower number of attempts and postoperative hemoglobin decrease were obtained with this new system.

1.2. Motivation

Percutaneous renal access is a surgical step daily used in operating rooms across the globe. It is crucial in the treatment of several kidney diseases, particularly nephrolithiasis through PCNL. The success of PCNL is highly dependent on the initial renal access where a precise needle puncture decreases the overall complications and facilitates the following surgical steps. Performing PRA successfully is associated with the surgeon's experience and the accessing technique. A highly experienced surgeon is one who already performed more than 100 renal accesses [33], which is challenging for trainees to achieve, commonly associated with higher complication rates and therefore discouraging them from obtaining PRA by their own.

Conventional techniques based on fluoroscopy are still being chosen by most of the surgeons, but, despite recent incorporation of low-dose fluoroscopy equipment and techniques, it still exposes patients, surgeons, and medical staff to radiation every day. Ultrasonography has gained supporters since it reduces and/or eliminates radiation exposure but images can be difficult to interpret, mainly due to the out-of-plane needle position. However, different solutions have recently been integrated to aid PRA in ultrasonography. EMT-based solutions demonstrated their potential in projecting the needle trajectory over the US images. At the same time, endoscopic approaches, as ureteroscopy which facilitates the internal visualization of the collecting system and the selection of a specific calyx to puncture, have been combined successfully with EMT systems as well, where the tracking of the tips of surgical instruments and sensors positioned internally in the human body is possible (an advantage over optical-based tracking systems). Specifically, Rodrigues and members of this Ph.D. project proposed an EMT and ureteroscopy-based solution to improve PRA. This solution allows no radiation exposure, accurate puncturing, 3D perception of needle-catheter trajectory in real-time, redefinition of needle-catheter trajectory, comfortable puncturing for the surgeon, shorter puncture time, and is performed in the supine position (no patient repositioning is necessary, reducing surgery time). Indeed, these authors created a solution easy-to-learn and use, which is an essential requirement to promote the technology adoption by surgeons [79]. However, this technology presents two main constrains. First, the inability to place the catheter in the desired calyx if fully occupied by a stone [47]. Indeed, if the calyx is not fully occupied by a stone, the direct access is straightforward since the flexible ureteroscope can be placed inside the calyx and the needle-catheter path can be performed with high accuracy using the EMT system. If fully occupied, safe access is very difficult since no catheter is inside the desired calyx and it is challenging to check the position of the catheter in the collecting system. Second, the lack of visualization of anatomical structures during puncture is another drawback of this solution [47]. Despite the pre-inspection of the needle-

catheter path with ultrasonography to plan the needle trajectory, the image appraisal requires an experienced user to select the optimal trajectory and avoid the closest organs, especially in obese patients. In fact, the correct calyx selection and needle trajectory is essential to distinguish if the needle will enter in the less vasculature zone of the calyx (*i.e.* Brodel's line) and straight to the collecting system, or not. These two aspects could have a great impact on surgical outcomes. However, both may not be completely accomplished with the system previously proposed. Indeed, understanding the kidney's shape and position is crucial for a correct and safe puncture which is only possible with a 3D perception of the anatomy. In the solution proposed by Rodrigues *et al.* and later clinically validated by Lima *et al.* [80][†], no augmented 3D perception of the kidney is available to help identify the correct entry site. The lack of 3D perception could be especially hard for less experienced surgeons and surgeons who face some difficulties in translating the patient's anatomy (evaluated through preoperative CT and intraoperative US) to the procedure. These facts might lead to a suboptimal entry site, potentially increasing complication rates or even requiring the use of conventional techniques if it fails, with their associated drawbacks. Moreover, adjacent anatomical structures may be injured if a suboptimal trajectory is followed, which may lead to significant complications as well. Thus, a 3D perception/visualization of the surgical site is important.

To intraoperatively obtain a 3D visualization of the surgical site, a 3D imaging system may be used. Despite the advantages, intraoperative 3D ultrasonography is not fully available in all hospitals/departments and the volumetric information is still proprietary (*i.e.* not freely released to third parties), hampering its application in novel image guidance systems. As an alternative, intraoperative CT has also been proposed for PRA. Despite its interesting results, it is associated with increased radiation exposure, while also significantly increasing the cost of the operation (a drawback also shared by recently proposed robotic-based solutions). Notwithstanding its shortcomings when used intraoperatively, CT is still the most feasible option to preoperatively diagnose kidney stones, particularly if using low-dose CT protocols for reduced radiation exposure and CT-angiography for enhanced kidney vasculature visualization.

Although several strategies proposing to fuse preoperative and intraoperative image data have been presented with successful results (enhancing the 3D location of the kidney and adjacent organs), several limitations remain. Specifically, the image fusion and PRA must be performed in a specific respiratory moment which may not be practical and accurate for all situations, a large number of the proposed strategies were based on optical tracking systems which are limited on tracking the needle bending inside the body and inherently the abdominal motion misrepresenting the image fusion, no organ-

tracking or real-time registration solutions were proposed, several fusion strategies were based on external markers which hamper the final registration, and the registration process was time consuming in some situations.

In short, despite the individual advantages of each solution, it is evident that the development of a robust solution is still necessary to improve PRA.

1.3. Aims

This thesis aims to make PRA easier and safer to perform. Therefore, the development of a novel surgical navigation system to support PRA is proposed here.

Taking advantage of the puncture precision obtained with EMT systems and ureteroscopy as proposed by Rodrigues *et al.*, the novel solution must integrate intraoperative imaging (*i.e.* ultrasonography) and image fusion with preoperative image data (*i.e.* computed tomography). This system
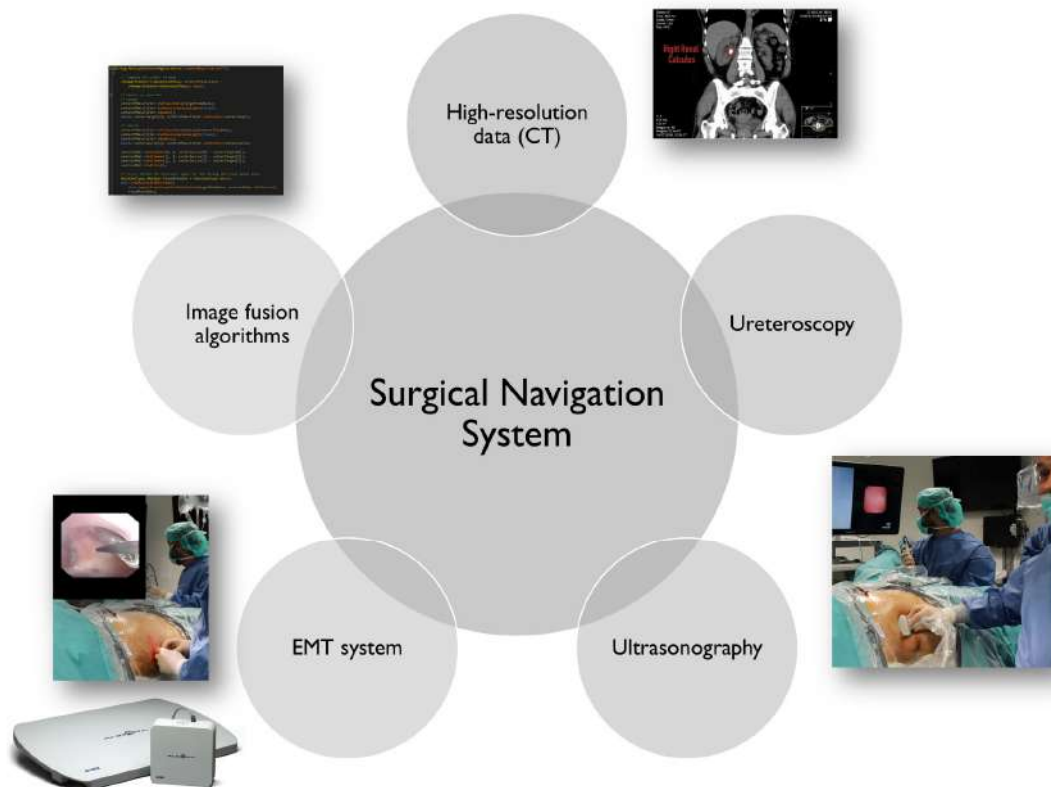
Figure 1.8 – Overview of the proposed surgical navigation system.
The surgical navigation system proposed to perform PRA must combine the following technologies: High-resolution data from preoperative computed tomography (CT); Ureteroscopy images to evaluate the renal collecting system and to place a catheter inside the desired calyx to be puncture; Ultrasonography images to intraoperatively evaluate the kidney and adjacent organs and to select the optimal needle trajectory; Electromagnetic-tracking (EMT) system to track surgical instruments and guide the puncture with high accuracy; and Image fusion algorithms to combine preoperative and intraoperative data in a computer-assisted solution to efficiently support the surgeon during puncture.

must be precise and, simultaneously, display in a virtual environment enough anatomical information to support the surgeon during PRA (Figure 1.8).

To date, no solution has been proposed that combines the potentialities of the abovementioned tools, which can be a step forward to create a universal, easy-to-use, easy-to-learn, safe, precise, and intraoperative radiation-free solution for PRA in PCNL.

The focus of this thesis is to study new strategies to perform preoperative and intraoperative image registration, and ultimately deliver a novel solution that can be translated to the clinic.

1.4. Contributions

This thesis includes the following main contributions (Figure 1.9):

A) *Electromagnetic tracking system performance assessment*: the impact of ureteroscopy and ultrasonography instruments in the EMT systems was studied in a surgical environment. Moreover, this assessment allowed us to identify the most suitable EMT system and surgical configuration to reduce EMT errors.

B) *CT- and US-compatible kidney phantom*: a kidney phantom model with multiple fiducials markers was developed to assess image fusion strategies between preoperative CT and intraoperative US image data in the context of PRA. Moreover, a multi-organ version of this phantom was developed to represent a wider region of the abdominal renal region, closely mimicking the real surgical scenario.

C) *Feasibility study of CT and US registration using partial point sets*: in an *in-silico* environment, the potential of a point set registration technique and an optimal US acquisition protocol to fuse 2D US and 3D CT data of the kidney was assessed and established, respectively.

D) *A new intraoperative image fusion approach:* a new strategy is proposed to intraoperatively fuse CT and US data based on a semi-automatic segmentation and point set registration algorithms. Both algorithms were thoroughly assessed, and the strategy's robustness evaluated for different US probes and image settings.

E) *A novel surgical navigation system:* a computer-assisted solution was developed to aid PRA that integrates the previous contributions (*i.e.* intraoperative CT-US fusion) and additional navigation features, such as: the projection of the needle trajectory and catheter over the US images, as well as its visualization in the 3D virtual environment; the referencing of the CT-

24
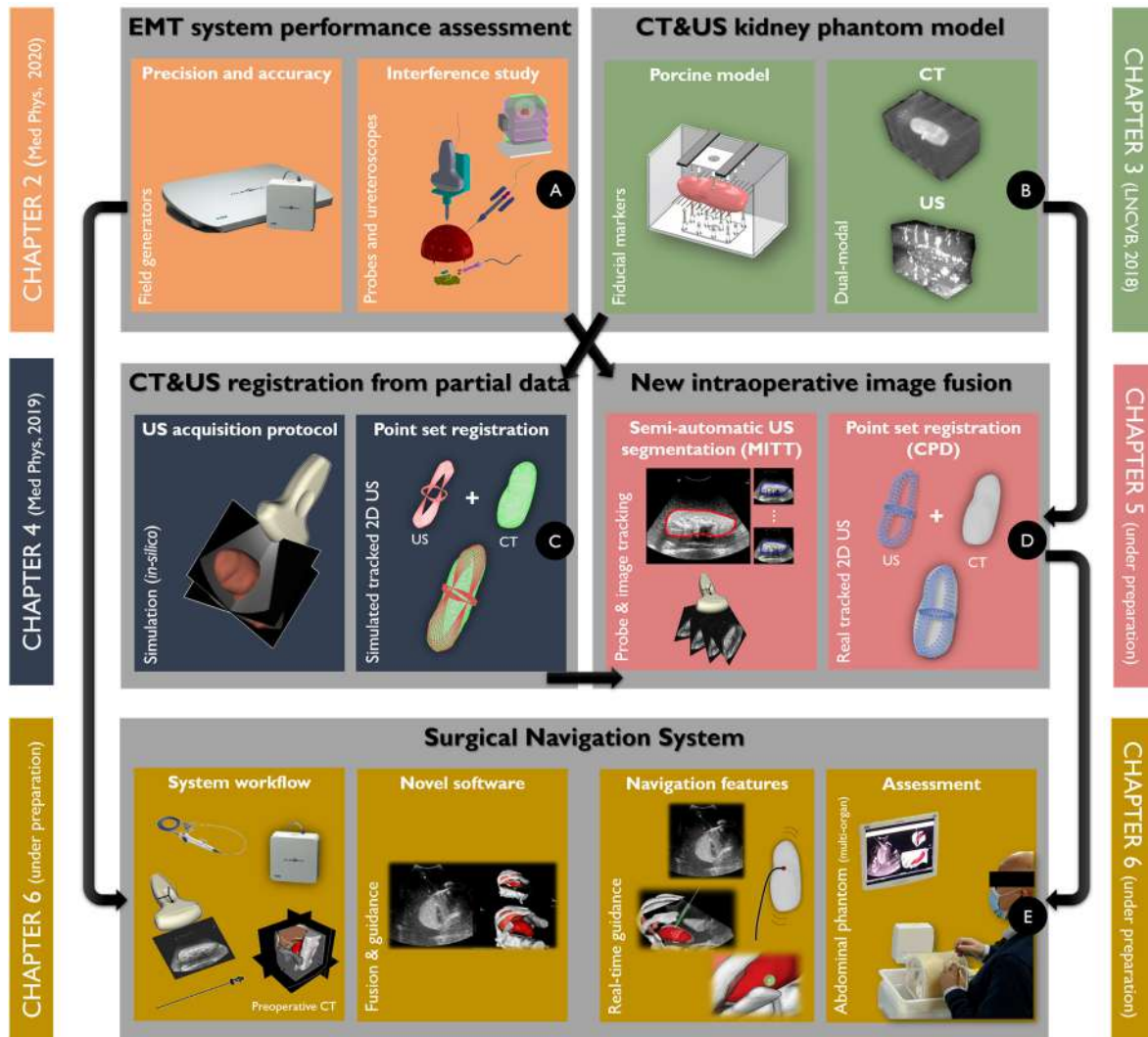
Figure 1.9 – Overview of the main contributions of this thesis.
The letters are linked to the contributions enumerated in Section 1.4. The associated journal manuscripts are indicated between parenthesis (abbreviated journal title, year). CPD – Coherent Point Drift; CT – Computed Tomography; EMT – Electromagnetic Tracking; MITT – Medical Image Tracking Toolbox; US – Ultrasound.

US fusion to the catheter allowing continuous organ-tracking and, thus, compensating respiratory and internal organ movements; and a needle guidance interface for visual feedback during puncture. This system improves on recent state-of-the-art solutions for PRA without significant additional costs. The solution was tested by surgeons in an abdominal phantom model.

The proposed navigation system delivers the following surgical benefits:

- improved renal access by performing a straight puncture, easing the subsequent surgical steps;
- mitigation of intraoperative radiation during PRA;

- increased 3D perception of the entire surgical environment, *i.e.* pose of surgical tools and relevant abdominal organs;

- reduction of surgical complication rates, such as kidney and adjacent organs injuries, increasing PRA overall safeness;

- increased surgeon's confidence to perform PRA, broadening its usage by less trained surgeons;

- reduced surgical and puncture times.

- improved renal access in other surgical interventions than PCNL (*e.g.* percutaneous ablations).

Regarding publications, this thesis has generated the following outputs:

International journals:

- B. Oliveira, ..., **J. Gomes-Fonseca** *et al.*, "A novel multi-atlas strategy with dense deformation field reconstruction for abdominal and thoracic multi-organ segmentation from computed tomography.," Med. Image Anal., vol. 45, pp. 108–120, Apr. 2018. https://doi.org/10.1016/j.media.2018.02.001.

- N. A. De Sousa Morais, **J. Gomes-Fonseca** *et al.*, "Ureteroscopy-assisted percutaneous kidney access with a novel navigation system using electromagnetic guidance: An updated clinical series," Eur. Urol. Suppl., vol. 17, no. 4, pp. e2128–e2129, May 2018. https://doi.org/10.1016/S1569-9056(18)32522-3.

- **J. Gomes-Fonseca** *et al.*, "Surface-based registration between CT and US for image-guided percutaneous renal access - A feasibility study," Med. Phys., vol. 46, no. 3, pp. 1115–1126, Mar. 2019. https://doi.org/10.1002/mp.13369.

- **J. Gomes-Fonseca** *et al.*, "Technical Note: Assessment of electromagnetic tracking systems in a surgical environment using ultrasonography and ureteroscopy instruments for percutaneous renal access," Med. Phys., vol. 47, no. 1, pp. 19–26, Jan. 2020. https://doi.org/10.1002/mp.13879.

- H. R. Torres, ..., **J. Gomes-Fonseca** *et al.*, "Kidney Segmentation in Three-Dimensional Ultrasound Images using a Fast Phase-based Approach", Transactions on Ultrasonics, Ferroelectrics, and Frequency Control, Nov. 2020. (*in press*) 10.1109/tuffc.2020.3039334.

International conference proceedings:

- **J. Gomes-Fonseca** *et al.*, "A Dual-Modal CT/US Kidney Phantom Model for Image-Guided Percutaneous Renal Access," in Lecture Notes in Computational Vision and Biomechanics, vol. 27, Springer Netherlands, 2018, pp. 378–387. https://doi.org/10.1007/978-3-319-68195-5_42.

Public dataset:

- **J. Gomes-Fonseca** *et al.*, "A Dual-Modal CT/US Kidney Phantom Model for Image-Guided Percutaneous Renal Access," Mendeley Data, v1. 18-Oct-2018. http://dx.doi.org/10.17632/vgmt7brcmw.1.

Publications under preparation:

- **J. Gomes-Fonseca** *et al.*, "A new intraoperative image fusion approach using partial US kidney segmentation and CT-US registration for percutaneous renal access", *under preparation to be submitted for publication as an original article in an international peer reviewed journal.*

- **J. Gomes-Fonseca** *et al.*, "Surgical navigation system for percutaneous renal access: Computed Tomography, Ultrasound, Ureteroscopy and Electromagnetic tracking guidance working together", *under preparation to be submitted for publication as an original article in an international peer reviewed journal.*

1.5. Thesis outline

This initial chapter presents a small historical perspective of PRA, the influence of PRA in the treatment of nephrolithiasis through PCNL, the relationship between the anatomy of the kidney and a safe puncture to the renal calyx, and the state-of-the-art of technologies to assist PRA. Moreover, motivation, aims, contributions and structure of this thesis are described. The following five chapters are presented as scientific papers.

Chapter 2 presents a study where two electromagnetic tracking systems were assessed in a realistic surgical environment. Precision and accuracy of both systems were assessed using a standardized protocol, and the influence of specific ultrasonography and ureteroscopy instruments was tested as well to quantitively understand their impact on the EMT performance.

Chapter 3 introduces the protocol of a kidney phantom model based on a porcine kidney combined with a tissue mimicking material and implanted fiducial markers. This phantom was proposed and used to validate image fusion strategies.

Chapter 4 focuses on assessing the best protocol to acquire partial US data to improve fusion between full CT and tracked US data using a point set registration technique. Different acquisition protocols were simulated *in silico* using image data from kidney phantom models proposed in Chapter 3.

Chapter 5 compiles the main outputs of Chapters 2 and 4 to present a new intraoperative image fusion approach to improve PRA. This new approach uses a partial US kidney segmentation, obtained from a semi-automatic algorithm, and a point set registration algorithm to fuse pre- and intraoperative data. It was evaluated in an *ex-vivo* setup. Different factors were considered during assessment: probes, image settings, US acquisition protocols, probe calibration, segmentation, and registration methods.

In Chapter 6, a surgical navigation system is presented. Here, a software with a graphical user interface that integrates information from CT, ultrasonography, ureteroscopy, and EMT system is shown. All steps needed to perform the image fusion and needle guidance during PRA are integrated into a virtual environment. New needle guidance techniques are presented. Initial tests were performed by surgeons in an abdominal phantom specifically designed for these tests.

Finally, Chapter 7 provides the main conclusions of the work described in this thesis and presents suggestions for future work.

Chapter 2

Assessment of electromagnetic tracking systems in a surgical environment using ultrasonography and ureteroscopy instruments for percutaneous renal access

Abstract

Electromagnetic tracking (EMT) systems have been proposed to assist the percutaneous renal access (PRA) during minimally invasive interventions to the renal system. However, the influence of other surgical instruments widely used during PRA (like ureteroscopy and ultrasound equipment) in the EMT system performance is not completely known. This work performs this assessment for two EMT systems (Aurora® *Planar Field Generator – PFG*; Aurora® *Tabletop Field Generator - $TTFG$*).

An assessment platform, composed by a scaffold with specific supports to attach the surgical instruments and a plate phantom with multiple levels to precisely translate or rotate the surgical instruments, was developed. The median accuracy and precision in terms of position and orientation were estimated for the PFG and $TTFG$ in a surgical environment using this platform. Then, the influence of different surgical instruments (alone or together), namely analogic flexible ureterorenoscope (AUR), digital flexible ureterorenoscope (DUR), 2D ultrasound (US) probe and 4D mechanical US probe, was assessed for both EMT systems by coupling the instruments to 5-DOF and 6-DOF sensors.

Overall, the median positional and orientation accuracies in the surgical environment were 0.85 mm and 0.42 ° for PFG, and 0.72 mm and 0.39 ° for $TTFG$, while precisions were 0.10 mm and 0.03 ° for PFG, and 0.20 mm and 0.12 ° for $TTFG$, respectively. No significant differences were found for accuracy between EMT systems. However, PFG showed a tendency for higher precision than $TTFG$. AUR, DUR, and 2D US probe did not influence the accuracy and precision of both EMT systems. In opposition, the 4D probe distorted the signal near the attached sensor, making readings unreliable.

Ureteroscopy and ultrasonography-assisted PRA based on EMT guidance are feasible with the tested AUR or DUR together with the 2D probe. More studies must be performed to evaluate the probes and ureterorenoscopes' influence before their use in PRA based on EMT guidance.

2.1. Introduction

Percutaneous renal access (PRA) is a surgical step where the surgeon inserts a surgical needle from the skin until the kidney target site. Percutaneous nephrolithotomy, kidney radiofrequency ablation of renal tumors, and kidney biopsies are minimally invasive interventions that use the PRA technique to reach the kidney.

In the past few years, continuous innovations have been proposed to improve practices and safeness in PRA [45], [47]. The use of electromagnetic tracking (EMT) systems, together with

ureteroscopy and ultrasound equipment, has been associated with promising results. Huber *et al.* presented an initial experience of a rendezvous approach for PRA using an EMT system [78]. Wegner *et al.* studied in a kidney phantom the accuracy and the isolate pitfalls for using multiple or adjacent EMT sensors in clinical routine under the influence of endo-urological instruments [101]. Lima *et al.* presented and validated a novel navigation system that uses ureteroscopy and an EMT system to perform PRA [79]–[81]. Li *et al.* assessed a real-time ultrasound (US) navigation-guided system (SonixGPS) for PRA, which uses special electromagnetic position sensors in the US probe and needle [71], [72]. Hamamoto *et al.* evaluated the clinical utility of a new real-time virtual sonography-guided system combined with an EMT system and ureteroscopy for PRA [100]. Despite the good results, these works use EMT systems that can be affected by the presence of different medical instruments inside the generated electromagnetic field [102].

Several researchers have previously developed specific protocols to assess EMT system' precision and accuracy [103]–[112]. These protocols were used to evaluate the performance of EMT systems in the clinical environment [113]–[117], using different surgical tools [110], [118]–[123], among others scenarios and applications [124].

To the best of our knowledge, a standardized assessment of this specific setup was not performed before, *i.e.* no study has quantitively evaluated the influence of the simultaneous use of ureteroscopy and/or ultrasonography instruments in the EMT system for this intervention in a realistic operating room. Thus, the aim of this work is to assess two EMT systems in a surgical environment, and to assess the interference of different US probes, flexible ureterorenoscopes and needles on the EMT systems' performance.

This technical note is structured as follows. In Section 2.2, we present our experimental setup to, first, evaluate the performance of the EMT systems in the surgical environment (characterizing the inner distortion), and, second, the influence of the different surgical tools in the EMT systems' performance. In section 2.3, we present the results based on standard metrics. In section 2.4 and 2.5, we discuss the results and present the main conclusions.

2.2. Materials and Methods

2.2.1. Field generators and electromagnetic sensors

In this study, we evaluated two field generators (FGs) from NDI (Northern Digital, Inc., Waterloo, Ontario, Canada): the NDI Aurora® V2 *Planar Field Generator* (PFG), and the NDI Aurora® V2 *Tabletop*
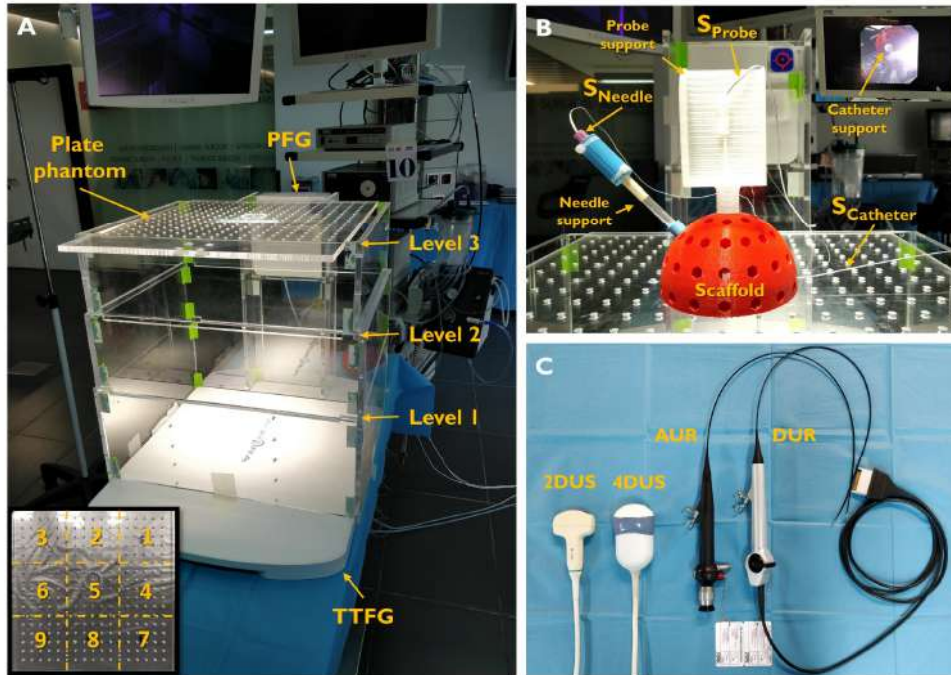
Figure 2.1 – Fields generators, electromagnetic sensors, assessment platform, and surgical instruments in the surgical environment.
A – Field generators used in this study: Aurora® Planar Field Generator (PFG); and Aurora® Tabletop Field Generator ($TTFG$). Experimental setup under surgical environment. The $TTFG$ was mounted on the surgical stretcher, while the PFG was placed above the surgical stretcher. The assessment platform was composed by a plate phantom with three levels and a scaffold. In each level, 9 equally spaced positions were acquired for each field generator. B – The scaffold holding the supports for ureterorenoscopes, US probes, and needles. Each support was attached to an electromagnetic sensor: $S_{Catheter}$ (5-DOF); S_{Probe} (6-DOF); and S_{Needle} (5-DOF). C – Different instruments under assessment in this study. From left to right: 2D US probe (GE C358, Convex probe, GE Vivid 3); 4D US probe (GE RAB4-8P, 4D Convex probe, GE Voluson 730); Analogic Flexible Ureterorenoscope (Flex-X2S, Karl Storz); Digital Flexible Ureterorenoscope (Flex-XC, Karl Storz).

Field Generator ($TTFG$), see Figure 2.1-A. The PFG generates a cubic electromagnetic volume, known as *Cube* (500x500x500 mm³), starting at approximately 50 mm from the physical generator, while the $TTFG$ generates an ellipsoid electromagnetic volume, known as *Dome* (600x420x600 mm³), starting at approximately 120 mm from the physical board. The manufacturer states that the system provides submillimetric and subdegree measurement accuracies. Similarly, they report different position and orientation errors according to FG type, measurement volume used, and sensor type (*i.e.* 5 or 6-degrees-of-freedom [DOF]) [125].

Three different electromagnetic sensors were used (see Figure 2.1-B), and they are named according to their typical position: (1) the Aurora® 5-DOF Flex Tube (1.0 mm diameter) was used as the catheter inserted on the working channel of the flexible ureterorenoscope (henceforward designated as $S_{Catheter}$); (2) the Aurora® 5-DOF Needle (18G/150 mm, Chiba), with a sensor in its tip, consisted of a stylet and an outer cannula (henceforward designated as S_{Needle}); and (3) the Aurora® 6-DOF Cable tool

(2.5 mm diameter), which was coupled to the US probe, tracking its movements (henceforward designated as S_{Probe}).

2.2.2. Assessment platform

The assessment platform was developed based on previous works of Hummel *et al.* [104], [105], Maier-Hein *et al.* [111] and Lugez *et al.* [116]. Inspired by Lugez *et al., a* scaffold (a hemispherical structure with hexagonal holes) was built to fix the sensors and instruments at specific positions and orientations. Then, a similar plate phantom with precisely drilled holes, as presented by Hummel *et al.,* was used, allowing to position the scaffold at known relative distances and orientations. As proposed by Maier-Hein *et al.*, a multiple level strategy was also applied (Figure 2.1-A/B).

The scaffold holds three specific supports which rigidly attach the US probes, ureterorenoscopes and needle to the scaffold (Figure 2.1-B). Each support holds one electromagnetic sensor, keeping it static. The scaffold and supports allow placing the sensors using comparable positions as used in ultrasonography and ureteroscopy-assisted PRA. Therefore, the *US probe support* was fixed at the center and at the top of the scaffold mimicking similar distances between skin and kidney. The *needle support* was aligned with the *US probe support* (*i.e.* parallel with the US image plane). The *catheter support* was fixed at the center and at the bottom of the scaffold, integrating a specific part that allowed the anchorage of an ureterorenoscope near the electromagnetic sensor. The supports were projected on the CAD software (SolidWorks, Dassault Systèmes, SolidWorks Corporation, Waltham, Massachusetts, United States) and then 3D printed in polylactic acid material using an Ultimaker II Plus (Ultimaker B.V., Geldermalsen, The Netherlands). This printer uses the fused deposition modelling technique, with a printing resolution ± 0.2 mm.

The plate phantom was 10 mm thick, 550 mm square acrylic glass plate with a grid of 17 x 17 holes, 25 mm apart. A three z-levels acrylic glass platform was built, with 150 mm between levels (see section 2.6.1 - Appendix A). Each level allows assembling the plate phantom rigidly. The distance between levels enables the assessment of the electromagnetic volumes with a higher coverage range when compared with Main-Hein *et al.*[111] (*i.e.,* 100 mm)*.* Moreover, the acrylic platform was specifically designed to attach the $TTFG$ on the bottom and the PFG on the lateral. The whole acrylic glass platform was projected on a CAD software and cut on a laser cutting machine (GN640; Gbos Laser Technology Company, Dongguan City, Guangdong Province, China) with a cutting precision of ± 0.04 mm. See appendix A (section 2.6.1) for more information.

2.2.3. Experiments

Experimental setup

The experiments were performed in the training operating room at Life and Health Sciences Research Institute (ICVS, School of Medicine, University of Minho, Braga, Portugal), giving similar conditions as a surgical environment. An aluminum surgical stretcher with an electromechanical system was used. Additionally, the surgical environment was enriched with typical surgical equipment, as laparoscopy towers, surgical lights, surgical monitors, ultrasound machines, and a ventilator support. The acrylic glass platform was positioned at the center and over the operating table. All experiments were performed with the platform at the same position (Figure 2.1-A).

Data acquisition

A custom software application using MATLAB® (version R2016b, The Mathworks Inc., Natick, MA) was developed to acquire the positions and orientations of each electromagnetic sensor and to configure the initial settings of both FGs. For each location, 400 samples were recorded, which corresponds to approximately 10 seconds of data stream at an update rate of 40 Hz (tracking frequency). Cartesian coordinates (x, y, and z) and quaternions (q_0, q_x, q_y, q_z) were recorded.

EMT systems precision and accuracy in a surgical environment

The accuracy and precision in terms of position and orientation were assessed for both EMT systems using the 5-DOF and 6-DOF sensors (*i.e.* $S_{Catheter}$, S_{Needle} and S_{Probe}).

The *position accuracy* Acc_P was calculated as the absolute difference between the ground-truth distance, d_{GT}, and the measured Euclidean distance, $\bar{d}_i$, between two locations, $\overline{\boldsymbol{p}}_i$, where $\bar{d}_i = \|\overline{\boldsymbol{p}}_i - \overline{\boldsymbol{p}}_{i+1}\|_2$; $\overline{\boldsymbol{p}}_i = \frac{\sum_{j=1}^{N_s} \boldsymbol{p}_{ij}}{N_s}$; $\overline{\boldsymbol{p}}_i \in \mathbb{R}^3$; $i = 1, \dots, N_L$ represents the number of locations; and $j = 1, \dots, N_s$ the number of samples (n = 400) per location. $\|\dots\|_2$ denotes the Euclidean distance. The Acc_P specifies how accurate the tracking is when the sensor is moved by a known distance. Thus, measurements were obtained changing the scaffold position along 9 different locations in the phantom plate (equally spaced by 150 mm in all directions [104], [111]) and along the 3 levels (similarly, spaced by 150 mm), *i.e.* $d_{GT} = 150$. In total, 54 position differences were obtained, *i.e.* 12 for each level (36 in total) plus 9 between levels (18 in total). See Figure 2.

The *orientation accuracy* Acc_O was calculated as the absolute difference between the angle ground-truth, a_{GT}, and the measured angle, $\bar{a}_i$, between two pairs of rotations, $\overline{\boldsymbol{q}}_i$, where $\bar{a}_i =$

34

$2 \, arccos(\overline{q}_i \overline{q}_{i+1}^*))$; and $i = 1, \ldots, N_o$, where N_o represents the number of tested rotations. Let $\overline{q}_i \overline{q}_{i+1}^*$ be the true difference between two quaternions, where q^* denote the quaternion conjugate. The average quaternion, $\overline{q}$, can be found by the following maximization procedure $\overline{q} = \underset{q \in \mathbb{S}^3}{\mathrm{argmax}} \, q^T M q$, where $M \triangleq \sum_{j=1}^{N_s} w_j q_j \, q_j^T$; $w_j = 1$; and $j = 1, \ldots, N_s$, where N_s is the number of samples (n = 400) per rotation. Thus, the average quaternion is the eigenvector of M corresponding to the maximum eigenvalue [126]. To simplify the experiments, we assume a ground-truth angle of zero degrees (*i.e.* $a_{GT} = 0$), meaning that no rotation exists between different scaffold locations. Indeed, the orientation accuracy was measured by comparing the quaternions at different positions in the plate phantom and levels but keeping the same sensor's orientation. This enables us to compare the orientation accuracy along the electromagnetic volume. As previously, 54 orientation differences were computed using adjacent locations.

The precision is commonly known as *jitter error*. The *position precision* Pre_P for each location was defined as the standard deviation of all positional samples p_j, $j = 1, 2, \ldots, N_s$. Thus, *position precision* is defined as $Pre_P = \sqrt{\frac{1}{N_s} \sum_{j=1}^{N_s} \left\| p_{ij} - \overline{p}_i \right\|_2^2}$.

Similarly, the *orientation precision* Pre_O for each rotation was defined as the standard deviation of all orientational samples q_j. Therefore, the *orientation precision* is defined as $Pre_O = \sqrt{\frac{1}{N_s} \sum_{j=1}^{N_s} (2 \, arccos(q_{ij} \overline{q}_i^*))^2}$.

In total, 27 values for orientation and position precisions were computed per EMT system and sensor under assessment.

The median values and 5th and 95th percentiles were calculated for accuracies and precisions. A statistical test (parametric or non-parametric according to the variables' normality) was performed to assess differences in performance between EMT systems ($p < 0.05$).

Ureteroscopy and ultrasonography-induced distortion error

The distortion errors induced by different instruments in the EMT system were assessed using two US probes and two flexible ureterorenoscopes. In this study, the following instruments were tested (Figure 2.1-C): (1) 2D US probe (GE C358, Convex probe, GE Vivid 3); (2) 4D US probe (GE RAB4-8P, 4D Convex probe, GE Voluson 730); (3) Analogic flexible ureterorenoscope (Flex-X2s, Karl Storz); (4) Digital flexible ureterorenoscope (Flex-Xc, Karl Storz). The 4D US probe uses an electromechanical system to perform 3D acquisitions in real-time.

The instruments were attached to specific supports and placed in the scaffold. The needle was used in all experiments. All sensors were acquired, *i.e.* S_{Needle}, S_{Probe} and $S_{Catheter}$, for each situation. The induced distortion errors were calculated against ground-truth values, which were obtained without any instrument attached to the support. Four different locations in level 2 were acquired to compute precision and accuracy. Both systems were evaluated.

2.3. Results

2.3.1. Accuracy and Precision in a surgical environment

Figure 2.2 reports the overall accuracies and precisions for different FGs and sensors considering the surgical environment and individualizes the accuracy and precision for the locations obtained by each sensor using different EMT systems. It is possible to observe the error configuration within the electromagnetic volumes, where the errors are superior in the zones further from the FGs. Overall, the
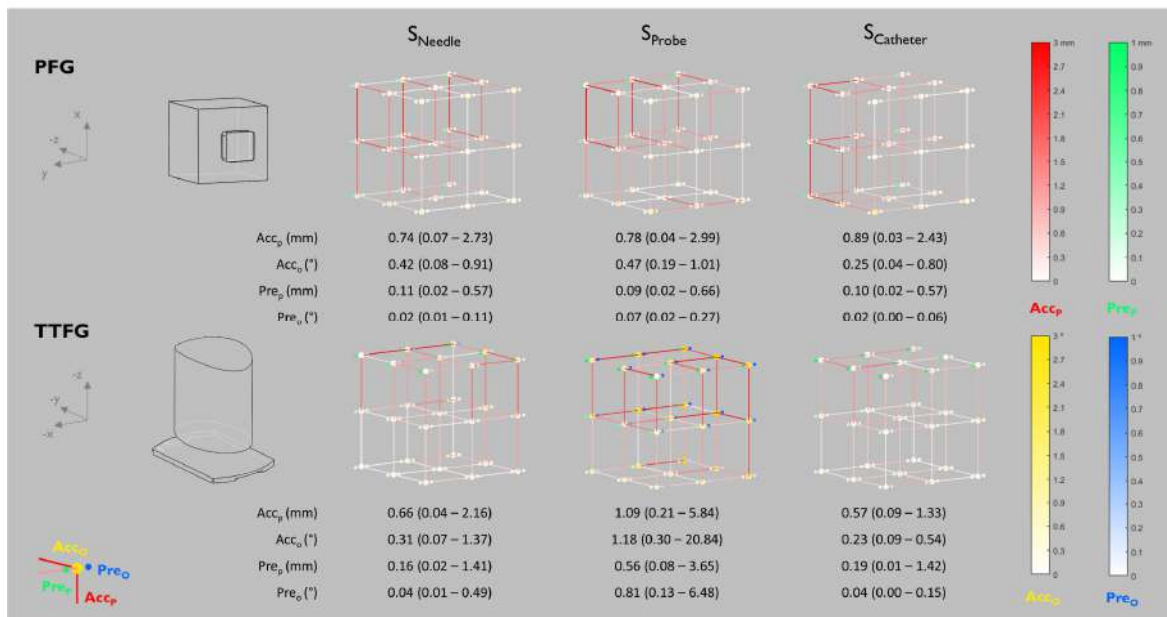
Figure 2.2 – Visual representation of EMT systems' assessment in a surgical environment.
Visual representation of accuracy (position, Acc_P, and orientation, Acc_O) and precision (position, Pre_P and orientation, Pre_O) for both EMT systems (PFG and $TTFG$) and the three electromagnetic sensors (S_{Needle}, S_{Probe} and $S_{Catheter}$) in the surgical environment. The accuracy and precision errors of the 27 locations arranged by level are represented. The errors are characterized in the color scale, where white color means values near zero millimeters or zero degrees. The Acc_P is represented by the red color scale and drawn as a line between different locations. Acc_O is represented by the yellow color scale and drawn as a sphere in each location (mean of differences between adjacent locations). In addition, in each location, the Pre_P and the Pre_O are drawn as spheres in green and blue color scales, respectively. Median, 5th and 95th percentiles are presented for Acc_P (n = 54), Acc_O (n = 54), Pre_P (n = 27) and Pre_O (n = 27) for each sensor in the EMT systems. The illustrations show the field generators' position, while the axes indicate the field generators' world coordinates in the experiments.

median position and orientation accuracies and precisions (*i.e.*, Acc_P, Acc_O, Pre_P, and Pre_O) were 0.85 mm, 0.42 °, 0.10 mm, and 0.03 ° for PFG; and 0.72 mm, 0.39 °, 0.20 mm, and 0.12 ° for $TTFG$, respectively.

The Wilcoxon Rank Sum test was employed to compare the performance of both systems using MATLAB®. While no statistically significant differences were found for positional (Z = 0.6696, p = 0.5031, r = 0.0372) and orientational accuracy (Z = -0.8285, p = 0.4074, r = -0.0460), positional (Z = -3.4871, p < 0.05, r = -0.2740) and orientational (Z = -4.1738, p < 0.05, r = -0.3279) precision were statistically different between EMT systems.

2.3.2. Instruments-induced distortion error

Figure 2.3 illustrates the accuracy and precision of different sensors when different instruments were within each electromagnetic volume. Based on previous measurements (Figure 2.2), each graph also presents the 95% percentile of errors at level 2 if no instruments are present inside the electromagnetic field.

Overall, position accuracy and precision were not affected for most of the tested scenarios, where the measured values stayed within the expected value. Both ureterorenoscopes and 2D US probe did not influence attached sensors, even when used together. However, values slightly higher than expected were found for the orientation accuracy (*i.e.* Acc_O) in S_{Probe} for PFG when the 2D probe was used, and significant differences were found (Z = -3.6662, p < 0.05, r = -0.7484), but the mean difference between having or not a 2D probe attached to the S_{Probe} was 0.58 ° only. No differences were found in $TTFG$
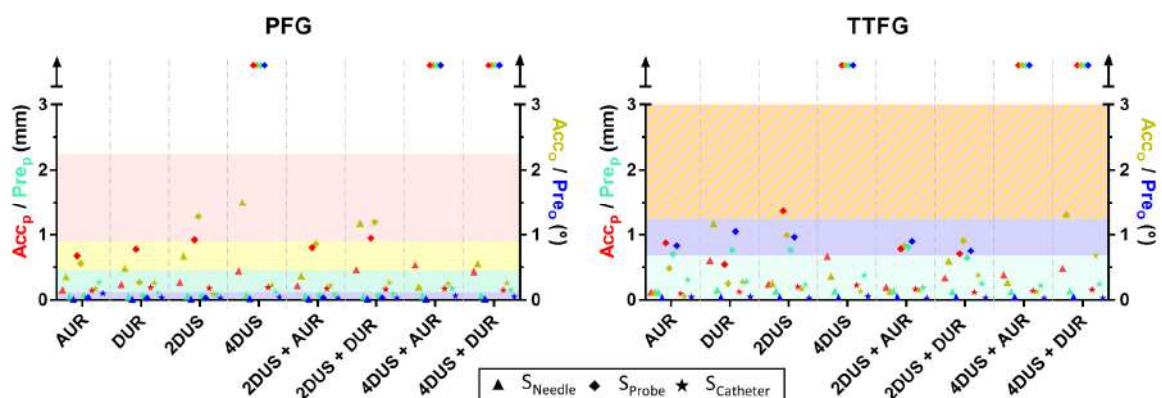
Figure 2.3 – Instruments-induced distortion error.
Median accuracies and precisions of S_{Needle}, S_{Probe} and $S_{Catheter}$ in the PFG and $TTFG$ considering the presence of different instruments. Left scale: Position accuracy (Acc_P– Red) and precision (Pre_P – Green). Right scale: Orientation accuracy (Acc_O – Yellow) and precision (Pre_O – Blue). The position and orientation results (for each dot symbol, n = 4) are in millimeters (mm) and degrees (°), respectively. The 95th percentile for each metric is delimited by the colored areas and it was established using results from level 2 computed in section 2.2.3 - *EMT systems precision and accuracy in a surgical environment* .

comparing the same scenarios. The 4D US probe was the only instrument introducing strong distortion in both systems under study, making it impossible to collect position and orientation data in the attached sensor. However, no interference was observed in the adjacent sensors (*i.e.* S_{Needle} and $S_{Catheter}$).

2.4. Discussion

Some attempts to assess EMT system in different clinical environments have been made in the past few years by different researchers. However, to the best of our knowledge, no work has ever quantified the accuracy and precision of these systems when simultaneously combining ureterorenoscopes, US probes and needles in the same environment. In this study, the PFG and $TTFG$ were assessed in an operating room suite using a new standardized protocol. Inspired by Lugez *et al.* [116], we added a scaffold to the multiple level protocol proposed Maier-Hein *et al.* [111], which allowed to mimic the instruments positions during PRA and assess them in the whole electromagnetic volume.

Overall, the obtained values for the characterization of EMT system in the surgical environment were close to the corresponding values reported in the literature for similar environments, suggesting that EMT systems achieve similar accuracy and precision values under these conditions. Indeed, for the PFG, under a clinical environment and using a 5-DOF sensor, RMS errors for position and orientation accuracies of 1.01 mm and 1.54° were found in Yaniv *et al.* [113], 0.79 mm and 1.57° in Bo *et al.* [115], and 1.40 mm and 1.00° in Lugez *et al.* [116], which compare favorably with the 1.35 mm and 0.51° reported in this study. Small differences between these studies may be related with differences in their protocols and environments. While Yaniv *et al.* and Bo *et al.* used a plexiglass phantom (cube), Lugez *et al.* used two distinct phantoms to measure positional and orientational accuracies/precisions at the center of the electromagnetic volume only. The differences in orientation accuracy could also be linked with the way orientation accuracy is measured across studies: in this study, orientation accuracy was measured between samples taken at different positions across the electromagnetic volume with the orientation fixed, while previous studies have measured the same position in the electromagnetic volume with different orientations. Another possible explanation may be related with the metrics calculation themselves; while we computed the differences directly based on quaternions, some researchers converted the quaternions to Euler angles and computed the differences after. Moreover, one must note that in some studies the calculus used was unclear. The tested environments can influence the measurements as well. Indeed, the focus of previous works was the radiology environments with computed tomography (CT) and C-arm

equipment. Notwithstanding, the comparative values were obtained from environments without CT and C-arm influence.

During experiments, the setup was surrounded by usual supporting equipment to obtain measurements as realistic as possible to those in a PRA surgical environment. The 5-DOF sensors presented slightly more consistent results than 6-DOF for $TTFG$. However, the lower accuracy and precision of S_{Probe} in $TTFG$ were mainly related with extreme positions at level 3. In fact, at level 3, S_{Probe} was positioned approximately 125 mm above both S_{Needle} and $S_{Catheter}$, which is close to the limits of the electromagnetic volume and thus explains the larger errors observed (see section 2.6.1 - Appendix A). When compared to the Maier-Hein *et al.*[111], the current precision error is also superior for $TTFG$. The main reason could be linked to the position of the sensor relatively to the FG. In Maier-Hein *et al.*, the distance between levels were 150, 250, and 350 mm, while in our study are at 150, 300 and 450 mm (in S_{Probe}, it must be added the 125 mm offset for each level). Indeed, it is possible to observe that accuracy and precision values increase along the z-axis, *i.e.* when the sensors were further from the FG. This was observed in both EMT systems (Figure 2.2). Another possible cause for the higher errors in precision for $TTFG$ than PFG might be the locations under assessment. Indeed, the locations in the $TTFG$ were closer to the limits of the EMT volume than PFG (see section 2.6.1 - Appendix A). These results are relevant because they suggest that navigation procedures based on EMT systems should be performed as close as possible to the FGs and, working close to the limits of EMT volumes may introduce additional errors.

The use of analogic and digital flexible ureterorenoscopes did not significantly influence the measurements (Figure 2.3). Indeed, a digital ureterorenoscope and PFG have been tested with excellent outcomes by Lima *et al.* [80]. Thus, these results corroborate that both digital and analogic flexible ureterorenoscopes can be safely used to perform ureteroscopy-assisted PRA based on these EMT systems, either with the PFG or $TTFG$. In addition, the 2D US probe did not influence the attached sensor either, which was not observed for the 4D US probe. Indeed, the 4D US probe introduced a strong distortion in both FGs due to its motor. During acquisition of the S_{Probe}, it was impossible to collect position and orientation data due to high signal distortion. However, this distortion mainly affected the US probe sensor (*i.e.* S_{Probe}) and not the remaining ones (*i.e.* S_{Needle} and $S_{Catheter}$). Similar conclusions were reported by Hastenteufel *et al.* when cardiac 3D US probes were tested [119]. They found that nonreal-time 3D probes (multiplane acquisition, 2D imaging sector technology) and real-time 3D probe (2D matrix array technology) do distort electromagnetic sensors more than a 2D probe (ultraband phased array). In the present study, similar results were found for abdominal US probes, namely the 4D convex

US probe, which uses a similar operating principle of nonreal-time 3D probes (although in real-time), and the 2D convex US probe. Moreover, Hastenteufel *et al.* warned that the choice of tracking technology is strongly dependent on the 3D US probe used, and the position to fixate the electromagnetic sensors. Positioning the sensor in a different zone of the probe (less affected by distortion) could improve accuracy and precision. Indeed, the further it is positioned from the 4D probe, the lower the precision errors seem to be (see section 2.6.2 - Appendix B). However, care should be taken, as sensor position, and thus its distance to the probe's axis/location, also affects probe calibration. Further research on this topic is therefore required. Franz *et al.* presented a comparative study of different 2D US probes which were coupled to a mobile EMT system, the *compact FG* [Northern Digital, Inc. (NDI), Waterloo, Ontario, Canada]. They concluded that, in most cases, 2D probes seem to have no influence on the *compact FG* tracking accuracy [121]. Marz *et al.* also assessed the *compact FG* attached to a 2D US probe, showing positive results [122]. Overall, these results reinforce the use of 2D probes in image-guided interventions based on EMT systems. Besides, some companies are currently commercializing US systems equipped with EMT systems. These systems have 2D US probes specifically built to work inside the EMT volume. While no novel 3D/4D US probe technology totally compatible with EMT systems is introduced (or vice-versa), the use of 2D probes is currently the most reliable option.

The needle sensor was not highly affected by the presence of different instruments at different positions and orientations. This result is in fact relevant for PRA, showing that EMT-based systems can be used for getting an unconstrained access to the kidney, even when the assessed instruments are inside the electromagnetic volume.

Some accuracies and precisions for the instruments-induced distortion and needle positioning were found outside the 95% percentile range (Figure 2.3). However, when comparing all situations (where different instruments were involved), no common pattern was found. Indeed, random errors were present in most cases or, when not random, they were constant in all setups. No causality was associated with different setups. In this sense, these differences may be related to momentary distortion of the signal or sub-millimetric misalignment during scaffold positioning, rather than additive distortion.

This study shows that accuracies and precisions are sufficient to safely reach the kidney, given the kidney calyx' size. Choosing proper instruments, which introduce minimum distortions to the EMT systems, may lead to safe and precise EMT-guided PRA. Other probes and ureterorenoscopes should be evaluated before their use with one of the FGs since they may include materials different from those investigated here.

Despite being a very specific assessment, *i.e.* directed for PRA, it is imperative to understand how all hardware components work together with the EMT system to optimize the setup of the FGs and to maximize tracking accuracy and precision in the area of interest. Guidance frameworks are composed by several systems which need to be fully understood to guide the surgeons precisely.

2.5. Conclusion

This work assessed the performance of EMT guidance for PRA in the operating room suite. Overall, this specific protocol used in this surgical environment suggests that PFG achieve 0.85 mm, 0.42 °, 0.10 mm, and 0.03 °; and $TTFG$, 0.72 mm, 0.39 °, 0.20 mm, and 0.12 ° for position and orientation accuracies/precisions. Both ureterorenoscopes and 2D US probe did not affected the precision and accuracy of the EMT systems, suggesting that these instruments may be used for a safe PRA. In opposition, the 4D US probe distorted the signal of the attached sensor. Studies must be performed to evaluate different US probes and ureterorenoscopes before their use in PRA using EMT guidance.

2.6. Appendixes

2.6.1. Appendix A – CAD drawing of assessment platform
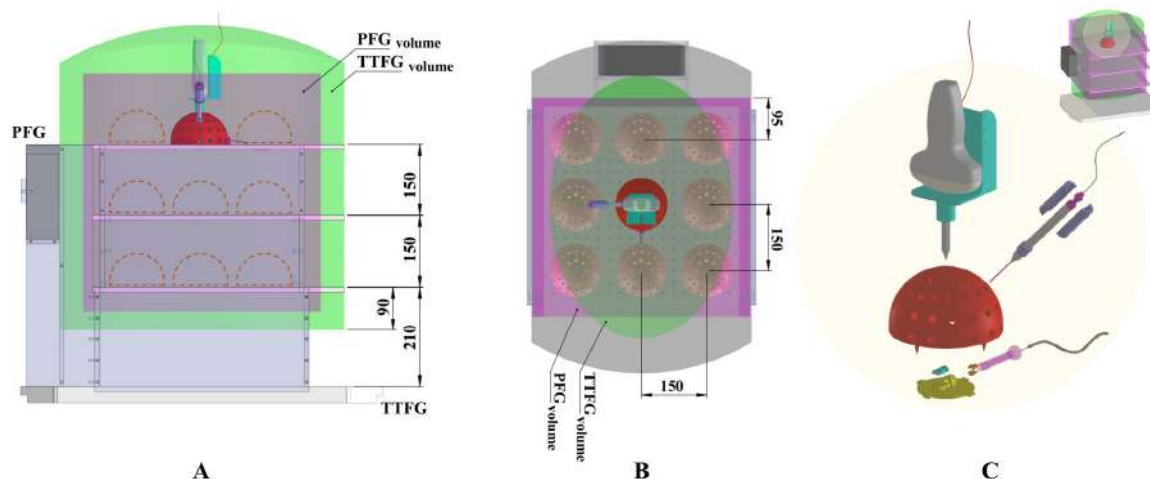
Figure 2.4 – CAD drawing of the assessment platform.
A – Lateral view of the assessment platform. Different levels and scaffold positions (red hemispherical structures with hexagonal holes and dashed lines) are sketched over the limits of the PFG (pink) and $TTFG$ (green) EMT volumes. Both EMT volumes are centered with each other. B – Top view. C - The scaffold and supports used to rigidly attach the EMT sensors and the surgical instruments under assessment. Each support includes several pieces.

This supplementary material shows the assessment platform as a CAD drawing in Figure 2.4. It is possible to visualize the position of the different levels according to each electromagnetic volume under assessment. Moreover, the 27 positions assessed (9 per level) during experiments are represented (Figure 2.4 – A/B). The scaffold and the specific supports used to rigidly attach the EMT sensors and the surgical instruments are also shown (Figure 2.4 – C).

2.6.2. Appendix B – Influence of sensor position in 4D Probe

This supplementary material reports an experiment where the precision of a 6-DOF sensor positioned in 5 different locations with respect to the 4D US probe was assessed. The first three positions were on the probe's surface, while the fourth and fifth positions correspond to the sensor positioned at 45 mm and 90 mm from the US probe using a 3D printed support (Figure 2.5). All coordinates were obtained with the 4D mode turned on.

The results revealed that when the sensors are positioned near the inner motor (positions 2 and 3, and in less extent the 4), the precision decreases. The other two positions get better precision.
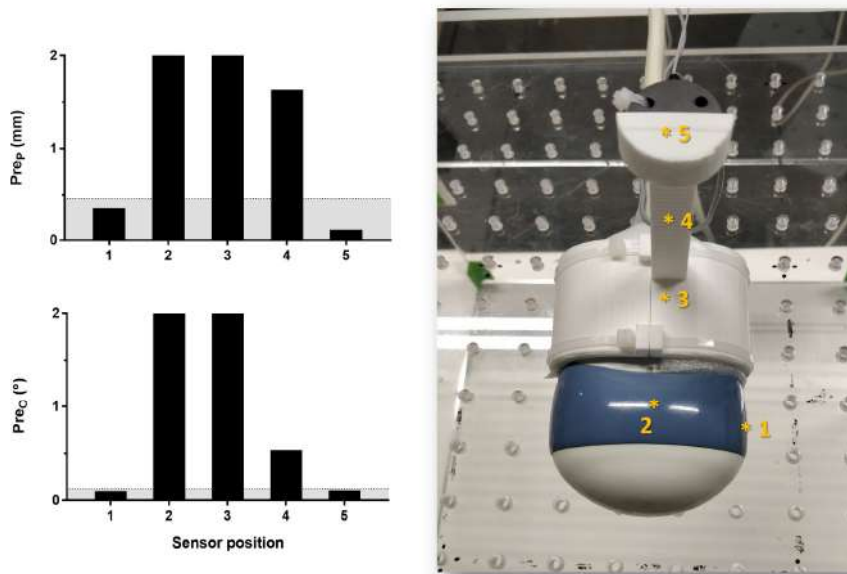
Figure 2.5 – Influence of EMT sensor position in 4D Probe.
Comparison of different positions along the 4D US probe assessing the precision of a 6-DOF sensor using PFG. The values represent the *jitter* errors. Position (Pre_P) and orientation (Pre_O) errors were measured in millimeters (mm) and degrees (°), respectively. The 95th percentile from section 2.2.3 - *EMT systems precision and accuracy in a surgical environment* is represented by the gray area.

Chapter 3

A dual-modal CT/US kidney phantom model for image-guided percutaneous renal access

Abstract

Percutaneous renal access (PRA) is a crucial step in some minimally invasive kidney interventions. During this step, the surgeon inserts a needle through the skin until the kidney target site using fluoroscopy and ultrasound (US) imaging. Recently, new concepts of image-guided and surgical navigation have been introduced in these interventions. However, their validation remains a challenging task. Phantom models have been presented to solve such challenge, using realistic anatomies in a controlled environment. In this work, we evaluate the accuracy of a porcine kidney phantom for validation of novel dual-modal computed tomography (CT)/US image-guided strategies for PRA.

A porcine kidney was combined with a tissue mimicking material (TMM) and implanted fiducial markers (FMs). While the TMM mimics the surrounding tissues, the FMs are used to accurately assess the registration errors between the US and CT images, providing a valid ground-truth.

US and CT image acquisitions of the phantom model were performed, and the FMs were manually selected on both images. A rigid alignment was performed between the selected FMs, presenting a root-mean-square error of 1.1 mm. Moreover, the kidney was manually segmented, presenting volumes of 203 ml and 238 ml for CT and US, respectively.

The initial results are promising on achieving a realistic kidney phantom model to develop new strategies for PRA, but further work to improve the manufacturing process and to introduce motion and anatomical artifacts in the phantom is still required.

3.1. Introduction

Percutaneous renal access (PRA) plays a key role in minimally invasive kidney interventions (MIKI), such as percutaneous nephrolithotomy, radiofrequency ablation of renal tumors, and kidney biopsies [14]. During the preoperative and intraoperative phases of MIKI that use PRA, they include two important steps: the surgical planning, which relies on the evaluation of richly-detailed preoperative data, namely computed tomography (CT) and during which the surgeon sets out the strategy of the intervention (*e.g.*, the preferred path to target the surgical site); and, the PRA, where the surgeon inserts a surgical needle from the skin until the kidney target site, guiding the needle position using intraoperative imaging. Fluoroscopy and two-dimensional (2D) ultrasound (US) are the most common imaging modalities for PRA, due to the real-time depiction of the renal system [23]. However, since fluoroscopy exposes both patients

and surgeons to a significant amount of radiation, pure US image guidance appears as a potential and attractive solution.

The surgeon's ability to visualize and reach the anatomical target during PRA restricts the MIKI success. The ideal PRA is one that allows an accurate access to the kidney target site minimizing the bleeding. Therefore, PRA remains a challenging task [33]. Inaccurate and multiple punctures often cause complications [38], where injuries to the kidney or contiguous organs can eventually prejudice the surgical outcome.

Many paths and technological advances have been proposed to improve the PRA, and, lately, the concepts of surgical navigation have been introduced for PRA [45]. Surgical navigation systems intend to aid physicians performing medical procedures with higher accuracy and minimizing the risks. These systems are built based on different concepts as imaging, tracking, segmentation, registration, visualization, and software [127]. Thus, as part of incorporation of surgical navigation concepts in PRA, motion tracking of surgical instruments has been studied. Combined with imaging modalities, optical or electromagnetic tracking proved its added-value for PRA [71], [79], [80], [98]. Regarding merely the medical imaging, several authors have explored multimodal imaging for PRA [89], [128], where they fused anatomical information of preoperative images - such as CT and Magnetic Resonance Imaging - with intraoperative images.

The development and incorporation in the clinical practice of new surgical navigation systems in PRA are limited by appropriate assessment. Currently, phantoms are accepted as gold-standard because they mimic the properties of the tissue in a controlled environment. Moreover, this type of validation is crucial before animal experiments and clinical trials, allowing software development and tuning.

Studies have been made to build kidney phantom models for the validation of image-guided frameworks. Xiang *et al.* developed a kidney phantom model based on a kidney porcine and an agar solution [129]. Hunt *et al.* described the manufacturing of low-cost renal phantoms models based on patient-specific kidney model from CT data and gelatin gel material [130]. Likewise, Ristolainen *et al.* developed a kidney phantom using concepts of three-dimensional (3D) printing and molding to create a kidney model with calyxes. Both gelatin and silicone are applied [131]. Following a similar methodology, Adams *et al.* presented a soft 3D-printed phantom of the kidney with collecting system [132]. They start by scanning human cadaveric kidneys and constructing phantoms using 3D wax printing and polymer molding.

Despite the current revolution of 3D-printed phantom models, there are limitations yet; mainly mimicking the whole characteristics of the different kidney tissues. Thus, the images should be closer to

the real ones. Phantom models of *ex-vivo* porcine organs have shown successful results in CT and US [129], [133], [134], where realistic images are acquired.

Therefore, this work aims to present a methodology to create a kidney phantom model that can be CT and US imaged. The accuracy of this phantom model will be preliminarily evaluated and compared with the expected restrictions of the PRA interventions.

3.2. Materials and Methods

In this section, we describe the protocol used to manufacture the kidney phantom model. This phantom is composed of three main components: a porcine kidney, a tissue mimicking material (TMM), and implanted fiducial markers (FMs).

3.2.1. Porcine kidney

The porcine kidney was obtained from a local slaughterhouse. The renal hilum, ureter, artery, and vein were undamaged. External cleaning was made, where fat tissue and renal capsule were removed. A saline solution was flushed via artery to remove blood. Then, a solution of a contrast agent (Telebrix® 35, France) was injected to enhance the kidney on CT images. In detail, 40 ml solution of contrast agent diluted in saline solution (1:20) was injected into the renal artery. Afterward, the renal artery and vein were closed with suture thread.

3.2.2. Tissue mimicking material

An agar-based tissue mimicking material (TMM), similar to the one presented by Terlinck *et al.* [135], was used to enclose the porcine kidney and allow acquisition through US. The composition (percentage by weight, *wt%*) was: 3% agar-agar; 11% glycerol; 83.25% distilled water; 2.5% flour; and 0.25% bleach. This agar percentage made the TMM robust to break or tear, the glycerol was required to adjust the speed of sound to 1540 m/s, and the flour was applied to enhance acoustic scattering [136]. Finally, bleach prevented the microorganisms growth [129].

Specifically, agar, glycerol and distilled water were mixed in a recipient and heated to 95°C for 1 hour. The reagents were stirred during the heating process. When the solution was uniform, the flour was
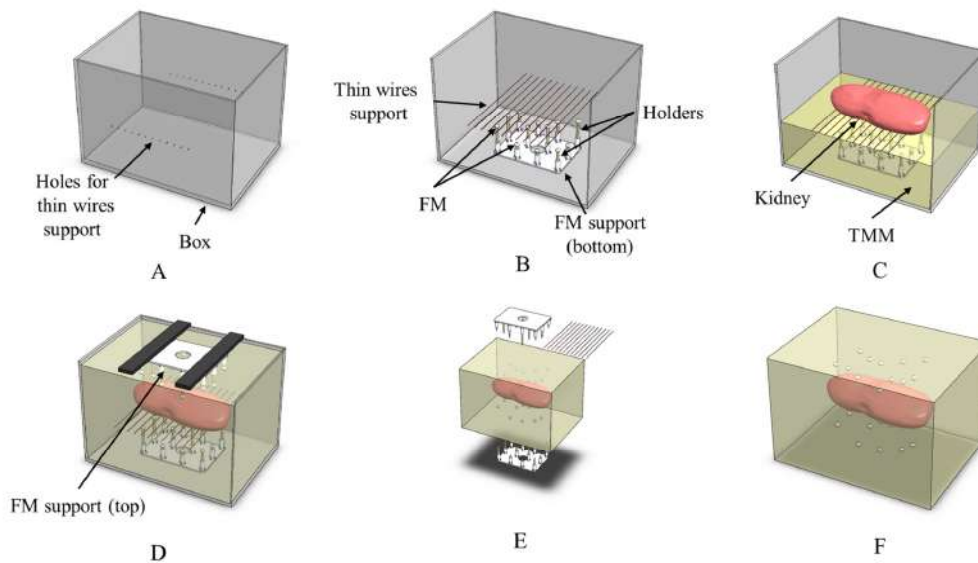
Figure 3.1 – Steps for the phantom construction.
A) Box with small holes for thin wires support. B) Fiducial markers (FMs) support is positioned at the bottom and the thin wires in the box holes. C) First pouring of the tissue mimicking material (TMM). D) After positioning the kidney, TMM pouring should continue until reaching the box top. E) During the TMM hardening, the thin wires are removed (after 1 hour) and then, the FMs supports are also carefully detached (after 8-10 hours), F) the FMs are located at specific positions.

added and mixed to prevent large clumps. The TMM was heated another 15 minutes, and then, it could cool at room temperature to 50 °C with continuous stirring. At the end, the bleach was added.

3.2.3. Fiducial markers

Each fiducial marker was a polystyrene sphere with 6 mm of diameter and with a hole to attach a holder. To locate the FMs into specific positions, two supports were designed. The supports intended to: 1) be positioned at the bottom and at the top of a box; 2) give enough space to position the kidney on the box; 3) be easily removed while FMs maintain the expected positions; 4) position the FMs around the kidney; 5) organize the FMs nonlinearly; and 6) spread the FMs' distribution [137].

According to these restrictions, bottom and top supports integrated twelve holders each, which were equally spaced (3 cm) in x and y. A different distribution in z was used. Thus, we spread four FMs in three different heights (3, 4 and 5 cm) varying their distribution along the support (Figure 3.1). To improve identification of the kidney orientation in US and CT images, the FMs were organized differently at the bottom and top supports.

3.2.4. Phantom construction

A box (Figure 3.1-A) with the following dimensions $16\times24\times15$ cm was prepared. To enclose the kidney into the TMM and to keep it centered on the box, we used a thin wires support (Figure 3.1–B). The thin wires support was positioned at 6.5 cm of the box bottom and the support held the kidney during pouring of the TMM.

The TMM was poured into the box until the thin wires support. Then, the kidney was placed on this support (Figure 3.1-C) and the pouring process continued until filling the box (Figure 3.1-D). After cooling for 1 hour, the wires were removed. TMM could harden for 8 – 10 hours at room temperature. When the hardening was complete, FMs supports were removed (Figure 3.1-E), without modifying their spatial location (Figure 3.1-F). Finally, empty spaces were filled with heated TMM.

3.3. Experiments

In this section, we describe how the dual-modal kidney phantom was evaluated.

3.3.1. CT and US images acquisition

The CT images were acquired using the Brilliance 64 Scanner (Philips Healthcare, Netherlands). The X-ray tube current was 313 mA and peak voltage was 120 kV, using the abdomen protocol. The image size was 512x512x302 with a pixel spacing of 0.701 mm, a slice thickness of 2 mm, and a space between slices of 1 mm.

The US images were acquired using the Voluson P6 US system (GE Healthcare, USA). The real-time four-dimensional (4D) convex abdominal transducer (RAB2-6-RS, 2-5 MHz) was used. According to the machine settings, 3D images were acquired using high quality, maximum field-of-view and a depth of 15.9 cm. An isotropic volume resolution of 0.667 mm and an image size of 235x172x197 was used.

3.3.2. Fiducial registration error and volume differences

To estimate the fiducial registration error between CT and US volumes, the *image-guided therapy toolbox,* implemented in 3D Slicer (version 4.6), was used. To manipulate the US volume, the DICOMatic software (Tomovision, Canada) was used to convert the files from the US machine. Initially, each marker was detected on both images. Note that the FMs is represented as brighter and darker structures in US
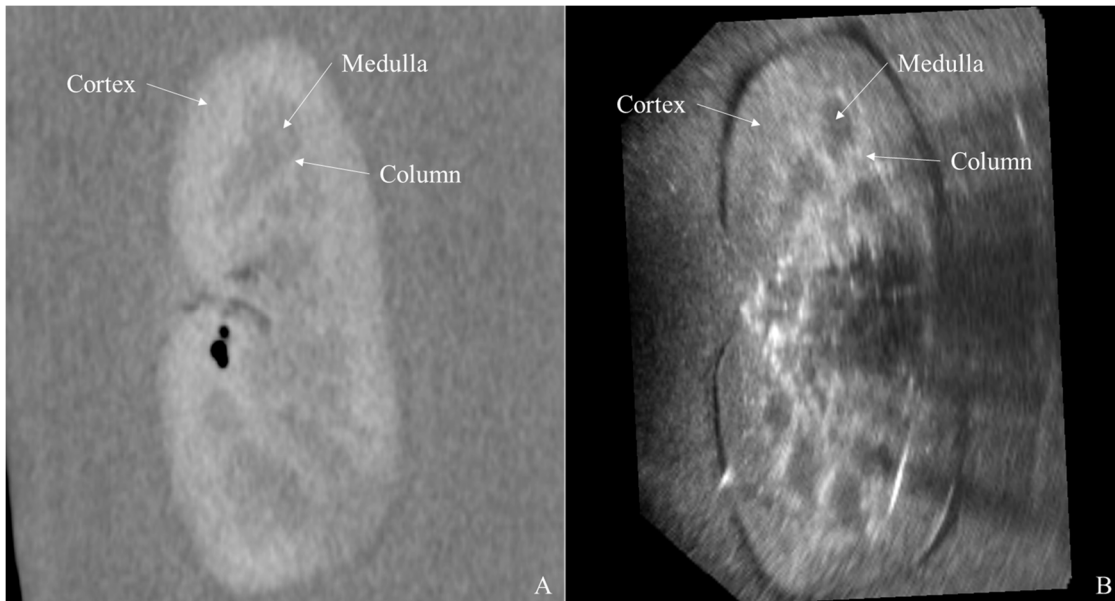
Figure 3.2 – Examples of phantom images.
A) CT and B) US images from the same phantom. Kidney boundaries and anatomical details are visible as renal cortex, renal medulla, and renal column.

and CT images, respectively. The manually detected markers were then aligned based on [138]. The root-mean-square (RMS) was used to assess the alignment error.

To estimate volume differences, one observer performed the manual segmentation of the kidney on both images. The segmentation was performed slice-by-slice along the axis plane. The volume and surface area of each model were compared.

3.4. Results

3.4.1. CT and US images acquisition

It was manufactured one phantom using the described protocol. Figure 3.2 shows the resulting CT and US images from the same phantom. The kidney boundaries and its inner body are visible in both cases. Anatomical details as renal medulla, cortex, and column are detected. Moreover, the results in Figure 3.3 prove that the contrast agent is essential to visualize the kidney on the CT images (Figure 3.3-A/B), while the flour contributes to enhancing the acoustic scattering on US (Figure 3.3-C/D/E).

Additionally, Figure 3.3 shows the FMs on the CT and US images. As expected, it is possible to observe that polystyrene material has a different contrast on CT and US. Besides, it is possible to observe an equal distribution of the FMs on both image modalities (Figure 3.3-F/G).
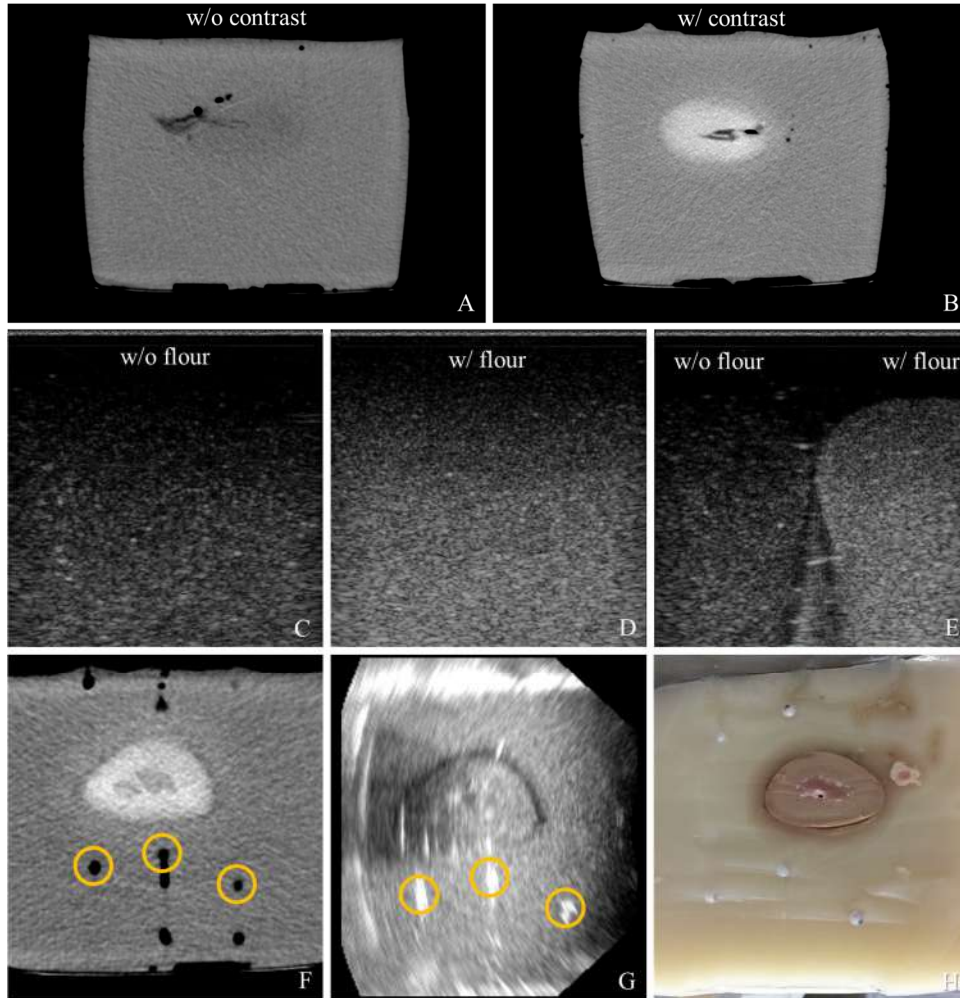
Figure 3.3 – Influence of contrast agent to enhance kidney in CT images, and flour to improve acoustic scattering in US images. Visualization of FMs on both images.
CT images of phantoms A) without and B) with contrast agent. US images of the TMM C) without and D) with flour. E) Both TMMs side-by-side. The same FMs visualized in F) CT and G) US images. The same FMs are marked with a yellow circle. H) Section of the phantom with implanted FMs.

3.4.2. Fiducial registration error and volume differences

Seventeen of the twenty-four correspondent FMs were manually selected on both CT and US volumes. One point on the surface of each fiducial marker was selected manually. The FRE was 1.1 mm. Visual inspection of the registration revealed a coherent overlap between structures and FMs (Figure 3.4).

Regarding segmentation, CT and US manual contours presented small differences (Figure 3.4). The CT images presented a surface area of 213 cm^2 and volume of 203 ml, while the US images obtained a surface area of 229 cm^2 and volume of 238 ml.

Extended results of the proposed protocol are presented in appendix A (section 3.7.1), which were used to accomplished the study presented in chapter 4.
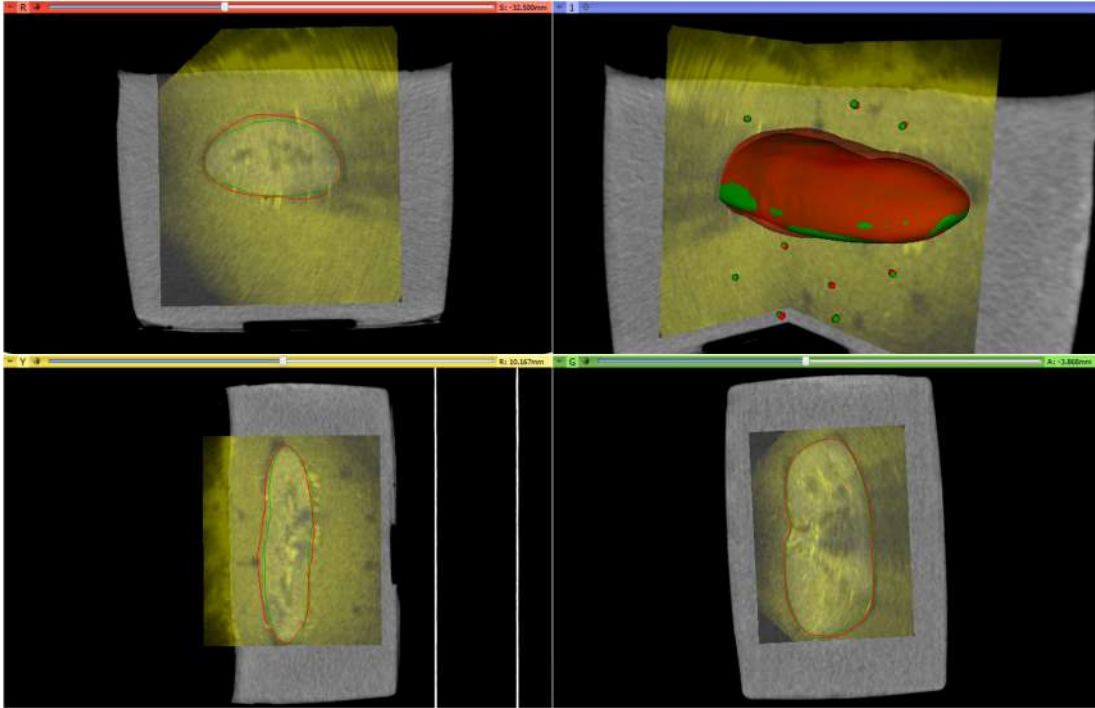
Figure 3.4 – Images and segmented surfaces aligned based on the selected FMs from both CT and US.
CT images, surfaces, and FMs are represented by gray level images, green surfaces and points, respectively, while US by yellow level images, red surfaces and points.

3.5. Discussion

We presented a protocol to construct a kidney phantom model made of the porcine kidney, the TMM and implanted FMs. The initial results are promising since the kidney is completely visible on both CT and US images. Despite *ex-vivo* tissues have a quicker degradation than artificial materials, their use shows promising results mainly due to the realistic images obtained. Relevant anatomical boundaries and some anatomical details are detected. Nonetheless, the renal cortex is usually more hypoechoic in human US images [139]. Overall, the TMM meets the requirements, which is essential, mainly, to obtain US images. Moreover, FMs are visible and can be easily targeted, which is extremely important for the registration validation stage. These results strongly suggest that this phantom model can be used to image-guided PRA since a valid ground-truth was achieved using realistic images. Thus, these models may lead to stronger surgical navigation methods before going forward to *in-vivo* validation. In addition, this phantom model has potential to be used for medical teaching and training. Specifically, it is possible to previously evaluate the kidney on CT images, and then, perform the PRA using intraoperative imaging.

Although the appearance of the CT images was slightly different, the contrast agent enhanced the kidney tissues with respect to the background, which is a common characteristic in the non-contrast

images. Indeed, without contrast agent, TMM and the kidney presented the same Hounsfield values, hampering their differentiation.

We believe that the manufacturing still presents some drawbacks, namely the presence of small air bubbles within the TMM and near the FMs. Indeed, this may disrupt the perception of the FMs on US images, with its correction potentially improving the sphere visualization and reducing the current fiducial registration error of 1.1 mm. However, the high number and non-linear (but known) distribution of the FMs tends to minimize the errors caused by the air bubbles and any intrinsic image alignment errors [137]. Moreover, it must be considered that the image resolution and even some image artifacts inherently influence the method's accuracy.

Surface and volume differences were observed between both US- and CT-based results. These are in part explained by the expected inter-modality variability throughout the segmentation stage. This fact must be addressed in a future study.

This work was strongly influenced by the work developed by Xiang *et al.*, where the authors used a porcine phantom model to study the registration of 3D US to CT angiography of the kidney [129]. We presented some modifications to their protocol, namely a different mixture of TMM, number and position of FMs, and construction method. These modifications bring relevant advantages for image-guided PRA since: 1) flour enhances speckle pattern around the kidney on the US images; 2) higher number and distributed FMs allow image acquisition with different transducer's positions and orientations without losing performance; 3) pouring the TMM solution at once reduces the number of undesirable interfaces on the US images. Nevertheless, we would like to emphasize that some factors on both protocols can change the kidney tissue properties, like the TMM temperature throughout the pouring and cooling stages that may change the natural tissue contrast and echogenicity in both CT and US images. These factors may be addressed in a future work.

Finally, as future work, we intend to introduce motion and common anatomical artifacts, as recently presented by Lee *et al.* [140] for high-intensity focused US.

3.6. Conclusion

We manufactured a kidney phantom model to test image-guided and surgical navigation concepts in PRA for dual modal CT and US imaging. Herewith, we obtained similar preoperative and intraoperative data of common MIKI and a valid ground-truth with enough accuracy to assess errors, which can be used to develop new methods and techniques.

Surgical navigation in the abdominal region is still a challenging task, due to the deformable nature and motion of the tissues. Despite this phantom does not consider these parameters, this work is a step forward on building a validation tool for these systems in PRA.

3.7. Appendixes

3.7.1. Appendix A - Extended results

Based on the proposed protocol, the following results were used in chapter 4. Registration and segmentation errors were computed. Considering landmark-pair registration, twelve FMs were selected to align both US and CT images, while the remaining ones were used to assess the registration performance. After rigid alignment, both fiducial registration error (FRE) and target registration error (TRE) were assessed, respectively (Figure 3.5). To depict an average ground-truth alignment, ten subsets with twelve FMs each were randomly selected per phantom. The subset with the median value of FRE was used as the ground-truth alignment.

Moreover, two 3D surfaces were created for each phantom, one using the CT images, and another based on the US images. Here, the segmentation differences between CT and US kidney surfaces were evaluated by computing the average distance (AVD), the 95th Hausdorff distance (HD), and the Dice
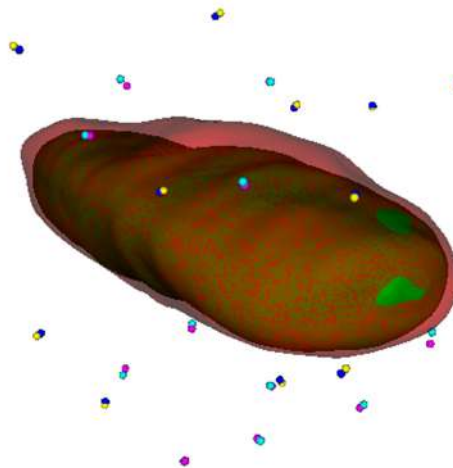
Figure 3.5 – Virtual representation of segmented surfaces and fiducial markers (FMs).
Fiducial registration error (FRE) and target registration error (TRE) were assessed using different FMs. Blue and yellow dots indicate FMs used to define the ground-truth alignment between CT and US data and use to compute the FRE. Magenta and cyan dots were used to assess the TRE in landmark-pair registration and point set registration algorithms.

similarity coefficient (DSC). Table 3.1 shows a complete description of the error metrics for the ten phantoms. Note that no outliers were observed.

Table 3.1 – Results of error metrics for ten kidney phantoms.
Fiducial registration error (FRE) and target registration error (TRE) for landmark-pair registration between both images, along with the 3D manual segmentation differences between CT and US surfaces. Dice similarity coefficient (DSC), Average Distance (AVD) and 95th Hausdorff Distance (HD) were used to assess the segmentation errors.

Phantom	Registration		Segmentation		
	FRE (mm)	TRE (mm)	DSC (%)	AVD (mm)	HD (mm)
A	1.10	1.45	91.47	1.81	4.03
B	1.23	1.51	88.34	2.30	5.52
C	1.21	1.40	88.19	2.04	5.15
D	1.51	1.74	92.52	1.75	3.36
E	1.43	1.54	90.86	1.82	5.17
F	1.10	1.25	91.16	1.48	3.08
G	1.17	1.43	92.87	1.76	2.75
H	1.07	1.55	90.69	1.99	4.84
I	1.43	1.91	94.37	1.19	2.82
J	1.32	1.46	86.82	1.96	4.84
Mean ± SD	1.26 ± 0.16	1.52 ± 0.18	90.73 ± 2.34	1.81 ± 0.31	4.16 ± 1.07

Chapter 4

Surface-based registration between CT and US for image-guided percutaneous renal access – a feasibility study

Abstract

As a crucial step in accessing the kidney in several minimally invasive interventions, percutaneous renal access (PRA) practicality and safety may be improved through the fusion of computed tomography (CT) and ultrasound (US) data. This work aims to assess the potential of a surface-based registration technique and establish an optimal US acquisition protocol to fuse 2D US and CT data for image-guided PRA.

Ten porcine kidney phantoms with fiducial markers were imaged using CT and 3D US. Both images were manually segmented and aligned. In a virtual environment, 2D contours were extracted by slicing the 3D US kidney surfaces and using usual PRA US-guided views, while the 3D CT kidney surfaces were transformed to simulate positional variability. Surface-based registration was performed using two methods of the iterative closest point algorithm (*point-to-point*, ICP-PT; and *point-to-plane*, ICP-PL), while four acquisition variants were studied: i) use of single-plane (transverse, SP_T; or longitudinal, SP_L) *vs.* bi-plane views (BP); ii) use of different kidney's coverage angles acquired by a probe's sweep; iii) influence of sweep movements; and iv) influence of the spacing between consecutive slices acquired for a specific coverage angle.

BP view showed the best performance (TRE = 2.26 mm) when ICP-PL method, a wide kidney coverage angle (20°, with slices spaced by 5°), and a large sweep along the central longitudinal view were used, showing a statistically similar performance (p = .097) to a full 3D US surface registration (TRE = 2.28 mm).

An optimal 2D US acquisition protocol was evaluated. Surface-based registration, using multiple slices and specific sweep movements and views, is here suggested as a valid strategy for intraoperative image fusion using CT and US data, having the potential to be applied to other image modalities and/or interventions.

4.1. Introduction

Percutaneous renal access (PRA) is a surgical step where the surgeon inserts a surgical needle from the skin until the kidney target site. It is used in several minimally invasive kidney interventions (MIKI), such as percutaneous nephrolithotomy, kidney radiofrequency ablation of renal tumors, and kidney biopsies [23], [38], and it remains a challenging task for surgeons [33]. To overcome this, many technological advances have been proposed [45]. Recently, PRA was performed with excellent results

using ureteroscopy and an electromagnetic tracking system [79], [80]. However, the authors mentioned the lack of visualization of anatomical structures in real-time during puncturing as an important limitation. In this context, over the past few years, concepts of surgical navigation have been studied for PRA to improve the surgeons' perception of the target site. In this sense, anatomical information from preoperative images - such as computed tomography (CT) or magnetic resonance imaging (MRI) – are fused with real-time intraoperative ultrasound (US) images, allowing to enhance the latter with preoperative planning information [85], [89], [90], [98], [128], [141]–[143].

One of the fundamental steps of surgical navigation is the registration between the preoperative and intraoperative image data, bringing them to the same coordinate system. Several registration methods have been presented in the literature, including landmark-based, intensity-based and segmentation-based ones [144]–[146]. Despite the primacy of intensity-based registration methods in recent years [145], segmentation-based followed by surface alignment has been shown to be more successful than landmark-based and intensity-based when the images present low quality or missing data [146]. Moreover, surface-based alignment methods are computationally attractive solutions, because they become independent of the image after segmentation and, usually, reduce the number of data under processing [147]. For further information, the reader is kindly directed to the extensive surveys on medical image registration found in Viergever *et al.*[144], [145], Alam *et al.* [146] and Ferrante *et al.* [147].

Previous works have tried to fuse two-dimensional (2D) US with preoperative data for MIKI based on surface-based registration. Ahmad *et al.* proposed to individually segment arbitrarily placed and oriented US slices using an optical tracker coupled to a laparoscopic US probe [148]. Based on the spatial location of the US probe, the three-dimensional (3D) surface of a kidney tumor phantom is reconstructed using two different segmentation approaches. Differences were measured after registration of the reconstructed surfaces with the ideal reference, corroborating the added-value of this strategy. Mozer *et al.* used multiple and sparse transverse and longitudinal contours to align US and CT data [85]. Li *et al.* used two pairs of orthogonal US slices to register with a MRI model [89]. In addition, the authors presented a respiratory gating technique to compensate for organ motion. The same authors presented a different approach based on statistical shape model (SSM), which was used to reconstruct kidney surfaces using sparse points from US images [90]. Finally, Seo *et al.* used two orthogonal 2D US probes to create a bi-plane US imaging of the kidney and, then, estimate the pose of a preoperative 3D model [149]. The proposed method showed high accuracy and robustness, being tested in different applications [150]–[152]. Overall, the previous works demonstrated that surface-based registration achieves good results. However, most of them acquired 2D US images from arbitrary and sparse longitudinal and transverse

views, using different strategies to maintain continuous and feasible registration, as respiratory gating, a simultaneous acquisition using two US probes, and robot motion compensation, which are not always accurate and practical to perform within the operating room.

Due to the improvements in real-time image processing, namely in segmentation [153], in tracking [154], and in general computational capabilities [155], [156], the continuous registration and monitoring of medical images are now possible. Notwithstanding, imaging should also be continuous to perform continuous organ monitoring. Since the direct access to online US raw data is restricted by most manufacturers, the usual approach is to grab the real-time data displayed on the screen, being therefore restricted to a 2D image view. Taking this into account, this work aims to assess the accuracy of surface-based registration between CT and 2D US images and establish the optimal US acquisition protocol to improve image-guided PRA. Thus, this work intends to assess four practical variants of the US acquisition: (1) the type of *US image view* used (single-plane *vs.* bi-plane); (2) the acquired *kidney's coverage angle* (by sweeping the probe); (3) the orientation of the *probe's sweep movement*; and (4) the *spacing between consecutive US slices* for a given coverage range.

This paper is structured as follows. In section 4.2, we present our experimental setup, which is based on phantoms manufactured for CT and US imaging. Additionally, we present our experimental design, which explains how the manually segmented 3D phantom models from CT and US are used to virtually simulate 2D US acquisitions in a controlled environment, as well as describes the different registration methods used in the assessment. In section 4.3, we present the results, which are discussed in section 4.4. In section 4.5, we present the main conclusions of our study.

4.2. Materials and methods

4.2.1. Experimental setup

Phantom preparation

Phantoms were constructed using the protocol presented in Gomes-Fonseca *et al.* [157] (Chapter 3). In short, the phantom was manufactured based on a porcine kidney combined with tissue mimicking material (TMM) and implanted fiducial markers (FMs), see Figure 4.1-A. While the TMM mimics the surrounding tissues of the kidney, the FMs were used to accurately align and assess the registration
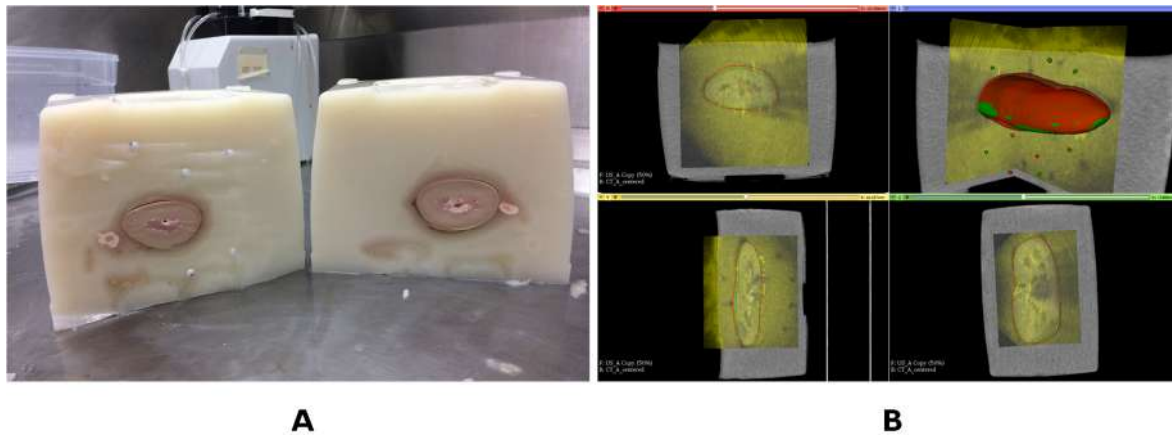
Figure 4.1 – A porcine kidney phantom model with 24 implanted fiducial markers (FMs).
(A) The image represents the phantom cut in half. (B) Ground-truth alignment. Images and segmented surfaces from both CT and US volumes of a kidney phantom model. Images are aligned based on landmark-pair registration using 12 FMs, and registration is assessed using the remaining FMs. CT images, surfaces and associated FMs are represented by gray level images, green surfaces and points, respectively, while yellow and red are used to represent US images, surfaces and points.

performance between US and CT images (Figure 4.1-B). Overall, ten phantoms were built with 24 FMs each. The FMs are made of polystyrene with a spherical shape and 6 mm of diameter. [1]

Image acquisition

The CT images were acquired using a Philips Brilliance 64 CT scanner (Philips Healthcare, Best, The Netherlands). The X-ray tube current and peak voltage were set to 313 mA and 120 kV, respectively. The abdomen protocol was selected. On average, the CT volume size was 512x512x300 with a voxel resolution of $0.701 \times 0.701 \times 1$ mm.

The US images were acquired using a Voluson P6 US system (GE Healthcare, Milwaukee, Wisconsin, USA). The 4D convex abdominal transducer (RAB2-6-RS, 2-5 MHz) was used. According to machine settings, 3D images were acquired using the high-quality mode (setting: high2), the maximum field-of-view (setting: B90°/V85°) and a depth of 15.9 cm. The voxel resolution was $0.667 \times 0.667 \times 0.667$ mm with a volume size of $235 \times 172 \times 197$.

4.2.2. Experimental design

Data preparation

Two segmented 3D surfaces were initially created for each phantom, one using the CT images and another based on the US images (Figure 4.2). In detail, the CT volume was delineated using the 3D

---

[1] More information available at: http://2ai.ipca.pt/kidneyphantom/

59
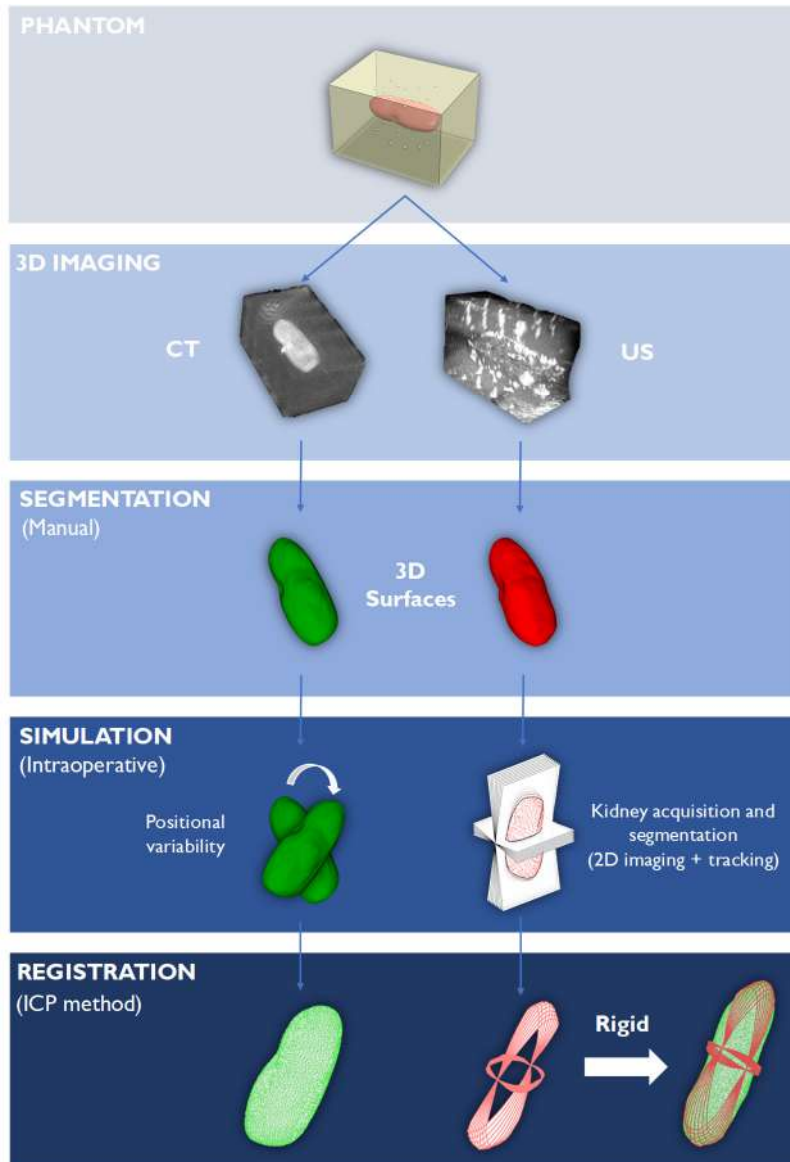
Figure 4.2 – Overview of the experimental design to simulate an image-guided PRA and evaluate the surface-based registration as a valid technique to fuse computed tomography (CT) and ultrasound (US) data during the procedure.

Slicer software (version 4.6) [158]. The files from the 3D US system were initially converted to Meta Image files using BabyOSlice software (Tomovision, Canada), and were then uploaded to the 3D Slicer software and manually delineated. In both cases, the manual delineation relied on multiple 2D contours followed by 3D interpolation to obtain the final 3D surface.

In addition, the implanted FMs were manually detected (using the image-guided therapy toolbox available on 3D Slicer) on both CT and US volumes of each phantom (Figure 4.1-B). Note that FMs are visible as brighter and darker structures in the US and CT images, respectively. Twelve FMs were selected to align both US and CT images, while the remaining ones were used to assess the registration

performance [159].[2] The selected FMs were rigidly aligned based on the strategy presented by Horn *et al.* [138].

Data simulation

To virtually simulate the normal variability found throughout an intervention, both in terms of US field-of-view and anatomical kidney positioning, the experimental data was simulated in two independent stages: 1) simulation of the variability associated with the probe position/orientation with respect to the patient's body in the operative room; and 2) simulation of the anatomical positional variability of the preoperative data. Both are explained in detail below.

Simulation of intraoperative kidney acquisition and segmentation of 2D US images

According to Chu *et al.* [160], during US-guided PRA, the US probe is typically positioned to capture longitudinal and/or transverse sections of the kidney (Figure 4.3-A and Figure 4.3-B). Thus, in these experiments, the kidney's central *longitudinal* and *transverse* sections were defined, per convention, to be aligned with the *xz* and *xy planes*, respectively (Figure 4.3-D). The US probe was virtually positioned 6 cm away from the center of the kidney US surface, mimicking the typical distance between kidney and skin [160], and the center of rotation defined at the probe's tip (Figure 4.3-C).
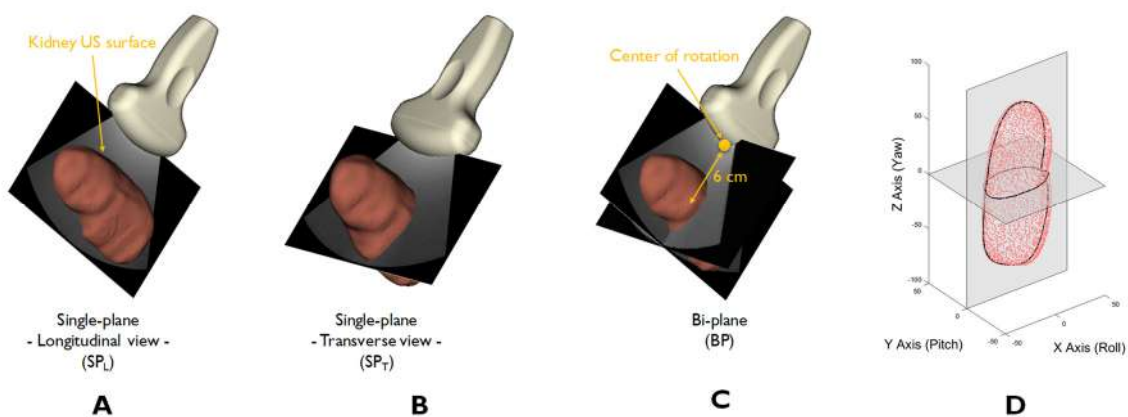
Figure 4.3 – Simulation of intraoperative kidney acquisition and segmentation.
Representation of single-plane acquisition for (A) *longitudinal* (SP_L) and (B) *transverse* (SP_T) *views*, and (C) bi-plane (BP) for *both* views in a virtual simulated and controlled environment. Surface-based registration for image-guided percutaneous renal access is assessed based on these probe's views. A single-oriented acquisition fixed on the center of rotation is performed, mimicking a continuous imaging of the kidney. (D) Representation of the standard coordinate system. Black lines correspond to the contours extracted by slicing the US kidney surface using planes with different orientations.

---

[2] The full dataset is available at: http://dx.doi.org/10.17632/vgmt7brcmw.1

61

Multiple 2D US slices and their respective 2D contours were generated by reformatting the original volume and surface. In this sense, multiple rotations (*i.e.*, *roll*, *pitch*, and *yaw*) of the central *longitudinal* and *transverse* planes were applied, and these planes sliced the US surface with different orientations. The surface points that are intersected by these planes set the extracted contours (Figure 4.3-D). Henceforth, the rotations linked to US imaging will be designated as $roll_{US}$, $pitch_{US}$, and yaw_{US}, each representing a different simulated *probe's sweep movement* and respective 2D contours with respect to the kidney. In this sense, probe's tracking was virtually simulated.

Simulation of preoperative CT kidney surfaces' positional variability

The anatomical positional variability expected before surface-based registration was simulated by applying transformations to the CT surface. The idea is to mimic the different orientations that the kidney can have before the fusion, which affect the initial alignment between modalities. These differences are usually related to the patient's body positioning during preoperative and intraoperative acquisitions. As performed above, changes in *roll*, *pitch*, and *yaw* orientations were applied with respect to the CT kidney surfaces' center. Notwithstanding, in this case, composite transformations were applied following the Euler convection (*yaw-pitch-roll*). Thus, four hundred composite transformations (randomly selected) were performed, ranging from -90° to 90° per orientation, creating 400 surfaces with different orientations per phantom. Henceforth, changes in orientation of the CT surfaces are termed as $roll_{CT}$, $pitch_{CT}$, and yaw_{CT}, according to the individual transformations that describe each composite transformation.

Registration algorithms

The tests were performed assuming rigid transformation models between surfaces. The iterative closest point (ICP) algorithm was used to estimate point correspondences between point clouds and compute the optimal transformation between them [161]–[163]. Usually, ICP is a fast technique, which is very important for image-guided interventions. In this work, two state-of-the-art variants of *error metric* were used:

1) the *point-to-point* error metric that sums the squared distances of source points to target points:

$$\boldsymbol{R}, \boldsymbol{t} \leftarrow \underset{\boldsymbol{R}, \boldsymbol{t}}{\arg\min} \sum_{i=1}^{N} \|(\boldsymbol{R}\boldsymbol{p}_i + \boldsymbol{t}) - \boldsymbol{q}_i\|^2 \tag{4.1}$$

where $\boldsymbol{p}_i$ is a source point and $\boldsymbol{q}_i$ a corresponding point in the target point cloud, while $\boldsymbol{R}$ is the rotation matrix and $\boldsymbol{t}$ is the translation vector that minimizes the distance between source and target. A

closed form solution for the minimization of the *point-to-point* error metric is the Singular Value Decomposition (SVD) algorithm [164]–[166]. Henceforward, this variant is termed ICP-PT.

2) and, the *point-to-plane* error metric that sums the distances of source points to the surface normal in which the matched target points reside:

$$R, t \leftarrow \underset{R,t}{\arg\min} \sum_{i=1}^{N} \left\| ((Rp_i + t) - q_i) \cdot \vec{n}_i \right\| \tag{4.2}$$

where $\vec{n}_i$ denotes the estimated surface normal at q_i. The only closed form solution for the minimization of the *point-to-plane* error metric is after linearization of the rotation matrix [164]–[166]. Henceforward, this variant is termed ICP-PL.

Finally, throughout these experiments, the CT surface was defined as the target point cloud, with the US surface being the source point cloud. For both variants, the iterative optimization was stopped after a fixed number of iterations (50 in the current experiments) or if the error difference between consecutive iterations was lower than a predefined threshold (10^{-3} mm).

Experiments

The experiments were designed to assess the four abovementioned variants:

The different *types of US image view* tested the registration performance of *longitudinal* and *transverse* slices (single-plane view), as well as the case in which *both* slices are used together (bi-plane view). These options test the use of both 2D and four-dimensional (4D) US probes, simulating the grabbing of real-time data displayed on the screen (as the direct access to online US raw data is restricted). To simplify the reading, single-plane view from longitudinal slices will be designated as SP_L; single-plane view from transverse sections as SP_T; and bi-plane view as BP.

The different *kidney's coverage angles* verified if increasing the coverage angle by acquiring multiple and sparse slices, obtained by sweeping the probe from a fixed position, may influence the registration between US and CT kidney surfaces.

The different *probe's sweep movements* tested if the registration between US and CT kidney surface is influenced by the orientation of the sweep. According to the US probe's center of rotation, $roll_{US}$, $pitch_{US}$, and yaw_{US} simulate different movements that differently slice the kidney.

Lastly, different *spacing between consecutive slices* tested, for a given *kidney's coverage angle*, if a different number of contours influences the performance of surface-based registration.

63

Since these four variants are intrinsically linked, they were assessed together. Each view was moved to simulate three initial positions during sweeping, *i.e.* three slices initially positioned at -10°, 0° and 10°. Then, these slices were sequentially transformed to obtain *kidney's coverage angle* of 0°, 5°, 10°, and 20°. This was performed by acquiring consecutive slices with increments of 2.5°, which resulted in 1, 3, 5 and 9 slices, respectively. In addition, increments of 5° and 10° were also tested. For each slice, the respective contour was obtained. Finally, each set of contours was registered against all *CT surfaces* for each phantom. The abovementioned options were applied to each *US image view*, *i.e.* SP_L, SP_T, and BP, and corresponding *probe's sweep movement*, *i.e.* $roll_{US}$, $pitch_{US}$, and yaw_{US}. It is important to mention that SP_L originates different contours when changing $roll_{US}$ and yaw_{US}, while SP_T the $roll_{US}$ and the $pitch_{US}$. Similarly, BP originates different contours when changing $roll_{US}$, $pitch_{US}$, and yaw_{US}. Furthermore, the experiments tested both variants of the ICP algorithm.

All experiments were implemented using MATLAB® (version R2016b, The Mathworks Inc., Natick, MA). The computer used to assess the registration performance was running Windows 10 (64-bit) with an Intel Core i7-2600K 3.40GHz CPU with 16 GB RAM, an NVIDIA GeForce GTX 590 with 1.5 GB RAM, and a hard disk drive.

4.2.3. Error metrics and statistical analysis

The segmentation differences between CT and US kidney surfaces were evaluated by computing the average distance (AVD), the 95th Hausdorff distance (HD), and the Dice similarity coefficient (DSC).

As abovementioned, FMs were used to establish the ground-truth alignment between CT and US images. In this sense, the fiducial registration error (FRE) describes the residual alignment error after landmark-pair registration, using the root-mean-square (RMS) distance between corresponding FMs. To depict an average ground-truth alignment, ten subsets with twelve FMs each were randomly selected per phantom. The subset with the median value of FRE was used as the ground-truth alignment. During the experiments, all applied transformations assumed the ground-truth alignment as the reference position.

To assess the error obtained in landmark-pair and surface-based registrations, the target registration error (TRE) was computed using the remaining FMs, by computing the RMS distance.

All statistical tests were conducted using MATLAB® (version R2016b, The Mathworks Inc., Natick, MA). The assumption of normality was assessed for all variables and, based on the results, parametric or nonparametric tests were applied accordingly. The effect size and statistical significance were reported. For normal distributions, mean and standard deviation (SD) were reported, while median

and interquartile range (IQR) were used for non-normal distributions. All statistics were considered significant if $p < 0.05$.

4.3. Results

4.3.1. General observations

All ten phantoms were successfully produced and imaged. On average, FRE was 1.26 ($\pm$0.16) mm, indicating a residual alignment error between US and CT images, and TRE was 1.52 ($\pm$0.18) mm, assessing the error of the landmark-pair registration. The manual segmentation presented a DSC, AVD, and HD of 90.73 ($\pm$2.34) %, 1.81 ($\pm$0.31) mm and 4.16 ($\pm$1.07) mm, respectively, showing the average differences between CT and US surfaces. For detailed information, please consult Table 3.1 in appendix A (Chapter 3 – Section 3.7.1).

4.3.2. Type of US image view

SP_L and BP revealed better performance than SP_T during surface-based registration. The average TRE for SP_L, SP_T and BP was 11.39 (26.28) mm, 29.34 (28.33) mm, and 5.31 (16.51) mm using ICP-PT; and 16.74 (61.53) mm, 44.12 (38.24) mm, and 4.08 (46.79) mm using ICP-PL (see Table 4.1, *kidney coverage angle* of 0°). The differences between SP_L, SP_T and BP were statistically significant for both ICP methods ($p < .001$). Pairwise comparisons revealed that all groups were statistically different ($p < .05$).

4.3.3. Kidney's coverage angle

Table 4.1 summarizes the results of using different *kidney's coverage angles*. The results proved that lower errors were obtained in SP_L, SP_T and BP ($p < .001$) when increasing the coverage angle. This fact was observed in all angles and in both ICP methods.

On average, the lowest errors were obtained when a coverage angle of 20° was used to create a sparse 3D model of the kidney. The optimal performance was obtained with the ICP-PL method. It is important to highlight that similar errors were obtained by SP_L and BP. Indeed, median values of TRE were 2.96 (38.93) mm and 3.02 (53.95) mm for BP and SP_L, respectively. In addition, for comparative purposes, Table 4.1 also presents the error of registering the 3D US surface with the CT surface. The TRE was 2.33 (4.75) mm and 2.28 (46.67) mm for ICP-PT and ICP-PL, respectively.

Table 4.1 – Registration results of different *kidney's coverage angles* (0º, 5º, 10º, and 20º) with CT kidney surface using different *types of US image view*, i.e. Longitudinal (SP_L), Transverse (SP_T) and Both (BP). Registration results of full 3D US kidney surface with CT kidney surface are also shown. Two iterative closest point methods are presented (ICP-PT – point-to-point error metric; ICP-PL – point-to-plane error metric). The target registration error (TRE) is used to assess the registration. The median, 25th and 75th percentiles are presented, as well as the non-parametric statistical tests performed and respective statistical significance and effect sizes. *Pairs of slices.

		TRE (mm)						
		ICP-PT			ICP-PL			
		25TH	MEDIAN	75TH	25TH	MEDIAN	75TH	PAIRED-SAMPLES SIGN TEST
SP_L								
	0º	4.58	11.39	30.86	4.74	16.74	66.27	$p < .001$, $r = .13$
	5º	3.93	9.75	26.24	3.21	9.22	62.99	$p < .001$, $r = .04$
	10º	3.09	6.41	20.76	2.63	4.45	61.19	$p < .001$, $r = .10$
	20º	2.46	3.65	13.72	2.31	3.02	56.26	$p < .001$, $r = .13$
SP_T								
	0º	18.35	29.34	46.68	22.33	44.12	60.57	$p < .001$, $r = .40$
	5º	17.89	28.75	46.45	18.33	39.84	57.49	$p < .001$, $r = .28$
	10º	17.08	28.03	46.11	15.59	35.77	55.32	$p < .001$, $r = .17$
	20º	14.27	25.80	44.86	9.55	25.58	52.75	$p < .001$, $r = .04$
BP*								
	0º	3.14	5.31	19.65	2.73	4.08	49.52	$p < .001$, $r = .16$
	5º	2.95	4.43	15.94	2.68	3.63	42.69	$p < .001$, $r = .17$
	10º	2.68	3.97	13.48	2.39	3.48	42.22	$p < .001$, $r = .19$
	20º	2.36	3.43	8.86	2.13	2.96	41.06	$p < .001$, $r = .18$
3D								
	SURFACE	2.05	2.33	6.80	2.04	2.28	48.71	$p < .001$, $r = .10$
KRUSKAL-WALLIS TEST		$p < .001$, $\eta^2 = .2001$			$p < .001$, $\eta^2 = .1746$			
		All groups, $p < .001$, Except: SP_T 0º - 5º, SP_T 5º - 10º			All groups, $p < .001$			

Figure 4.4 presents the median, 25th, and 75th percentiles of the TRE for each angle, *i.e.* $roll_{CT}$, $pitch_{CT}$, and yaw_{CT}, applied to simulate different orientations of the CT models. These graphs describe the TRE for SP_L and BP, when using either 10° or 20° of *coverage angle*. Both ICP-PT and ICP-PL results are presented. Throughout the applied rotations, SP_L and BP had the best registration performance when a *kidney coverage angle* of 20° was used. Similar results were obtained with 10° for BP. Misalignments over ±50° on the CT surface were typically associated with higher errors, while over ±30° with higher variability.

4.3.4. Probe's sweep movement

Considering the previous results, Figure 4.5 shows the influence of different *probe's sweep movements* ($roll_{US}$, $pitch_{US}$, and yaw_{US}) when using SP_L and BP *views* with a *kidney's coverage*
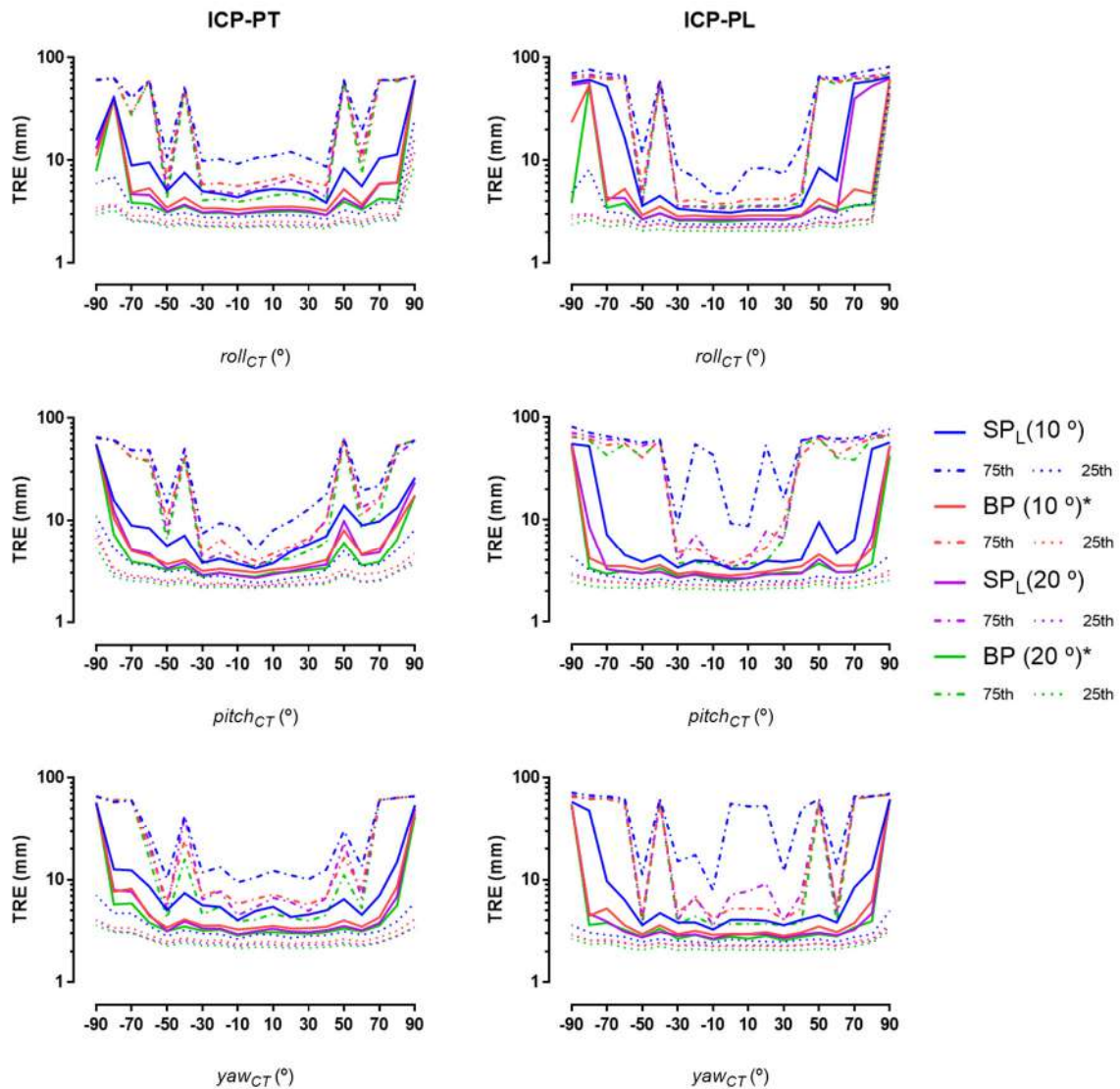
Figure 4.4 – Results of ICP-PT and ICP-PL methods for two *kidney's coverage angles* with respect to different orientations of CT surfaces.

The graphs link the results of each angle applied through composite transformations. The line graphs represent the median (solid), 25th (dotted), and 75th (dashed) percentiles of the TREs linked to a specific angle, and each color represents different views (SP_L, and BP) and respective *kidney's coverage ranges* used (10° or 20°). *Pairs of slices.

angle of 20°. The results revealed that using yaw_{US} *movement* together with SP_L or BP *views* presented lower errors, independently of the CT kidney orientation (*i.e.* for different CT misalignments). Moreover, the ICP-PL presented the lowest TREs. The $pitch_{US}$ *movement* together with BP *view* and the $roll_{US}$ combined with SP_L presented the worst results. Table 4.2 describes the results of sweeping the kidney in different positions, dividing them into three positions (*i.e.* centered at -10°, 0° and 10°). In most cases, the sweep position centered at 0° (*i.e.*, when the central longitudinal slices were captured, see Table 4.2 values of *position 0*) presented the best results for both BP and SP_L (p <.001).

67
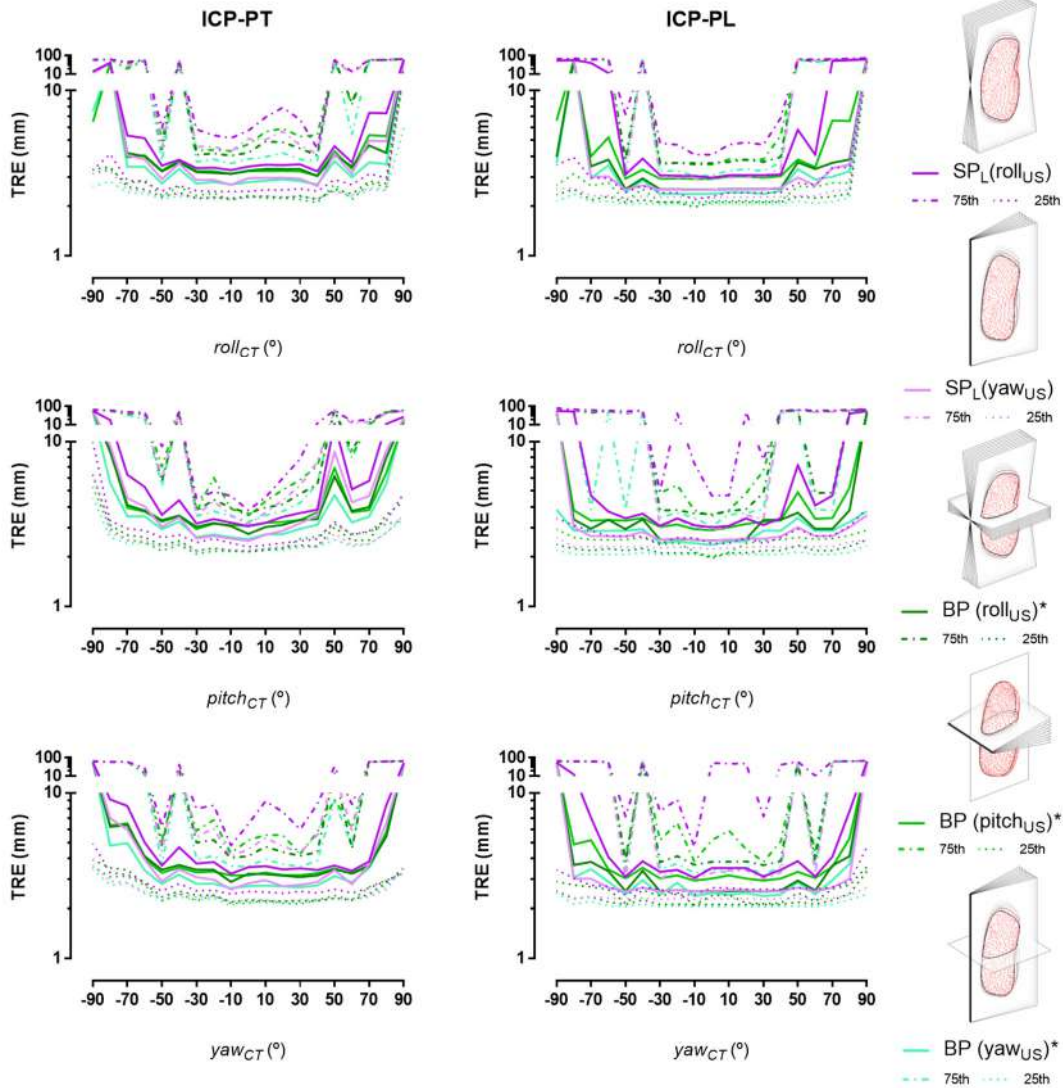
Figure 4.5 – Results for different *probe's sweep movements* ($roll_{US}$, $pitch_{US}$, and yaw_{US}) applied for both SP_L and BP *views*.

Graphs show results of using 20° of *kidney's coverage angle* for ICP-PT and ICP-PL methods. Line graphs represent the median (solid), 25th (dotted), and 75th (dashed) percentiles of TREs linked to a specific angle applied through composite transformations, and each color represents different *types of US image views* and respective *probe's sweep movements* used.

4.3.5. Spacing between consecutive slices

Due to the positive results of yaw_{US}, this *probe's sweep movement* was used to further explore if the *spacing between consecutive slices* influences the surface-based registration. This experiment was performed by capturing a *kidney coverage angle* of 20° (*i.e.* optimal value obtained in the previous experiments). Table 4.2 describes the results of sweeping the kidney using three distinct spacings (2.5°, 5° and 10° corresponding to 9, 5, and 3 slices, respectively). The use of 5° presented the best registration performance in most cases when compared to 2.5° and 10° (*p* <.001). Again, BP presented a lower variability than SP_L.

68

Table 4.2 – Results of different US probe's sweep positions (centered at -10º, 0º, and 10º) and *spacing between consecutive slices* (2.5º, 5º, and 10º).

A fixed *kidney coverage angle* of 20° and a *US probe's sweep movement* of yaw_{US} were considered. The respective number of slices is shown. Both SP_L and BP results are presented for ICP-PL method. The median, 25th and 75th percentiles are presented, as well as the non-parametric statistical tests performed and respective statistical significance and effect sizes (W = Kendall's W). *Pairs of slices.

	TRE (mm)									
	SPACING 2.5º (9 SLICES)			SPACING 5º (5 SLICES)			SPACING 10º (3 SLICES)			
	25ᵀᴴ	MEDIAN	75ᵀᴴ	25ᵀᴴ	MEDIAN	75ᵀᴴ	25ᵀᴴ	MEDIAN	75ᵀᴴ	FRIEDMAN TEST
SP_L										
POSITION -10º	2.31	2.67	48.92	2.44	2.65	48.98	2.54	2.84	48.92	*p < .001, W = .022, All groups, p < .001, Except: 9-5*
POSITION 0º	1.88	2.66	53.45	2.00	2.49	53.02	1.92	2.37	51.09	*p < .001, W = .003, All groups, p < .001, Except: 9-5*
POSITION 10º	2.29	2.64	47.20	2.22	2.49	47.23	2.26	3.24	52.98	*p < .001, W = .022, All groups, p < .001*
FRIEDMAN TEST	*p < .001, W = .032, All groups, p < .001*			*p < .001, W = .058, All groups, p < .001*			*p < .001, W = .161, All groups, p < .001*			
BP *										
POSITION -10º	2.36	2.96	3.72	2.33	2.86	3.93	2.19	2.87	4.06	*p < .001, W = .021, All groups, p < .001*
POSITION 0º	2.05	2.37	3.60	1.95	2.26	3.67	1.93	2.44	3.23	*p < .001, W = .006, All groups, p < .001*
POSITION 10º	2.05	2.87	3.88	1.96	2.44	3.87	1.95	2.73	4.55	*p < .001, W = .017, All groups, p < .001*
FRIEDMAN TEST	*p < .001, W = .093, All groups, p < .001*			*p < .001, W = .116, All groups, p < .001*			*p < .001, W = .039, All groups, p < .001*			

Position -10° Position 0° Position 10° Position -10° Position 0° Position 10° Position -10° Position 0° Position 10°

4.4. Discussion

In this work, we studied the feasibility of surface-based registration for fusing 2D US and CT data to hereafter improve PRA procedures. Different settings were tested using kidney phantom models and hundreds of thousands of surface-based registrations were performed, allowing an accurate evaluation of their performance. In summary, we found that surface-based registration had the best performance when the ICP-PL method was used and US acquisitions were acquired using the following conditions: bi-plane view; kidney's coverage range of 20°; sweep movement of yaw_{US}; and spacing between slices of 5°;

presenting a performance comparable to the full 3D surface registration. The relevance of these results was reinforced since manual segmentation of both image modalities simulated common differences between US and CT segmentation methods. To the best of our knowledge, this is the first study that assesses the optimal 2D US acquisition protocol to improve surface-based registration between 2D US and CT data for image-guided PRA.

With respect to the *type of US image view* used, globally, bi-plane acquisitions had a better performance. This is expected since more details of the kidney anatomy are captured (*i.e.* when orthogonal images are acquired), which ultimately enhances the performance of the ICP method to automatically align intraoperative and preoperative data. Overall, and despite the method's performance being interesting when compared to other state-of-the-art solutions using orthogonal acquisitions, the results presented lower accuracy. Seo *et al.* reported a TRE of 1.68 mm in one phantom model (with biplane acquisition at the surface's center using two orthogonal 2D probes) [149], and our study obtained a TRE of 4.08 mm (using a *kidney's coverage angle* of 0°, BP and ICP-PL, see Table 4.1). However, higher anatomical variability (10 phantoms in total) and higher positional variability before surface-based registration (400 different orientations per assessment, with up to ±90° of rotation per axis) was assumed in the current study. Moreover, it is relevant to mention that Seo *et al.* assumed the registration of the preoperative surface with multiple biplane US contours as gold-standard to assess the TRE, and not well-known landmarks (as used in this work). The concept of real-time biplane US imaging has also been used in other medical fields, particularly in cardiology, with good outcomes. Lang *et al.* evaluated the accuracy and robustness of a surface-based registration method for intraoperative use. They found that the use of bi-plane contours had the best accuracy with respect to other approaches, with TREs lower than 5 mm, even in clinical data [167]. These results are therefore corroborated in this study. Furthermore, the same authors also showed the potential of surface-based registration for real-time image-guided interventions [168].

Considering in more detail the use of a different *kidney's coverage angle*, it was possible to observe a superior performance of the registration method when higher ranges were used. SP_L and BP showed similar TREs when 20° were used (see Table 4.1). This suggests that SP_L acquisitions can have the same performance of BP acquisitions, meaning that a 2D single-plane US with a wider coverage range can potentially achieve the same accuracy of 2D bi-plane US. However, the errors' variability was superior when using SP_L, which indicates that it is less reproducible than BP. As previously mentioned, other works have tried to register 2D US with CT or MRI for image-guided PRA based on surface-based registration. Mozer *et al.* considered rigid transformations between pre- and intraoperative data, where

CT and sparse 2D US (coupled to an optical tracker) images were used. They reported a repeatability and closed-loop accuracy of 0.79 mm and 1.2 mm, respectively [85]. However, no gold standard was available, and the authors tested the registration strategy using a single patient. Li *et al.* presented an orthogonal-ICP strategy using two pairs of orthogonal US images (spaced, aligned and parallel to transverse and longitudinal planes of the kidney), which were selected from sparse images at the maximum exhalation position. The results revealed a TRE of 3.53 mm in four healthy volunteers when fused with MRI data [89]. This result is close to our results when a similar number of slices were used during the registration process. Indeed, when using a BP to acquire a coverage range of 5° (*i.e.* three pairs of orthogonal slices), a TRE of 3.63 mm was obtained (using the ICP-PL method, see Table 4.1). Moreover, this TRE decreased when a specific US sweeping was used (Figure 4.5). Despite the interesting results, Li *et al.* required the use of an optical tracking based respiratory gating technique to obtain the maximum exhalation position. All steps were performed at this specific position, including image capture, registration, segmentation, and puncture. We believe that a safer interventional strategy should rely on the continuous monitoring of the kidney position based on US images. Li *et al.* also tested the same approach in a pig model, although using a SSM to three-dimensionally reconstruct the kidney, with a surface distance (no TRE was assessed) around 1 mm [90]. Thus, 3D kidney reconstruction from 2D US images has the potential to be used in image-guided PRA, and new strategies should be studied to improve these methodologies. The concept of 2D US with surface reconstruction has also been used for bone [169] and artery [170] interventions.

Regarding the *probe's* sweep *movement*, the results proved that different movements could give a better performance during the registration process. The results suggested that yaw_{US} (*i.e.* a sweep movement along the longitudinal view, see Figure 4.5) leads to a better performance, in both SP_L and BP acquisitions with an average TRE of 2.66 mm and 2.87 mm, respectively. This suggests that a sweep from a fixed position may obtain a valid alignment when 2D single-plane US acquisitions are used. This can be relevant because 2D probes are more common in the urology field than 4D ones. Although yaw_{US} movements using BP presented slightly higher errors when compared with single-plane yaw_{US} motion, they had lower variability (see Figure 4.5 and Table 4.2 - 9 contours column). It is relevant to mention that yaw_{US} movements sliced the kidney equally for BP and SP_L. However, BP differed on the presence of the central transverse plane (see Figure 4.5). Therefore, this transverse plane seems to positively affect the registration process by reducing the method's sensitivity to the contours and to the initial alignment. Moreover, Table 4.2 suggests that slicing the kidney along the central longitudinal view may improve the registration acquired through a yaw_{US} movement. This may be related with the full slicing of the

longitudinal view that preserves more shape information of the kidney. In addition, the results presented in Figure 4.4 and Figure 4.5 revealed that when $roll_{CT}$, $pitch_{CT}$, and yaw_{CT} ranged between -50° and 50°, the average errors were below 3 mm for the ICP-PL method. As such, an initial and rough pre-alignment of the preoperative data with the intraoperative one seems to be mandatory for the ICP method. Among the two studied ICP methods, different performances and error magnitudes were obtained throughout this study, as expected. Previous studies revealed that the *point-to-plane* metric (*i.e.* ICP-PL) converges quicker and, typically, with lower errors [161]. However, it presents higher variability due to the linearization of the rotation matrix $\boldsymbol{R}$ in equation (4.2) during minimization which is only correct for smaller angles [166].

Regarding the *spacing between consecutive slices,* the results revealed that higher spacings, for the same coverage angle, may improve the final registration. This suggests that the *kidney's coverage angle* is more relevant than the spacing between slices acquired. Particularly, when a spacing of 5° were used for BP (TRE = 2.26 mm), the registration error was approximately the same of the full 3D US surface (TRE = 2.28 mm), with no statistical differences (Z = 1.660, p = .097, r = .026). Additionally, this last observation is important because a lower number of contours means lower computational time, which is a crucial feature for image-guided surgery. Indeed, spacings of 2.5°, 5°, and 10° (*i.e.* 9, 5, and 3 contours) presented a computational time of 0.60 (0.48) seconds, 0.32 (0.25) seconds, 0.23 (0.16) seconds per registration, respectively.

Overall, the results suggest that surface-based registration for image-guided PRA is a valid strategy for intraoperative image registration, even from a fixed position. In addition to be a multi-modal approach, which can extend these results to MRI for example, this approach has the potential to be applied to different interventions. Indeed, the segmentation algorithm can be adapted for different anatomical structures under intervention. In our work, although we studied only the fusion based on the kidney surface, segmentation of internal structures [171] (such as renal calyx, renal medulla, renal cortex, renal column, etc.) and adjacent organs [172] (such as liver, intestines, vessels, etc.) may help improve the intraoperative fusion. However, future work must be performed to assess this hypothesis.

It should be noted that, during the registration process, rigid movements were assumed between tests, while scale, shear or nonrigid changes were disregarded. However, these can occur in real scenarios, namely due to respiratory and small non-rigid movements of the tissues, which can affect the alignment results. Although this is a limitation of this study, only a 4D US acquisition would provide the necessary information to manage the full set of possible transformations and, as far as we know, this information is not yet freely shared by manufacturers. As an advantage, 2D US data has usually better

image quality and higher amount of details than 3D/4D volume data, being a widely used tool in urological interventions. These reasons support the use of 2D US imaging for multi-modal fusion, with our findings being directly applicable in clinical practice if real-time segmentation and registration algorithms are developed. Moreover, during the abovementioned experiments, we assumed that the US probe's tracking was not affected by errors. Tracking errors can occur in practice, which may introduce further errors during fusion. Likewise, we considered this fact a limitation of the present work. We must nevertheless highlight that these errors are influenced by the type of tracking system used, the calibration techniques employed, the operating environment, among other factors. Notwithstanding, the focus of this study was to evaluate if a 2D US image acquisition could be optimized to improve the registration between CT and US data, even when their respective segmentations have differences.

In the future, the current strategy should be embedded and tested in an image-guided framework, integrating an automatic segmentation of both image modalities, an inter-modality registration strategy, tracking and puncture guidance in real-time.

4.5. Conclusion

This work assessed the optimal 2D US acquisition protocol to improve surface-based registration between CT and US data for image-guided PRA. It was observed that the acquisition of slices covering a wider range, correctly spaced and using a specific sweep movement of the US probe, may be crucial to improve the final registration between CT and US data. Surface-based registration for image-guided PRA is therefore suggested as being a valid strategy for intraoperative image fusion. This strategy has the potential to be applied to different image modalities and interventions, and the presented methodology has the potential to be used to assess their feasibility.

Chapter 5

A new intraoperative image fusion approach using partial US kidney segmentation and CT-US registration for percutaneous renal access

The results presented in this chapter are under preparation to be submitted for publication as an original article in an international peer reviewed journal: **J. Gomes-Fonseca**, S. Queirós, P. Morais, A.C.M. Pinho, J. Fonseca, J. Correia-Pinto, E. Lima, J. L. Vilaça, "A new intraoperative image fusion approach using partial US kidney segmentation and CT-US registration for percutaneous renal access".

Abstract

Focused on image tracking, segmentation, and registration, this work aims to assess a new intraoperative image fusion approach to assist percutaneous renal access.

Using intraoperative two-dimensional (2D) ultrasound (US) images tracked with an electromagnetic tracking (EMT) system, a partial US kidney model is reconstructed. Here, a semi-automatic segmentation strategy is applied by manually delineating the kidney in one frame and using an image tracking algorithm (Medical Image Tracking Toolbox) to track the contour in the following images. Then, a point set registration algorithm (Coherent Point Drift [CPD]) is performed to register this partial US with preoperative kidney models. Three important steps were evaluated, namely probe calibration, segmentation, and registration. Different probes (2D and 4D) were calibrated and tested using the N-wire method, the segmentation strategy was studied in different synthetic and realistic image settings, and the proposed registration algorithm was compared against 6 state-of-the-art algorithms.

The 2D probe obtained the best probe calibration error (1.15 mm). The larger error for the 4D probe (>1.50 mm) may be linked with the distance needed between probe and EMT sensor to avoid signal distortions. The segmentation strategy presented an average Dice of 95.59%. No significant differences were observed between image settings, but lower frame rates lean towards better results. CPD with an outlier ratio of 10% exhibited the best performance across the tested algorithms with an average target registration error (TRE) of 5.22 mm. TRE improved when the kidney's coverage range was higher than 60% (TRE = 4.24 mm), approximating what would be obtained if the full kidney was used to register both modalities (TRE = 3.46 mm).

A close to real acquisition protocol was assessed, evaluating a new image fusion approach to perform PRA. The results suggested that the proposed segmentation and registration strategies achieve superior outcomes when a 2D probe is used. The proposed approach is therefore suggested as a valid solution, being accurate and fast. This new approach has the potential to be applied to different image modalities and other interventions.

5.1. Introduction

A previous work presented by Gomes-Fonseca *et al.* [173] demonstrated, *in silico*, that it is possible to accurately register two-dimensional (2D) ultrasound (US) data with preoperative computed tomography (CT) data by aligning a partial kidney model extracted from the former with a full model from

the latter. The goal was to prove the validity of a novel image fusion strategy to safely perform percutaneous renal access (PRA), a surgical step where the surgeon inserts a surgical needle from the skin until the kidney target site. Despite the initial results, the work did not analyze the impact of other steps that can harm the final registration in a real scenario. Among them are: (1) the error from probe calibration which is inherently correlated with the type of tracking system used; (2) the error from the segmentation algorithm; and (3) the cumulative error of the final registration.

Thus, using an experimental setup closer to a real one, this study focuses on assessing the pipeline of image fusion between intraoperative US images tracked by an electromagnetic tracking (EMT) system and preoperative CT data, whose pipeline is presented here for the first time. Therefore, we intend to quantify the errors linked to each module of the pipeline. For that, different experiments were performed: (i) a probe calibration method is tested with different acquisition systems and settings; (ii) a semi-automatic US segmentation strategy used to create a partial kidney model is evaluated; and (iii) a point set registration algorithm to align US and CT models is assessed.

This paper is structured as follows. In section 5.2, we present the novel image fusion approach and the respective pipeline. Section 5.3 presents the probe calibration technique and results for different probe settings. In the same section, it is assessed the segmentation and registration strategies, and their results based on kidney phantoms are presented. All results are discussed in section 5.4. In section 5.5, we present the main conclusions.

5.2. Methods

5.2.1. Overview

An overview of the general workflow, and its main elements, proposed to develop the new intraoperative image fusion approach for percutaneous renal access is here presented.

The hardware consists of an US system and an EMT system that intraoperatively tracks the position of the US probe. A video grabber is used to capture images from the US system monitor to the computer, while the EMT system plugs directly on the computer.

The Public software Library for Ultrasound (PLUS) was used since it interfaces with different ultrasound scanners, tracked devices and grabber systems only by modifying the configuration files [174]. Using a set of calibration parameters, PLUS performs the synchronization between US images and probe's sensor data. The images and transformation data are streamed using a network protocol for image-guided environments, the OpenIGTLink [175], which connects to the developed software.
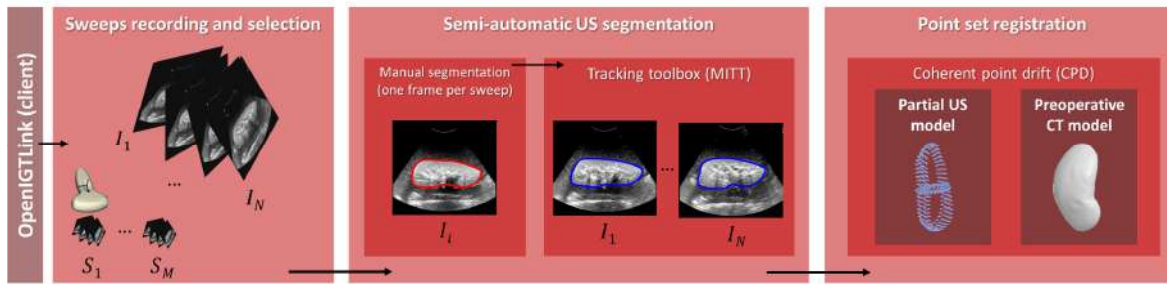
Figure 5.1 – Overview of the new intraoperative approach and its main steps.
Through the openIGTlink protocol, several sweeps, S_M, containing tracked US images, I_N, can be recorded into the computer's memory. Each sweep can be selected and segmented using a semi-automatic segmentation strategy. Therefore, one frame, I_i, is manually segmented and used as the initialization of an image tracking algorithm, i.e. the Medical Image Tracking Toolbox (MITT), that tracks the manual segmentation in the remaining images. A partial intraoperative model of the kidney is obtained as output. Finally, a point set registration algorithm, specifically the coherent point drift (CPD), is applied to fuse the partial US model with the preoperative CT model.

The developed software combines all steps of the proposed intraoperative image fusion approach (Figure 5.1). Each step is detailly described in the following section.

5.2.2. New intraoperative image fusion approach

Sweeps recording and selection

First, intraoperatively, the surgeon must sweep the puncture zone with a tracked US probe and the software records the US images and the transformation data into the computer's memory. Several sweeps can be performed and recorded. These sweeps must be focused on acquiring the organ under evaluation in all frames and preferentially with a wider range and without repeating anatomical zones.

Semi-automatic US segmentation

A semi-automatic US segmentation is applied to the selected sweeps. It consists of manually delineating the kidney in one frame of the sweep and use this delineation as initialization of a tracking algorithm. Here, we propose to use the Medical Image Tracking Toolbox (MITT) [6]. The MITT includes an object-oriented image tracking module based on the anatomical affine optical flow (AAOF) algorithm, including 2D+t and 3D+t implementations of both global [176] and localized [177] versions of AAOF, and permitting the tracking of multiple types of objects (*i.e.* contours, multi-contours, surfaces and multi-surfaces) with several customization features. The key principle of AAOF is to estimate an object's motion between adjacent frames using optical flow, where it uses the a priori knowledge about the object of interest to anatomically constrain the motion estimation step to the region of interest around the tracked object (*i.e.,* defining a window function with respect to the object).

77

In our case, the proposed approach does not capture the natural motion of the organ (as it happens in, *e.g.*, cardiac images) but instead captures the motion of the object of interest (*i.e.* the kidney) as a result of sweeping the probe.

Due to the versatility of MITT, several features (the reader is kindly directed to the original paper [154] for a detailed explanation of the tracking framework) were defined to improve the tracking performance in the proposed approach based on 2D+t image sequences. Specifically, (1) *tracking propagation scheme* was defined as bidirectional, where tracking is performed from the reference frame (manually delineated) to the last frame and from the reference frame to the first frame, without assuming a complete cycle (since we are sweeping the organ without any predefined cyclic probe motion). The reference frame was selected according to the most common kidney shape in all frames of the sweep and where the kidney was clearly visible; (2) *motion type* was defined as affine, allowing to describe the motion as a combination of translation, rotation, scaling and shearing; (3) *tracking type* was defined as local (displacement vector estimated per contour point), which gives more degrees of freedom during contour tracking and allows contour's local deformation to account for the variable shape imaged during the sweep. (4) *mesh topology/dimensionality* is set as a contour type where objects are entered as a 1D structured grid; (5) *anatomical boundary mapping* is defined as periodic since it is a closed contour; and (6) *object regularization* is used to ignore image intensity content out and near the limits of the field-of-view. The field-of-view is defined using a binary image mask. Based on the anatomical topology of the contour, the motion is estimated within a localized anatomical region-of-interest (whose size is defined by the parameter *BoxRadii*) and, then, anatomically constrained based on its neighbor points (which can be controlled by a Gaussian-based weight, *SigL*). Besides, all spatial derivatives are computed after pre-processing the image with a gaussian filter (whose sigma is defined by the parameter *SigGaussian*).

MITT is used for several reasons: it is versatile, easy to use and to incorporate, computationally efficient, and capable to track the contours even in noisy images or in the presence of artifacts, like shadows or echogenic changes. This is possible due to the anatomical topology and localized nature of the AAOF algorithm. Summarizing, MITT will propagate the initial contour to the remaining frames performing a partial 3D segmentation of the organ.

Point set registration

This step uses a point set registration to fuse information from preoperative CT data and intraoperative US data. Point set registration methods play an important role in medical image registration due to their simplicity, accuracy and low computational burden over intensity-based registration methods,

mainly when multimodal registration is necessary [178]. In this context, recently, we have shown that a high accuracy can be obtained by aligning a partial intraoperative US model with a complete preoperative CT model of the kidney using the iterative closest point (ICP) method [173]. Here, we propose to explore the potential of the coherent point drift (CPD) algorithm.

CPD is a robust and efficient pairwise point set registration method which fits into the probability-based category [179]. CPD is an extension of the gaussian mixture model (GMM) for rigid and non-rigid registration. Therefore, it considers the registration of two point sets as a probability density estimation problem. One point set is represented by GMM centroids, and the other point set is fitted to those of the first point set by maximizing the likelihood and forcing GMM centroids to move coherently as a group, preserving the topological structure [180]. One of the crucial parameters of CPD is the weight parameter that specifies the expected ratio of noise and outlier points in point sets.

Since we are expecting some noise, outliers and missing data among the point set extracted with the proposed semi-automatic segmentation strategy, namely due to contour drifting when using MITT or due to occlusions during image acquisition, CPD is an interesting option due to its low sensitivity to noise, high accuracy and robustness compared to other point set registration algorithms [178].

5.3. Experiments and Results

We assessed the proposed intraoperative approach by conducting a set of experiments using kidney phantom models, where their images were used to assess segmentation and registration.

A software prototyped in MATLAB® (The Mathworks Inc., Natick, MA) was developed, which allows to perform sweep recording and selection, perform the semi-automatic US segmentation, and point set registration.

All statistical tests were conducted using MATLAB® as well. The assumption of normality was assessed for all variables and based on the results, parametric or nonparametric tests were applied accordingly. The effect size and statistical significance were reported. For normal distributions, mean and standard deviation (SD) were reported, while median and interquartile range (IQR) were used for non-normal distributions. All statistics were considered significant if $p < 0.05$.

5.3.1. Kidney phantoms

Phantoms were constructed using the protocol presented in Gomes-Fonseca *et al.* [157] (Chapter 3). In short, the phantom was manufactured based on a porcine kidney combined with tissue mimicking

material (TMM) and implanted fiducial markers (FMs). While the TMM mimics the surrounding tissues of the kidney, the FMs were used to accurately align and assess the registration performance between US and CT data. Some adjustments were introduced in the protocol to reduce the amount of air in the phantom. Specifically, a plastic tube was introduced in the ureter until the renal pelvis, and water was injected to remove air. Besides, the kidney is submerged in a water tank (6-8h) while the plastic tube remained open to remove the residual air bubbles. At the end, the tube with water was closed. Moreover, the percentage of agar-agar was reduced to 1.5% to reduce stiffness and no flour was used to improve contrast between TMM and kidney. Overall, ten phantoms were built with 24 FMs each.

5.3.2. Experimental setup

The experimental setup relied on ultrasound image acquisition using a Voluson 730 Pro V machine (GE Healthcare, Milwaukee, Wisconsin, USA) with two probes: a 4D convex abdominal probe (RAB 4-8P, 2 – 7 MHz), and a 2D convex abdominal probe (AB 2-7, 2 – 7 MHz); an NDI Aurora® V3 Planar Field Generator (Northern Digital, Inc., Waterloo, Ontario, Canada), coupled with 6-DOF EMT sensors; an Epiphan's video grabber (DVI2USB 3.0, Epiphan Systems Inc., Palo Alto, California, USA); and a computer running Windows 10 (64-bit) with an Intel® Core™ i7 CPU at 2.8 GHz, with 16 GB of RAM, a NVIDIA Quadro® K2100M with 2 GB and a Samsung SSD 850 EVO. The MATLAB® version was R2016b, and the PLUS toolkit version 2.6 was used.

Data acquisition

CT images of the phantoms were acquired using a Philips Brilliance 64 CT scanner (Philips Healthcare, Best, The Netherlands). The X-ray tube current and peak voltage were set to 313 mA and 120 kV, respectively. The abdomen protocol was selected. On average, the CT volume size was $512 \times 512 \times 650$ with a voxel resolution of $0.550 \times 0.550 \times 0.450$ mm. Each phantom was imaged in two different positions to introduce pose variability during CT acquisitions.

Tracked US images were acquired using the 4D convex abdominal probe, and the 2D convex abdominal probe. Each probe was coupled with an Aurora® 6-DOF sensor using specifically designed supports. The 4D probe was used in two acquisition modes, *i.e.* 2D and 4D modes. 2D mode displayed on the monitor offered an image size of 542×438 pixels and a pixel resolution of 0.346×0.346 mm, while the 4D mode presented an image size of 280×212 pixels with 0.719×0.719 mm. The 2D probe achieved a pixel resolution of 0.366×0.366 mm with an image size of 542×442 pixels (Table 5.1). During acquisition, presets of the US machine for imaging the kidney anatomy were used. Hereafter, 2D

and 4D modes will be mentioned as *single-plane* and *bi-plane* acquisitions, respectively, since the first one only captures one image from the monitor, while the second relies on two orthogonal slices. In bi-plane acquisitions, the second image (due to the orthogonal view) was spatially calibrated by applying a 90° rotation to the calibration transformation calculated for the first image. Moreover, to assess different image settings when 4D mode is used, the parameter that influences the image quality of the volume acquisition was changed, hereafter know as, *max quality*, *high quality* and *low quality*. Thus, in total, five different probe configurations were tested.

Each probe configuration was used to capture and record multiple tracked US images while two main probe's movements were used, hereafter designated as (1) *yaw* – parallel movement along the longitudinal axis of the kidney, and (2) *roll* – rotational movement along the longitudinal axis of the kidney (Figure 5.2). These two movements have been previously tested *in silico* and shown to improve the registration result [173]. Similar to the CT acquisitions, each probe movement was captured twice to increase variability.

Moreover, offline acquisitions were also performed to establish the ground-truth data. Thus, US volumes and tracked US images of the complete kidney and fiducials markers were acquired achieving a voxel resolution and volume size of $0.670 \times 0.670 \times 0.670$ mm and $304 \times 275 \times 231$, and $0.5 \times 0.5 \times 0.5$ mm and $477 \times 654 \times 340$, respectively.

During all US acquisitions, a reference 6-DOF sensor was attached to the phantoms to compensate for small phantom movements throughout the experiments (Figure 5.2).
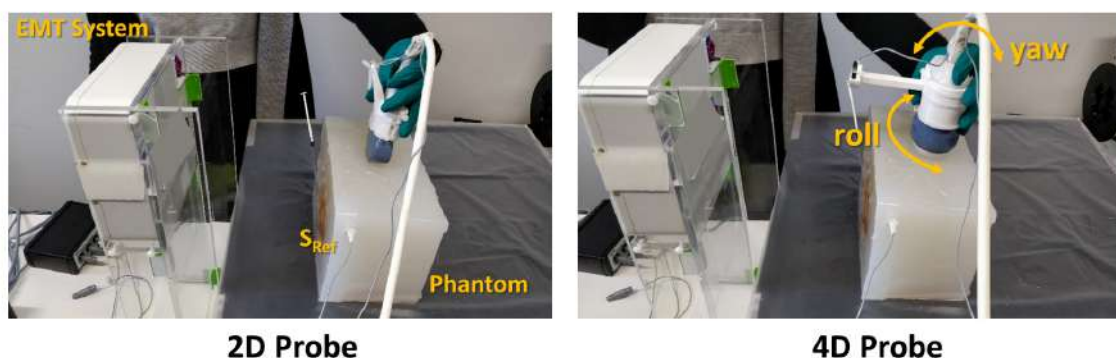
Figure 5.2 – Experimental setup using a EMT system, kidney phantom model, and two different US probes. Each probe uses a specific support and 6-DOF EMT sensors. The sensor of the 4D probe is away from the center to reduce motor interferences in the EMT signal. Two different types of sweep movements were acquired (i.e. *roll* and *yaw*) and one 6-DOF reference sensor (S_{Ref}) was attached to the phantom to compensate for small movements.
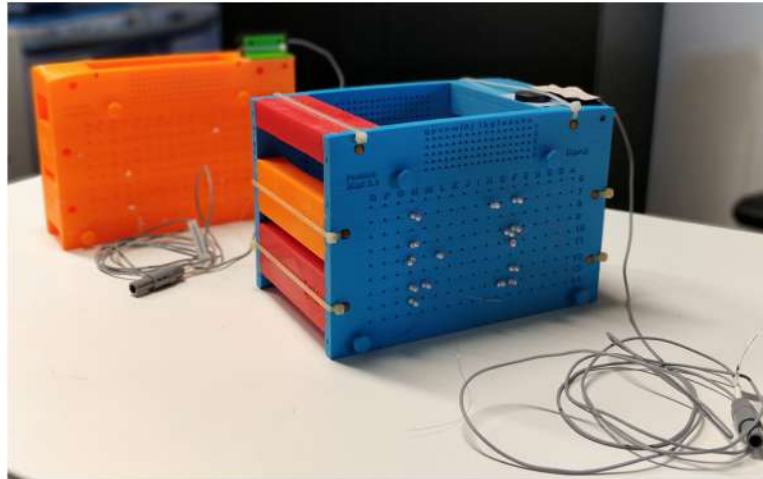
Figure 5.3 – Extended calibration phantom (blue box) to improve 4D probe spatial calibration.
Larger aperture enabled more flexibility on positioning and orienting the 4D probe during calibration when compared to the standard calibration phantom (orange box).

US probe calibration

Before US acquisitions, probe calibration is required, where temporal and spatial calibration must be performed to link US images position and orientation to the EMT sensor with the correct time latency. A US probe calibration based on N-wire method was accomplished [181], [182], by sequentially performing the N-wire phantom calibration, temporal calibration and spatial calibration.

Based on Perklab[3], a N-wire phantom for spatial calibration for deep structures was built. The N-wire phantom was expanded to enable 4D probe calibration (Figure 5.3). Specific supports to attach the sensors and probes were built. The sensor in the 4D probe support was shifted 9 cm to reduce signal distortion between 4D probe and electromagnetic sensor, as observed by Gomes-Fonseca *et al.* [183] (Chapter 2), while in the 2D Probe, the sensor was positioned in the center and close to the probe's body (Figure 5.2). N-wire phantom and supports were 3D printed in polylactic acid material using an Ultimaker II Plus (Ultimaker B.V., Geldermalsen, The Netherlands) with a printing resolution ± 0.2 mm.

The N-wire phantom was calibrated by computing the transformation between the phantom coordinate system and the coordinate system of the EMT sensor attached to the phantom by point matching. Point coordinates were defined in the phantom coordinate system and coordinates of the same points were also acquired in the EMT coordinate system by using a tracked stylus (with the sensor on its tip).

To improve calibration of curvilinear transducers, decreasing image distortion after scan conversion, a mixture of 9.5% of ethanol and distilled water was used to fix the speed of sound in 1540

---

[3] http://perk-software.cs.queensu.ca/plus/doc/nightly/modelcatalog/

m/s (the typical speed in soft tissue and assumed by most ultrasound imaging systems). The temperature of ethanol/water mixture was maintained at approximately 20°C [184]. Both temporal and spatial calibration were performed using this ethanol/water mixture.

After attaching the EMT sensor to the probe, temporal calibration was performed to estimate the time offset between data streams acquired by different devices, *i.e.* imaging and tracking systems. By imaging the bottom of a water tank (planar object) with a probe undergoing an up-down motion, a sequence of line motifs is introduced in the image data. To improve line detection, 1 cm of cork was applied to the bottom of the water tank to reduce reflection artifacts. Then, the positions of the bottom of the water tank (derived from the line motifs) along with those of the probe (derived from the tracker data) are computed. The temporal offset is then taken as the temporal shift that best aligns the image position and tracker position signals [185], [186]. The calibration algorithm requires data acquired while performing up-down motion for at least 5 full periods. The time required to perform these 5 full periods is dependent on the frame rate of the image acquisition (which depends on the equipment, but especially of the acquisition parameters).

During spatial calibration, 5 N-wires were used to improve spatial calibration in depth. Thus, a real-time spatial calibration procedure was performed where the nylon wires (diameter = 0.3 mm) were

Table 5.1 – Temporal and spatial calibration results for 5 different probe configurations.
Specific settings are presented for each configuration. Median and interquartile range are shown, and respective statistical significance and effect sizes. FPS – frames per second; FOV – field of view

	PROBE	ACQUISITION TYPE	SETTINGS	TEMPORAL CALIBRATION ERROR (s)	SPATIAL CALIBRATION ERROR (mm)
1.	2D	single-plane	FPS: 36Hz | FOV-1: 70° | Depth: 15.2 cm | Image size: 542 x 442 | Pixel resolution: 0.366 x 0.366 mm	0.071 (0.005)	1.15 (0.78)
2.	4D	single-plane	FPS: 36Hz | FOV-1: 65° | Depth: 14.4 cm | Image size: 542 x 438 | Pixel resolution: 0.346 x 0.346 mm	0.068 (0.003)	1.67 (0.60)
3.	4D	bi-plane	FPS: 1.1Hz | FOV-1: 65° | FOV-2: 65° | Depth: 14.4 cm | Volume quality: Max | Image size: 280 x 212 | Pixel resolution: 0.719 x 0.719 mm	0.848 (0.063)	1.79 (0.76)
4.	4D	bi-plane	FPS: 2Hz | FOV-1: 65° | FOV-2: 65° | Depth: 14.4 cm | Volume quality: High1 | Image size: 280 x 212 | Pixel resolution: 0.719 x 0.719 mm	0.436 (0.077)	1.69 (0.32)
5.	4D	bi-plane	FPS: 4Hz | FOV-1: 68° | FOV-2: 65° | Depth: 14.4 cm | Volume quality: Low | Image size: 280 x 212 | Pixel resolution: 0.719 x 0.719 mm	0.294 (0.025)	1.50 (0.33)
	INDEPENDENT-SAMPLES KRUSKAL-WALLIS TEST				$p < .001$, $\eta^2 = 0.288$ $p < .05$ for groups 1-2; 1-3; 1-4

automatically segmented (collinear bright spots) during a continuous image acquisition (approximately 1000 images). The successfully segmented N-wires, together with their corresponding physical coordinates collected in the phantom space, fed a closed-form solution to calculate the calibration parameters [181]. The method proposed by Carbajal *et al.* (namely *in-plane error method*) was used to estimate the calibration matrix which allowed minimizing the calibration error in a much larger image area, reducing tilting, and rotation errors [182]. An isotropic image resolution was assumed.

Each calibration step was repeated at least 6 times. A mean calibration transformation was computed for phantom and spatial calibration [126], and the mean time offset was used for temporal calibration.

Table 5.1 presents the calibration results. No significant differences were found for spatial calibration between different 4D probe configurations. However, statistically significant differences were found between 2D and 4D probes.

5.3.3. Segmentation assessment

We assessed the proposed segmentation strategy using images collected from 10 different phantoms, different probe configurations and movements. Segmentation results were compared against manual delineations (others than the initial frame). 80 images were selected and assessed randomly. Thus, each image was manually segmented (two times) by two observers and automatically segmented by the proposed strategy. The parameters *BoxRadii*, *SigL*, and *SigGaussian* (referenced in section 5.2.2 - *semi-automatic US segmentation*) were fixed to 3 mm, 40%, and 1 mm, respectively. The segmentation differences were evaluated by computing the average distance (AVD), the 95th Hausdorff distance (HD), and the Dice similarity coefficient (DSC).

An example of the manual initialization of the image tracking algorithm is shown in Figure 5.4 – A, as well as, two different segmentation results obtained in the same sweep (Figure 5.4 – B and C). Both
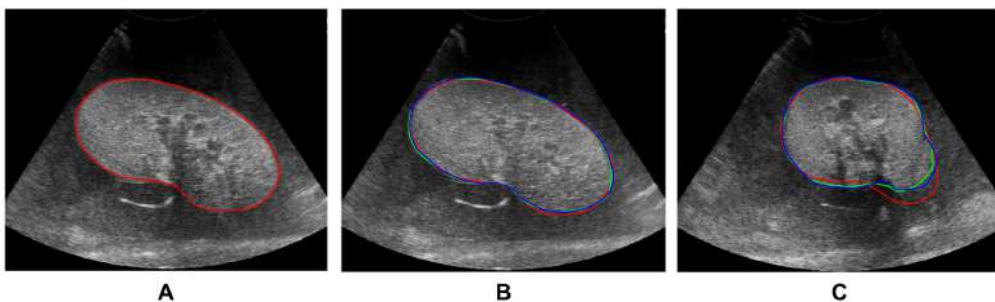
Figure 5.4 – Examples of the segmentation results for the same sweep.
A) Manual initialization of the image tracking algorithm at frame 114. Two different tracking results at B) frame 122 and C) frame 4 are compared against two observers. The image tracking algorithm is shown as red line, while the first and second observers are represented as green and blue lines, respectively.

Table 5.2 – Segmentation assessment results.
Intra-observer variability, inter-observer variability, observer 1 vs. proposed algorithm (medical imaging tracking toolbox - MITT) differences and proposed algorithm initialized by two different manual contours (named as *Init 1* and *Init 2*). Dice similarity coefficient (DSC), Average Distance (AVD), and 95th Hausdorff Distance (HD) define the differences for each phantom. Median and interquartile range (N = 80), as well as nonparametric statistical tests performed and respective statistical significance and effect sizes (W = Kendall's W), are reported.

		AVD (mm)	HD (mm)	DSC (%)
1.	**INTRA-OBSERVER 1 VARIABILITY**	0.75 (0.33)	1.70 (1.45)	98.43 (1.22)
2.	**INTER-OBSERVER VARIABILITY**	1.02 (0.52)	3.24 (2.93)	97.53 (1.64)
3.	**OBSERVER 1 VS. PROPOSED (INIT 1)**	1.69 (0.87)	5.15 (3.60)	95.59 (2.99)
4.	**PROPOSED (INIT 1) VS. PROPOSED (INIT 2)**	1.18 (0.49)	2.76 (1.90)	97.65 (1.83)
	RELATED-SAMPLES FRIEDMAN'S TEST	$p < .001$, $W = 0.596$ — All groups $p < .001$ Except: 2-4	$p < .001$, $W = 0.412$ — All groups $p < .001$ Except: 2-4	$p < .001$, $W = 0.627$ — All groups $p < .001$ Except: 2-4

US images present observers' manual delineations against the results of image tracking algorithm. Usually, the manual initialization was performed in a middle frame of the sequence where the kidney was clearly visible.

Table 5.2 summarizes the segmentation results, comparing the automated strategy against manual delineation. For comparison purposes, we also report the intra-observer and inter-observer variabilities. In addition, the results of the automated strategy when initialized with different contours (at the same frame) are also presented.

It is possible to observe that intra-observer and inter-observer differences are low, with the latter presenting slightly larger errors as expected. When compared against manual delineation, although the proposed segmentation strategy presents a significantly higher error, it still presents a segmentation overlap over 95% and an average distance lower than 2 mm. When two different initializations (at the same frame) were tested, errors similar to the intra- and interobserver variabilities were found, suggesting that the contour propagation along the frame sequence was similar in both cases.

Figure 5.5 shows the 5th, 50th, and 95th percentiles of the segmentation results, presenting the following average distances 0.92 mm, 1.69 mm, and 3.71 mm, respectively.

Table 5.3 presents the averages distances when the segmentation results are grouped using different probes' configurations (detailed information in Table 5.1). In addition, the processing time was also measured for both CPU and GPU versions of MITT. No statistical differences were obtained, however slightly lower errors were found when bi-plane acquisitions were used, particularly for the *max* and *high-quality* probe configurations.
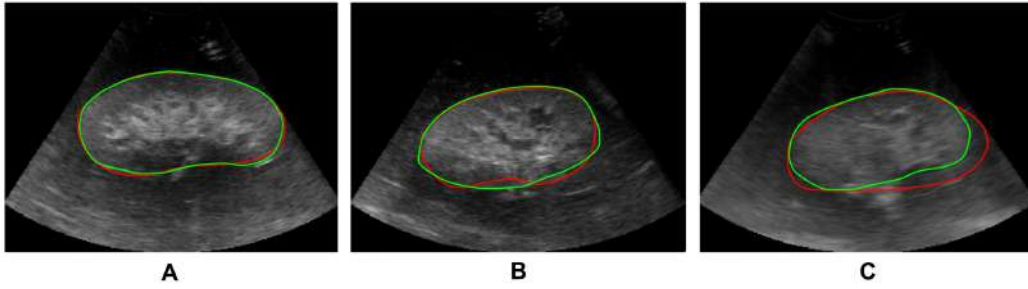
Figure 5.5 – Depiction of (A) the 5th percentile, (B) the 50th percentile, and (C) the 95th percentile result of the segmentation assessment.
Green – observer 1 contour; Red – Semi-automatic segmentation result based on MITT algorithm

Best performance was associated with the GPU implementation of MITT, especially when larger image sizes and frame rates were used (GPU spent 27 ms while CPU 59 ms to compute each frame). In this work, this setting was linked with single-plane acquisitions. In opposite, CPU implementations performed slightly better when bi-plane acquisitions were used, *i.e.* lower image sizes and frame rates (GPU spent 21 ms while CPU 16 ms to compute each frame).

An additional analysis was made to evaluate the propagation/drift error of MITT throughout the sweep. Thus, the spatial distance between the initialization frame and the segmented ones was measured, with higher distances generally denoting higher shape differences. The spatial distance was obtained by transforming each image to its spatial position and computing an average pixel-to-pixel distance. Errors were grouped according to spatial distances and are presented in Figure 5.6-left.

Table 5.3 – Average distances (AVD) grouped according to probe configuration.
The processing time of the proposed segmentation algorithm was obtained in both CPU and GPU versions. The processing time comprehends the time needed to track the initial contour over all frames. The processing time of the bi-plane acquisitions was computed using only one image (not both). Median and interquartile range, as well as nonparametric statistical tests performed and respective statistical significance and effect sizes, are reported.

		AVD (mm)	CPU (s)	GPU (s)
1.	SINGLE-PLANE (2D PROBE), N = 16	1.75 (0.52)	12.29 (6.99)	5.93 (2.40)
2.	SINGLE-PLANE (4D PROBE), N = 16	1.83 (0.97)	11.67 (5.85)	5.81 (2.41)
3.	BI-PLANE (4D PROBE - MAX), N = 20	1.58 (0.84)	0.47 (0.28)	0.66 (0.19)
4.	BI-PLANE (4D PROBE - HIGH), N = 16	1.59 (1.03)	0.67 (0.26)	0.78 (0.31)
5.	BI-PLANE (4D PROBE - LOW), N = 12	2.20 (2.01)	1.33 (1.73)	1.31 (1.18)
	INDEPENDENT-SAMPLES KRUSKAL-WALLIS TEST	$p = .266, \eta^2 = .050$		
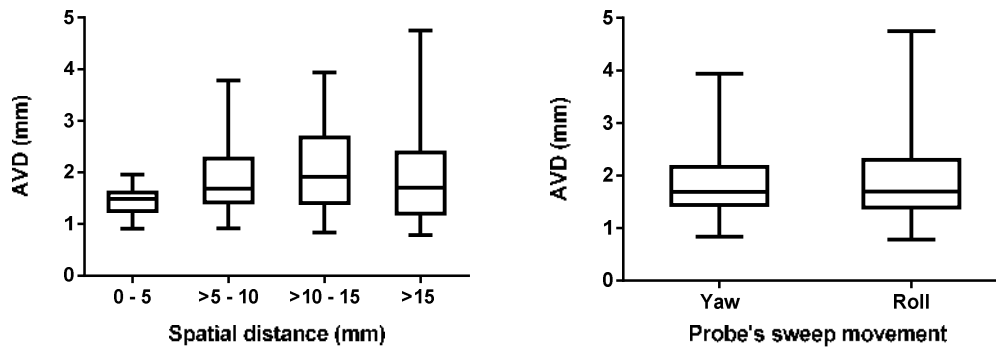
Figure 5.6 – Average distance (AVD) grouped according to: (Left) *spatial distance* **between initialization frame and frames segmented by the proposed method. (Right) type of** *probe's sweep movement* **during US acquisition,** *i.e.* **Yaw and Roll.**
No statistical differences were observed.

No statistical differences were found, however a tendency for a higher error variability is present when the spatial distance is over 5 mm. Additionally, in Figure 5.6-right, differences between *probe's sweep movement* were tested and no statistical differences were found as well.

5.3.4. Registration assessment

Segmented 3D surfaces were initially created for each phantom, namely one per CT volume. In detail, the CT volume was delineated using the 3D Slicer software (version 4.6) [158]. The manual delineation relied on multiple 2D contours followed by 3D interpolation to obtain the final 3D surface. The same strategy was used in the US volumes to use as reference. In detail, the raw files from the 3D US system were initially converted to Meta Image files using BabyOSlice software (Tomovision, Canada), and were then uploaded to the 3D Slicer software and manually delineated. This process was repeated two times for both CT and US acquisitions to increase variability. In addition, the implanted FMs were manually detected (using the image-guided therapy toolbox available on 3D Slicer) on both CT and US volumes of each acquisition of each phantom (two times too). In addition, implanted FMs were manually detected in tracked 2D US images by sweeping the phantom and recording the images. Note that FMs are visible as brighter and darker structures in the US and CT images, respectively. Twelve FMs were selected to align both US and CT images, while the remaining ones were used to assess the registration performance. The selected FMs were rigidly aligned based on the strategy presented by Horn *et al.* [138]. Thus, FMs were used to establish the ground-truth alignment between CT and US images. In this sense, the fiducial registration error (FRE) describes the residual alignment error after landmark-pair registration, using the root-mean-square (RMS) distance between corresponding FMs. To depict an average ground-truth alignment, ten subsets with twelve FMs each were randomly selected per phantom. The subset with the

median value of FRE was used as the ground-truth alignment. During the experiments, all applied transformations assumed the ground-truth alignment as the reference position. To assess the error obtained in landmark-pair and point set registrations, the target registration error (TRE) was computed using the remaining FMs, by computing the RMS distance.

Thus, FRE was 1.92 (±0.29) mm, and TRE was 2.29 (±0.35) mm when 3D US volumes were used (*Landmark-based 3D*), while FRE was 1.58 (±0.34) mm and TRE was 1.84 (±0.43) mm when using 2D tracked US images (*Landmark-based 2D*). All ten phantoms were successfully segmented in both modalities, with differences between both models (upon registering using the fiducial markers) being 92.28 (±1.39) %, 1.69 (±0.24) mm and 3.65 (±0.64) mm for DSC, AVD and HD, respectively.

The experiments were performed assuming a rigid transformation (translation and rotation) between models. Moreover, throughout the experiments, the CT model was defined as the target point set, with the US model being the source point set. Besides partial models from 2D tracked images, complete models from 3D US volumes were also used to obtain a reference for an ideal case (in which the full kidney is imaged and segmented). Finally, besides using one type of probe movement only (either *roll* or *yaw*), a *mixed* scenario was also considered by merging the point sets obtained by performing *roll* and *yaw* sweep movements.

The performance of CPD was compared against six state-of-the-art point set registration algorithms: (1) iterative closest point (ICP) based on point-to-point metric (**ICP-PT**) [162]; (2) ICP-PT with 10% of outlier ratio [187]; (3) ICP based on point-to-plane metric (**ICP-PL**) [188]; (4) ICP-PL with 10% of outlier ratio [187]; (5) Gaussian mixture models registration (**GMMREG**) [189]; and (6) Discriminative

Table 5.4 – Target registration error (TRE) grouped by point set registration algorithm.
The proposed algorithm, *i.e.* Coherent Point Drift (CPD) with and without 10% outlier ratio (OR), was compared against six algorithms. The iterative closest point (specifically, ICP-PL, ICP-PT), Gaussian Mixture Models registration (GMMREG) and Discriminative Optimization (DO) were tested. Median and interquartile range (N = 19200), as well as nonparametric statistical tests performed and respective statistical significance and effect sizes (W = Kendall's W), are reported.

	ALGORITHMS	TRE (mm)	CPU (s)
1.	ICP-PL	6.33 (3.71)	0.33 (0.05)
2.	ICP-PL (OR 10%)	6.40 (3.75)	0.32 (0.04)
3.	ICP-PT	6.19 (3.22)	0.27 (0.05)
4.	ICP-PT (OR 10%)	6.55 (3.19)	0.28 (0.06)
5.	GMMREG	5.61 (2.40)	2.34 (0.25)
6.	DO	6.59 (3.38)	1.95 (0.97)
7.	CPD	6.64 (3.28)	5.18 (2.04)
8.	**CPD (OR 10%)**	**5.22 (2.28)**	**8.75 (0.69)**
		$p < .001$; $W = 0.154$	
	RELATED-SAMPLES FRIEDMAN'S TEST	All groups, $p < .001$	
		Except: 2-4	

optimization (**DO**) [190]. Moreover, two tests were made to analyze the influence of the outlier ratio in **CPD**, *i.e.* with 0% or 10% outlier ratio. The algorithms were implemented using publicly available code.

Specific parameters were used for each algorithm. In **CPD** and **ICP**-based algorithms, the convergency stopped after 25 iterations. **GMMREG** used just one level of the multiscale strategy with a sigma value of 0.1 for the gaussian mixture model, and 200 function evaluations. **DO** was trained by generating 2000 training samples mimicking different partial acquisitions of the kidney with different parameters (number of slices, number of vertices, rotation, translation, number of outliers, adding gaussian noise, coverage range) per CT model and a total of 30 maps for the sequence of update maps.

All 3D models from CT and US volumes were down sampled to 20.000 points, while 2.000 points were sampled from each point set extracted from the tracked 2D US images. Before point set registration, a transformation was applied to pre-align the CT and EMT system world coordinates for each phantom.

Table 5.4 summarizes the performance of the tested algorithms on aligning 3D models from CT with partial 3D models from tracked 2D US images. CPD with 10% outlier ratio was significantly better than others. On average, the TRE was around 5 mm while other algorithms showed errors closer or higher than 6 mm. However, CPD showed to be slower to converge, taking approximately 9 seconds. GMMREG had an alignment performance close to CPD with 10% of outlier ratio and even better than CPD with 0% outlier ratio.

Figure 5.7 shows the target registration errors grouped according to *probe's configurations* and *probe's sweep movement* using CPD with 10% outlier ratio. No statistically significant differences were
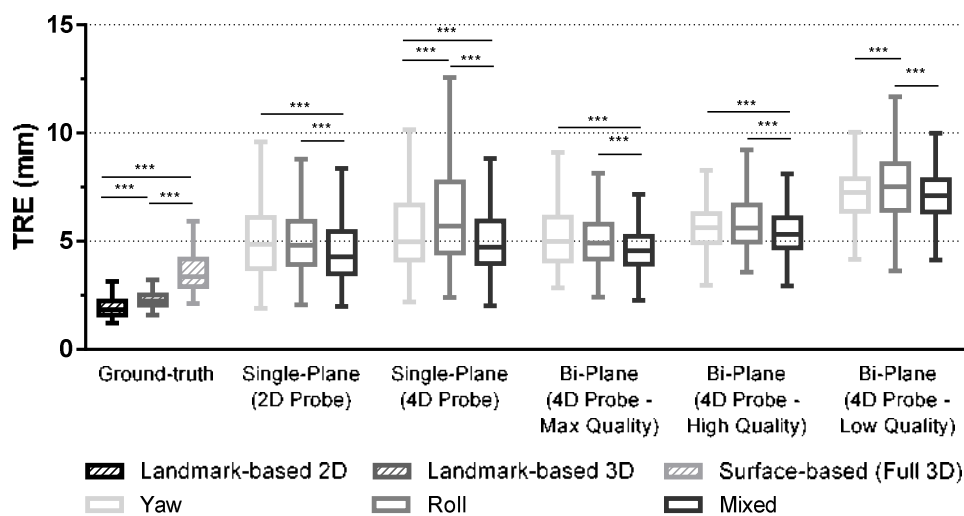
Figure 5.7 – Target registration error (TRE) grouped according to probe configuration and probe's sweep movement (*i.e.* Yaw, Roll and both movements – Mixed) using the CPD algorithm (with 10% outlier ratio).
Landmark-based registration using 2D and 3D acquisitions and a surface-based registration using a complete US surface were used as references and compared. *** $p < .001$

Table 5.5 – Errors grouped by kidney's coverage range when using the CPD algorithm (10% outliers).
The median and interquartile range are presented (N = 19200).

	KIDNEY'S COVERAGE RANGE	TRE (mm)
1.	< 20 % (n = 151)	7.39 (2.04)
2.	20 – 30% (N = 1610)	7.21 (2.13)
3.	30 – 40 % (n = 4178)	6.30 (2.13)
4.	40 – 50 % (N = 7054)	5.12 (1.96)
5.	50 – 60 % (N = 4875)	4.63 (1.57)
6.	60 – 70 % (N = 1112)	4.24 (1.27)
7.	70 – 80 % (N = 220)	4.35 (0.89)
	INDEPENDENT-SAMPLES KRUSKAL-WALLIS TEST	$p < .001$; $\eta^2 = 0.217$ All groups, $p < .001$. Except: 1-2, 6-7

found between *yaw* and *roll* movements, except for single-plane using 4D probe. Nonetheless, when compared to the *mixed* setting, significant differences were observed. Indeed, the average TRE values for both single-plane and bi-plane (*max quality*) acquisitions were close to 4.5 mm. However, these average values are higher than the references, namely when compared to the registration of complete CT and US models (TRE = 3.46 [IQR: 1.34] mm). Moreover, the worst TREs were obtained with bi-plane acquisitions using high- and low-quality configurations.

An additional test was performed to assess if the amount of kidney covered by the sweep affects the final registration. Thus, based on the ground-truth alignment, the percentage of the sweeping that covers the full surface of kidney was calculated and linked to the measured TRE. Table 5.5 summarizes the results. It was observed that when more than 60% of the kidney is imaged, a superior performance is obtained, with average TREs lower than 4.5 mm. Moreover, no statistically significant differences were observed between 60-70% and 70-80% groups. However, when comparing both groups to the full 3D surface registration, they still present statistically significant differences ($p < .001$).

5.4. Discussion

In this work, we studied the feasibility of a new intraoperative image fusion approach to enhance the percutaneous renal access. During this work, different experiments were performed to assess the pipeline employed to achieve the final fusion between preoperative and intraoperative data.

An initial and important step for the proposed approach is the probe calibration in which the temporal and spatial calibration errors may influence the final registration according to the probe configuration used. Table 5.1 compiles all information on the temporal and spatial calibration errors. As

expected, the temporal calibration error was mainly influenced by the frame rate of the US machine, which varied between 1.1 to 36Hz. Higher frame rates induced lower temporal offsets (and vice-versa) since the acquisition rate of the EMT system was 40 Hz. However, lower frame rates introduced additional difficulties because slower movements and a longer acquisition is required to achieve a proper temporal calibration. Moreover, the water tank with cork-based bottom reduced the US reflections and created a brighter interface on the images improving the line detection during up-down movements and consequently leading to a better temporal calibration.

Additionally, the selected parameters to enhance the spatial calibration of curvilinear probes, as 9.5% ethanol solution, extended calibration phantom, use of 5 N-wires (instead of 3 N-wires), and the method proposed by Carbajal *et al.* were shown to facilitate the calibration procedure. Such improvements were important, since the spatial calibration errors using curvilinear probes are usually superior when compared to linear ones, as shown in [182]. The spatial calibration does not seem to be influenced by the temporal calibration, as no significant differences were found when the 4D probe was tested for different probe configurations. However, statistically significant differences were found between 2D and 4D probes ($p < .05$). The higher spatial errors of the 4D probe configurations may be related to the position of the EMT sensor in the support. Indeed, it was positioned 9 cm away from the 4D probe (to avoid interferences), which may lead to an increase in the lever arm effect during calibration.

The proposed segmentation strategy based on the MITT, which tracks the kidney contour in a sequence of 2D US images after a manual delineation in one frame, presented interesting results when compared to typical errors of other segmentation strategies [171]. Indeed, this proposed strategy achieved an average Dice of 95.59%, while more recent works to segment kidneys on US images using deep neural networks reached values equal or lower to 94.51% (the performance decreased to 92.31% when the testing images were rotated by 30 degrees) [191]. However, different inter-observer variabilities were reported, *i.e.* 97.53% and 96%, since phantom and real images were used, respectively. Despite being automatic, which may increase repeatability and reduce segmentation variability during surgical planning, they need a large dataset with manual delineations to perform training for each surgical scenario which may be difficult to collect. The proposed semi-automatic strategy is more versatile and has other advantages. First, since it is a tracking algorithm, it can be used in different scenarios without requiring additional training. Indeed, it follows the movement of each contour point without the need for a priori knowledge on the image or object of interest. Second, the initialization of the algorithm in one frame by surgeons is important since they can use their experience to delineate the kidney with very distinct appearances, *i.e.* in the presence of different pathologies like kidney stones and tumors, or US artifacts

like shadows. Third, the algorithm is also reproducible, as observed in Table 5.2, where different initializations presented equivalent results and no differences were observed when compared to the inter-observer variability. Notwithstanding, significant shape or echogenic transitions near the kidney must be prevented during sweep acquisition (for example, performing smaller acquisitions) since the tracking algorithm may require a re-initialization or contour adjustment for drift correction. In addition, the tracking algorithm is fast (see Table 5.3), achieving comparable computational burden as presented in [191]. In fact, the computation time varies between some milliseconds to seconds depending on image size, frame rate, parameters, and implementation type, showing its potential for real interventional scenarios. Using GPU implementation, the images with higher frame rates and image sizes required ~6 seconds per sweep, while smaller images with lower frame rates took ~1 second only. For detailed information about probe configurations please consult Table 5.1. On average, GPU implementation of MITT used 23 ms to compute each frame. As suggested in [154], to reduce even more the computational burden, one could decrease the number of points to represent the structure of interest or down-sample the images (either spatially, temporally or both). Regarding differences between probe configurations, it was observed that lower frame rates may produce lower segmentation errors, which was visible with the 4D probe (max/high quality). Thus, an additional test was done using images from the 2D probe with a subsampling of the frame rate (10 times). The results revealed that average errors decreased to values observed with the 4D probe, *i.e.* 1.55 mm (IQR: 0.64). Moreover, no statistical differences were observed when the spatial distance between the initialization and the segmented frames was higher. However, a superior variance was observed in spatial distances above 5 mm (see Figure 5.6). Therefore, the subsampling (in higher frame rates) may reduce this variance and improve the overall segmentation. The main reason might be associated with the tracking algorithm (especially being a gradient-based optical flow strategy), as the number of propagation steps (*i.e.* the number of frames to be tracked in each direction) is directly proportional to the observed contour drift. Additionally, no statistical difference between *roll* and *yaw* movements were observed, demonstrating that the algorithm robustly tracks the kidney boundaries despite the considerable differences in kidney shape across the sweep.

CPD has been used in medical image registration, although it is still an emerging algorithm with several potential applications and improvements [178]. In this work, we tested its potential to be used for intraoperative registration of preoperative CT data and intraoperative US data.

To evaluate the performance, CPD was compared against 6 state-of-the-art algorithms. Moreover, the influence of the outlier ratio in the CPD algorithm was also evaluated for this application. It was observed that the use of CPD with 10% outlier ratio had the best performance compared to all algorithms

tested, achieving an average TRE around 5 mm. Indeed, the use of 10% outlier ratio was fundamental to improve the accuracy of the point set registration. Despite being widely used for rigid registration due to its simplicity and low computational complexity, ICP is usually affected by inaccurate initializations which may lead to the convergence to a local minimum. This limitation may explain its results, even when different minimization metrics and outlier ratios were used. Likewise, the performance of the DO algorithm was also suboptimal. A better performance was expected since DO is, in theory, robust to different number of points, noise, initial angle, number of outliers, and incomplete models [190]. The main reason for this poor performance may be related with the insufficient training (with only 2000 training samples) or less robustness to noise comparatively to CPD. GMMREG presented interesting results although slightly higher than CPD. This difference may be linked with the fact that GMMREG does not incorporate the detailed information among the feature points in the registration, which leads to a decrease in registration accuracy [178].

Evaluating the performance of the CPD when different sweep acquisitions were performed (*i.e. roll* and *yaw* movements), no considerable differences were visible within different probe configurations (please consult Figure 5.7). However, different probe configurations presented distinct TREs. Two reasons may have influenced these results. First, low image quality inherently harmed the segmentation and ultimately the registration, which is visible when 4D Probe – *low quality* is used. Second, it was empirically observed that specific motor rotations of the 4D probe (particularly, *high quality*) induced higher interferences in the EMT sensor signal, even when distanced by 9 cm from the motor.

When both sweep movements were merged (*i.e. mixed*), the improvements in registration accuracy were significant among all probe configurations. This is linked with the higher coverage range that is obtained when using both sweeps together. Indeed, higher coverage ranges were linked to lower average TRE, as shown in Table 5.5. However, the results suggest that no significant improvement is obtained after 60% coverage. The coverage range might be a useful information to support surgeons during registration process. Even though the full 3D surface registration is still the strongest option to achieve the best alignment, the proposed approach achieves considerable close registration accuracy to the full 3D. Additionally, no strong correlation was found between TREs and the range of distances of the implanted fiducials to the kidney surface ($r = 0.137$), where the mean distance was 23.36 ± 9.47 mm (range: 0.45 - 48.92 mm). This suggests that the distribution of the registration error around the kidney is uniform and this can be used to define a safety distance between registered data and the needle.

The potential of CPD to register a partial and a full model was shown here, as well as the importance of the outlier ratio which strongly influences the algorithm output. The automatic selection of

the outlier ratio , as proposed by Peng *et al.* [192], could help further improve the results. Moreover, CPD is widely used for non-rigid registration. Indeed, the rigid registration can be improved by the subsequent application of the non-rigid version of CPD. However, intraoperative usage time may increase considerably due to its processing time. Furthermore, beyond non-rigid registration, different strategies can be applied to improve intraoperative alignment. For example, Li *et al.* proposed a respiratory gating technique to synchronize registration and respiratory movements during PRA [89]. In this regard, we believe one can take advantage of the technique proposed by Lima *et al.* [79]–[81], where a EMT sensor is positioned inside the kidney, which allows the registration to be linked to this sensor and more precise information about the kidney's pose can be obtained in real-time during PRA.

The results presented in this work are promising since this new approach is simple, fast, and accurate. It only uses 2D tracked images which usually have superior image quality and are easier to interpret and segment. Then, just one image needs to be delineated to perform the segmentation of the full sequence, and the proposed point set registration algorithm presents a sufficiently good accuracy to align both modalities. The processing time is crucial within the operating scenario, with both algorithms revealing to fit the needs of this application (even if the registration needs to be recomputed to perform corrections).

5.5. Conclusion

This work assessed a new approach to perform PRA. The results suggest that the semi-automatic segmentation strategy achieves interesting performance. Moreover, the CT-US registration strategy, with the CPD algorithm, of a full 3D surface and a partial kidney representation, respectively, shown to be accurate. A good performance was achieved with different probe settings, but the lowest errors were accomplished with the 2D probe. The lower spatial calibration and segmentation errors may have explained the superior registration accuracy. In the future, further improvements are possible, namely by subsampling the image sequence (mimicking a lower frame rate) to improve tracking (and consequently the segmentation) or implementing an automatic outlier ratio calculation to improve registration.

The proposed approach is therefore suggested as being a valid strategy for intraoperative image fusion, being fast to perform and accurate. This new approach has the potential to be applied to different image modalities and other interventions.

Chapter 6

Surgical navigation system for percutaneous renal access:

Computed Tomography, Ultrasonography, Ureteroscopy and Electromagnetic guidance working together

Abstract

Electromagnetic tracking (EMT)-based solutions have been used to perform percutaneous renal access (PRA) in nephrolithotomy with high success. However, key limitations still exist. To mitigate them, this work aims to present and assess a novel surgical navigation system for PRA combining the EMT system with computed tomography (CT), ultrasonography and ureteroscopy.

Three solutions with distinct levels of assistance were assessed, named as (i) **NAV**$_{EMT}$ (EMT only), (ii) **NAV**$_{EMT-US}$ (EMT and ultrasonography), and (iii) **NAV**$_{EMT-VR}$ (the proposed system). All use the ureteroscopy to position an EMT catheter as a target inside the renal calyx. Using an abdominal phantom model specifically developed for this study, eleven medical doctors tested all solutions in three scenarios common in nephrolithiasis: (a) *test 1*, puncture a calyx with a target sensor inside; (b) *test 2*, puncture an obstructed calyx with an incorrectly positioned target; and (c) *test 3*, puncture a calyx with a target sensor but from a difficult tract. For each solution and scenario, puncture success and time, and number of attempts and collisions were recorded, and participants were asked about their confidence level and willingness to change the final tract. In the end, a questionnaire evaluated the participants' opinion.

Overall, **NAV**$_{EMT-VR}$ presented the best performance in all tests compared to other solutions. In *test 1*, differences in performance were not significant since all participants were able to successfully complete the puncture in a similar time. However, the confidence level was significantly superior ($p = .01$) for **NAV**$_{EMT-VR}$, which was also observed in *tests 2* and *3* ($p < .001$). In *test 2*, all participants were able to target the calyx with **NAV**$_{EMT-VR}$, which did not occur with the other solutions. Moreover, **NAV**$_{EMT}$ and **NAV**$_{EMT-US}$ needed more time to puncture the calyx and the willingness to change the final tract was more frequent. Similarly, in *test 3*, **NAV**$_{EMT-VR}$ presented a lower number of collisions and attempts compared to the other solutions. The participants adjectivized the **NAV**$_{EMT-VR}$ as safe, accurate, good for complex punctures, easy-to-learn and comfortable. It was considered the safest solution.

A new system for PRA was proposed and assessed in phantoms, demonstrating a high performance and obtaining an excellent feedback by the participants. The proposed system has potential to assist during renal access in nephrolithotomy and may even be extended to other interventions.

6.1. Introduction

In the past few years, several innovations have been introduced to improve percutaneous renal access (PRA) [45]–[47], [49], [50]. Electromagnetic tracking (EMT)-based approaches have been

demonstrating their potential to perform a precise puncture to the collecting system. Indeed, Rodrigues *et al.* combined ureteroscopy and EMT-based strategies to place inside the renal calyx an EMT catheter (target) and puncture using an EMT needle supported by a specific software [79], [80]. This approach has 100% success rate in the first attempt with an average puncture time of 20-22 seconds [80], [81]. Despite the success rate, there are still limitations linked to this technique. The navigation using only EMT sensors can be affected by the lack of visualization of the anatomical structures in the puncture path or the target positioning could be compromised if the calyx is fully occupied by stones. Alternatively, the use of ultrasound (US) imaging combined with an EMT system aids in the identification of the missing information, and allows to overlap the trajectory of a needle over the image, when compared with pure EMT solutions [71]. Previous results of this combined approach demonstrated a success rate on the first attempt of 84%, with an average puncture time of 6.62 minutes [72]. The lower success rate and superior puncture time may be related to i) the longer learning curve associated with US image interpretation; ii) the lack of three-dimensional (3D) perception of the organs; and iii) the absence of an easily identifiable target inside the calyx.

Considering the limitations described above and the need to improve PRA safety, we previously proposed a new intraoperative image fusion approach (chapter 5), using an EMT system, US and computed tomography (CT) imaging, that provides the means to present in real-time 3D anatomical information during renal interventions. Building on this approach, this work aims to present and evaluate a novel complete surgical navigation system, combining CT, US, ureteroscopy and a EMT system, to safely perform the PRA. To the authors' best knowledge, this is the first time that such a system is proposed.

This chapter is structured as follows. In section 6.2, we present an overview and specific technical information about the system. In section 6.3, we present the experiments to assess the performance of the proposed system against other solutions, which was accomplished using an abdominal phantom specifically developed for these experiments. Section 6.4 presents the experiments' results, which are discussed in section 6.5. In section 6.6, we present the main conclusions.

6.2. Materials and Methods

6.2.1. Surgical step workflow

The navigation workflow of this surgical step derives from the technique presented by Lima *et al.* [80], [81]. The patient is placed in the supine position allowing a flexible ureteroscopy and percutaneous

nephroscopy. The field generator is placed near the patient to create an electromagnetic field covering the surgical zone (*i.e.* the abdomen) where the EMT sensors attached to the surgical instruments work (needle, catheter, US probe). Next, a cystoscope is inserted to identify the ureteral meatus, and a hydrophilic guidewire is inserted through it. The hydrophilic guidewire is then used to guide a flexible ureterorenoscope up to the renal pyelocaliceal system. The guidewire is removed and a flexible catheter with an EMT sensor (on its tip) is inserted through the working channel of the flexible ureterorenoscope. The surgeon selects the best calyx for PRA and places the catheter in the fornix of the calyx (if possible, otherwise placed in a non-obstructed region inside the kidney). An US system with an attached EMT sensor is used to acquire images of the puncture zone and a registration technique fuses this intraoperative US data to the preoperative CT one. The selected calyx is punctured using a needle with an EMT sensor (on its tip). Puncturing is supported in real-time by a navigation software where it is possible to virtually visualize the needle trajectory, catheter, ultrasound images and registered CT models. A successful puncture is confirmed using the ureteroscopy images and the virtual environment.

6.2.2. Surgical navigation system overview

Figure 6.1 summarizes the proposed surgical navigation system to perform the PRA. This system consists of an EMT system, an ureteroscopy system, an ultrasound system, and a computer with a navigation software where registration between CT and US segmented data is performed followed by surgical guidance.
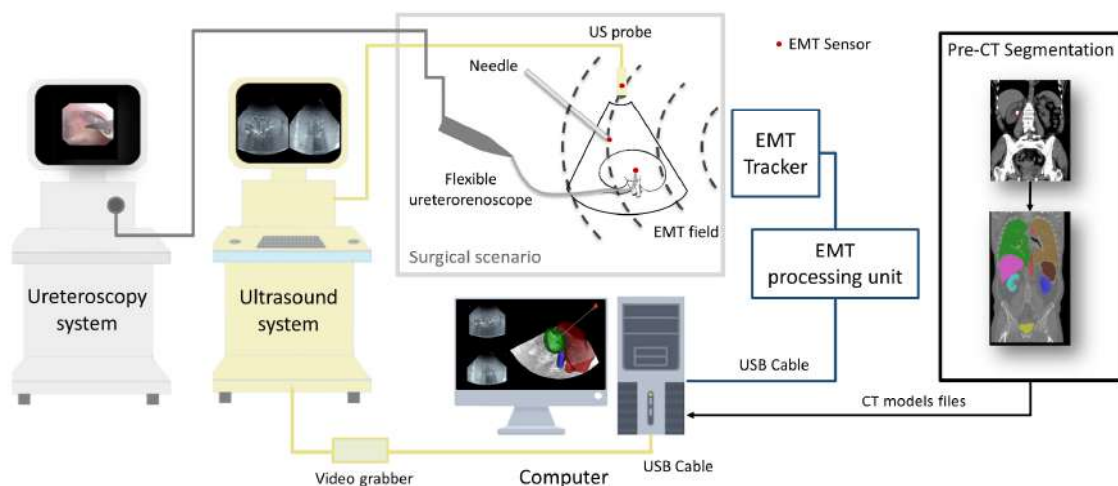
Figure 6.1 – Illustration of all the components involved in the proposed surgical navigation system.
Pre-CT – Preoperative Computed Tomography. EMT – Electromagnetic tracking; USB - Universal Serial Bus.

The EMT system allows tracking of surgical instruments both inside and outside the patient's body. The electromagnetic sensors are rigidly attached to US probe, needle tip and catheter tip. Orientational and positional data of all sensors are collected by the EMT system and streamed to the computer.

As previously mentioned, ureteroscopy is used to position the catheter in the correct calyx inside the kidney. The catheter creates a rigid relationship between the kidney and the catheter tip, allowing tracking the kidney position in real-time (*e.g.*, measuring respiratory movements) and targeting the calyx to be punctured.

US images (displayed in the US system monitor) are sent to the computer using a video grabber which is connected to the output video channel, and their position and orientation are given by the EMT sensor attached to the probe.

The navigation software workflow is presented in Figure 6.2. The Public software Library for Ultrasound (PLUS) was used since it interfaces with different ultrasound systems, tracked devices and grabber systems only by modifying the configuration files [174]. Based on calibration parameters, PLUS performs the synchronization between US images and probe's sensor data. The images and transformations data are streamed to the navigation software using a network protocol for image-guided
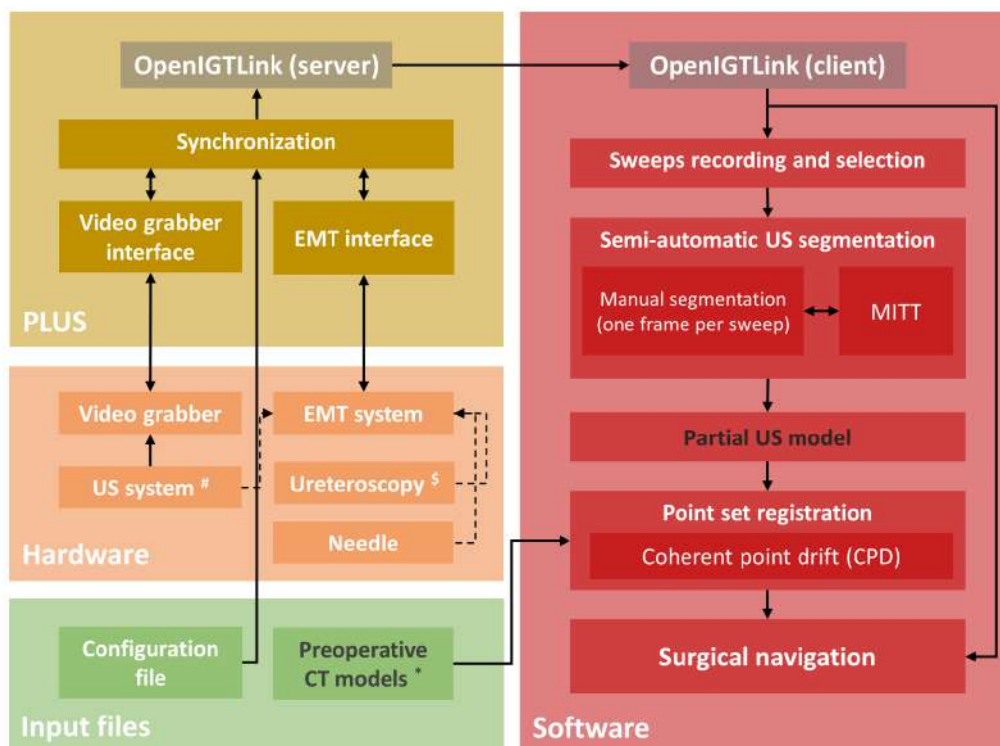
Figure 6.2 – Navigation software workflow running on a computer.
*Models are generated from *preoperative CT segmentation*. #EMT sensor is attached to the US probe. $A catheter with an EMT sensor is positioned inside the working channel of the flexible ureterorenoscope.

99

environments, namely OpenIGTLink [175]. The navigation software was developed in C++ language using Qt, VTK, ITK, and OpenIGTLink libraries. Moreover, the navigation software is divided in five steps (Figure 6.2): (1) preoperative CT segmentation; (2) sweeps recording and selection; (3) intraoperative semi-automatic US segmentation; (4) point set registration between preoperative CT and intraoperative US data; and (5) surgical navigation.

6.2.3. Preoperative CT segmentation

Preoperative CT data must be prepared before intraoperative fusion by segmenting the kidney and nearby organs. Multi-atlas segmentation (MAS) strategies have been widely used to solve the problem of multiple organ segmentation. This approach performs multiple registrations between the target image and a set of known atlases, combining their results to obtain the final segmentation.

While typical MAS strategies subdivide the segmentation process into multiple ones (per organ), losing the spatial relationship among nearby organs, a spatially coherent MAS approach was proposed in [172] and is here employed. After an initial global alignment using the entire image, multiple local transformations are computed in the region of interest of each organ. Then, to guarantee spatial coherence, all local transformations are combined into a single map using a dense deformation field reconstruction. Additionally, a deformable registration method is applied to refine the atlas information to the patient-specific anatomy. Finally, a label fusion strategy is used, which employs an organ-wise statistical selection method and a local weight voting strategy. The former eliminates the worst registered atlases per organ, while the latter assigns a different weight to each voxel per its similarity with the same anatomical position in the unlabeled image (Figure 6.3).
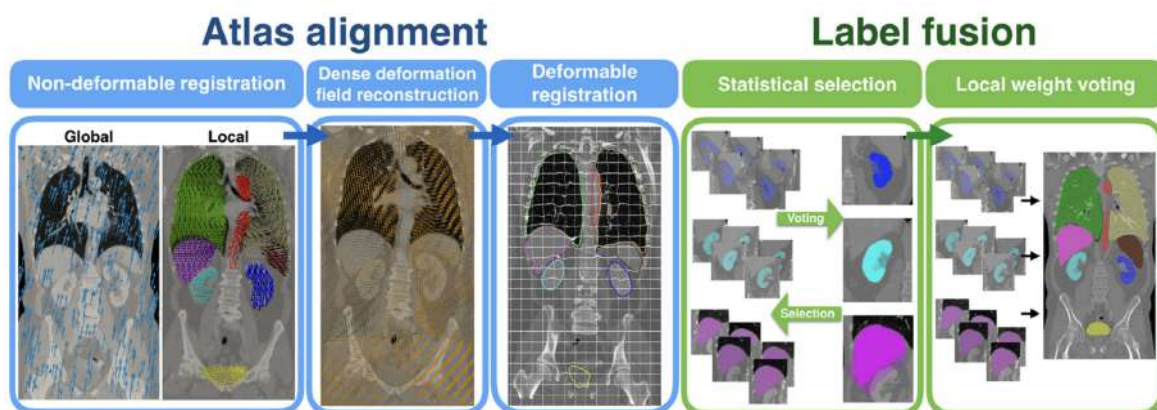
Figure 6.3 – The spatially coherent MAS strategy proposed in [172].

6.2.4. Surgical navigation software

Calibration file and streamed information

Using a predetermined calibration between the EMT system and the US system (as suggested in chapter 5), a file must be loaded into the software. This file contains information about the systems and the calibration parameters needed for accurate synchronization. This file is used to turn on the PLUS server and, subsequently, a TCP/IP connection is established between the software and the PLUS server through the OpenIGTLink protocol. When the connection is established, the software immediately shows the US images captured from the US monitor (when biplane mode is activated, two images are shown). Besides, specific transformations are streamed which enables to virtually represent the pose of the images, needle, and catheter in a three-dimensional (3D) environment. Transformations are computed using the catheter as *world origin* (Figure 6.4). Optionally, a reference in the surgical table can be used to inform on the real world's up-vector.
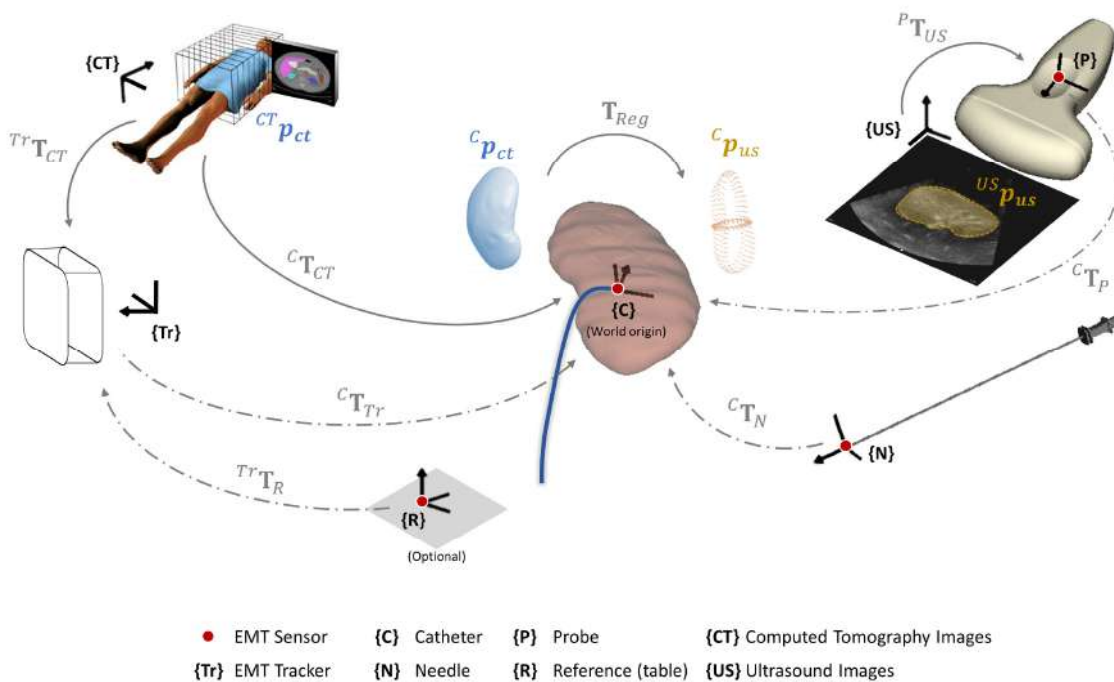
Figure 6.4 – Overview of the components' transformations during intraoperative use.
All transformations are computed using the catheter as *world origin.* Dashed arrows represent transformations computed and updated from the electromagnetic sensors in real-time, such as: tracker to catheter, $^{C}\mathbf{T}_{Tr}$; probe to catheter, $^{C}\mathbf{T}_{P}$; needle to catheter, $^{C}\mathbf{T}_{N}$; and reference to tracker, $^{Tr}\mathbf{T}_{R}$. Solid arrows represent static transformations computed pre- and intraoperatively, such as: probe calibration, $^{P}\mathbf{T}_{US}$; CT to tracker prealignment, $^{Tr}\mathbf{T}_{CT}$; CT to catheter, $^{C}\mathbf{T}_{CT} = {}^{C}\mathbf{T}_{Tr}{}^{Tr}\mathbf{T}_{CT}$; and CT-US registration, $\mathbf{T}_{Reg}$. Registration is performed with both models in the catheter's local coordinates, i.e. $^{C}\boldsymbol{p}_{ct}$ and $^{C}\boldsymbol{p}_{us}$. Reference in the surgical table can be used to inform on the real world's up-vector. All transformations belong to the three-dimensional (3D) space $\mathbb{R}^{3}$, where $\mathbf{T} \in \boldsymbol{SE}(3)$.
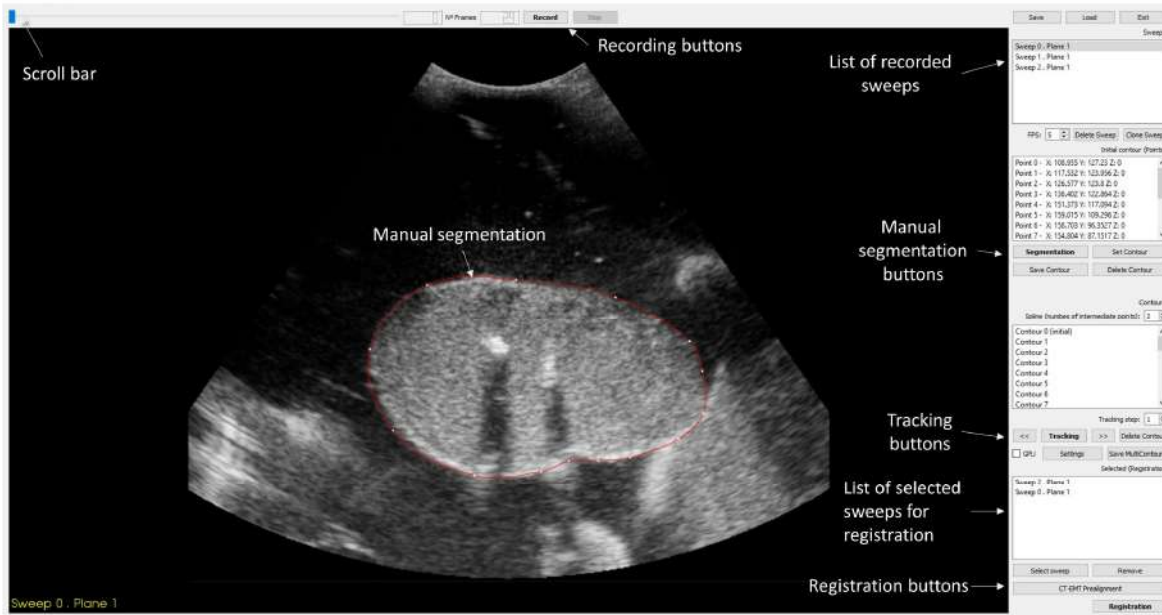
Figure 6.5 – GUI for intraoperative sweeps recording, semi-automatic US segmentation, and registration.
Several sweeps can be recorded and saved into a list of recordings. One frame per sweep must be manually segmented, and subsequently the tracking algorithm segments the remaining images. Finally, the registration process can be triggered after selecting which sweeps must be used.

Intraoperative sweeps recording and selection

Sweeps recording and selection is performed in a different graphical user interface (GUI) that can be opened from the main one. Here, the surgeon can record several tracked US images of the kidney into the computer's memory. Indeed, in chapter 4 and 5, we observed that multiple sweeps along the central longitudinal plane of the kidney with a wider coverage range improved the final registration. The record and save processes are triggered by an interface button. The recording is preceded by a preparation time of 5 sec. Since the *world origin* is linked to the catheter, which is positioned inside the kidney through a flexible ureterorenoscope, all sweeps are captured based on this internal EMT sensor. This allows to compensate for respiratory and internal movements during image acquisition. Each sweep is added into a list of recordings, enabling the selection of which ones to segment and use when creating the partial kidney model (Figure 6.5).

Intraoperative semi-automatic US segmentation

Here, a semi-automatic segmentation strategy is proposed to partially reconstruct the kidney surface, where a manual delineation followed by a tracking algorithm is applied. In the same GUI (Figure 6.5), the semi-automatic segmentation is initialized by manually segmenting one frame (freely chosen by the user). After confirming the delineation, the tracking algorithm (medical imaging tracking toolbox –

MITT [154]) can be triggered. The tracking settings can be changed through a specific GUI before running the tracking algorithm, where three main parameters can be set, *i.e.* size of the tracking neighborhood (*box radius*, mm), the influence of adjacent contour points on the tracking (*sigma length*, %), and the pre-processing image filtering (*sigma gaussian*, mm). GPU implementation can be used as well. Depending on the image size and number of frames, the run-time of the tracking algorithm varies between milliseconds to seconds. After running the tracking algorithm, it is possible to visualize, eliminate and correct the contours in all frames (if necessary), including propagating this correction to subsequent frames by running the tracking algorithm again. The abovementioned strategy can be performed in all recorded sweeps.

Intraoperative point set registration

After performing the segmentation, the surgeon can choose, from the list of recordings, which sweeps can be used to partially reconstruct the kidney. Then, when the registration is activated, the partial kidney model is built by merging the contours, $^{US}\boldsymbol{p}_{us}$, which were previously transformed using the transformation matrix from US image to catheter associated to each tracked image ($^{C}\mathbf{T}_{US} = {}^{C}\mathbf{T}_{P}\ {}^{P}\mathbf{T}_{US}$, where $^{P}\mathbf{T}_{US}$ is the transformation from US image to probe's sensor, *i.e.* the calibration matrix, and, $^{C}\mathbf{T}_{P}$, from probe's sensor to catheter updated in real-time). As result of this step, the contours are given with respect to the catheter, $^{C}\boldsymbol{p}_{us}$.

Subsequently, the CT models can be uploaded and pre-aligned with the EMT system based on both patient and tracker's orientation in the operating room. Six pre-configured transformations from CT images to tracker, $^{Tr}\mathbf{T}_{CT}$, are available (Figure 6.6).

Before computing the registration transformation between CT and US kidney models ($\mathbf{T}_{Reg}$), a fixed transformation from CT models to the catheter, $^{C}\mathbf{T}_{CT}$, is initially calculated to place the CT models in the same coordinate system of the partial US model:

$$^{C}\mathbf{T}_{CT} = {}^{C}\mathbf{T}_{Tr}\ {}^{Tr}\mathbf{T}_{CT} \tag{6.1}$$

where $^{C}\mathbf{T}_{Tr}$ is a transformation from tracker to catheter. After applying this transformation, the CT models are given with respect to the catheter, $^{C}\boldsymbol{p}_{ct}$, as well.

Then, the CT and partial US kidney models are registered using a point set registration algorithm, specifically the coherent point drift method (CPD) [180]. Indeed, the registration algorithm computes the transformation, $\mathbf{T}_{Reg}$, from CT model, $^{C}\boldsymbol{p}_{ct}$, to US model, $^{C}\boldsymbol{p}_{us}$, ultimately fusing the preoperative data
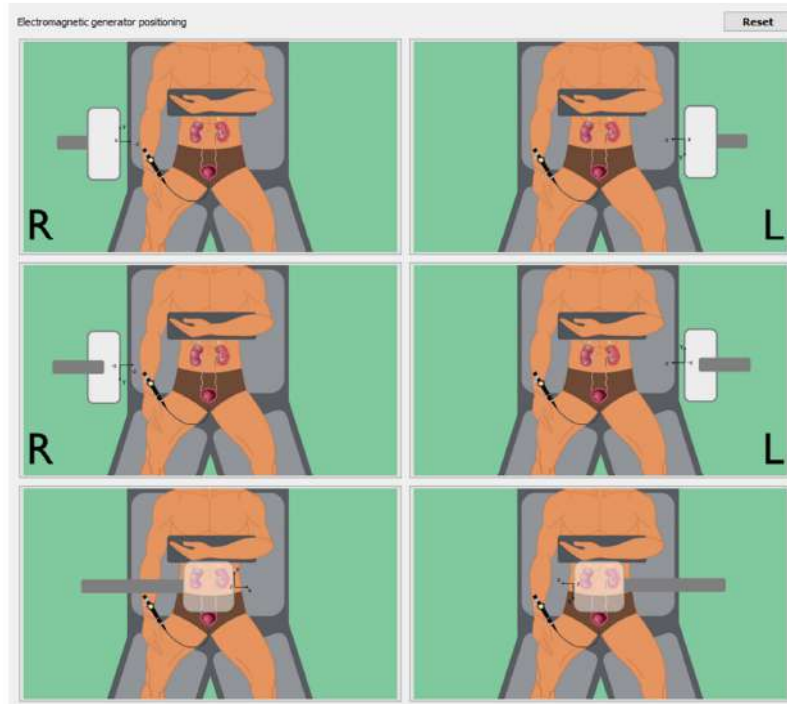
Figure 6.6 – Six pre-configured transformations to pre-align CT data and EMT tracker before final registration.

to the intraoperative stream. The transformation, $\mathbf{T}_{Reg}$, updates the position of CT models relatively to catheter, as follows:

$$^{C}\mathbf{T}_{CT}^{*} = \mathbf{T}_{Reg} \ ^{C}\mathbf{T}_{Tr} \ ^{Tr}\mathbf{T}_{CT} \qquad\qquad (6.2)$$

Real-time surgical navigation

When the registration process is completed, the surgical navigation is activated (Figure 6.7). Since all information is register to the catheter (which is inside the kidney), the preoperative registered data, $^{C}\boldsymbol{p}_{ct}$, moves with the catheter, following the intra-abdominal movements.

During navigation, if the position of the catheter relative to the patient body does not change, patient or tracker repositioning are possible without losing the registration.

Similarly, if required, one may also enable the catheter repositioning after registration, but neither patient nor tracker movements must occur while doing it. To this end, one may momentarily fix the registered data to the tracker, rather than the catheter, using $^{Tr}\mathbf{T}_{C}$ (which represents the tracker pose with respect to the catheter at the instant of unfixing), and revert this operation upon finishing to reposition the catheter.

104

These operations of relocating the registration data between parts of the EMT system without compromising the image fusion are only possible if an EMT sensor with six degrees-of-freedom is used for the catheter.

Furthermore, the navigation system is composed by three guidance views which are combined in one GUI. These views can be used individually or together (Figure 6.7). Each one is described as follows.

US image overlaid with needle projections and registered data

In this guidance view (Figure 6.7-A), the surgeon is capable to visualize in real-time the projections, entry point and contours of the needle, the catheter tip, and the contours over the US images from the registered preoperative CT models.

3D virtual environment

The 3D virtual environment displays in real-time the pose of the tracked US images, 3D models of needle and catheter tip, registered preoperative CT models and intraoperative partial US kidney model,
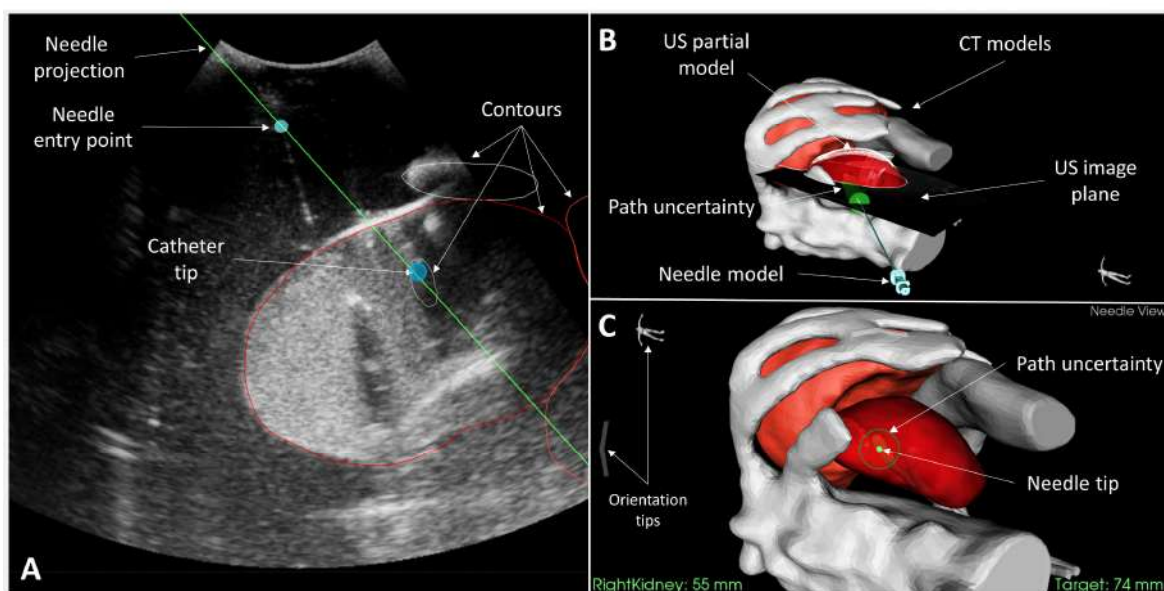
Figure 6.7 – GUI for surgical navigation.
The environment presents three guidance views which are updated in real-time: (A) Left: US image overlaid with needle projections and entry point, catheter tip, and contours from registered data. (B) Top-Right: The 3D virtual environment with registered CT models and surgical instruments. US partial model can be visualized as well. (C) Bottom right: The puncture view focused on the needle tip. Path uncertainty is displayed according to a defined tolerance. Different colors, distances information and orientation tips aid percutaneous renal access.

as well as the trajectory of the needle (Figure 6.7-B). If necessary, the virtual environment can be rotated, panned, or zoomed to improve visualization.

Puncture view (focused on the needle tip)

The third view presents a 3D visualization focused on the needle tip (Figure 6.7-C). The idea of this view is to use a sight to visually assist the puncture. The sight will help line up the needle and the catheter tip, so that the former may reach the latter easily. A sight tolerance is virtually defined around the catheter (Figure 6.8-A).

To measure if the needle is pointing to the catheter, the distance between the catheter and the needle projection line, d_0, is compute as follows:
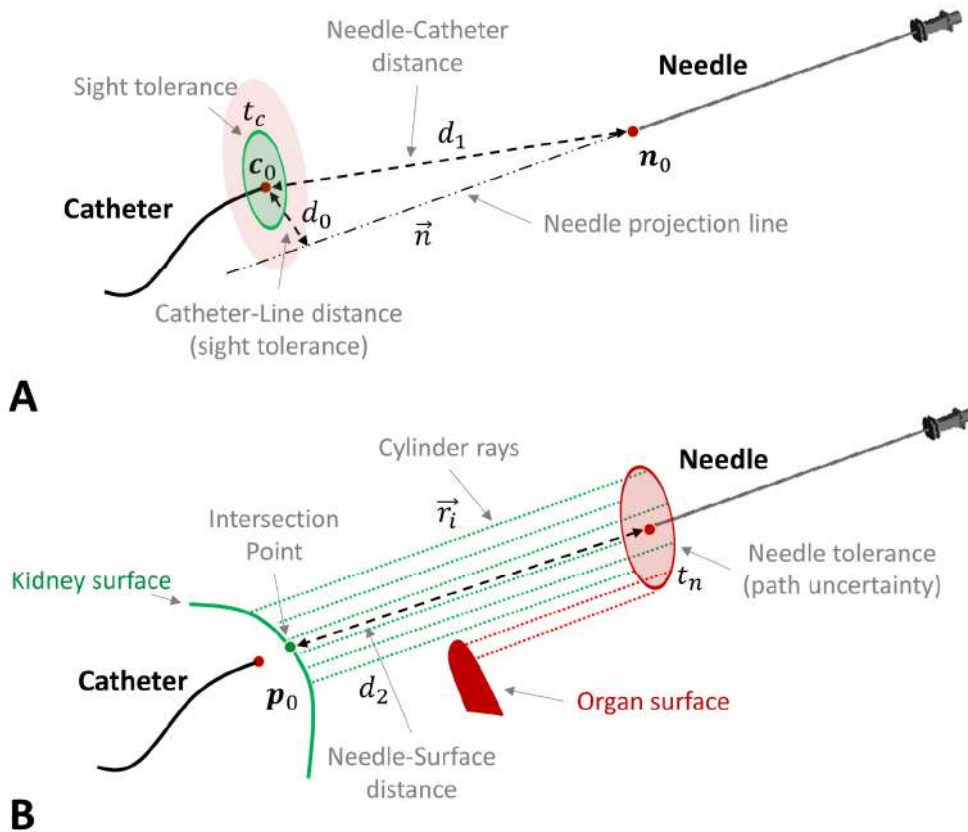
Figure 6.8 – Illustration of principles under puncture view (focused on the needle tip).
(A) Estimation of the catheter-line distance, d_0, to specify if the needle trajectory is lined up with the catheter according to the sight tolerance, t_c. If $d_0 < t_c$, the needle trajectory is lined up. Moreover, Euclidean distance between needle and catheter, d_1, is also computed. (B) The needle tolerance, t_c, defines the path uncertainty, i.e. the cylinder diameter. Cylinder' rays, $\vec{r}_i$, are used to inspect possible interactions with organs along the needle trajectory. In this example, one organ (other than kidney, in red) is within the needle tolerance and the trajectory is considered unsafe. The cylinder's color represents the puncture safeness (red and green for unsafe and safe, respectively). The needle-surface distance, d_2, is also computed, *i.e.* the distance from the needle tip until an intersection point, p_0, in an organ surface.

$$d_0 = \frac{\|\vec{n} \times (\boldsymbol{n}_0 - \boldsymbol{c}_0)\|_2}{\|\vec{n}\|_2} \tag{6.3}$$

where $\times$ denotes the cross product, $\| \quad \|_2$ the Euclidean norm, $\vec{n}$ the needle vector, $\boldsymbol{n}_0$ the position of the EMT needle, and $\boldsymbol{c}_0$ the position of the EMT catheter. If the distance, d_0, is lower than the defined sight tolerance, t_c (default value: 3 mm), the needle is considered accurately pointed towards the catheter. During the procedure, guidance messages are used to alert the surgeon. If catheter and needle are lined up, the green color is used, if not, the red color. Moreover, yellow color is used to represent when the user is pointing the needle to the kidney but not correctly aligned with the catheter. Moreover, white arrows on the sides of the window indicate the required needle repositioning to point to the catheter position. This visual feedback is provided by changing the arrows' opacity value:

$$op_k = \tanh(\frac{d_0}{t_c})|v_j| \tag{6.4}$$

where $k = 1, \dots, 4$ represents each arrow, the $\tanh$ is the hyperbolic tangent function, and v_j is a coordinate of $|\vec{v}| = [v_x, v_y]$ which is a normalized vector that defines the correction of the needle in x and y according to image plane generated based on the needle tip, $\boldsymbol{n}_0$, and the normal vector of needle, $\vec{n}$. To display the needle movements on the camera according to real needle movements during puncture (*i.e.* replicate up, down, right, and left movements), a transformation was applied to align the camera up-vector with the operating room (OR) up-vector, which is obtained by the reference sensor attached to the surgical table. Moreover, a body reference is also displayed (Figure 6.7-C, top-left corner) which is aligned according to the intraoperative registration. This provides information about the body's pose in the OR and the camera orientation is updated according to the needle direction as well.

The Euclidean distance between the needle and catheter, $d_1 = \|\boldsymbol{n}_0 - \boldsymbol{c_0}\|_2$, is calculated and displayed on the interface (Figure 6.7-C, bottom right corner). Moreover, the intersection point between the needle projection and organs surfaces, as well as the distance between it and the needle tip, are also computed based on ray tracing [193] (Figure 6.8-B), being the intersection distance, $d_2 = \|\boldsymbol{n}_0 - \boldsymbol{p_0}\|_2$, displayed on the interface as well (Figure 6.7-C, bottom left corner).

The path uncertainty is also shown by expanding the needle diameter which creates a virtual cylinder (Figure 6.8-B), that symbolizes "safe" or "unsafe" puncture paths. Thus, if the rays, $\vec{r_i}$, representing the cylinder boundaries virtually intersect a surface from an organ other than the kidney, the path is considered "unsafe". By default, we set the uncertainty tolerance, t_n, to approximately two times
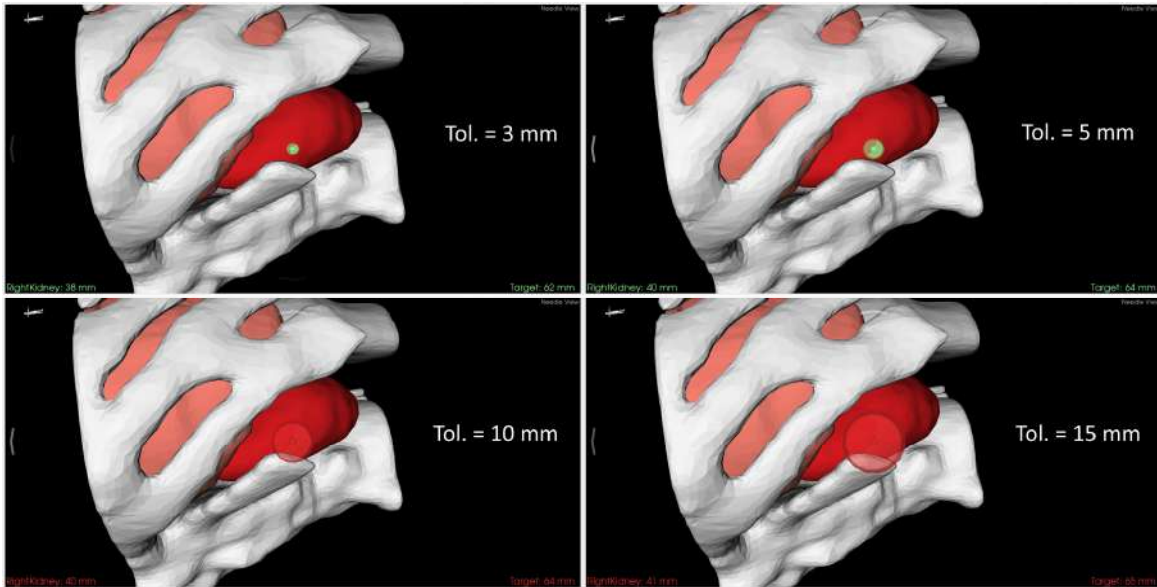
Figure 6.9 – Different tolerances to define path uncertainty.
The path uncertainty is shown by expanding the needle diameter according to pre-defined tolerances. This expansion creates a virtual cylinder that symbolizes "safe" or "unsafe" puncture paths. If the cylinder touches organs, except for the kidney, the path is considered "unsafe". Green color means a "safe" path, and red an "unsafe" one.

the target registration error computed in chapter 5, *i.e.* t_n= 10 mm. The uncertainty information is accompanied by visual information as color code (green and yellow – safe; red – unsafe), blinking strategies, and text messages to provide feedback. The uncertainty tolerance can be manually selected by the surgeon to reduce possible interaction with organs to a minimum (Figure 6.9).

Thus, the *needle view* shows a fixed dot on the center of the GUI representing the needle tip. It displays a puncture view using the tracked needle tip as the focal point. Each needle movement redefines the displayed image, giving the perception that we are looking from the needle tip. This will give visual information if any organ is on the path, and if the needle is correctly pointing to the catheter position.

6.3. Experiments

Experiments were performed using an abdominal phantom model specifically designed and built to assess the proposed system. Made of tissue mimicking material, this phantom enables CT and US imaging (Figure 6.10). For detailed information, please consult appendix A (section 6.7.1). The following section explains the assessment methodology used.
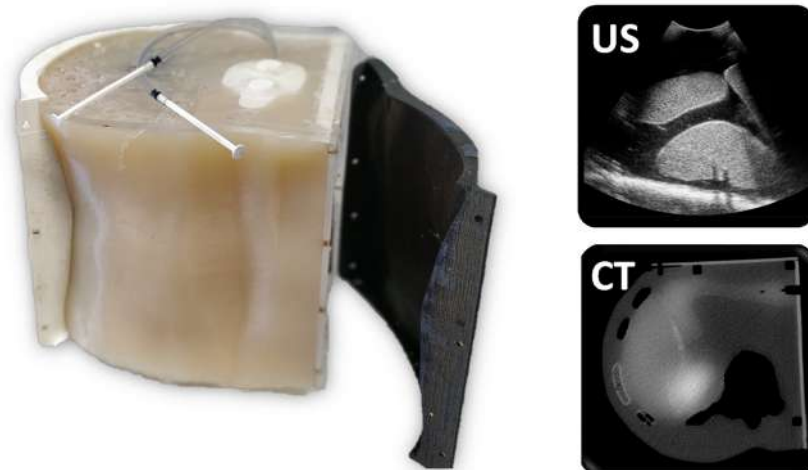
Figure 6.10 – Abdominal phantom model specifically designed for this assessment.

6.3.1. Assessment methodology

Workflow

Experiments were restricted to needle navigation in PRA. The assessment was carried out considering three tests comparing three EMT-based solutions with different aiding levels. Thus, three solutions were implemented in the software whose features were changed according to the solution under evaluation.

The three surgical solutions consisted of:

- Solution 1, henceforward known as **NAV**$_{EMT}$, is based on the original strategy proposed by Rodrigues *et al.* [45]. Here, a catheter is positioned inside the renal calyx through ureteroscopy. Puncture is supported using a puncture view that displays the tips of the needle and catheter with distance information provided by EMT sensors (Figure 6.11). The center was focused on the catheter tip (named target view and replicating [45]). To reach the catheter, the user must orient the needle from the skin using a trajectory that will allow reaching the target. For that, the user must overlap the needle tip (moving sphere) with the catheter tip (fixed sphere). Moreover, preoperative CT data and intraoperative US images are provided for planning and supporting the puncture, respectively, if asked by the participant.

- *Solution 2,* henceforward known as **NAV**$_{EMT-US}$, is similar to the previous one but integrates ultrasonography. This allows to project the needle trajectory, needle entrance point, and
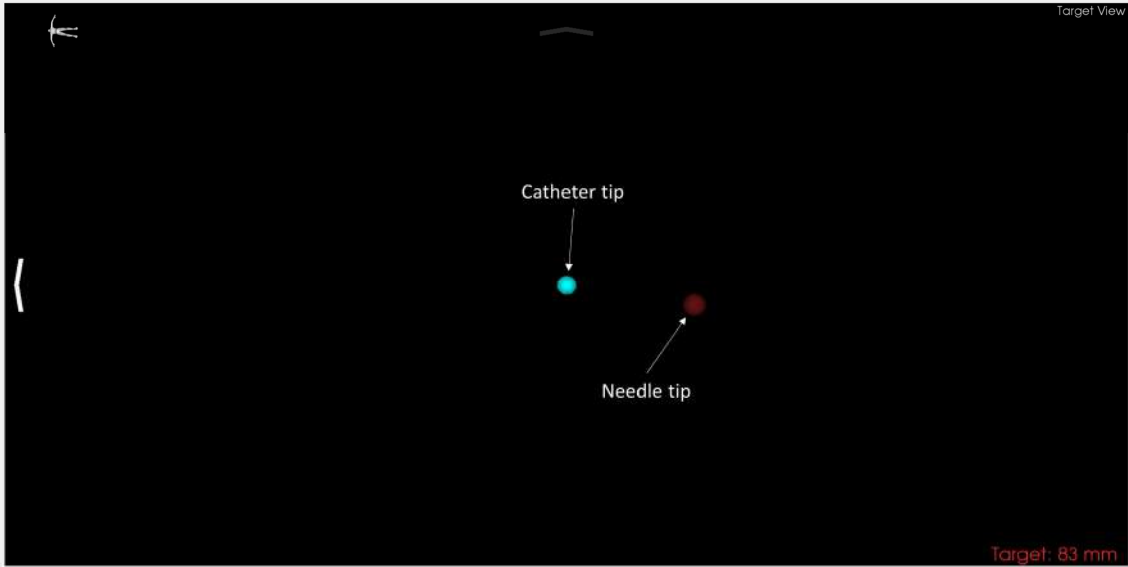
Figure 6.11 – Information provided using NAV$_{EMT}$.
This view provides only the needle and catheter tips' position, some guidance suggestions (white arrows on the sides), and distance information between needle and catheter. The catheter tip is fixed on the center of the image while the needle tip must be reoriented to the center.

catheter position over the US images. Here, puncture is supported by two windows, one containing ultrasound images overlapped with needle and catheter information, while the puncture view is equal to **NAV$_{EMT}$** (Figure 6.12). To reach the catheter, the user must image the puncture site with the tracked US probe. The user can use the US image to select a safe window to puncture by changing the US probe and needle positions. At the
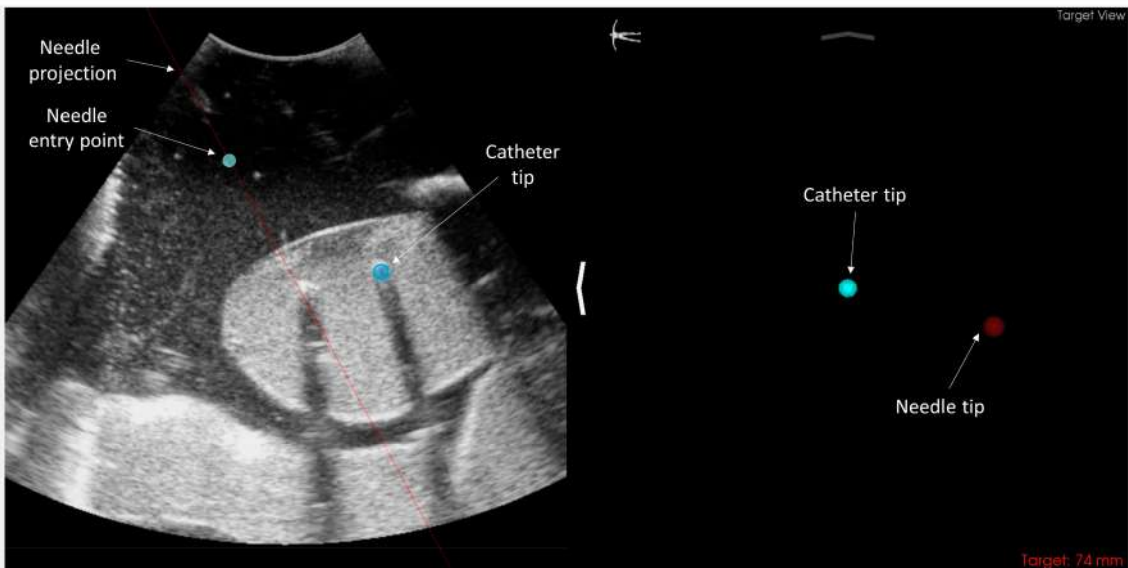
Figure 6.12 – Information provided using NAV$_{EMT-US}$.
The US image is integrated with the EMT system, and needle projection, needle entry point and catheter tip can be displayed over the US images. The puncture view is the same as in NAV$_{EMT}$ (see caption of Figure 6.11).

110

same time, the user must monitor the needle projection, entry point and the catheter tip over the US images. Besides, the user can also overlap the needle tip (moving sphere) with the catheter tip (fixed sphere) in the second window.

- *Solution 3*, henceforward known as **NAV**$_{EMT-VR}$, represents the proposed strategy, where 3D anatomical data aids the puncture. Here, three guidance views support the PRA, as detailly described in section 6.2.4 – *Real-time surgical navigation* (please consult Figure 6.7). The user must orient the needle from the skin based on the registered data presented on the interface. Specifically, the user must point the needle tip (fixed sphere on center) to the kidney surface and target the catheter tip within the calyx, while simultaneously avoiding the overlap between needle trajectory and other organs (to avoid injuries). In addition, the user may also rely on the images provided by the tracked US probe, reorienting the needle based on its projection over the US image or by interpreting the image and the displayed organs' contours.

The three tests (Figure 6.13) consist of:

- *Test 1*, the participant was asked to puncture the middle calyx after a flexible ureteroscope was positioned inside with an EMT catheter.
- *Test 2*, the participant was asked to puncture the lower calyx. However, the flexible ureteroscope with an EMT sensor was positioned in the middle calyx. This test simulated the potential obstruction of the lower calyx, precluding the positioning of the flexible ureteroscope (and the target) in it.
- *Test 3,* the participant was asked to puncture the middle calyx from a difficult tract, *i.e.* a narrow tract close to adjacent organs. This test allows to simulate the need to puncture from an uncommon tract, which can happen in clinical practice.

Each solution was explained to the participants and they were able to get familiar for a few minutes before performing the tests.

Preoperative data acquisition and preparation

The CT images were acquired using a Philips Brilliance 64 CT scanner (Philips Healthcare, Best, The Netherlands). The X-ray tube current and peak voltage were set to 30 mA and 120 kV, respectively.
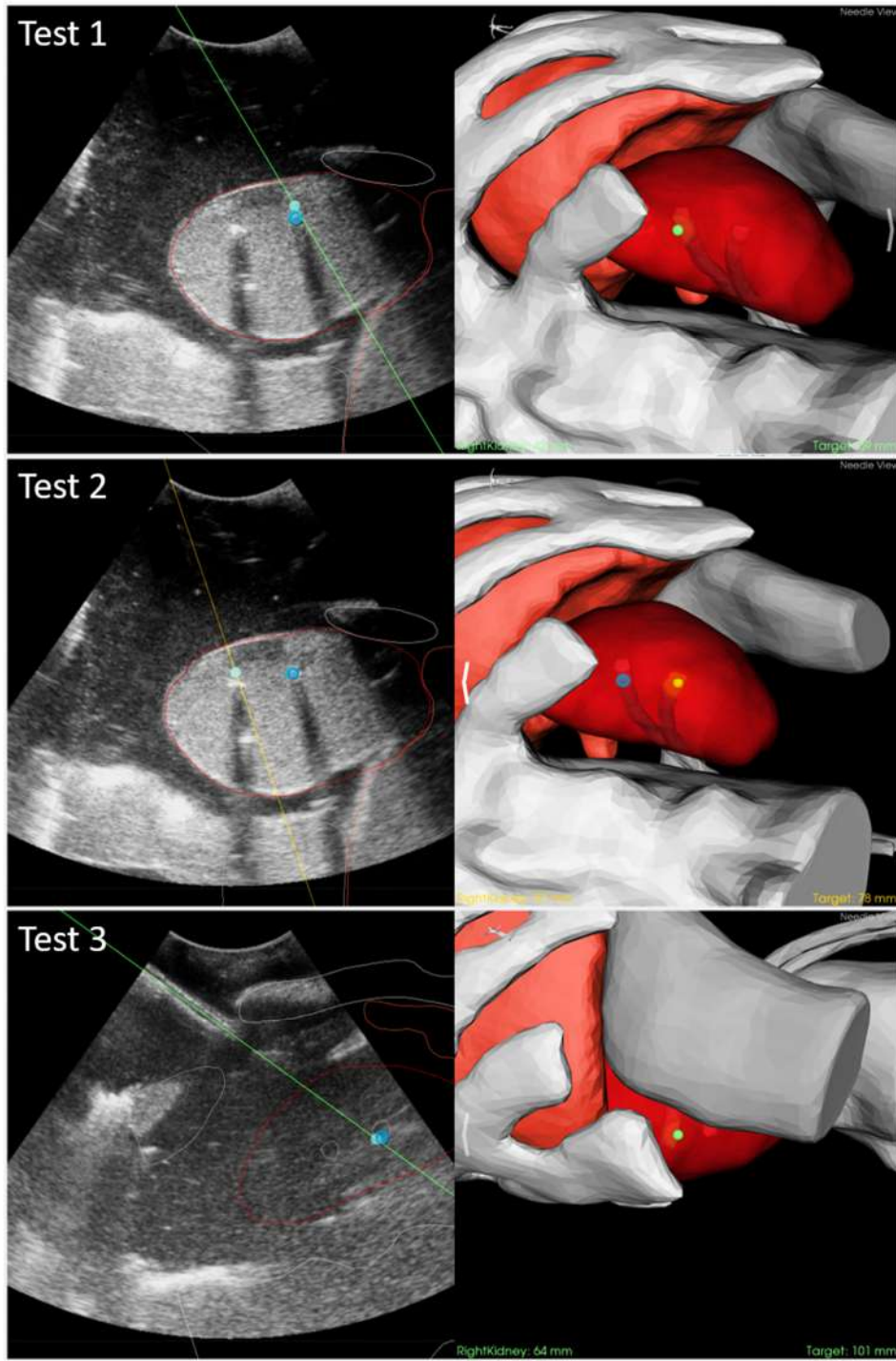
Figure 6.13 – Visual depiction of the proposed experimental scenarios.
Three different tests were proposed to simulate three different puncture scenarios. *Test 1*: simple puncture to middle calyx; *Test 2*: puncture lower calyx without no catheter support (simulates lower calyx obstruction); and *Test 3:* complex puncture to middle calyx (simulates difficult anatomies).

The abdomen protocol was selected. On average, the CT volume size was $512 \times 512 \times 200$ with a voxel resolution of $0.652 \times 0.652 \times 1.50$ mm.

Segmented 3D surfaces were created for each organ, namely kidney, liver, colon, ribs, and spine, using the strategy present in appendix A (section 6.7.1 – *3D segmentation and surface processing*). Since
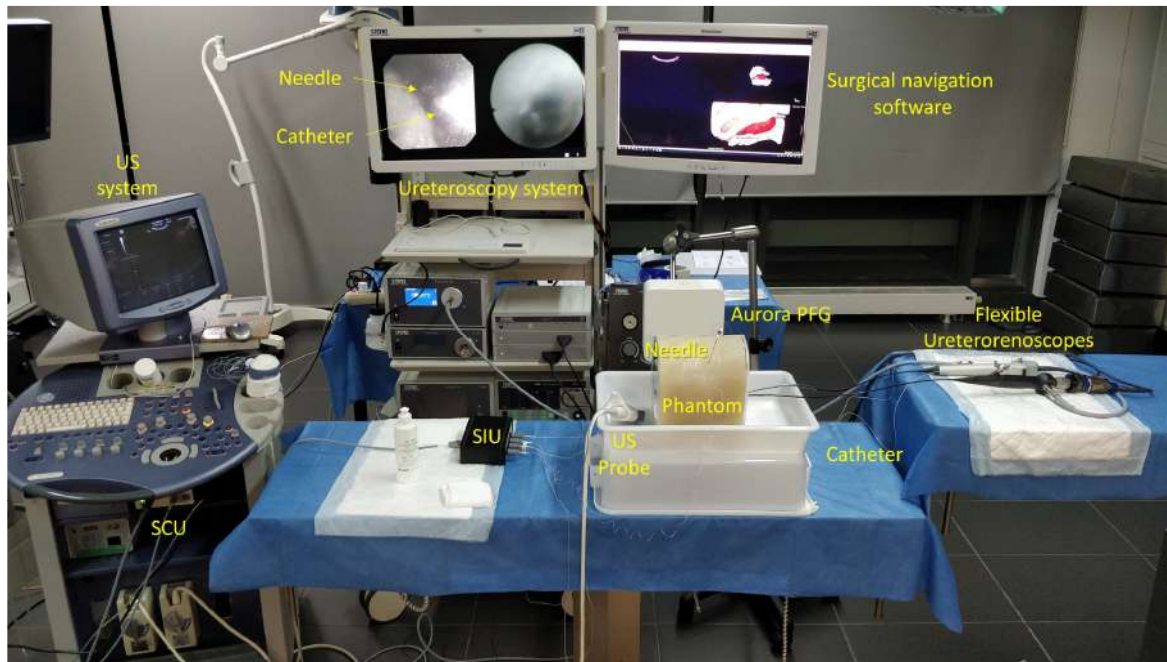
Figure 6.14 – Experimental setup mounted in a training surgical room.
US - Ultrasound; SIU – sensor interface unit; SCU – system control unit; PFG - Planar field generator.

no multi-atlas database is available for the abdominal phantom, we were not able to apply the proposed MAS strategy (section 6.2.3).

Experimental setup

The experiments were performed in the training operating room at Life and Health Sciences Research Institute (ICVS, School of Medicine, University of Minho, Braga, Portugal), giving similar conditions as a surgical environment. An aluminum surgical stretcher with an electromechanical system was used. The experimental setup consisted of (see Figure 6.14):

- The US system, *i.e.* the Voluson 730 Pro V machine (GE Healthcare, Milwaukee, Wisconsin, USA) with a 2D convex abdominal probe (AB 2-7), which achieved a pixel resolution of 0.366×0.366 mm. The presets for imaging the kidney were used. The Epiphan's video grabber (DVI2USB 3.0, Epiphan Systems Inc., Palo Alto, California, USA) transmitted the monitor image to the computer.

- Two flexible ureterorenoscopes, *i.e.* the Flex-X^c and the Flex-X^{2s} (Karl Storz), were positioned in the middle and lower calyxes, respectively, and connected to a Karl Storz Tower to display internal images of both calyxes.

- The electromagnetic tracking system, *i.e.* the Aurora® Planar Field Generator (PFG) from NDI (Northern Digital, Inc., Waterloo, Ontario, Canada). One electromagnetic sensor, the

113

Aurora® 5-DOF Flex Tube (1.0 mm diameter), was used as catheter being inserted on the working channel of the Flex-X^c. One Aurora® 5-DOF Needle (18G/150 mm, Chiba) was used as needle. One Aurora® 6-DOF Cable tool (2.5 mm diameter) was coupled to the US probe. One Aurora® 6-DOF Reference (25 mm Disc) was positioned over the table. Before experiments, probe calibration was performed (see details in chapter 5).

- A computer running Windows 10 (64-bit) with an Intel® Core™ i7 CPU at 2.8 GHz, with 16 GB of RAM, a NVIDIA Quadro® K2100M with 2 GB VRAM and a Samsung SSD 850 EVO. The software was displayed on a specific surgical monitor, *i.e.* Karl Storz WideView™ HD.

US and CT data were fused before the experiments using the proposed strategy.

Outcome measurements

The following parameters were obtained to assess the performance of the three solutions in each test:

- Puncture success: confirmed when the tip of the needle is visualized in the ureteroscope images, which are positioned inside the calyxes (Yes/No).
- Puncture time: time needed to perform a successful puncture from the skin until the kidney target site after defining the needle trajectory (in seconds).
- Number of attempts: number of punctures until reaching the kidney target site successfully or until reaching the maximum puncture time allowed (see below).
- Number of collisions: how many times the needle touched or punctured organs instead of the kidney.
- Confidence level: the participants were asked after executing each technique to rate their confidence level in each test (1 – Not confident; 5 – Totally confident).
- Tract trajectory: upon finishing, the participants could carefully visualize the needle trajectory in the 3D environment and were asked if they would change the obtained tract (Yes/No).

Each participant was allowed a maximum of 4 min to complete the procedure. Failed puncture was defined by an incapacity to reach the target within the 4 min period, if the puncture did not accurately reach the target upon validation, or if the needle punctures a nearby organ. To avoid possible bias, the order of techniques assessment was defined randomly per participant.

After performing the tests, the participants answered a questionnaire. Please consult appendix B (section 6.7.2) for more details. In short, the questionnaire asks the participants: to choose, among a set of adjectives, five that describe each solution; and to order the three solutions (1 – Best; 3 –Worst) according to specific characteristics. Moreover, some open-ended questions about advantages and disadvantages of the proposed solution were made.

All statistical tests were conducted using MATLAB® (version R2020a, The Mathworks Inc., Natick, MA). The assumption of normality was assessed for all variables, and based on the results, parametric or nonparametric tests were applied accordingly. The effect size and statistical significance were reported. All statistics were considered significant if $p < 0.05$.

6.4. Results

Eleven participants attempted the experiments. Senior urologists (n=3, who performed more than 150 percutaneous nephrolithotomy or percutaneous nephrostomy accesses), senior-level residents (n=3, who performed at least 10 percutaneous nephrolithotomy or percutaneous nephrostomy accesses), junior-level residents (n = 3, who had not yet performed accesses as a primary surgeon), and specialists from a different medical field but with puncture experience (n = 2) integrated the cohort. Differences between groups were not calculated since the sample size was low. Moreover, it was not the focus of the work.

Figure 6.15 – Participant successfully performing renal access using the proposed surgical navigation system, *i.e.* the NAV$_{EMT-VR}$.

Table 6.1 – Measurements obtained in *test 1*.

A simple puncture was performed to the middle calyx. Statistical significance and effect sizes (W = Kendall's W, and eta-squared η^2) are shown per measurement (N = 11).

	1. NAV$_{EMT}$	2. NAV$_{EMT-US}$	3. NAV$_{EMT-VR}$	STATISTICAL TEST
PUNCTURE SUCCESS	11/11	11/11	11/11	$p > .999$; $\eta^2 = 0.000$ [c]
PUNCTURE TIME (s) [A]	25 (11)	24 (32)	20 (11)	$p = .643$; $W = 0.040$ [D]
NUMB. OF ATTEMPTS	11/11	11/11	11/11	$p > .999$; $W = 0.000$ [D]
NUMB. OF COLLISIONS [B]	0	0	0	$p > .999$; $W = 0.000$ [D]
CONFIDENCE LEVEL (1-5) [A]	4 (2)	4 (1)	5 (0)	$p = .010$; $W = 0.417$; 1-3: $p = .043$ [D]
CHANGE FINAL TRACT	0/11	1/11	1/11	$p = .368$; $\eta^2 = 0.091$ [c]

[A] *Median and interquartile range.* [B] *Sum of collisions of all participants.*
[C] *Related-Samples Cochran's Q Test.* [D] *Related-Samples Friedman's Test.*

Each participant was challenged to perform 9 renal accesses (Figure 6.15), *i.e.* 3 different tests using 3 different solutions. Four abdominal phantoms were successfully produced. Each phantom was used only by 2-3 participants to preserve the echogenic conditions during experiments.

6.4.1. Solutions assessment

Test 1

The results of *test 1* are summarized in Table 6.1. All participants completed the renal punctures with all strategies. Indeed, on average, puncture times for all techniques were performed equal to or less than 25 seconds.

No statistical differences were observed in puncture success, puncture time, number of attempts, number of collisions, and willingness to change the final tract between different techniques. However, participants had a higher confidence level with **NAV$_{EMT-VR}$** (on average the score was 5) when compared to other solutions, being these differences statistically significant ($p = .010$) and with a high effect size ($W = 0.417$). After multiple comparisons correction, differences between **NAV$_{EMT-VR}$** and **NAV$_{EMT}$** were still significant ($p = .043$).

Test 2

Table 6.3 summarizes the results obtained in *test 2*. In this experiment, all participants were able to successfully puncture the calyx using **NAV$_{EMT-VR}$**, which was not accomplished with others. In fact, the puncture success was achieved only by seven participants with **NAV$_{EMT}$** and eight participants with **NAV$_{EMT-US}$**. Despite not being significant, the effect size indicates that differences are large ($\eta^2 = 0.197$).

Table 6.3 – Measurements obtained in *test 2.*
A puncture was performed to the lower calyx with the EMT catheter positioned in the middle calyx (simulating an obstructed calyx). Statistical significance and effect sizes (W = Kendall's W, eta-squared η^2) are shown per measurement (n = 11).

	1. NAV$_{EMT}$	2. NAV$_{EMT-US}$	3. NAV$_{EMT-VR}$	STATISTICAL TEST
PUNCTURE SUCCESS	7/11	8/11	11/11	$p = 0.115$; $\eta^2 = 0.197$ [c]
PUNCTURE TIME (s) [a]	47 (135)	114 (133)	34 (38)	$p = .020$; $W = 0.355$; 2-3: $p = .017$ [b]
NUMB. OF ATTEMPTS	13/11	15/11	12/11	$p = .232$; $W = 0.133$ [b]
NUMB. OF COLLISIONS [b]	1	1	0	$p = .368$; $W = 0.091$ [b]
CONFIDENCE LEVEL (1-5) [a]	3 (2)	3 (1)	4 (1)	$p < .001$; $W = 0.814$; 1-3, 2-3: $p < .01$ [b]
CHANGE FINAL TRACT	4/7	2/8	0/11	$p < .01$; $\eta^2 = 0.445$; 1-3: $p < .01$ [c]

[a] *Median and interquartile range.* [b] *Sum of collisions of all participants.*
[c] *Related-Samples Cochran's Q Test.* [b] *Related-Samples Friedman's Test.*

Table 6.2 – Measurements obtained in *test 3*
A puncture was performed to the middle calyx using a complex path (with nearby organs). Statistical significance and effect sizes (W = Kendall's W) are shown per measurement (n = 11).

	1. NAV$_{EMT}$	2. NAV$_{EMT-US}$	3. NAV$_{EMT-VR}$	STATISTICAL TEST
PUNCTURE SUCCESS	9/11	10/11	11/11	$p = .368$; $\eta^2 = 0.091$ [c]
PUNCTURE TIME (s) [a]	59 (100)	70 (63)	31 (23)	$p = .001$; $W = 0.662$; 2-3: $p = .001$ [b]
NUMB. OF ATTEMPTS	14/11	16/11	12/11	$p = .144$; $W = 0.176$ [b]
NUMB. OF COLLISIONS [b]	3	5	1	$p = .444$; $W = 0.074$ [b]
CONFIDENCE LEVEL (1-5) [a]	3 (2)	3 (2)	4 (1)	$p < .001$; $W = 0.725$; 1-3: $p = .001$ [b]
CHANGE FINAL TRACT	1/9	2/10	1/11	$p = .449$; $\eta^2 = 0.073$ [c]

[a] *Median and interquartile range.* [b] *Sum of collisions of all participants.*
[c] *Related-Samples Cochran's Q Test.* [b] *Related-Samples Friedman's Test.*

The puncture time was lower for **NAV$_{EMT-VR}$**, where participants reached the target in 34 seconds, on average. The participants needed more time to perform the same task with other solutions ($p = .020$), where the **NAV$_{EMT-US}$** was the most time-consuming ($p = .017$). In addition, more attempts to achieve the calyx and superior willingness to change the obtained tract after carefully analyze its final trajectory ($p < .01$) were observed in **NAV$_{EMT}$** and **NAV$_{EMT-US}$**.

NAV$_{EMT-VR}$ was rated once again as the strategy with the highest confidence level ($p < .001$). On average, the participants rated **NAV$_{EMT-VR}$** with 4, and other solutions with 3.

Test 3

Anew, all participants were able to successfully puncture the kidney based on **NAV$_{EMT-VR}$**, while two failed when using **NAV$_{EMT}$** and one failed with **NAV$_{EMT-US}$** (Table 6.2). Puncture with **NAV$_{EMT-VR}$** was, once again, less time-consuming than others ($p = .001$), with participants spending, on average, 31 sec. The
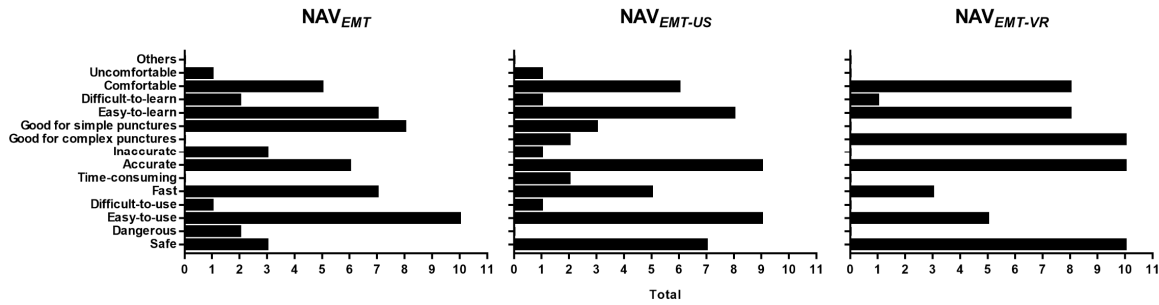
Figure 6.16 – Questionnaire results (adjectives).
The number of times each adjective was selected per solution. Each participant selected five adjectives to characterize each solution.

number of attempts and collisions during puncture was also higher for **NAV**$_{EMT}$ and **NAV**$_{EMT-US}$ compared to **NAV**$_{EMT-VR}$.

Similarly, the confidence level of **NAV**$_{EMT-VR}$ was superior for this test ($p < .001$).

6.4.2. Questionnaire

Figure 6.16 outlines the adjectives selected by participants for each solution. Considering the five most voted adjectives, **NAV**$_{EMT}$ was signaled as easy-to-use (score: 10), good for simple punctures (8), easy-to-learn (7), fast (7), and accurate (6). **NAV**$_{EMT-US}$ was marked as accurate (score: 9), easy-to-use (9), easy-to-learn (8), safe (7), and comfortable (6). Finally, **NAV**$_{EMT-VR}$ was defined as safe (score: 10), accurate (10), good for complex punctures (10), easy-to-learn (8), and comfortable (8).

Figure 6.17 reveals the results when participants were asked to order the strategies according to specific characteristics. In general, the **NAV**$_{EMT-VR}$ was considered the best in all. Indeed, all participants indicated that it was the safest, and the most appropriate to complex anatomies, to obstructed calyces, to obtain the optimal path and to improve the next surgical steps. Despite being rated as the easiest technique to learn (54.55%) and use (63.64%) by most participants, it is important to mention that the answers varied the most for these two characteristics.

6.5. Discussion

In this work, we present and validate in phantom models a new surgical navigation system for percutaneous renal access. This system was tested by medical doctors and compared against other solutions with distinct levels of assistance. The purpose of this study was to assess the impact that the proposed guidance solution has on safety during different clinical situations in PRA, and not to assess the
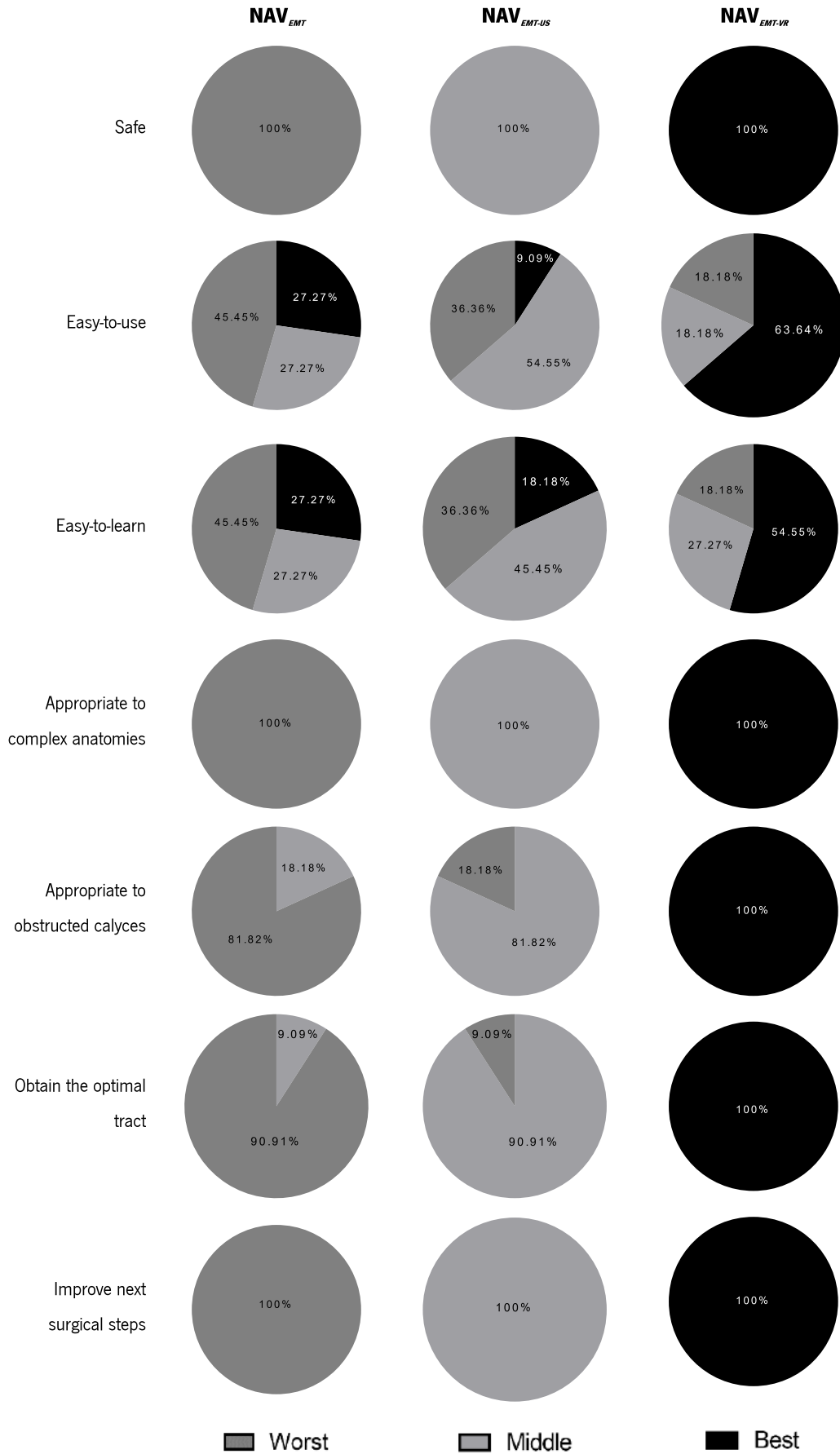
Figure 6.17 – Questionnaire results (ordering from worst to best for each feature).

total workflow of the proposed system. During these experiments, we were able to demonstrate the benefits of the proposed solution, which were confirmed by the positive feedback given by the medical doctors.

Looking closely to each solution, the **NAV**$_{EMT}$ suggested to be adequate for simple punctures, as it was demonstrated in *test 1*. Indeed, no differences to other techniques were observed for the puncture success, puncture time, number of attempts, number of collisions, and willingness to change the final tract. However, its confidence level was lower compared to the proposed one, *i.e.* **NAV**$_{EMT-VR}$, which was also observed in *tests 2* and *3*. Besides, it was observed that in more difficult scenarios, *i.e. test 2* and *test 3*, the performance of the participants decreased. Not all participants were able to successfully complete the PRA. Particularly, in *test 2*, only seven participants completed the task, and four of them considered changing the final tract. In this case, the decrease in performance seems to be related to the fact that the PRA was US-guided only, since the EMT system did not provide reliable information (as the EMT catheter was not inside the target calyx due to a simulated obstruction). This fact increases the need for a different type of aiding during PRA. In *test 3*, the puncture success rate increased because the EMT catheter is positioned inside the calyx; however, the number of collisions to the nearby organs was higher. Collisions were mainly against the ribs. Indeed, some participants mentioned that the lack of integration between different systems gives the feeling of insecurity during the puncture. This solution forces the surgeon to do a mental representation of the anatomy (supported by external US imaging) and join it with the needle trajectory during PRA. The feeling of insecurity is confirmed by the questionnaire results (Figure 6.16), with **NAV**$_{EMT}$ being classified as dangerous and inaccurate more times than any other solution. Moreover, comparatively to others, **NAV**$_{EMT}$ was considered by the participants as the less safe, less appropriate for complex anatomies, less appropriate to obstructed tract, less appropriate to obtain the optimal tract, and less capable to improve the next surgical steps (Figure 6.17). Most participants (45.45%) also considered it the least easy to learn or use. These opinions may be related with higher difficulties on performing more difficult tasks, *i.e. test 2* and *test 3*. Both situations require higher US-guidance skills. Indeed, in *test 2*, to accomplish the task successfully, the participant must rely on US guidance only, whereas, in *test 3,* ultrasonography was mandatory to select the safest path, with US image and needle guidance information being provided separately.

The **NAV**$_{EMT-US}$ improved the success rate slightly compared to **NAV**$_{EMT}$. However, the results suggest that users tended to spend more time during puncture and had a superior number of attempts with this technique in *tests 2* and *3*. This fact may be related with the attempt to simultaneously understand the image, as well as to position the catheter and the projection of the needle properly in the

image. Indeed, some participants mentioned that a needle support to attach to the US probe could be interesting to improve this solution. Moreover, the number of collisions was higher on *test 3*. As observed in **NAV**$_{EMT}$, most of the collisions using **NAV**$_{EMT-US}$ were associated with touching the ribs, however, one participant punctured the colon. Nevertheless, most participants considered this technique easy-to-learn and easy-to-use (Figure 6.17). Compared to **NAV**$_{EMT}$, it was also classified as safer, as well as more appropriate for complex anatomies, obstructed calyces, obtain the optimal tract and improve next surgical steps. This superior preference may be related to the fact that the participants were able to see more information integrated into the same environment.

Finally, the **NAV**$_{EMT-VR}$ demonstrated to be superior in all tests. The participants were able to accomplish punctures in all situations in less time that other techniques. Additionally, the proposed technique obtained the highest confidence level for all tests, demonstrating that participants felt safer during PRA. The fusion of preoperative CT data with intraoperative US data and the synergy with the EMT system brought significant improvements in confidence when executing this surgical step in more difficult scenarios. Indeed, in *test 2*, the participants were able to successfully target the lower calyx only based on the registered data, which can be promising in other clinical situations (*e.g.* percutaneous ablation). Similarly, in *test 3,* they were able to puncture the middle calyx using a difficult tract. Even though one collision was observed using the proposed technique, it was associated with a brief contact with a rib, with the trajectory being immediately corrected by the participant. The participants were generally satisfied with the obtained tract (Tables 6.1 to 6.3). Furthermore, most of them adjectivized the **NAV**$_{EMT-VR}$ as safe, accurate, good for complex punctures, comfortable, and easy-to-learn. Actually, in open-ended questions, the participants expressed opinions like: "*NAV$_{EMT-VR}$ is more safe and the surgeon can choose the best route for calyx*", "*NAV$_{EMT-VR}$ allows exact puncture location based on CT data*", "*NAV$_{EMT-VR}$ improves the feeling of safety*", "*NAV$_{EMT-VR}$ allows anatomical evaluation, total control, and safety*", "*NAV$_{EMT-VR}$ is the best technique for complex situations*", and "*NAV$_{EMT-VR}$ gives 3D understanding of the surrounding anatomy and may shorten the learning curve, as well as the length of the surgery*". One other participant mentioned *"the two 3D views give a real sensation of what is happening inside the abdomen"*. These opinions reinforce the idea that preoperative image data combined with the EMT system for performing PRA is beneficial*.*

When compared to **NAV**$_{EMT-US,}$ they mentioned that *"NAV$_{EMT-VR}$ is easier to use because the puncture based on ultrasonography needs experience and skills"*, *"the anatomy reconstruction in NAV$_{EMT-VR}$ improves the accuracy"*, and *"we do not need time to get familiar with NAV$_{EMT-VR,}$ which is not true for NAV$_{EMT-US}$"*. Oppossingly, some participants mentioned that "*due to many guidance information provided*

by NAV_{EMT-VR}, *it can be difficult to understand initially, although when learned it became simple and advantageous*". The lack of consensus in the learning process is also observed when the participants were asked to order the techniques as easy-to-learn (Figure 6.17). Just 54.45% of participants considered NAV_{EMT-VR} as the easiest technique to learn. Nevertheless, when put together, these results point to the fact that NAV_{EMT-VR} may present a short learning curve.

Technically, we presented in this work the main ideas of a new surgical navigation system and explained the main steps to use it in a surgical scenario. During the development process, we tried to mitigate and simplify the fusion step without substantially changing the current technique present by Lima *et al.* [80]. However, the participants mentioned as limitation "*the larger time required to prepare the setup*" compared to other techniques. This fact is true because the fusion process, despite fast, requires time to record sweeps, manual segmentation followed by image tracking, and registration, which can be higher if some refinement is required to improve fusion (*e.g.*, new sweeps recording, contours correction, and re-registration). However, the cost-benefit of spending more time with the setup of NAV_{EMT-VR} is still worth it in PRA. On the other hand, the potentially higher cost of the NAV_{EMT-VR} was also mentioned by some participants. Nonetheless, compared to NAV_{EMT} and NAV_{EMT-US}, the proposed system only adds one (or two, if one is added to the surgical table) EMT sensors. The EMT system can also be affected by external sources (*e.g.* ferromagnetic devices), which can affect visualization. Thus, the surgical setup must be carefully prepared.

Furthermore, the participants also mentioned that "NAV_{EMT-VR} *can be a source of errors if the fusion is not accurate*". Since the registration is anchored to the EMT sensor of the catheter, organ-tracking is possible which may significantly reduce the errors related to intra-abdominal movements. However, nearby organs to the kidney may present some misalignments if the body pose during surgery differs significantly from the one during CT acquisition. One suggestion to mitigate this problem is to replicate the fusion process done for the kidney to each nearby organ, but it could significantly increase the setup time. Another option would be to take advantage of automatic algorithms, like novel deep learning-based techniques, to segment and/or register all data. It would reduce the setup time while potentially improving image fusion accuracy. However, these techniques require a large amount of data from real clinical scenarios, which is challenging to gather and annotate.

Additionally, despite the interesting results, the abdominal phantom model used has limitations comparatively to an *in vivo* model. Indeed, differences on US images may improve their interpretation since phantoms images are echogenically simpler. This fact may improve the performance of less experienced users with US imaging. Moreover, no respiratory movements were simulated, limiting organ-

tracking assessment, and organs deformation was not present as well, which may not reveal the limitations of the proposed image fusion strategy. Thus, besides improving the image fusion strategy, future work may include animal studies to further test the proposed system in a closer-to-real situation before clinical trials. However, advanced imaging facilities with CT or MRI for animals would be essential.

Overall, the proposed system framework has the potential to grow and new modules can be added to improve PRA or even translate to other surgical interventions, like percutaneous ablations of renal tumors, and percutaneous access to anatomical zones close to the kidney, since the puncture is not limited only to reach the EMT catheter. The provided preoperative data can also reveal intraoperatively the renal calculus in percutaneous nephrolithotomy which may help surgeons performing the next surgical steps. Hence, studies must proceed to improve and expand the proposed system.

6.6. Conclusion

A new surgical navigation system for PRA was assessed in this work. Tested in phantoms by medical doctors, the results suggest a superior performance of the proposed solution, especially in complex situations. Besides, a superior confidence level and the positive feedback received support the idea that the fusion of preoperative CT data and intraoperative US data together with the EMT system can bring significant improvements to PRA.

The proposed system has the potential to assist in renal access during percutaneous nephrolithotomy and broaden to other surgical interventions.

6.7. Appendixes

6.7.1. Appendix A – Abdominal phantom model

The abdominal phantom was developed to mimic human tissue properties in CT and US imaging based on a realistic anatomy. The phantom was designed based on image segmentation of magnetic resonance imaging (MRI) data and computer-aided design (CAD). It was produced based on rapid prototyping and tissue mimicking materials.

Acquisition of the template

MRI data was acquired from a healthy subject using the Magnetom Avanto 1.5 T MRI scanner (Siemens Medical Solutions, Forchheim, Germany). For the structural acquisition, 64 images with a slice

thickness of 3 mm, a matrix of 288×216, and a pixel spacing of 1.319×1.319 mm were obtained with the subject laying on supine position. A 3D T1-weighted sequence was used.

3D segmentation and surface processing

The phantom was conceived using the right side of the abdominal cavity. Thus, the right kidney, liver, colon, ribs, and spine were manually segmented in the MRI data using an interactive segmentation framework, 3D Slicer software (version 4.10) [158]. The manual delineation relied on multiple 2D contours followed by 3D interpolation to obtain the final 3D surface of each organ.

Phantom design

The Geomagic software (3D Systems, Rock Hill, South Carolina, United States) was used to convert the previous surfaces into solid objects. Then, these solids were exported in step file format into a CAD software (SolidWorks, Dassault Systèmes SolidWorks Corporation, Waltham, Massachusetts, United States). Based on these solids, a specific phantom was designed including all technical details to easily assemble all components during the manufacturing process.

Thus, the base structure is composed by four acrylic plates with specific fittings and a support to improve fixation of these plates. One acrylic plane has one hole where it is possible to pour the tissue mimicking material. Part of the base structure mimics the skin contour of the posterior and lateral flank of the abdomen, which are the most common zones used to perform PRA.

Specific molds were designed from the negative imprint of the kidney, liver, and colon models from MRI (Figure 6.18). Ribs and spine do not required molds and were joined in one piece.

Phantom production

At this point, the designed molds, ribs, spine, and plates support, as well as specific dowels and coverings, were converted to gcode file format using the Cura software (Ultimaker B.V., Geldermalsen, The Netherlands) and then 3D printed in polylactic acid (PLA) material using an Ultimaker II (Ultimaker B.V., Geldermalsen, The Netherlands). This printer uses the fused deposition modelling technique, with a printing resolution of ± 0.2 mm. Moreover, two plastic tubes with 6 mm of diameter were added into the kidney mold to mimic ureter and calyces, enabling two different PRA assessments. A wire was used to position the tubes inside the kidney during molding.
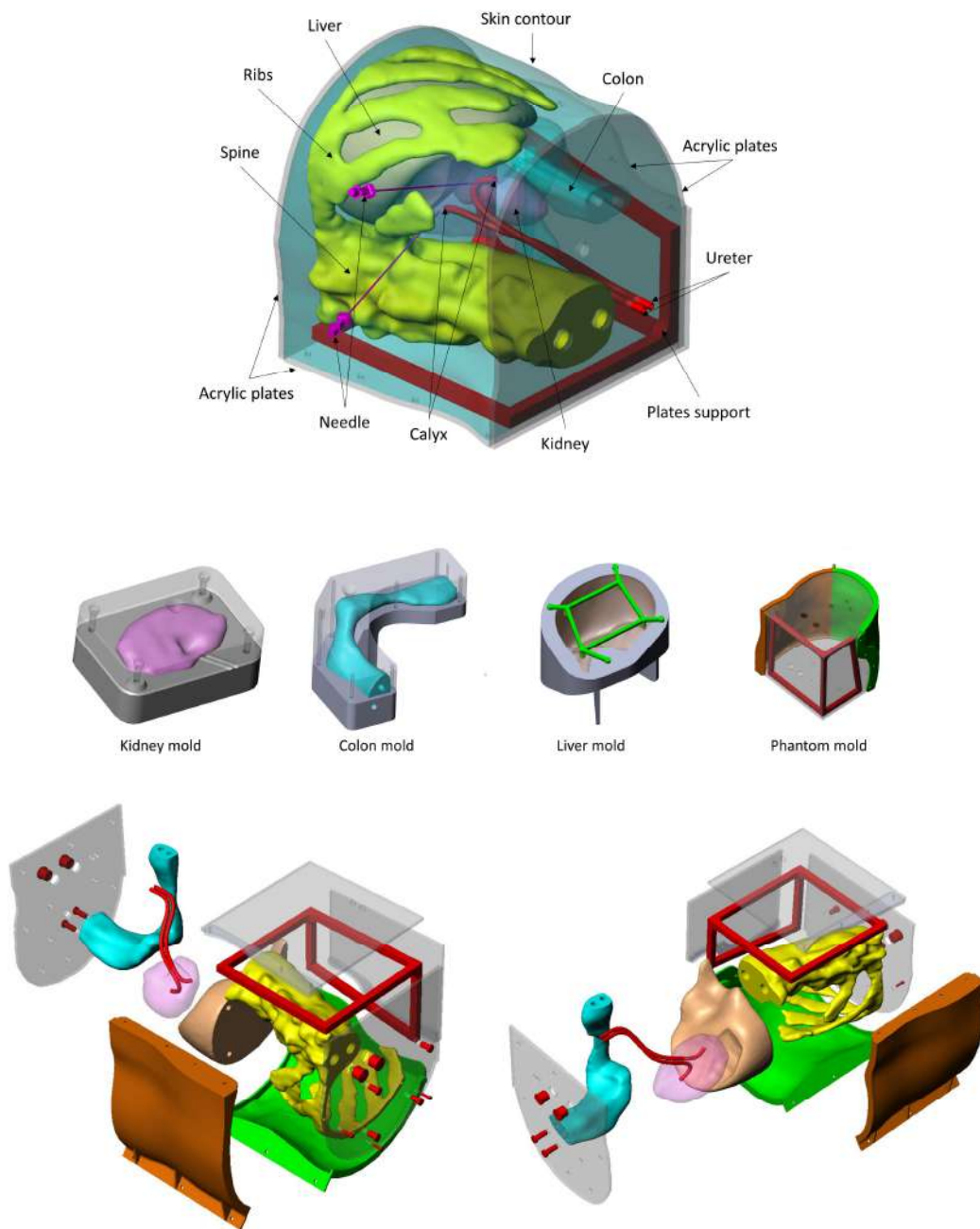
Figure 6.18 – Phantom model, respective molds, and assembling of all components designed in CAD software.

The plates, made of acrylic with 5 mm thickness, were cut using a laser cutting machine (GN640; Gbos Laser Technology Company, Dongguan City, Guangdong Province, China) with a cutting precision of ± 0.04 mm.

The phantom was formed out using two different tissue mimicking materials: polyvinyl alcohol cryogel (PVA-C) and agar. PVA-C was used to create kidney, liver, and colon, while agar was used to fill the abdominal cavity and support the organs.

125

PVA-C was produced by physical cross-linking using freezing and thawing cycles. A deionized water solution consisting of 10 *wt%* PVA (Sigma-Aldrich Corp., St. Louis, MO) with a molecular weight of approximately 89000-98000 and a hydrolysis degree of more than 99% was used. The solution was heated to approximately 95 °C for 2 hours and stirred during the heating process until it became fully dissolved. Then, the solution was gradually cooled down to room temperature. A contrast agent (Telebrix® 35, France) was added to the PVA-C using different percentages to enhance the kidney (4 *wt%*), liver (2 *wt%*), and colon (1 *wt%*) on CT images. Moreover, 2.5 *wt%* of graphite was added to enhance all organs on US images. Both agents were added and stirred by hand. The solutions were left resting for ~10 min to purge any bubbles formed. Next, each solution was poured carefully into the respective mold and placed in a freezer at -20 °C. Then, two consecutive cycles of freezing for 12 hours and thawing for 12 hours were completed for all molds (Figure 6.19 – A).

The agar-based material was composed (*wt%*) by 3% agar-agar; 11% glycerol; 83.25% distilled water; and 0.25% bleach. Specifically, agar, glycerol and distilled water were mixed in a recipient and heated to 95°C for 1 hour. The reagents were stirred during the heating process. Then, it was left cooling at room temperature to 50 °C with continuous stirring. At the end, the bleach was added.
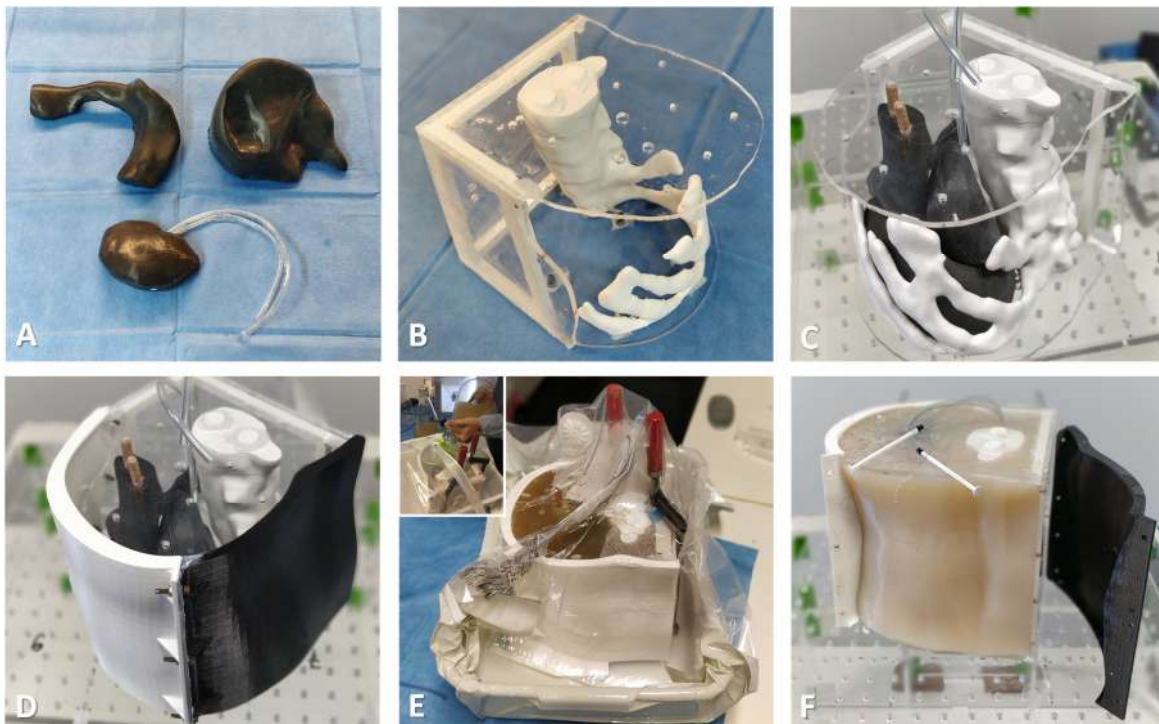
Figure 6.19 – Production of the abdominal phantom model (multi-organ).
(A) Mimicking organs produced using PVA-C (after two freezing- thawing cycles); (B) Assembling of structural components of the phantom; (C) Assembling of mimicking organs; (D) Phantom closed for pouring process using coverings; (E) Hardening in a vacuum to remove remaining air bubbles after pouring process; and (F) Coverings removed.

The phantom was assembled when all components were produced (Figure 6.19 – B). After placing the organs in their predesigned positions aided by specific dowels (Figure 6.19 - C) and the phantom mold closed with coverings (Figure 6.19 - D), the agar-based material was poured, filling the abdominal cavity. Upon placing it under vacuum to remove any remaining air bubbles, it was left hardening for 8 – 10 hours at room temperature (Figure 6.19 - E). After the hardening process, the coverings were removed (Figure 6.19 - F).

Good quality images were obtained for both CT and US, where all anatomical structures were clearly visible (Figure 6.20).
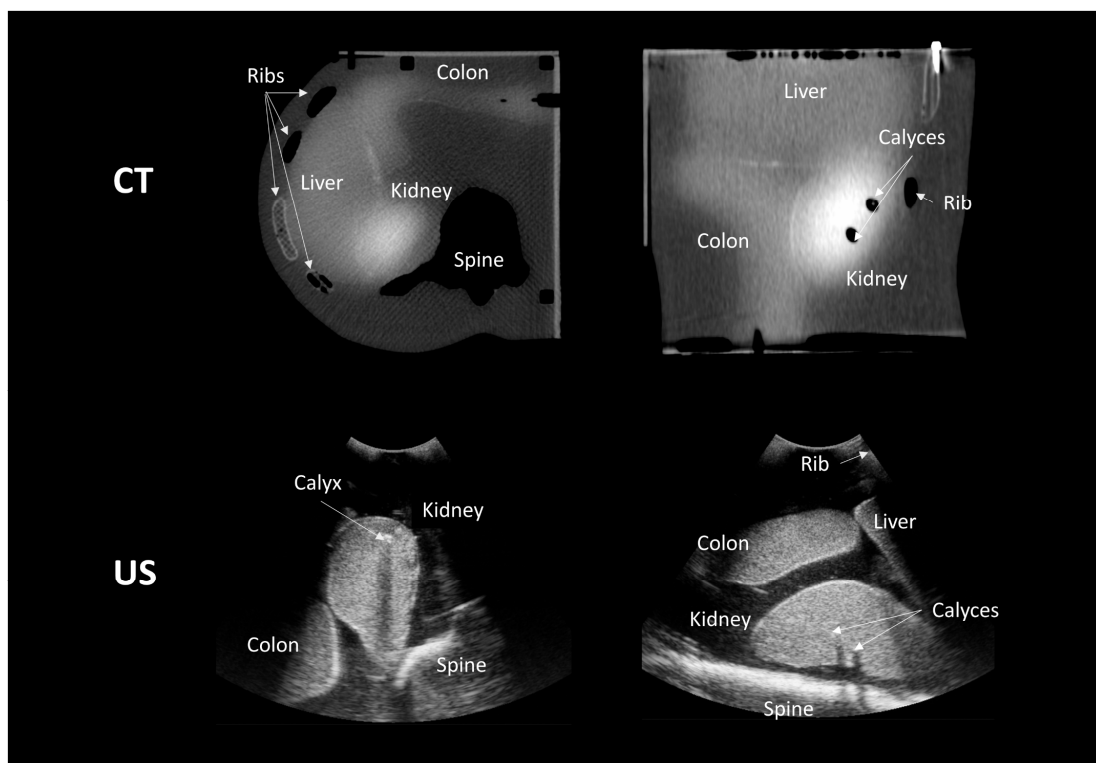
Figure 6.20 – Examples of computed tomography (CT) and ultrasound (US) images of the proposed abdominal phantom model.

6.7.2. Appendix B – Questionnaire

Participant number: _____

Date: _____

Choose five adjectives that describe solution 1 (electromagnetic tracking sensors)?

☐ Safe	☐ Dangerous	☐ Easy-to-use
☐ Difficult-to-use	☐ Fast	☐ Time-consuming
☐ Accurate	☐ Inaccurate	☐ Good for complex punctures
☐ Good for simple punctures	☐ Easy-to-learn	☐ Difficult-to-learn
☐ Comfortable	☐ Uncomfortable	☐ _____
☐ _____	☐ _____	☐ _____

Choose five adjectives that describe solution 2 (electromagnetic tracking sensors with ultrasound image)?

☐ Safe	☐ Dangerous	☐ Easy-to-use
☐ Difficult-to-use	☐ Fast	☐ Time-consuming
☐ Accurate	☐ Inaccurate	☐ Good for complex punctures
☐ Good for simple punctures	☐ Easy-to-learn	☐ Difficult-to-learn
☐ Comfortable	☐ Uncomfortable	☐ _____
☐ _____	☐ _____	☐ _____

Choose five adjectives that describe solution 3 (solution 2 with virtual reality)?

☐ Safe	☐ Dangerous	☐ Easy-to-use
☐ Difficult-to-use	☐ Fast	☐ Time-consuming
☐ Accurate	☐ Inaccurate	☐ Good for complex punctures
☐ Good for simple punctures	☐ Easy-to-learn	☐ Difficult-to-learn
☐ Comfortable	☐ Uncomfortable	☐ _____
☐ _____	☐ _____	☐ _____

Order (1– Best; 3 – Worst) the three solutions according to the following characteristics:

Safe	☐ Solution 1	☐ Solution 2	☐ Solution 3
Easy-to-use	☐ Solution 1	☐ Solution 2	☐ Solution 3
Easy-to-learn	☐ Solution 1	☐ Solution 2	☐ Solution 3
Applicable to complex anatomies	☐ Solution 1	☐ Solution 2	☐ Solution 3
Appropriate to obstructed calyces	☐ Solution 1	☐ Solution 2	☐ Solution 3
Obtain the optimal tract	☐ Solution 1	☐ Solution 2	☐ Solution 3
Improve next surgical steps	☐ Solution 1	☐ Solution 2	☐ Solution 3

What advantages and disadvantages do you observe in solution 3 over solution 1?

Advantages	
Disadvantages	

What advantages and disadvantages do you observe in solution 3 over solution 2?

Advantages	
Disadvantages	

What limitations do you observe in solution 3?

Chapter 7

Conclusions and future

perspectives

7.1. General conclusions

This thesis focused on developing a novel surgical navigation system to safely perform PRA. Using a needle to accurately create a tract from the skin to the renal calyx is still a demanding task to perform, with associated risks. Indeed, a suboptimal puncture can cause injuries to the kidney and/or adjacent organs, compromising the percutaneous access and even the surgical outcome.

Recently, EMT-based solutions have proven to be a promising technique to perform PRA, but some limitations still exist. Aiming to improve these systems' performance and utility in clinical practice, this thesis proposed to integrate data from multiple sources, as preoperative CT, intraoperative ultrasonography, ureteroscopy and EMT, into a single framework to ultimately enhance the guidance feedback provided to the surgeon during PRA. Key contributions towards the development of such framework were presented in each chapter, culminating in the implementation and experimental validation of a novel surgical navigation system.

Given the goal of intraoperatively combine an EMT system with imaging devices, **chapter 2** focused on studying the limitations and differences between two EMT systems, and the influence of simultaneously use ureteroscopy and ultrasonography instruments within the electromagnetic field. The results suggested that flexible ureterorenoscopes do not change the signal of EMT sensors since their precision and accuracy were not affected. This outcome was important not only to define the internal EMT sensor as a target to be reached, but also as the *world origin* for intraoperative US acquisitions and as the reference to attach preoperative data after image fusion (allowing continuous organ-tracking). In contrast, the tested ultrasonography instruments presented mixed results. While the 2D US probe did not significantly influence the signal of the EMT sensor, the 4D US probe distorted the signal of the attached sensor considerably, presumably due to the motorized principle of the latter when capturing 3D images. However, in complementary work, it was verified that the EMT sensor can also be used with a mechanical 4D US probe if attached far from the motor. Nevertheless, given that real-time streaming of volumetric information from 4D US probe is not yet freely available, only bi-plane image capturing may be used. Altogether, one has shown the potential of both types of probes for intraoperative image fusion.

In **chapter 3**, a protocol to create a kidney phantom model was proposed. This phantom model was based on a porcine kidney combined with tissue mimicking material (TMM) and implanted fiducial markers (FMs). The phantom models created from this protocol were used in the following studies and they were fundamental to establish a proper strategy to fuse pre and intraoperative data. Since they were built using porcine kidneys, we were able to test strategies using realistic data where variability in size

and shape was also present, which is common in clinical practice. Besides, the implanted FMs (non-uniformly distributed around the kidney) were essential to perform a rigorous assessment of the fusion strategies, with half being used to define the ground-truth and half used to measure the target registration errors.

Chapter 4 assessed the potential of a surface-based registration strategy and established an optimal US acquisition protocol to fuse 2D US and CT data in the context of PRA. Based on the results obtained in **chapter 2** and using the phantom models of **chapter 3**, acquisitions from 2D and 4D tracked probes were simulated *in silico*, and extensively studied. Parameters such as probe's coverage angle, sweep movement type and spacing between slices were studied using both probes. The tests demonstrated that sweeps along the central longitudinal plane of the kidney with a wider coverage angle and adequate inter-slice spacing improved the final registration for both probes. These results revealed that, with a specific acquisition protocol and parameters, tracked US data can be used to reconstruct a partial 3D representation of the kidney and achieve registration errors similar to the ones obtained if the full 3D kidney model was used. Among the two probes, the 4D one presented the best performance, showing that the use of bi-plane image data, not common in the field of urology, brings benefits to the intraoperative image fusion. Notwithstanding, interesting results were also obtained with the 2D probe (single-plane). Additionally, the influence of the positional variability of the CT model in the registration was studied. This analysis led to the conclusion that an initial and rough pre-alignment of the preoperative data with the intraoperative one is mandatory. Finally, we envision that the proposed *in silico* pipeline could be applied to other similar clinical problems, allowing to simulate and evaluate the best strategies to acquire tracked US images to ultimately improve image fusion.

Following the abovementioned results, a new intraoperative image fusion approach was presented in **chapter 5**. Here, a close to real protocol to fuse CT and US data based on a new strategy was assessed. EMT tracked US probes, a semi-automatic segmentation strategy, and a point-set registration algorithm were combined to accurately fuse a partial US kidney model with a full CT kidney model. A specific protocol was used to calibrate the US probe, and the influence of probe and calibration settings on the final registration was evaluated. The calibration protocol was more effective in the 2D US probe, most likely because the EMT sensor was positioned close to the probe's body when compared to the 4D probe. Regarding the segmentation strategy, it was the first time that the Medical Image Tracking Toolbox (MITT) was used as a tool to segment intraoperative images, which in turn presented promising results. Here, MITT does not capture the natural motion of the organ as originally suggested, but instead captures the motion of the object of interest as a result of sweeping the probe. Since the motion between

frames is estimated within a localized anatomical region-of-interest and anatomically constrained based on its neighbor points, it was possible to estimate the contours in all frames of the sweep from a manual initialization in a single frame. Furthermore, as an emerging algorithm in the field, coherent point drift was revealed to be the most robust algorithm to register pre- and intraoperative point sets in this setting. Its higher performance was suggested to be linked to its capacity to deal with noisy point sets. Overall, the proposed pipeline of segmentation and registration presented interesting results for image fusion in the context of PRA.

Finally, all above-mentioned ideas and strategies were incorporated into a surgical navigation system, which was presented and assessed in **chapter 6**. This navigation software integrates into the same virtual environment data from the EMT system, ureteroscopy, ultrasonography, and computed tomography. Taking advantage of this integrative environment, new guidance information is provided to the surgeon during PRA. The EMT system provides the pose of the needle, catheter, and US probe in real-time. Together with ureteroscopy, the EMT catheter provides a specific target site (*i.e.* renal calyx) to puncture, with the ureteroscopy imaging allowing to verify the adequateness of the performed access. During fusion, the EMT catheter has here a new role since it was used as *world origin*, *i.e.* taking advantage of the rigid relationship between kidney and EMT catheter, misalignments can be compensated during US image acquisition and, consequently, improve the image fusion. Similarly, this rigid relationship was then explored to allow organ-tracking in real-time after fusion. To the author's best knowledge, this is the first time that such strategy is employed in PRA to compensate for internal organ movements. Moreover, ultrasonography data is now enhanced with contours from preoperative data and with the catheter position, as well as the needle trajectory projection and its entry point on the image plane. With this information, the surgeon can better understand the relationship between the needle trajectory, the target site, and the imaging data. Additionally, a needle-based puncture view is proposed to guide the surgeon, whose main idea is to use the needle as a sight and enhance the view with 3D preoperative registered data and guidance tips. The latter include information on how to orient the needle to reach the catheter and how to avoid potential needle collisions with organs.

To compare the potentialities of the proposed system, surgeons tested it against other EMT-based solutions. The results demonstrated that higher performance is achieved with the proposed system. All participants were able to reach the renal calyx in all scenarios, which did not occur with the alternative solutions. The positive feedback provided by the surgeons also demonstrated the benefits of the proposed solution, as they felt safer and more comfortable with the proposed system and considered it easy-to-learn and accurate as well.

Table 7.1 – Comparative table between the conventional techniques (fluoroscopy and ultrasonography [US]) and electromagnetic tracking (EMT)-based solutions (NAV$_{EMT}$, NAV$_{EMT-US}$ and NAV$_{EMT-VR}$).

	FLUOROS.	US	NAV$_{EMT}$ [A.B.]	NAV$_{EMT-US}$ [B.]	NAV$_{EMT-VR}$ [B.]
EQUIPMENT					
EMT	○	○	●	●	●
URETEROSCOPY	○	○	●	●	●
FLUOROSCOPY	●	○	● (planning)	○	○
ULTRASONOGRAPHY	○	●	● (planning)	● (guidance)	● (guidance)
CT	● (pre-op)	● (pre-op)	● (pre-op)	● (pre-op)	● (pre-op & guidance)
PROCEDURAL FEATURES					
INTRAOPERATIVE RADIATION FREE	○	●	○ / ● [D.]	●	●
PUNCTURE TIME [C.]	-	-	▼▼▼	▼▼	▼▼▼
GUIDANCE FEATURES					
ANATOMY ASSESSMENT	2D	2D	None	2D	2D/3D
INTEGRATED IMAGING AND TRACKING	*n.a.*	*n.a.*	○	●	●
NEEDLE TRAJECTORY PROJECTION	○	○	●	●	●
NEEDLE-TARGET DISTANCE	○	○	●	●	●

n.a. – not applicable. ○ / ● – No / Yes.

[A.] Based on Rodrigues *et al.* [79] and Lima *et al.* [80].

[B.] Based on chapter 6.

[C.] Considering US as baseline. Puncture time for fluoroscopy (7.7 min) and US (7.2 min) was obtained from Zhu *et al.* [54].

[D.] Depending on the intraoperative imaging used for planning.

The focus of this thesis was to mitigate limitations that were observed in EMT-based solutions for PRA. Table 1 summarizes and compares some features of conventional techniques, and the EMT solutions tested in **chapter 6**. It is possible to observe that the proposed system, **NAV$_{EMT-VR}$**, brought significant improvements. Indeed, it eliminates intraoperative radiation when compared to fluoroscopy-based guidance; it takes advantage of the superior performance of EMT systems when compared to fluoroscopy and ultrasonography to target the desired calyx; it adds the possibility to simultaneously assess the anatomy during guidance when compared to the solution presented by Rodrigues *et al.* (named here as **NAV$_{EMT}$**); and it provides a 3D perception of the anatomy, something unfeasible if one would integrate the EMT system with ultrasonography only (**NAV$_{EMT-US}$**). Contrariwise, one may notice that the setup time (*i.e.* the time needed to prepare the system in the operating room) may be higher for the proposed system. Further work is required to correctly assess the setup time *in-vivo*. Moreover, the *in-vivo* assessment may be crucial to understand which technical and methodological improvements may be required to translate this system to clinical practice (see the section below for further discussion).

In summary, the main objectives of this thesis were accomplished. Altogether, the proposed system may improve PRA by aiding surgeons to obtain safe and accurate access to the kidney.

7.2. Future perspectives

Despite the contributions presented in this work, further improvements to the proposed surgical navigation system may be foreseen, namely allowing the translation of the developed technology to clinical practice. The following sections highlight and discuss some of these potential future developments.

7.2.1. Assessment improvements

Even though the assessment of the proposed system has been made with phantoms with interesting results, animal models would allow the assessment in a closer to real scenario. It would be important to assess the performance of the proposed system with real abdominal anatomy and movements. The results from this assessment would help highlight the advantages of the proposed system and help identify strategies to reduce any limitation before clinical studies. However, animal imaging facilities with CT (or MRI) would be essential to perform these tests, but access to these facilities is not straightforward to obtain. Thus, to accomplish these tests, logistic issues must first be solved.

Moreover, it would be also important to increase the number of participants with different levels of expertise to understand which disadvantages and advantages are highlighted according to each level. This information can be used to optimize the surgical setup and the surgical navigation system.

7.2.2. Technical improvements

Technically, the proposed system is dependent on different technologies. Regarding the EMT system, the accuracy and precision of the EMT sensors decreases in the zones farther from the field generator. This fact can hamper the fusion, especially when the US image acquisition is performed close to the field limits, as occurs in obese patients. Thus, strategies for surgical setup optimization may need to be studied to support the selection of which field generator must be used, where to position the field generator, and which tracking volume should be used according to the patient body. Alternatively, and following recent innovations in the field of EMT, systems with a wider tracking volume could be used [194].

Furthermore, the proposed system requires a calibration between the US probe and the EMT sensor. The calibration process is established between specific settings of the US image, which cannot be changed after calibration. Therefore, strategies to quickly calibrate the US probe in the operating room must be developed. Such strategies may, for example, include a portable calibration phantom (based on

tissue-mimicking materials instead of water) together with an automatic algorithm to enable fast intraoperative temporal and spatial calibration.

On the other hand, a future commercial solution may directly integrate both US and EMT systems, allowing probe calibration to be performed at the factory for all possible image settings. The same integration could be interesting for ureteroscopy, where the EMT sensor could be integrated into the tip of the flexible ureterorenoscope. This would reduce the setup time since there would be no need to insert the catheter into the working channel during the procedure.

7.2.3. Methodological improvements

From a methodological point of view, potential improvements may also be foreseen.

Considering the proposed system, the segmentation of anatomical structures has a crucial role. Indeed, CT segmentation is mandatory to enhance intraoperative data. Our team proposed a method to perform a multi-atlas segmentation [172]. This method was tested in healthy patients with interesting results. However, the extension to non-healthy patients (for example, nephrolithiasis) must be accomplished to evaluate the effectiveness in those cases. Refinement algorithms must be developed to enable a reliable segmentation and enhance more anatomical details such as renal vessels, pelvis, calyces, etc. Additionally, despite the good results, the computational burden of the proposed strategy must be reduced. Currently, the framework takes almost one day to process a 3D CT volume, which is impractical. Thus, optimization of the proposed framework must be accomplished. Another option could be to use deep learning-based strategies, which may have significant impact on improving segmentation and reducing computational time [195]–[198].

Intraoperative US segmentation is also relevant on the pipeline. In this thesis, a semi-automatic strategy is proposed. Despite the interesting results, an automatic algorithm would benefit the reproducibility and the setup time. Hereto, deep learning strategies could have an important role to improve the proposed system. Nonetheless, going forward with this approach would require the collection and annotation of a significant amount of patient data by experts. A multicenter work may accelerate these data curation efforts. These data and algorithms could also be extended to allow the segmentation of different kidney structures, which would improve fusion and intraoperative information.

Regarding intraoperative fusion, the proposed system uses partial US data, but the amount of kidney coverage range was found to be important to improve the fusion. Thus, tools to inform the surgeon if the coverage range gathered is enough must be developed. Moreover, the current solution assumes a rigid alignment between pre- and intraoperative modalities, even though the kidney and, mainly, the

nearby organs are subject to deformations. Nevertheless, note that a non-rigid deformation is usually easier to compute if a reliable rigid initialization is provided. Thus, a rigid transformation would always be necessary first. Moreover, the focus was put on a rigid registration since a partial representation of the kidney is obtained from tracked US data, being more challenging to determine non-rigid deformations from incomplete data. A possible solution to mitigate this problem would be to use 3D/4D US imaging to fully delineate the kidney in intraoperative data and then, use it to perform rigid and non-rigid alignment with the preoperative model. If the same point-set registration strategy is preserved, 3D organ segmentation may be necessary. In this regard, our team has recently proposed a 3D kidney segmentation strategy in US with promising results [199]. Segmenting the nearby organs may benefit the deformation estimation as well, but the computational burden associated with multiple 3D segmentations and registrations may increase the setup time. In addition, as previously mentioned, 3D/4D US imaging is limited by the current technical difficulties in extracting 3D/4D images in real-time from the US system. Significant work and improvements would thus be required in this field. Hereupon, and using the current strategy based on tracked US data, another option could be to three-dimensionally reconstruct the kidney and adjacent organs from partial information. Statistical shape models could be an interesting solution to obtain a close representation of each organ. By estimating the shape coefficients from partial segmented data, it is possible to reconstruct the 3D shape that represents each organ. Indeed, our team is currently exploring this idea using deep learning techniques. The exploration of the concept of 4D statistical shape models together with the information provided by the EMT catheter would be another option to improve motion estimation during PRA.

Visual representation of the uncertainty associated with the needle path can also be improved by propagating the error associated with the instrument tracking, imaging techniques, calibration, segmentation, and registration to the needle tip. One way to propagate and obtain this uncertainty could be through covariance matrices, which represent the noise model of each element [200]. Therefore, noise models must be computed to evolve with this concept and dynamically represent the uncertainty on the software, helping surgeons to make informed decisions.

7.2.4. Other applications

In addition to being used as an assessment tool for image fusion, the phantom model presented in **chapter 3** has the potential for PRA training. In fact, it has the potential to be utilized with different techniques and procedures. Considering the protocol adjustments proposed in **chapter 5**, where the ureter is simulated by assembling a tube to the renal pelvis, access to the renal collecting system is now

possible, enabling procedures such as ureteroscopy or contrast injection for fluoroscopy. Similarly, the multi-organ phantom model proposed in **chapter 6** can be used for training purposes. Although the previous version presents more renal anatomical details, the latter simulates a wider abdominal area. Therefore, studies to evaluate the usability of both types of phantom as a training tool must be performed in the future.

Although the development of this surgical navigation system was primarily focused on accessing the renal calyx in PCNL, as proved in **chapter 6,** once the registration is obtained, the access to different kidney zones is potentiated. This fact opens the scope to different surgical interventions, such as the percutaneous ablation of renal tumors (*e.g.* by radiofrequency, cryoablation or thermal ablation techniques). Moreover, accessing adjacent organs to the kidney could be attractive as well.

Bibliography

[1]   D. A. Bloom, R. J. Morgan, and P. L. Scardino, "Thomas Hillier and percutaneous nephrostomy," *Urology*, vol. 33, no. 4, pp. 346–350, Apr. 1989.

[2]   N. Alwall, "Aspiration biopsy of the kidney, including i.a. a report of a case of amyloidosis diagnosed through aspiration biopsy of the kidney in 1944 and investigated at an autopsy in 1950.," *Acta Med. Scand.*, vol. 143, no. 6, pp. 430–5, Sep. 1952.

[3]   R. M. Kark and R. C. Muehrcke, "Biopsy of kidney in prone position," *Lancet*, vol. 263, no. 6821, pp. 1047–1049, May 1954.

[4]   W. E. Goodwin, W. C. Casey, and W. Woolf, "Percutaneous trocar (needle) nephrostomy in hydronephrosis," *J. Am. Med. Assoc.*, vol. 157, no. 11, pp. 891–894, Mar. 1955.

[5]   W. C. Casey and W. E. Goodwin, "Percutaneous Antegrade Pyelography and Hydronephrosis," *J. Urol.*, vol. 74, no. 1, pp. 164–173, Jul. 1955.

[6]   I. Fernström and B. Johansson, "Percutaneous Pyelolithotomy," *Scand. J. Urol. Nephrol.*, vol. 10, no. 3, pp. 257–259, Jan. 1976.

[7]   P. Alken, G. Hutschenreiter, R. Günther, and M. Marberger, "Percutaneous Stone Manipulation," *J. Urol.*, vol. 125, no. 4, pp. 463–466, Apr. 1981.

[8]   J. E. A. Wickham, M. J. Kellett, and R. A. Miller, "Elective Percutaneous Nephrolithotomy in 50 Patients:an Analysis of the Technique, Results and Complications," *J. Urol.*, vol. 129, no. 5, pp. 904–905, May 1983.

[9]   E. C. White and A. D. Smith, "Percutaneous Stone Extraction from 200 Patients," *J. Urol.*, vol. 132, no. 3, pp. 437–438, Sep. 1984.

[10]   P. K. Reddy *et al.*, "Percutaneous Removal of Renal and Ureteral Calculi: Experience with 400 Cases," *J. Urol.*, vol. 134, no. 4, pp. 662–665, Oct. 1985.

[11]   R. C. Pfister and S. P. Dretler, "Percutaneous chemolysis of renal calculi," *Urol. Radiol.*, vol. 6, no. 1, pp. 138–143, Dec. 1984.

[12]   A. D. Smith, E. Orihuela, and A. R. Crowley, "Percutaneous management of renal pelvic tumors: A treatment option in selected cases," *J. Urol.*, vol. 137, no. 5, pp. 852–856, May 1987.

[13]   A. D. Smith, "Percutaneous ureteral surgery and stenting," *Urology*, vol. 23, no. 5, pp. 37–42, May 1984.

[14]   R. Marcovich and A. D. Smith, "Percutaneous renal access: tips and tricks," *BJU Int.*, vol. 95, no. s2, pp. 78–84, Mar. 2005.

[15]   V. Romero, H. Akpinar, and D. G. Assimos, "Kidney stones: a global picture of prevalence, incidence, and associated risk factors.," *Rev. Urol.*, vol. 12, no. 2–3, pp. e86-96, 2010.

[16]   L. Mayans, "Nephrolithiasis," *Prim. Care Clin. Off. Pract.*, vol. 46, no. 2, pp. 203–212, Jun. 2019.

[17]   K. R. Ghani *et al.*, "Percutaneous Nephrolithotomy: Update, Trends, and Future Directions," *Eur. Urol.*, vol. 70, no. 2, pp. 382–396, Aug. 2016.

[18]   Y. . Türk, C.; Neisius, A.; Petrik, A.; Seitz, C.; Skolarikos, A.; Thomas, K.; Davis, N.F.; Donaldson, J.F.; Lombardo, R.; Grivas, N.; Ruhayel, "European Association of Urology: Guidelines on Urolithiasis." [Online]. Available: https://uroweb.org/guideline/urolithiasis/. [Accessed: 01-Jul-2020].

[19]   I. Sorokin, C. Mamoulakis, K. Miyazawa, A. Rodgers, J. Talati, and Y. Lotan, "Epidemiology of stone disease across the world," *World J. Urol.*, vol. 35, no. 9, pp. 1301–1320, Sep. 2017.

[20]   C. D. Scales, A. C. Smith, J. M. Hanley, and C. S. Saigal, "Prevalence of kidney stones in the United States," *Eur. Urol.*, vol. 62, no. 1, pp. 160–165, Jul. 2012.

[21]   J. A. Antonelli, N. M. Maalouf, M. S. Pearle, and Y. Lotan, "Use of the National Health and Nutrition Examination Survey to Calculate the Impact of Obesity and Diabetes on Cost and Prevalence of Urolithiasis in 2030," *Eur. Urol.*, vol. 66, no. 4, pp. 724–729, Oct. 2014.

[22]   N. L. Miller, B. R. Matlaga, S. C. Kim, and J. E. Lingeman, "Access Techniques for Percutaneous Renal Surgery," in *Interventional Management of Urological Diseases*, S. Baba and Y. Ono, Eds. Tokyo: Springer Japan, 2006, pp. 1–23.

[23]   T. Knoll, M. S. Michel, and P. Alken, "Surgical atlas percutaneous nephrolithotomy: The Mannheim technique," *BJU Int.*, vol. 99, no. 1, pp. 213–231, Jan. 2007.

[24]   D. R. Webb, "Applied Anatomy for Percutaneous Access," in *Percutaneous Renal Surgery*, Cham: Springer International Publishing, 2016, pp. 1–17.

[25]   J. S. Wolf, "Percutaneous Approaches to the Upper Urinary Tract Collecting System | Abdominal Key." [Online]. Available: https://abdominalkey.com/percutaneous-approaches-to-the-upper-urinary-tract-collecting-system/. [Accessed: 05-Jul-2020].

[26]   A. Van Der Merwe, A. Bachmann, and C. Heyns, "Percutaneous Nephrolithotomy (PCNL) - A Manual for the Urologist," 2015.

[27]   V. Macchi *et al.*, "Anatomic and Radiologic Study of Renal Avascular Plane (Brödel's Line) and Its Potential Relevance on Percutaneous and Surgical Approaches to the Kidney," *J. Endourol.*, vol. 32, no. 2, pp. 154–159, Feb. 2018.

[28]   F. J. B. Sampaio and A. H. M. Aragao, "Anatomical Relationship Between the Intrarenal Arteries and the Kidney Collecting System," *J. Urol.*, vol. 143, no. 4, pp. 679–681, Apr. 1990.

[29]   J. M. Boon, B. Shinners, and J. H. Meiring, "Variations of the position of the colon as applied to percutaneous nephrostomy," *Surg. Radiol. Anat.*, vol. 23, no. 6, pp. 421–425, Apr. 2002.

[30]   W. Brisbane, M. R. Bailey, and M. D. Sorensen, "An overview of kidney stone imaging techniques," *Nat. Rev. Urol.*, vol. 13, no. 11, pp. 654–662, Nov. 2016.

[31]   T. Tailly and J. Denstedt, "Innovations in percutaneous nephrolithotomy," *Int. J. Surg.*, vol. 36, no. PD, pp. 665–672, Dec. 2016.

[32]   S. Rais-Bahrami, J. I. Friedlander, B. D. Duty, Z. Okeke, and A. D. Smith, "Difficulties with access in percutaneous renal surgery," *Ther. Adv. Urol.*, vol. 3, no. 2, pp. 59–68, Apr. 2011.

[33]   J. J. M. C. H. de la Rosette, M. P. Laguna, J. J. Rassweiler, and P. Conort, "Training in Percutaneous Nephrolithotomy—A Critical Review," *Eur. Urol.*, vol. 54, no. 5, pp. 994–1003, Nov. 2008.

[34]   O. Negrete-Pulido, M. Molina-Torres, E. Castaño-Tostado, A. M. Loske, and J. Gutiérrez-Aceves, "Percutaneous renal access: The learning curve of a simplified approach," *J. Endourol.*, vol. 24, no. 3, pp. 457–460, Mar. 2010.

[35]   C. L. Lee, J. K. Anderson, and M. Monga, "Residency training in percutaneous renal access: Does it affect urological practice?," *J. Urol.*, vol. 171, no. 2 I, pp. 592–595, Feb. 2004.

[36]   J. M. Speed *et al.*, "The Effect of Physician Specialty Obtaining Access for Percutaneous Nephrolithotomy on Perioperative Costs and Outcomes," *J. Endourol.*, vol. 31, no. 11, pp. 1152–1156, Nov. 2017.

[37]   G. Jayram and B. R. Matlaga, "Contemporary Practice Patterns Associated with Percutaneous Nephrolithotomy Among Certifying Urologists," *J. Endourol.*, vol. 28, no. 11, pp. 1304–1307, Nov. 2014.

[38]   J. de la Rosette *et al.*, "The Clinical Research Office of the Endourological Society Percutaneous Nephrolithotomy Global Study: Indications, Complications, and Outcomes in 5803 Patients," *J. Endourol.*, vol. 25, no. 1, pp. 11–17, Jan. 2011.

[39]   A. A. Ahmad *et al.*, "Current trends in percutaneous nephrolithotomy: an internet-based survey,"

Ther. Adv. Urol., vol. 9, no. 9–10, pp. 219–226, Sep. 2017.

[40]   J. J. Tomaszewski, T. D. Ortiz, B. A. Gayed, M. C. Smaldone, S. V. Jackman, and T. D. Averch, "Renal access by urologist or radiologist during percutaneous nephrolithotomy," *J. Endourol.*, vol. 24, no. 11, pp. 1733–1737, Nov. 2010.

[41]   J. D. Watterson, S. Soon, and K. Jana, "Access Related Complications During Percutaneous Nephrolithotomy: Urology Versus Radiology at a Single Academic Institution," *J. Urol.*, vol. 176, no. 1, pp. 142–145, Jul. 2006.

[42]   M. S. Michel, L. Trojan, and J. J. Rassweiler, "Complications in percutaneous nephrolithotomy.," *Eur. Urol.*, vol. 51, no. 4, pp. 899–906, Apr. 2007.

[43]   G. Labate *et al.*, "The percutaneous nephrolithotomy global study: Classification of complications," *J. Endourol.*, vol. 25, no. 8, pp. 1275–1280, Aug. 2011.

[44]   C. Seitz *et al.*, "Incidence, Prevention, and Management of Complications Following Percutaneous Nephrolitholapaxy," *Eur. Urol.*, vol. 61, no. 1, pp. 146–158, Jan. 2012.

[45]   P. L. Rodrigues, N. F. Rodrigues, J. Fonseca, E. Lima, and J. L. Vilaça, "Kidney Targeting and Puncturing During Percutaneous Nephrolithotomy: Recent Advances and Future Perspectives," *J. Endourol.*, vol. 27, no. 7, pp. 826–834, Jul. 2013.

[46]   F. J. Detmer, J. Hettig, D. Schindele, M. Schostak, and C. Hansen, "Virtual and Augmented Reality Systems for Renal Interventions: A Systematic Review," *IEEE Rev. Biomed. Eng.*, vol. 10, pp. 78–94, Sep. 2017.

[47]   E. Lima, P. L. Rodrigues, M.-C. Rassweiler-Seyfried, and J. L. Vilaça, "New Concepts of Renal Access," in *Smith's Textbook of Endourology*, Chichester, UK: John Wiley & Sons, Ltd, 2018, pp. 244–254.

[48]   I. M. Sabler, I. Katafigiotis, O. N. Gofrit, and M. Duvdevani, "Present indications and techniques of percutaneous nephrolithotomy: What the future holds?," *Asian J. Urol.*, vol. 5, no. 4, pp. 287–294, Oct. 2018.

[49]   D.-D. Nguyen, J. W. Luo, T. Tailly, and N. Bhojani, "Percutaneous Nephrolithotomy Access: A Systematic Review of Intraoperative Assistive Technologies," *J. Endourol.*, vol. 33, no. 5, pp. 358–368, May 2019.

[50]   M. Hajiha and D. D. Baldwin, "New Technologies to Aid in Percutaneous Access," *Urol. Clin. North Am.*, vol. 46, no. 2, pp. 225–243, May 2019.

[51]   S. Andonian *et al.*, "Does Imaging Modality Used for Percutaneous Renal Access Make a Difference? A Matched Case Analysis," *J. Endourol.*, vol. 27, no. 1, pp. 24–28, Jan. 2013.

[52]   K. M. Alotaibi, "Retrograde nephrostomy access for percutaneous nephrolithotomy: a simple and safe technique," *Urolithiasis*, vol. 48, no. 2, pp. 175–181, Apr. 2020.

[53]   D. L. Smith *et al.*, "Radiation Exposure During Continuous and Pulsed Fluoroscopy," *J. Endourol.*, vol. 27, no. 3, pp. 384–388, Mar. 2013.

[54]   W. Zhu *et al.*, "A prospective and randomised trial comparing fluoroscopic, total ultrasonographic, and combined guidance for renal access in mini-percutaneous nephrolithotomy," *BJU Int.*, vol. 119, no. 4, pp. 612–618, Apr. 2017.

[55]   J. B. Wynberg, J. F. Borin, J. Z. Vicena, V. Hannosh, and S. A. Salmon, "Flexible ureteroscopy-directed retrograde nephrostomy for percutaneous nephrolithotomy: Description of a technique," *J. Endourol.*, vol. 26, no. 10, pp. 1268–1274, Oct. 2012.

[56]   F. Khan, J. F. Borin, M. S. Pearle, E. M. McDougall, and R. V. Clayman, "Endoscopically guided percutaneous renal access: 'Seeing is believing,'" *J. Endourol.*, vol. 20, no. 7, pp. 451–455, Jul. 2006.

[57]   M. Alsyouf *et al.*, "Direct Endoscopic Visualization Combined with Ultrasound Guided Access during Percutaneous Nephrolithotomy: A Feasibility Study and Comparison to a Conventional Cohort," *J. Urol.*, vol. 196, no. 1, pp. 227–233, Jul. 2016.

[58] A. D. Zarrabi, J. P. Conradie, C. F. Heyns, C. Scheffer, and K. Schreve, "Development of a computer assisted gantry system for gaining rapid and accurate calyceal access during percutaneous nephrolithotomy," *Int. braz j urol*, vol. 36, no. 6, pp. 738–748, Dec. 2010.

[59] N. Khater *et al.*, "Bench-Top Feasibility Testing of a Novel Percutaneous Renal Access Technique: The Laser Direct Alignment Radiation Reduction Technique (DARRT)," *J. Endourol.*, vol. 30, no. 11, pp. 1155–1160, Nov. 2016.

[60] J. Wu *et al.*, "Novel laser positioning navigation to aid puncture during percutaneous nephrolithotomy: a preliminary report," *World J. Urol.*, vol. 37, no. 6, pp. 1189–1196, Jun. 2019.

[61] M. Wilkinson *et al.*, "PD22-06 Bench-top comparison of conventional bulls-eye, the laser direct alignment radiation reduction technique ans a novel low-radiation targeting needle to reduce fluroscopy during percutaneous renal access," *J. Urol.*, vol. 199, no. 4S, p. e476, Apr. 2018.

[62] R. E. Hopkins and M. Bradley, "In-vitro visualization of biopsy needles with ultrasound: A comparative study of standard and echogenic needles using an ultrasound phantom," *Clin. Radiol.*, vol. 56, no. 6, pp. 499–502, Jun. 2001.

[63] S. Cheung and R. Rohling, "Enhancement of needle visibility in ultrasound-guided percutaneous procedures," *Ultrasound Med. Biol.*, vol. 30, no. 5, pp. 617–624, May 2004.

[64] "Ultrasound Needle Visualization X-Shine | BK Ultrasound." [Online]. Available: https://www.bkmedical.com/x-shine/. [Accessed: 14-Jul-2020].

[65] X. W. Cui, A. Ignee, T. Maros, B. Straub, J. G. Wen, and C. F. Dietrich, "Feasibility and Usefulness of Intra-Cavitary Contrast-Enhanced Ultrasound in Percutaneous Nephrostomy," *Ultrasound Med. Biol.*, vol. 42, no. 9, pp. 2180–2188, Sep. 2016.

[66] M. Usawachintachit, D. T. Tzou, J. Mongan, K. Taguchi, S. Weinstein, and T. Chi, "Feasibility of Retrograde Ureteral Contrast Injection to Guide Ultrasonographic Percutaneous Renal Access in the Nondilated Collecting System," *J. Endourol.*, vol. 31, no. 2, pp. 129–134, Feb. 2017.

[67] Z.-C. Li, K. Li, K. Chen, S. Liang, J. Gu, and L. Wang, "Comparison of 2D and 3D Ultrasound Guided Percutaneous Renal Puncture," in *World Congress on Medical Physics and Biomedical Engineering May 26-31, 2012, Beijing, China*, vol. 39 IFMBE, M. Long, Ed. Berlin, Heidelberg: Springer Berlin Heidelberg, 2013, pp. 708–711.

[68] H. Hongzhang *et al.*, "Usefulness of real-time three-dimensional ultrasonography in percutaneous nephrostomy: an animal study," *BJU Int.*, vol. 122, no. 4, pp. 639–643, Oct. 2018.

[69] P. J. Stolka, P. Foroughi, M. Rendina, C. R. Weiss, G. D. Hager, and E. M. Boctor, "Needle guidance using handheld stereo vision and projection for ultrasound-based interventions.," *Med Image Comput Comput Assist Interv*, vol. 17, no. Pt 2, pp. 684–91, 2014.

[70] A. Thomas *et al.*, "Conventional *vs* Computer-Assisted Stereoscopic Ultrasound Needle Guidance for Renal Access: A Randomized Crossover Bench-Top Trial," *J. Endourol.*, vol. 32, no. 5, pp. 424–430, May 2018.

[71] X. Li, Q. Long, X. Chen, H. Dalin, and H. He, "Real-time ultrasound-guided PCNL using a novel SonixGPS needle tracking system," *Urolithiasis*, vol. 42, no. 4, pp. 341–346, Aug. 2014.

[72] X. Li, Q. Long, X. Chen, D. He, and H. He, "Assessment of the SonixGPS system for its application in real-time ultrasonography navigation-guided percutaneous nephrolithotomy for the treatment of complex kidney stones," *Urolithiasis*, vol. 45, no. 2, pp. 221–227, Apr. 2017.

[73] H. L. Chau, H. C. W. Chan, T. B. T. Li, M. H. P. Cheung, K. M. J. Lam, and H. S. So, "An Innovative Free-Hand Puncture Technique to Reduce Radiation in Percutaneous Nephrolithotomy Using Ultrasound with Navigation System under Magnetic Field: A Single-Center Experience in Hong Kong," *J. Endourol.*, vol. 30, no. 2, pp. 160–164, Feb. 2016.

[74] Y. Chen, H. Zheng, Z. Zang, X. Hong, W. Cai, and Y. Fang, "Real-Time Ultrasound-Guided Percutaneous Nephrolithotomy Using Newly Developed Wireless Portable Ultrasound: A Single-Center Experience," *Surg. Innov.*, vol. 25, no. 4, pp. 333–338, Aug. 2018.

[75]   M. J. Bader, C. Gratzke, M. Seitz, R. Sharma, C. G. Stief, and M. Desai, "The 'all-seeing needle': Initial results of an optical puncture system confirming access in percutaneous nephrolithotomy," *Eur. Urol.*, vol. 59, no. 6, pp. 1054–1059, Jun. 2011.

[76]   M. Ritter, M. C. Rassweiler, and M. S. Michel, "The Uro Dyna-CT enables three-dimensional planned laser-guided complex punctures," *Eur. Urol.*, vol. 68, no. 5, pp. 880–884, Nov. 2015.

[77]   D. Jiao, Z. Zhang, Z. Sun, Y. Wang, and X. Han, "Percutaneous nephrolithotripsy: C-arm CT with 3D virtual navigation in non-dilated renal collecting systems," *Diagnostic Interv. Radiol.*, vol. 24, no. 1, pp. 17–22, Jan. 2018.

[78]   J. Huber *et al.*, "Navigated renal access using electromagnetic tracking: an initial experience," *Surg. Endosc.*, vol. 25, no. 4, pp. 1307–1312, Apr. 2011.

[79]   P. L. Rodrigues *et al.*, "Collecting System Percutaneous Access Using Real-Time Tracking Sensors: First Pig Model In Vivo Experience," *J. Urol.*, vol. 190, no. 5, pp. 1932–1937, Nov. 2013.

[80]   E. Lima *et al.*, "Ureteroscopy-assisted Percutaneous Kidney Access Made Easy: First Clinical Experience with a Novel Navigation System Using Electromagnetic Guidance (IDEAL Stage 1)," *Eur. Urol.*, vol. 72, no. 4, pp. 610–616, Oct. 2017.

[81]   N. A. De Sousa Morais *et al.*, "Ureteroscopy-assisted percutaneous kidney access with a novel navigation system using electromagnetic guidance: An updated clinical series," *Eur. Urol. Suppl.*, vol. 17, no. 4, pp. e2128–e2129, May 2018.

[82]   M. S. Borofsky, M. E. Rivera, C. A. Dauw, A. E. Krambeck, and J. E. Lingeman, "Electromagnetic Guided Percutaneous Renal Access Outcomes Among Surgeons and Trainees of Different Experience Levels: A Pilot Study," *Urology*, vol. 136, pp. 266–271, Feb. 2020.

[83]   L.-M. Su *et al.*, "Robotic Percutaneous Access to the Kidney: Comparison with Standard Manual Access," *J. Endourol.*, vol. 16, no. 7, pp. 471–475, Sep. 2002.

[84]   M. M. Oo *et al.*, "Automated Needle Targeting with X-ray (ANT-X) – Robot-assisted device for percutaneous nephrolithotomy (PCNL) with its first successful use in human.," *J. Endourol.*, Apr. 2018.

[85]   P. Mozer, A. Leroy, Y. Payan, J. Troccaz, E. Chartier-Kastler, and F. Richard, "Computer-assisted access to the kidney.," *Int. J. Med. Robot. Comput. Assist. Surg. MRCAS*, vol. 1, no. 4, pp. 58–66, Dec. 2005.

[86]   P. Mozer *et al.*, "Aid to percutaneous renal access by virtual projection of the ultrasound puncture tract onto fluoroscopic images," *J. Endourol.*, vol. 21, no. 5, pp. 460–465, May 2007.

[87]   T. Oliveira-Santos *et al.*, "Computer aided surgery for percutaneous nephrolithotomy: Clinical requirement analysis and system design," in *2010 Annual International Conference of the IEEE Engineering in Medicine and Biology*, 2010, pp. 442–445.

[88]   Z. Li, J. Gu, J. Chakareski, and L. Wang, "Ultrasound-based surgical navigation for percutaneous renal intervention: In vivo measurements and in vitro assessment," in *2011 18th IEEE International Conference on Image Processing*, 2011, pp. 2185–2188.

[89]   Z.-C. Li, K. Li, H.-L. Zhan, K. Chen, J. Gu, and L. Wang, "Augmenting intraoperative ultrasound with preoperative magnetic resonance planning models for percutaneous renal access," *Biomed. Eng. Online*, vol. 11, no. 1, pp. 60–76, Aug. 2012.

[90]   Z.-C. Li, Geng Niu, K. Li, H.-L. Zhan, Yao-Qin Xie, and L. Wang, "Augmented reality using 3D shape model for ultrasound-guided percutaneous renal access: A pig model study," in *The 7th 2014 Biomedical Engineering International Conference*, 2014, pp. 1–4.

[91]   Z.-C. Li *et al.*, "Augmenting interventional ultrasound using statistical shape model for guiding percutaneous nephrolithotomy: Initial evaluation in pigs," *Neurocomputing*, vol. 144, pp. 58–69, Nov. 2014.

[92]   S. Liang, X. Sheng, L. Zhang, and B. Cao, "Computer-Assisted Percutaneous Renal Access Using Intraoperative Ultrasonography," in *Proceedings of the 2nd International Conference on Computer*

Science and Electronics Engineering (ICCSEE 2013), 2013, vol. 347–350, pp. 1022–1027.

[93]   H. Li, Y. Chen, C. Liu, B. Li, K. Xu, and S. Bao, "Construction of a three-dimensional model of renal stones: comprehensive planning for percutaneous nephrolithotomy and assistance in surgery," *World J. Urol.*, vol. 31, no. 6, pp. 1587–1592, Dec. 2013.

[94]   J. J. Rassweiler *et al.*, "IPad-assisted percutaneous access to the kidney using marker-based navigation: Initial clinical experience," *European Urology*, vol. 61, no. 3. pp. 628–631, Mar-2012.

[95]   M. Müller *et al.*, "Mobile augmented reality for computer-assisted percutaneous nephrolithotomy," *Int. J. Comput. Assist. Radiol. Surg.*, vol. 8, no. 4, pp. 663–675, Jul. 2013.

[96]   M. C. Rassweiler-Seyfried *et al.*, "iPad-assisted percutaneous nephrolithotomy (PCNL): a matched pair analysis compared to standard PCNL," *World J. Urol.*, vol. 38, no. 2, pp. 447–453, Feb. 2020.

[97]   A. Marien *et al.*, "Three-dimensional navigation system integrating position-tracking technology with a movable tablet display for percutaneous targeting," *BJU Int.*, vol. 115, no. 4, pp. 659–665, Apr. 2015.

[98]   T. Ungi *et al.*, "Tracked ultrasonography snapshots enhance needle guidance for percutaneous renal access: a pilot study.," *J. Endourol.*, vol. 28, no. 9, pp. 1040–1045, Sep. 2014.

[99]   D. Zhang, Z. Li, K. Chen, J. Xiong, X. Zhang, and L. Wang, "An optical tracker based robot registration and servoing method for ultrasound guided percutaneous renal access," *Biomed. Eng. Online*, vol. 12, no. 1, p. 47, May 2013.

[100] S. Hamamoto *et al.*, "A New Navigation System of Renal Puncture for Endoscopic Combined Intrarenal Surgery: Real-time Virtual Sonography-guided Renal Access," *Urology*, vol. 109, pp. 44–50, Nov. 2017.

[101] I. Wegner *et al.*, "Pitfalls of electromagnetic tracking in clinical routine using multiple or adjacent sensors," *Int. J. Med. Robot. Comput. Assist. Surg.*, vol. 9, no. 3, pp. 268–273, Sep. 2013.

[102] W. Birkfellner *et al.*, "Systematic distortions in magnetic position digitizers," *Med. Phys.*, vol. 25, no. 11, pp. 2242–2248, Nov. 1998.

[103] D. D. Frantz, A. D. Wiles, S. E. Leis, and S. R. Kirsch, "Accuracy assessment protocols for electromagnetic tracking systems," *Phys. Med. Biol.*, vol. 48, no. 14, pp. 2241–2251, Jul. 2003.

[104] J. B. Hummel *et al.*, "Design and application of an assessment protocol for electromagnetic tracking systems.," *Med. Phys.*, vol. 32, no. 7, pp. 2371–9, Jul. 2005.

[105] J. Hummel *et al.*, "Evaluation of a new electromagnetic tracking system using a standardized assessment protocol," *Phys. Med. Biol.*, vol. 51, no. 10, pp. 205–210, May 2006.

[106] C. Nafis, V. Jensen, L. Beauregard, and P. Anderson, "Method for estimating dynamic EM tracking accuracy of surgical navigation tools," in *Proc. SPIE Med. Imag. Visualizat., Image-Guided Procedures Model*, 2006, vol. 6141, p. 61410K.

[107] E. Wilson *et al.*, "A hardware and software protocol for the evaluation of electromagnetic tracker accuracy in the clinical environment: a multi-center study," in *Proc. SPIE 6509, Medical Imaging 2007: Visualization and Image-Guided Procedures*, 2007, vol. 6509, p. 65092T.

[108] C. Nafis, V. Jensen, and R. von Jako, "Method for evaluating compatibility of commercial electromagnetic (EM) microsensor tracking systems with surgical and imaging tables," in *Proc. SPIE 6918, Medical Imaging 2008: Visualization, Image-Guided Procedures, and Modeling*, 2008, vol. 6918, p. 691820.

[109] D. M. Kwartowitz, M. E. Rettmann, D. R. Holmes III, and R. A. Robb, "A novel technique for analysis of accuracy of magnetic tracking systems used in image guided surgery," in *Proc. SPIE 7625, Medical Imaging 2010: Visualization, Image-Guided Procedures, and Modeling*, 2010, vol. 7625, p. 76251L.

[110] T. Haidegger, B. Sirokai, G. Fenyvesi, L. Kovács, B. Benyó, and Z. Benyó, "Repeatable assessment protocol for electromagnetic trackers," in *Proc. SPIE 8316, Medical Imaging 2012: Image-Guided*

Procedures, Robotic Interventions, and Modeling, 2012, vol. 8316, p. 83161S.

[111] L. Maier-Hein *et al.*, "Standardized assessment of new electromagnetic field generators in an interventional radiology setting.," *Med. Phys.*, vol. 39, no. 6, pp. 3424–34, Jun. 2012.

[112] T. Koivukangas, J. P. Katisko, and J. P. Koivukangas, "Technical accuracy of optical and the electromagnetic tracking systems.," *Springerplus*, vol. 2, no. 1, p. 90, Dec. 2013.

[113] Z. Yaniv, E. Wilson, D. Lindisch, and K. Cleary, "Electromagnetic tracking in the clinical environment," *Med. Phys.*, vol. 36, no. 3, pp. 876–892, Feb. 2009.

[114] M. Matinfar, G. Narayanasamy, L. Gutierrez, R. Chan, and A. Jain, "Absolute vs. relative error characterization of electromagnetic tracking accuracy," in *Proc. SPIE 7625, Medical Imaging 2010: Visualization, Image-Guided Procedures, and Modeling*, 2010, vol. 7625, p. 762524.

[115] L. E. Bø, H. O. Leira, G. A. Tangen, E. F. Hofstad, T. Amundsen, and T. Langø, "Accuracy of electromagnetic tracking with a prototype field generator in an interventional OR setting," *Med. Phys.*, vol. 39, no. 1, pp. 399–406, Dec. 2011.

[116] E. Lugez, H. Sadjadi, D. R. Pichora, R. E. Ellis, S. G. Akl, and G. Fichtinger, "Electromagnetic tracking in surgical and interventional environments: usability study," *Int. J. Comput. Assist. Radiol. Surg.*, vol. 10, no. 3, pp. 253–262, Mar. 2015.

[117] M. Kellermeier, J. Herbolzheimer, S. Kreppner, M. Lotter, V. Strnad, and C. Bert, "Electromagnetic tracking (EMT) technology for improved treatment quality assurance in interstitial brachytherapy.," *J. Appl. Clin. Med. Phys.*, vol. 18, no. 1, pp. 211–222, Jan. 2017.

[118] S. Boutaleb *et al.*, "Performance and suitability assessment of a real-time 3D electromagnetic needle tracking system for interstitial brachytherapy," *J. Contemp. Brachytherapy*, vol. 4, no. 4, pp. 280–289, Aug. 2015.

[119] M. Hastenteufel, M. Vetter, H.-P. Meinzer, and I. Wolf, "Effect of 3D ultrasound probes on the accuracy of electromagnetic tracking systems," *Ultrasound Med. Biol.*, vol. 32, no. 9, pp. 1359–1368, Sep. 2006.

[120] O. V. Solberg *et al.*, "Navigated ultrasound in laparoscopic surgery," *Minim. Invasive Ther. Allied Technol.*, vol. 18, no. 1, pp. 36–53, Jan. 2009.

[121] A. M. Franz *et al.*, "Electromagnetic tracking for US-guided interventions: standardized assessment of a new compact field generator," *Int. J. Comput. Assist. Radiol. Surg.*, vol. 7, no. 6, pp. 813–818, Nov. 2012.

[122] K. März *et al.*, "Interventional real-time ultrasound imaging with an integrated electromagnetic field generator," *Int. J. Comput. Assist. Radiol. Surg.*, vol. 9, no. 5, pp. 759–768, Sep. 2014.

[123] E. Bonmati *et al.*, "Assessment of Electromagnetic Tracking Accuracy for Endoscopic Ultrasound," in *Computer-Assisted and Robotic Endoscopy 2016. Lecture Notes in Computer Science. vol. 10170*, vol. 10170, T. Peters, G.-Z. Yang, N. Navab, K. Mori, X. Luo, T. Reichl, and J. McLeod, Eds. Cham: Springer International Publishing, 2017, pp. 36–47.

[124] A. M. Franz, T. Haidegger, W. Birkfellner, K. Cleary, T. M. Peters, and L. Maier-Hein, "Electromagnetic Tracking in Medicine—A Review of Technology, Validation, and Applications," *IEEE Trans. Med. Imaging*, vol. 33, no. 8, pp. 1702–1725, Aug. 2014.

[125] NDI Europe GmbH, "Aurora V2 User Guide," 2013.

[126] F. L. Markley, Y. Cheng, J. L. Crassidis, and Y. Oshman, "Averaging Quaternions," *J. Guid. Control. Dyn.*, vol. 30, no. 4, pp. 1193–1197, Jul. 2007.

[127] K. Cleary and T. M. Peters, "Image-Guided Interventions: Technology Review and Clinical Applications," *Annu. Rev. Biomed. Eng.*, vol. 12, no. 1, pp. 119–142, Jul. 2010.

[128] A. Leroy, P. Mozer, Y. Payan, and J. Troccaz, "Rigid Registration of Freehand 3D Ultrasound and CT-Scan Kidney Images," in *Medical Image Computing and Computer-Assisted Intervention – MICCAI 2004: 7th International Conference, Saint-Malo, France, September 26-29, 2004. Proceedings, Part I*, C. Barillot, D. R. Haynor, and P. Hellier, Eds. Berlin, Heidelberg: Springer

Berlin Heidelberg, 2004, pp. 837–844.

[129] J. Xiang, S. Gill, C. Y. Nguan, P. Abolmaesumi, and R. N. Rohling, "Registration of ultrasound to CT angiography of kidneys: a porcine phantom study," in *Proceedings of SPIE 7625*, 2010, vol. 7625, pp. 762518–8.

[130] A. Hunt, A. Ristolainen, P. Ross, R. Öpik, A. Krumme, and M. Kruusmaa, "Low cost anatomically realistic renal biopsy phantoms for interventional radiology trainees," *Eur. J. Radiol.*, vol. 82, no. 4, pp. 594–600, Apr. 2013.

[131] A. Ristolainen, P. Ross, J. Gavšin, E. Semjonov, and M. Kruusmaa, "Economically affordable anatomical kidney phantom with calyxes for puncture and drainage training in interventional urology and radiology.," *Acta Radiol. short reports*, vol. 3, no. 5, p. 2047981614534231, Jun. 2014.

[132] F. Adams *et al.*, "Soft 3D-Printed Phantom of the Human Kidney with Collecting System," *Ann. Biomed. Eng.*, vol. 45, no. 4, pp. 963–972, Apr. 2017.

[133] S. M. Thompson *et al.*, "Porcine ex vivo liver phantom for dynamic contrast-enhanced computed tomography: development and initial results.," *Invest. Radiol.*, vol. 46, no. 9, pp. 586–93, Sep. 2011.

[134] T. H. Baron and T. M. DeSimio, "New ex-vivo porcine model for endoscopic ultrasound-guided training in transmural puncture and drainage of pancreatic cysts and fluid collections (with videos).," *Endosc. ultrasound*, vol. 4, no. 1, pp. 34–9, 2015.

[135] C. J. Teirlinck *et al.*, "Development of an example flow test object and comparison of five of these test objects, constructed in various laboratories.," *Ultrasonics*, vol. 36, no. 1–5, pp. 653–60, Feb. 1998.

[136] M. Earle, G. De Portu, and E. DeVos, "Agar ultrasound phantoms for low-cost training without refrigeration," *African J. Emerg. Med.*, vol. 6, no. 1, pp. 18–23, Mar. 2016.

[137] N. Bao *et al.*, "Fiducial markers configuration optimization in image-guided surgery," *Biomed. Mater. Eng.*, vol. 24, no. 6, pp. 3361–3371, 2014.

[138] B. K. P. Horn, "Closed-form solution of absolute orientation using unit quaternions," *J. Opt. Soc. Am. A*, vol. 4, no. 4, p. 629, Apr. 1987.

[139] K. Hansen, M. Nielsen, and C. Ewertsen, "Ultrasonography of the Kidney: A Pictorial Review," *Diagnostics*, vol. 6, no. 1, p. 2, Dec. 2015.

[140] D. Lee *et al.*, "Construction of kidney phantom model with acoustic shadow by rib bones and respiratory organ motion," in *AIP Conference Proceedings*, 2017, vol. 1821, no. 1, p. 150007.

[141] W. Wein, S. Brunke, A. Khamene, M. R. Callstrom, and N. Navab, "Automatic CT-ultrasound registration for diagnostic imaging and image-guided intervention.," *Med. Image Anal.*, vol. 12, no. 5, pp. 577–585, Oct. 2008.

[142] P. L. Rodrigues *et al.*, "Preliminary clinical trial in percutaneous nephrolithotomy using a real-time navigation system for percutaneous kidney access," in *Proc. SPIE 9036, Medical Imaging 2014: Image-Guided Procedures, Robotic Interventions, and Modeling*, 2014, vol. 9036, p. 903606.

[143] P. L. Rodrigues, N. F. Rodrigues, J. C. Fonseca, and J. L. Vilaça, "Validation of percutaneous puncture trajectory during renal access using 4D ultrasound reconstruction," in *Proc. SPIE 9415, Medical Imaging 2015: Image-Guided Procedures, Robotic Interventions, and Modeling*, 2015, vol. 9415, p. 94152D.

[144] J. B. A. B. Maintz and M. A. Viergever, "A survey of medical image registration," *Med. Image Anal.*, vol. 2, no. 1, pp. 1–36, Mar. 1998.

[145] M. A. Viergever, J. B. A. Maintz, S. Klein, K. Murphy, M. Staring, and J. P. W. Pluim, "A survey of medical image registration – under review," *Med. Image Anal.*, vol. 33, no. 1, pp. 140–144, Oct. 2016.

[146] F. Alam, S. U. Rahman, S. Ullah, and K. Gulati, "Medical image registration in image guided

surgery: Issues, challenges and research opportunities," *Biocybern. Biomed. Eng.*, vol. 38, no. 1, pp. 71–89, Jan. 2018.

[147] E. Ferrante and N. Paragios, "Slice-to-volume medical image registration: A survey," *Med. Image Anal.*, vol. 39, pp. 101–123, Jul. 2017.

[148] A. Ahmad, D. Cool, B. H. Chew, S. E. Pautler, and T. M. Peters, "3D segmentation of kidney tumors from freehand 2D ultrasound," in *Proc. SPIE 6141, Medical Imaging 2006: Visualization, Image-Guided Procedures, and Display*, 2006, vol. 6141, p. 61410S.

[149] J. Seo *et al.*, "Biplane US-Guided Real-Time Volumetric Target Pose Estimation Method for Theragnostic HIFU System," *J. Robot. Mechatronics*, vol. 23, no. 3, pp. 400–407, Jun. 2011.

[150] N. Koizumi *et al.*, "Robust kidney stone tracking for a non-invasive ultrasound theragnostic system-Servoing performance and safety enhancement-," in *2011 IEEE International Conference on Robotics and Automation*, 2011, pp. 2443–2450.

[151] J. Seo *et al.*, "Visual servoing for a US-guided therapeutic HIFU system by coagulated lesion tracking: a phantom study," *Int. J. Med. Robot. Comput. Assist. Surg.*, vol. 7, no. 2, pp. 237–247, Jun. 2011.

[152] J. Seo, N. Koizumi, M. Mitsuishi, and N. Sugita, "Ultrasound image based visual servoing for moving target ablation by high intensity focused ultrasound," *Int. J. Med. Robot. Comput. Assist. Surg.*, vol. 13, no. 4, p. e1793, Dec. 2017.

[153] D. Barbosa, T. Dietenbeck, J. Schaerer, J. D'hooge, D. Friboulet, and O. Bernard, "B-spline explicit active surfaces: an efficient framework for real-time 3-D region-based segmentation.," *IEEE Trans. Image Process.*, vol. 21, no. 1, pp. 241–51, Jan. 2012.

[154] S. Queiros, P. Morais, D. Barbosa, J. C. Fonseca, J. L. Vilaca, and J. D'Hooge, "MITT: Medical Image Tracking Toolbox," *IEEE Trans. Med. Imaging*, vol. 37, no. 11, pp. 2547–2557, Nov. 2018.

[155] L. Shi, W. Liu, H. Zhang, Y. Xie, and D. Wang, "A survey of GPU-based medical image computing techniques.," *Quant. Imaging Med. Surg.*, vol. 2, no. 3, pp. 188–206, Sep. 2012.

[156] E. Smistad, T. L. Falch, M. Bozorgi, A. C. Elster, and F. Lindseth, "Medical image segmentation on GPUs – A comprehensive review," *Med. Image Anal.*, vol. 20, no. 1, pp. 1–18, Feb. 2015.

[157] J. Gomes-Fonseca *et al.*, "A Dual-Modal CT/US Kidney Phantom Model for Image-Guided Percutaneous Renal Access," in *Lecture Notes in Computational Vision and Biomechanics*, vol. 27, Springer Netherlands, 2018, pp. 378–387.

[158] R. Kikinis, S. D. Pieper, and K. G. Vosburgh, "3D Slicer: A Platform for Subject-Specific Image Analysis, Visualization, and Clinical Support," in *Intraoperative Imaging and Image-Guided Therapy*, New York, NY: Springer New York, 2014, pp. 277–289.

[159] J. Gomes-Fonseca *et al.*, "A Dual-Modal CT/US Kidney Phantom Model for Image-Guided Percutaneous Renal Access," *Mendeley Data, v1*. 18-Oct-2018.

[160] C. Chu *et al.*, "Ultrasound-Guided Renal Access for Percutaneous Nephrolithotomy: A Description of Three Novel Ultrasound-Guided Needle Techniques," *J. Endourol.*, vol. 30, no. 2, pp. 153–158, Feb. 2016.

[161] S. Rusinkiewicz and M. Levoy, "Efficient variants of the ICP algorithm," in *Proceedings Third International Conference on 3-D Digital Imaging and Modeling*, 2001, pp. 145–152.

[162] P. J. Besl and N. D. McKay, "A method for registration of 3-D shapes," *IEEE Trans. Pattern Anal. Mach. Intell.*, vol. 14, no. 2, pp. 239–256, Feb. 1992.

[163] A. Segal, D. Haehnel, and S. Thrun, "Generalized-ICP," in *Robotics: Science and Systems V*, 2009, pp. 1–8.

[164] B. Bellekens, V. Spruyt, and M. Weyn, "A Survey of Rigid 3D Pointcloud Registration Algorithms," in *AMBIENT 2014, The Fourth International Conference on Ambient Computing, Applications, Services and Technologies. 2014.*, 2014, no. c, pp. 8–13.

[165] B. Bellekens, V. Spruyt, R. Berkvens, R. Penne, and M. Weyn, "A Benchmark Survey of Rigid 3D

Point Cloud Registration Algorithms," *Int. J. Adv. Intell. Syst.*, vol. 8, no. 1, pp. 118–127, 2015.

[166] H. M. Kjer and J. Wilm, "Evaluation of surface registration algorithms for PET motion correction," Technical University of Denmark, 2010.

[167] P. Lang, M. W. A. Chu, D. Bainbridge, G. M. Guiraudon, D. L. Jones, and T. M. Peters, "Surface-Based CT–TEE Registration of the Aortic Root," *IEEE Trans. Biomed. Eng.*, vol. 60, no. 12, pp. 3382–3390, Dec. 2013.

[168] P. Lang, M. Rajchl, F. Li, and T. M. Peters, "Towards Model-Enhanced Real-Time Ultrasound Guided Cardiac Interventions," in *2011 International Conference on Intelligent Computation and Bio-Medical Instrumentation*, 2011, pp. 89–92.

[169] M. Ciganovic, F. Ozdemir, F. Pean, P. Fuernstahl, C. Tanner, and O. Goksel, "Registration of 3D freehand ultrasound to a bone model for orthopedic procedures of the forearm," *Int. J. Comput. Assist. Radiol. Surg.*, vol. 13, no. 6, pp. 827–836, Jun. 2018.

[170] E. Smistad and F. Lindseth, "Real-Time Automatic Artery Segmentation, Reconstruction and Registration for Ultrasound-Guided Regional Anaesthesia of the Femoral Nerve.," *IEEE Trans. Med. Imaging*, vol. 35, no. 3, pp. 752–61, Mar. 2016.

[171] H. R. Torres, S. Queirós, P. Morais, B. Oliveira, J. C. Fonseca, and J. L. Vilaça, "Kidney segmentation in ultrasound, magnetic resonance and computed tomography images: A systematic review," *Comput. Methods Programs Biomed.*, vol. 157, pp. 49–67, Apr. 2018.

[172] B. Oliveira *et al.*, "A novel multi-atlas strategy with dense deformation field reconstruction for abdominal and thoracic multi-organ segmentation from computed tomography," *Med. Image Anal.*, vol. 45, pp. 108–120, Apr. 2018.

[173] J. Gomes-Fonseca *et al.*, "Surface-based registration between CT and US for image-guided percutaneous renal access - A feasibility study," *Med. Phys.*, vol. 46, no. 3, pp. 1115–1126, Mar. 2019.

[174] A. Lasso, T. Heffter, A. Rankin, C. Pinter, T. Ungi, and G. Fichtinger, "PLUS: Open-Source Toolkit for Ultrasound-Guided Intervention Systems," *IEEE Trans. Biomed. Eng.*, vol. 61, no. 10, pp. 2527–2537, Oct. 2014.

[175] J. Tokuda *et al.*, "OpenIGTLink: an open network protocol for image-guided therapy environment," *Int. J. Med. Robot. Comput. Assist. Surg.*, vol. 5, no. 4, pp. 423–434, Dec. 2009.

[176] D. Barbosa, B. Heyde, T. Dietenbeck, D. Friboulet, J. D'hooge, and O. Bernard, "Fast Left Ventricle Tracking in 3D Echocardiographic Data Using Anatomical Affine Optical Flow," in *Lecture Notes in Computer Science (including subseries Lecture Notes in Artificial Intelligence and Lecture Notes in Bioinformatics)*, vol. 7945 LNCS, Springer, Berlin, Heidelberg, 2013, pp. 191–199.

[177] S. Queirós, J. L. Vilaça, P. Morais, J. C. Fonseca, J. D'hooge, and D. Barbosa, "Fast left ventricle tracking using localized anatomical affine optical flow," *Int. j. numer. method. biomed. eng.*, vol. 33, no. 11, p. e2871, Nov. 2017.

[178] S.-Y. Guan, T.-M. Wang, C. Meng, and J.-C. Wang, "A Review of Point Feature Based Medical Image Registration," *Chinese J. Mech. Eng.*, vol. 31, no. 1, p. 76, Dec. 2018.

[179] H. Zhu *et al.*, "A Review of Point Set Registration: From Pairwise Registration to Groupwise Registration," *Sensors*, vol. 19, no. 5, p. 1191, Mar. 2019.

[180] A. Myronenko and Xubo Song, "Point Set Registration: Coherent Point Drift," *IEEE Trans. Pattern Anal. Mach. Intell.*, vol. 32, no. 12, pp. 2262–2275, Dec. 2010.

[181] T. K. Chen, A. D. Thurston, R. E. Ellis, and P. Abolmaesumi, "A Real-Time Freehand Ultrasound Calibration System with Automatic Accuracy Feedback and Control," *Ultrasound Med. Biol.*, vol. 35, no. 1, pp. 79–93, Jan. 2009.

[182] G. Carbajal, A. Lasso, Á. Gómez, and G. Fichtinger, "Improving N-wire phantom-based freehand ultrasound calibration," *Int. J. Comput. Assist. Radiol. Surg.*, vol. 8, no. 6, pp. 1063–1072, Nov. 2013.

[183]   J. Gomes-Fonseca *et al.*, "Technical Note: Assessment of electromagnetic tracking systems in a surgical environment using ultrasonography and ureteroscopy instruments for percutaneous renal access," *Med. Phys.*, vol. 47, no. 1, pp. 19–26, Jan. 2020.

[184]   K. Martin and D. Spinks, "Measurement of the speed of sound in ethanol/water mixtures," *Ultrasound Med. Biol.*, vol. 27, no. 2, pp. 289–291, Feb. 2001.

[185]   G. M. Treece, A. H. Gee, R. W. Prager, C. J. C. Cash, and L. H. Berman, "High-definition freehand 3-D ultrasound," *Ultrasound Med. Biol.*, vol. 29, no. 4, pp. 529–546, Apr. 2003.

[186]   E. M. Moult, A. Lasso, T. Ungi, C. Pinter, M. Welch, and G. Fichtinger, "Improved Temporal Calibration of Tracked Ultrasound: An Open-Source Solution," *J. Med. Robot. Res.*, vol. 02, no. 04, p. 1750008, Dec. 2017.

[187]   D. Chetverikov, D. Stepanov, and P. Krsek, "Robust Euclidean alignment of 3D point sets: The trimmed iterative closest point algorithm," *Image Vis. Comput.*, vol. 23, no. 3, pp. 299–309, Mar. 2005.

[188]   Y. Chen and G. Medioni, "Object modelling by registration of multiple range images," *Image Vis. Comput.*, vol. 10, no. 3, pp. 145–155, Apr. 1992.

[189]   Bing Jian and B. C. Vemuri, "Robust Point Set Registration Using Gaussian Mixture Models," *IEEE Trans. Pattern Anal. Mach. Intell.*, vol. 33, no. 8, pp. 1633–1645, Aug. 2011.

[190]   J. Vongkulbhisal, F. De la Torre, and J. P. Costeira, "Discriminative Optimization: Theory and Applications to Point Cloud Registration," in *2017 IEEE Conference on Computer Vision and Pattern Recognition (CVPR)*, 2017, vol. 2017-Janua, pp. 3975–3983.

[191]   S. Yin *et al.*, "Automatic kidney segmentation in ultrasound images using subsequent boundary distance regression and pixelwise classification networks," *Med. Image Anal.*, vol. 60, p. 101602, Feb. 2020.

[192]   L. Peng, G. Li, M. Xiao, and L. Xie, "Robust CPD Algorithm for Non-Rigid Point Set Registration Based on Structure Information," *PLoS One*, vol. 11, no. 2, p. e0148483, Feb. 2016.

[193]   A. Formella and C. Gill, "Ray tracing: A quantitative analysis and a new practical algorithm," *Vis. Comput.*, vol. 11, no. 9, pp. 465–476, Sep. 1995.

[194]   F. Attivissimo, A. M. L. Lanzolla, S. Carlone, P. Larizza, and G. Brunetti, "A novel electromagnetic tracking system for surgery navigation," *Comput. Assist. Surg.*, vol. 23, no. 1, pp. 42–52, Jan. 2018.

[195]   G. Litjens *et al.*, "A survey on deep learning in medical image analysis," *Med. Image Anal.*, vol. 42, pp. 60–88, Dec. 2017.

[196]   J. S. Suri, "State-of-the-art review on deep learning in medical imaging," *Front. Biosci.*, vol. 24, no. 3, p. 4725, Jan. 2019.

[197]   N. Tajbakhsh, L. Jeyaseelan, Q. Li, J. N. Chiang, Z. Wu, and X. Ding, "Embracing imperfect datasets: A review of deep learning solutions for medical image segmentation.," *Med. Image Anal.*, vol. 63, p. 101693, Jul. 2020.

[198]   Y. Fu, Y. Lei, T. Wang, W. J. Curran, T. Liu, and X. Yang, "Deep learning in medical image registration: a review," *Phys. Med. Biol.*, vol. 65, no. 20, p. 20TR01, Oct. 2020.

[199]   H. R. Torres *et al.*, "Kidney Segmentation in Three-Dimensional Ultrasound Images using a Fast Phase-based Approach," *IEEE Trans. Ultrason. Ferroelectr. Freq. Control*, vol. PP, pp. 1–1, Nov. 2020.

[200]   A. L. Simpson, B. Ma, E. M. Vasarhelyi, D. P. Borschneck, R. E. Ellis, and A. James Stewart, "Computation and visualization of uncertainty in surgical navigation," *Int. J. Med. Robot. Comput. Assist. Surg.*, vol. 10, no. 3, pp. 332–343, Sep. 2014.